

**Optimierung von radialen Verdichterlaufrädern
unter Berücksichtigung empirischer und
analytischer Vorinformationen mittels eines
mehrstufigen Sampling Verfahrens**

(Optimization of Centrifugal Compressor Impellers by a
Multi-fidelity Sampling Method Taking Analytical and
Empirical Information into Account)

DISSERTATION

zur Erlangung des akademischen Grades
Doktor-Ingenieur (Dr.-Ing.)

eingereicht an der Fakultät Bauingenieurwesen
der Bauhaus-Universität Weimar

vorgelegt von
M.Eng. Christoph Schemmann
geb. am 20.07.1982 in Hagen

Weimar, Juli 2018

1. Gutachter: Prof. Dr.-Ing. habil. Carsten Könke
2. Gutachter: Prof. Dr.-Ing. Tim Ricken
3. Gutachter: Prof. Dr.-Ing. Marius Geller

Tag der Disputation: 28.05.2019

Für Gina und Alexander.

“The story so far:

In the beginning the universe was created.

This has made a lot of people very angry and
been widely regarded as a bad move.”

Douglas Adams (1952-2001), *The Restaurant at the End of the Universe*

Acknowledgments

I thank Prof. Dr.-Ing. habil. Carsten Könke and Prof. Dr.-Ing. Marius Geller for giving me the opportunity to work on an interesting research topic and write this PhD thesis at the Bauhaus University Weimar and the Dortmund University of Applied Sciences and Arts, and for their professional advice. Furthermore, I would like to thank Prof. Dr.-Ing. Tim Ricken for taking the position of a co-examiner of this thesis. Finally, I thank Dr.-Ing. habil. Thomas Most for establishing the contact to the Bauhaus University Weimar, many interesting technical discussions and the helpful advices.

I thank the team at the research center “Computer Simulation in Mechanical Engineering“ at the Dortmund University of Applied Sciences and Arts. My special thanks go to Dipl.-Ing. Norbert Kluck who supported my work by countless technical discussions and advices.

I would also like to thank all people who supported me in writing this thesis, especially my wife Gina, my son Alexander and my parents. Without their continuous support and understanding this work would not have been possible.

To conclude, I thank the PhD funding of the Dortmund University of Applied Sciences and Arts which supported my work.

Abstract

Turbomachinery plays an important role in many cases of energy generation or conversion. Therefore, turbomachinery is a promising approaching point for optimization in order to increase the efficiency of energy use. In recent years, the use of automated optimization strategies in combination with numerical simulation has become increasingly popular in many fields of engineering. The complex interactions between fluid and solid mechanics encountered in turbomachines on the one hand and the high computational expense needed to calculate the performance on the other hand, have, however, prevented a widespread use of these techniques in this field of engineering. The objective of this work was the development of a strategy for efficient metamodel based optimization of centrifugal compressor impellers. In this context, the main focus is the reduction of the required numerical expense. The central idea followed in this research was the incorporation of preliminary information acquired from low-fidelity computation methods and empirical correlations into the sampling process to identify promising regions of the parameter space. This information was then used to concentrate the numerically expensive high-fidelity computations of the fluid dynamic and structure mechanic performance of the impeller in these regions while still maintaining a good coverage of the whole parameter space. The development of the optimization strategy can be divided into three main tasks. Firstly, the available preliminary information had to be researched and rated. This research identified loss models based on one dimensional flow physics and empirical correlations as the best suited method to predict the aerodynamic performance. The loss models were calibrated using available performance data to obtain a high prediction quality. As no sufficiently exact models for the prediction of the mechanical loading of the impeller could be identified, a metamodel based on finite element computations was chosen for this estimation. The second task was the development of a sampling method which concentrates samples in regions of the parameter space where high quality designs are predicted by the preliminary information while maintaining a good overall coverage. As available methods like rejection sampling or Markov-chain Monte-Carlo methods did not meet the requirements in terms of sample distribution and input correlation, a new multi-fidelity sampling method called “Filtered Sampling“ has been developed. The last task was the development of an automated computational workflow. This workflow encompasses geometry parametrization, geometry generation, grid generation and computation of the aerodynamic performance and the structure mechanic loading. Special emphasis was put into the development of a geometry parametrization strategy based on fluid mechanic considerations to prevent the generation of physically inexpedient designs. Finally, the optimization strategy, which utilizes the previously developed tools, was successfully employed to carry out three optimization tasks. The efficiency of the method was proven by the first and second testcase where an existing

compressor design was optimized by the presented method. The results were comparable to optimizations which did not take preliminary information into account, while the required computational expense could be halved. In the third testcase, the method was applied to generate a new impeller design. In contrast to the previous examples, this optimization featured larger variations of the impeller designs. Therefore, the applicability of the method to parameter spaces with significantly varying designs could be proven, too.

Kurzfassung

Turbomaschinen sind eine entscheidende Komponente in vielen Energiewandlungs- oder Energieerzeugungsprozessen und daher als vielversprechender Ansatzpunkt für eine Effizienzsteigerung der Energie- und Ressourcennutzung anzusehen. In Laufe des letzten Jahrzehnts haben automatisierte Optimierungsmethoden in Verbindung mit numerischer Simulation zunehmend breitere Verwendung als Mittel zur Effizienzsteigerung in vielen Bereichen der Ingenieurwissenschaften gefunden. Allerdings standen die komplexen Interaktionen zwischen Strömungs- und Strukturmechanik sowie der hohe numerische Aufwand einem weitverbreiteten Einsatz dieser Methoden im Turbomaschinenbereich bisher entgegen. Das Ziel dieser Forschungsaktivität ist die Entwicklung einer effizienten Strategie zur metamodelbasierten Optimierung von radialen Verdichterlaufrädern. Dabei liegt der Schwerpunkt auf einer Reduktion des benötigten numerischen Aufwandes. Der in diesem Vorhaben gewählte Ansatz ist das Einbeziehen analytischer und empirischer Vorinformationen ("low-fidelity") in den Sampling Prozess, um vielversprechende Bereiche des Parameterraumes zu identifizieren. Diese Informationen werden genutzt um die aufwendigen numerischen Berechnungen ("high-fidelity") des strömungs- und strukturmechanischen Verhaltens der Laufräder in diesen Bereichen zu konzentrieren, während gleichzeitig eine ausreichende Abdeckung des gesamten Parameterraumes sichergestellt wird. Die Entwicklung der Optimierungsstrategie ist in drei zentrale Arbeitspakete aufgeteilt. In einem ersten Schritt werden die verfügbaren empirischen und analytischen Methoden gesichtet und bewertet. In dieser Recherche sind Verlustmodelle basierend auf eindimensionaler Strömungsmechanik und empirischen Korrelationen als bestgeeignete Methode zur Vorhersage des aerodynamischen Verhaltens der Verdichter identifiziert worden. Um eine hohe Vorhersagegüte sicherzustellen, sind diese Modelle anhand verfügbarer Leistungsdaten kalibriert worden. Da zur Vorhersage der mechanischen Belastung des Laufrades keine brauchbaren analytischen oder empirischen Modelle ermittelt werden konnten, ist hier ein Metamodel basierend auf Finite-Element Berechnungen gewählt worden. Das zweite Arbeitspaket beinhaltet die Entwicklung der angepassten Samplingmethode, welche Samples in Bereichen des Parameterraumes konzentriert, die auf Basis der Vorinformationen als vielversprechend angesehen werden können. Gleichzeitig müssen eine gleichmäßige Abdeckung des gesamten Parameterraumes und ein niedriges Niveau an Eingangskorrelationen sichergestellt sein. Da etablierte Methoden wie Markov-Ketten-Monte-Carlo-Methoden oder die Verwerfungsmethode diese Voraussetzungen nicht erfüllen, ist ein neues, mehrstufiges Samplingverfahren ("Filtered Sampling") entwickelt worden. Das letzte Arbeitspaket umfasst die Entwicklung eines automatisierten Simulations-Workflows. Dieser Workflow umfasst Geometrieparametrisierung, Geometrieerzeugung, Netzerzeugung sowie die Berechnung des aerodynamischen Betriebsverhaltens und der strukturmechanischen Belastung. Dabei liegt ein Schwerpunkt auf

der Entwicklung eines Parametrisierungskonzeptes, welches auf strömungsmechanischen Zusammenhängen beruht, um so physikalisch nicht zielführende Parameterkombinationen zu vermeiden. Abschließend ist die auf den zuvor entwickelten Werkzeugen aufbauende Optimierungsstrategie erfolgreich eingesetzt worden, um drei Optimierungsfragestellungen zu bearbeiten. Im ersten und zweiten Testcase sind bestehende Verdichterlaufräder mit der vorgestellten Methode optimiert worden. Die erzielten Optimierungsergebnisse sind von ähnlicher Güte wie die solcher Optimierungen, die keine Vorinformationen berücksichtigen, allerdings wird nur die Hälfte an numerischem Aufwand benötigt. In einem dritten Testcase ist die Methode eingesetzt worden, um ein neues Laufraddesign zu erzeugen. Im Gegensatz zu den vorherigen Beispielen werden im Rahmen dieser Optimierung stark unterschiedliche Designs untersucht. Dadurch kann an diesem dritten Beispiel aufgezeigt werden, dass die Methode auch für Parameterräume mit stark variierenden Designs funktioniert.

Contents

1	Introduction	1
1.1	Motivation	1
1.2	Aim	3
1.3	Outline	4
2	Theoretical Fundamentals	5
2.1	Thermodynamics	5
2.1.1	Fundamental Laws	5
2.1.1.1	The Equation of Continuity	5
2.1.1.2	The First Law of Thermodynamics	5
2.1.1.3	The Second Law of Thermodynamics	7
2.1.1.4	The Momentum Equation	8
2.1.2	Gas Properties	8
2.1.3	Thermodynamic Processes	9
2.2	Fluid Dynamics	11
2.2.1	Bernoulli's Equation	11
2.2.2	Navier Stokes Equations	11
2.2.2.1	The Conservation of Mass	11
2.2.2.2	The Conservation of Momentum	12
2.2.2.3	The Conservation of Energy	14
2.2.2.4	Further Equations	16
2.2.3	Turbulence	18
2.2.3.1	$k - \varepsilon$ Turbulence Model	19
2.2.3.2	$k - \omega$ Turbulence Model	19
2.2.3.3	SST Turbulence Model	20
2.3	Computational Fluid Dynamics	21
2.3.1	Discretization by Finite Volumes	21
2.4	Turbomachines	22
2.4.1	Dimensionless Numbers for Turbomachines and Similitude	22
2.4.2	Coordinate Systems and Conventions	27
2.4.3	Centrifugal Compressors	29
2.4.4	Operation Characteristics	30
2.4.5	Flow in Centrifugal Compressors	31
2.4.5.1	Euler and Lagrange Description	32
2.4.5.2	Rotating Reference Frame	33
2.4.5.3	Velocity Triangles	35

2.4.5.4 Euler's Turbomachinery Equation	35
2.4.5.5 Flow in the Meridional Plane	37
2.4.5.6 Flow in the Crosswise Plane	37
2.4.5.7 Secondary Flow	39
2.4.5.8 Slip factor	40
2.5 Solid Mechanics	42
2.5.1 Cinematics of the Continuum	42
2.5.2 Stress	46
2.5.3 Material Law	47
2.5.4 Governing equations	48
2.6 Statistics	49
2.6.1 Sampling Methods	49
2.6.1.1 Monte Carlo Simulation	50
2.6.1.2 Latin Hypercube Sampling	50
2.6.2 Metamodeling	51
2.6.2.1 Least Squares Method	51
2.6.2.2 Moving Least Squares	52
2.6.2.3 Kriging	53
2.6.2.4 Error Measurements	54
2.6.2.5 Metamodel of Optimal Prognosis	55
2.7 Optimization	56
2.7.1 Nature Inspired Optimization Methods	57
2.7.1.1 Evolutionary Algorithms	58
2.7.1.2 Particle Swarm Optimization	58
2.8 Computer Graphics	59
2.8.1 Bézier Splines	59
3 Preliminary Information and Low-fidelity Methods	61
3.1 Investigation of Available Information	61
3.1.1 Empirical Correlations	62
3.1.1.1 The Cordier Diagram	62
3.1.1.2 Slip Factor Correlations	62
3.1.1.3 Efficiency Correlations	64
3.1.2 Preliminary Design Methods	65
3.1.3 Loss Model Performance Prediction	67
3.1.4 Stream Surface Performance Prediction	69
3.1.5 Prediction of Structure Mechanical Performance	72
3.2 Review and Selection of Models	73
4 Statistical Model	75
4.1 Investigation of Available Methods	76
4.1.1 Test Functions	77
4.1.2 Acceptance / Rejection Sampling	79

4.1.3 Bayesian Updating	81
4.1.3.1 Metropolis Hastings Algorithm	81
4.1.3.2 Advanced Metropolis Hastings Algorithm	84
4.2 Review and Rating	87
5 Filtered Sampling	89
5.1 Method	90
5.1.1 Implementation	90
5.1.2 Distance Metrics	91
5.1.2.1 Euclidean Distance	91
5.1.2.2 Manhattan Distance	92
5.1.2.3 Mahalanobis Distance	93
5.2 Example	93
6 Computational Model	97
6.1 Preliminary Design	98
6.2 Geometric Modeling	105
6.2.1 Definition of the Meridional Contours	105
6.2.1.1 Definition of the Hub Contour	106
6.2.1.2 Definition of the Shroud Contour	109
6.2.2 Definition of the Leading Edge	113
6.2.3 Definition of the Blade	113
6.2.4 Definition of the Impeller Disc	116
6.2.5 Overview of the Parametrization	117
6.3 One Dimensional Loss Modeling	118
6.3.1 Consideration of Splitter Blades	118
6.3.2 Impeller Meanline Analysis	118
6.3.3 Computation of Losses	123
6.3.4 Characteristic Prediction	129
6.3.5 Model Calibration	130
6.3.5.1 Problem Definition	131
6.3.5.2 Methodology	132
6.3.5.3 Optimization	134
6.3.5.4 Results	135
6.4 Computational Fluid Dynamics Model	139
6.4.1 Grid Generation and Grid Independence	139
6.4.2 Boundary Conditions	141
6.4.3 Characteristics Computation	142
6.4.4 Post Processing	143
6.5 Finite Elements Modeling	145
6.5.1 Boundary Conditions	145
6.5.2 Post Processing	146
6.5.3 Structure Mechanical Metamodel	147
6.6 Workflow	148

7 Application and Proof-of-Concept	151
7.1 Testcase 1: Mid-Pressure Impeller Design-Optimization	152
7.1.1 DOE results	155
7.1.2 Metamodel results	158
7.1.3 Optimization results	162
7.2 Testcase 2: High-Pressure Impeller Design-Optimization	165
7.2.1 DOE results	169
7.2.2 Metamodel results	172
7.2.3 Optimization results	176
7.3 Testcase 3: Design by Optimization of a Mid-Pressure Impeller	179
7.3.1 DOE results	181
7.3.2 Metamodel Results	182
7.3.3 Optimization results	185
8 Conclusions	187
Bibliography	193
Academic Curriculum Vitae	209

Acronyms

Notation	Description
CAE	Computer Aided Engineering
CFD	Computational Fluid Dynamics
CoD	Coefficient of Determination
CoP	Coefficient of Prognosis
DOE	Design of Experiments
FEA	Finite Element Analysis
MOP	Metamodel of Optimal Prognosis
RANS	Reynolds Averaged Navier-Stokes-Equations
RMSE	Root Mean Square Error
SST	Shear Stress Transport

List of Symbols

Notation	Description
A	area
a	acceleration
\mathcal{B}	continuum body
B	Bernstein polynomial, blockage factor
C	right Cauchy-Green tensor, curve
c	velocity
\mathbb{C}	stiffness tensor
C_p	specific heat capacity at constant pressure
cr	contraction ratio
C_v	specific heat capacity at constant volume
D	diameter
d	distance
D_{eq}	equivalent diffusion factor

Notation	Description
DF	distortion factor
E	energy, Young's modulus, Green-Lagrangian strain tensor
e	elastic strain energy density
F	force, deformation gradient
g	gravitational constant
h	enthalpy
I	identity tensor, impeller work input coefficient
I_D	diffusion loss
k	turbulent kinetic energy
L	length
M	rotation matrix
m	mass, meridional coordinate
Ma	Mach number
\dot{m}	mass flow rate
N	amount
n	hub to shroud direction, Beziér spline degree, polytropic index
o	width, position of optimum
P	material point, Piola stress, probability, spline control point
p	pressure
Q	heat
\dot{q}	heat flux rate
R	gas constant, rothalpy
r	radius, residual, radial coordinate
R^2	coefficient of determination
Re	Reynolds number
S	material surface

Notation	Description
s	entropy, streamwise coordinate, spacial surface
T	temperature, first Piola-Kirchhoff traction vector
t	time, Cauchy traction vector, thickness
U	material displacement
u	internal energy, circumferential velocity, spatial displacement
V	volume
v	specific volume
\dot{V}	volume flow rate
w	relative velocity, weighting function
w_t	technical work
\dot{w}	work input
X	material point, choking parameter
x	cartesian x-coordinate, spatial point, arbitrary parameter
y	cartesian y-coordiante, arbitrary response
z	number of blades, altitude, axial coordinate, cartesian z-coordiante

List of Greek Symbols

Notation	Description
α	generic angle, absolute flow angle, step probability
β	relative flow angle, regression coefficient
χ	motion
δ	specific diameter, boundary layer thickness
ε	turbulent kinetic energy dissipation, distance, regression error
η	efficiency, curvilinear η -coordinate
Γ	material curve
γ	heat capacity ratio, spatial curve

Notation	Description
κ	curvature, mapping function
λ	thermal conductivity, loss model coefficient, strain, scaling factor, speedline coefficient
μ	dynamic viscosity, Minderleistungsfaktor, mean value
ν	kinematic viscosity, geometric ratio
Ω	speed of rotation, configuration
ω	vorticity, turbulent frequency
$\bar{\omega}$	generic loss coefficient
φ	flow coefficient
Π	pressure ratio
Ψ	work coefficient
ρ	density
Σ	covariance matrix
σ	Cauchy stress, specific speed, slip factor, standart deviation
σ^2	variance
τ	torque, shear stress
ϑ	circumferential coordinate, circumferential blade extent
ξ	curvelinear ξ -coordinate

List of Subscripts

Notation	Description
b	quantity of the blade
d	condition at discharge
i	condition at intake, inertial frame of reference
is	isentropic quantity
LE	quantity at leading edge
m	meridional direction

Notation	Description
<i>pol</i>	polytropic quantity
<i>r</i>	rotating frame of reference, radial direction
<i>rev</i>	reversible
<i>s</i>	streamwise direction
<i>SL</i>	slip
<i>t</i>	total quantity
<i>TE</i>	quantity at trailing edge
<i>Th</i>	quantity at the impeller throat
<i>∂</i>	circumferential direction
<i>x</i>	x-direction
<i>y</i>	y-direction
<i>z</i>	z-direction, axial direction

CHAPTER 1

Introduction

1.1 Motivation

The continuously rising global demand for energy together with simultaneously decreasing resources has made the topic of energy efficiency - and therefore optimization - one of the fundamental questions of our time. Turbomachinery is one of the most important parts of the process chain in nearly every case of energy conversion. This makes the turbomachine a promising approach point for optimizations. The special relevance of this topic in regard to the global challenge of climate change can be illustrated by a simple calculation: If the efficiency of a turbo compressor with a power consumption of 15MW is improved by one percent, approximately 2t CO_2 per day or over 760t CO_2 per year can be saved.¹

Optimizing a turbomachine is a complex task as the flow inside the machine is fully three-dimensional. Furthermore, it is not sufficient to optimize the machine in a single operation point. To obtain a reliable optimum, the complete operation characteristic has to be considered as the machine is not always operated at the same conditions. On top of that, the mechanical performance of the machine is of particular importance. Modern compressor impellers are subject to high structural loads. Therefore, the structural integrity of each possibly optimal design has to be considered carefully. The combination of complex flow, a varying operation range and high structural loads results in a complex high-dimensional and multicriterial optimization scenario.

The established approach for design and optimization of turbomachinery is mainly based on simplified preliminary design methods and empirical knowledge. Furthermore, new designs are often created by modifying existing designs. This strategy results in an iterative design process.

In recent years, the use of simulation based automated optimization methods has become a common practice in many fields of scientific and industrial research. Today, there is a great variety of established optimization tools both commercial and academic and the use of such tools has lead to new and innovative designs in many fields of engineering. Thereby, two main strategies can be distinguished: “direct optimization“ where an algorithm proposes new designs candidates until no further improvement of the objective can be observed and “metamodel based optimization“ where a surrogate model is generated based on a set of design candidates on which the optimum is determined. For applications with a high numerical cost for each design evaluation, like turbomachinery, the metamodel

¹ "Development of the specific carbon dioxide emissions in German electricity production from 1990 to 2015", German Environment Agency (<http://www.umweltbundesamt.de>)

based optimization approach is preferable as the number of required computations can be estimated before starting the optimization.

In the field of turbomachinery however, simulation based automated optimization is not widely established yet. This can be explained by several reasons. Firstly, the correlations between the geometry and the fluid dynamic performance are complex and highly non linear. Therefore, many geometrically valid designs proposed by an optimization algorithm are infeasible in terms of the flow physics. A large number of infeasible designs will significantly slow the convergence of the optimization algorithm. Furthermore, each design has to be investigated in terms of structural integrity. In many cases, the structural and the fluid dynamic performance act as conflicting objectives. Finally, as mentioned before, the operation characteristic of every design has to be considered. This adds additional objectives to the optimization process.

Taking these considerations into account, the numerical expense for each design point is very high as the complete operation characteristic has to be computed by computational fluid dynamics (CFD) together with a finite element method (FEA) simulation to obtain the structural performance. This combination of a large numerical expense for a single design point with a slow convergence of the optimization has yet prevented a wide use of automated optimization in the field of turbomachinery.

Based on this situation, a great need for research in the field simulation based automated turbomachinery optimization can be identified.

1.2 Aim

The goal of this work is the development of an efficient strategy for the metamodel based optimization of centrifugal compressor impellers. The main focus lies on the reduction of the numerical expense needed to determine an optimal design.

The basic idea is to use preliminary information from empirical data or fast low-fidelity analytical methods to identify regions of the parameter space which are promising in terms of both aerodynamic and structural performance. Then, these areas are observed at a higher resolution while still maintaining a good coverage of the whole applicable design space. This ensures that no beneficial designs are ruled out which were not recommended by preliminary information.

This goal will be accomplished by the development of a turbomachinery specific, multi-fidelity sampling method. This method is applied to generate the design of experiments on which the metamodels used for the optimization are based.

As mentioned before, the complex correlations between geometry and aerodynamic performance can lead to many non meaningful designs. Therefore, a sophisticated concept for the description of the impeller geometry will be developed, which is based on fluid dynamic considerations. This will ensure that the amount of fluid dynamically infeasible designs is strongly reduced.

Furthermore the operation characteristic of each design has to be investigated. This will be accomplished by an automation method for the computation of operation characteristics.

1.3 Outline

This work consists of eight chapters. Following this introduction, the second chapter gives an overview of the theoretical fundamentals needed in the following chapters. These fundamentals encompass thermodynamics, fluid and solid mechanics, an introduction on turbomachinery and the employed statistical methods.

In the third chapter available preliminary information is reviewed. This includes preliminary design methods, empirical correlations, simplified low-fidelity flow computation methods and models for predicting the structure mechanical performance. All methods are discussed and finally the best suited methods are chosen.

The fourth chapter deals with the development of the turbomachinery specific sampling method. The available methods are reviewed and analyzed for the given problem. Based on the review, all method have proven to be not applicable.

As the methods observed in the fourth chapter turned out to be not applicable, a novel multi-fidelity sampling method is developed and evaluated in the fifth chapter.

The sixth chapter describes the applied computational model. This encompasses the geometrical model, the applied simplified low-fidelity flow computation methods, the prediction method for the structure mechanical performance, the CFD and FE models and finally the applied workflow.

In the seventh chapter the developed workflow is applied to three testcases. In the first two testcases, existing centrifugal compressor impellers from different performance ranges are optimized (“Design-Optimization“). The results of these optimizations are compared to optimizations which did not take preliminary information into account. In the third testcase, a new impeller is generated by the optimization process (“Design-by-Optimization“). In contrast to the previous optimizations, a wider parameter range is considered to ensure that the method is able to deal with strong changes in the impeller designs within an optimization.

The last chapter summarizes and assesses the presented results. This chapter is concluded by an outlook on further research activities in this field.

CHAPTER 2

Theoretical Fundamentals

This chapter provides the theoretical fundamentals needed in the following chapters. Each section gives a short overview of the respective topic. This chapter is not intended to give complete derivations of the presented concepts as these can be found in standard textbooks.

2.1 Thermodynamics

All considerations on the aerodynamic design and analysis of turbomachines are based on thermodynamics. The key thermodynamic principles are introduced in this chapter with special emphasis on the intended application. A brief introduction can be found in [Dix10] or [Aug00].

2.1.1 Fundamental Laws

2.1.1.1 The Equation of Continuity

The flow \dot{m} with velocity c of a fluid of density ρ through a surface of area dA is given by Eq. 2.1.

$$d\dot{m} = \rho c dA \quad (2.1)$$

For a one-dimensional flow through a duct or passage the *equation of continuity* becomes

$$\dot{m} = \rho_1 c_1 A_1 = \rho_2 c_2 A_2 \quad (2.2)$$

as no fluid gets accumulated or lost inside the volume.

2.1.1.2 The First Law of Thermodynamics

The first law of thermodynamics is the conservation of energy. For a system in equilibrium, it is given by Eq. 2.3

$$d\dot{q} - d\dot{w} = 0 \quad (2.3)$$

where $d\dot{q}$ represents the heat flux through the system and $d\dot{w}$ the work done by the system. If the state of the system changes, the amount of energy within the system changes.

Therefore, Eq. 2.3 becomes

$$d\dot{q} - d\dot{w} = \Delta E = \dot{m}\Delta \left[u + \frac{1}{2}c^2 + gz + pv \right] \quad (2.4)$$

with the energy E , the inner energy u , the acceleration of gravity g , the geodetic altitude z , the pressure p and the specific volume v .

The term pv represents the flow work, which is required to move the fluid across the systems boundaries. By introducing the specific enthalpy h (Eq. 2.5), the first law can be written according to Eq. 2.6.

$$h = u + pv \quad (2.5)$$

$$d\dot{q} - d\dot{w} = \dot{m}\Delta \left[h + \frac{1}{2}c^2 + gz \right] \quad (2.6)$$

The common form of the first law used in turbomachinery applications is given by Eq. 2.7. This equation can be derived by applying the first law to the steady flow through a control volume representing the turbomachine. For most turbomachines, except hydraulic machines, the contribution of the term $\dot{m}gz$ can usually be ignored. Figure 2.1 shows a systematic representation of a turbomachine with numbers indicating the inflow (1) and the outflow (2), \dot{q} as an internal heat source and \dot{w} as the mechanical work input into the system.

$$\dot{q} - \dot{w} = \dot{m} \left[(h_2 - h_1) + \frac{1}{2}(c_2^2 - c_1^2) \right] \quad (2.7)$$

In many cases of fluid dynamics, a thermodynamic parameter and the contribution of the kinetic energy to its value are combined into a single quantity called total (or stagnation) condition. Such a quantity is indicated by the subscript 't'. This represents the value this parameter would take, if the fluid would be brought to zero velocity without any losses. Applying this concept to the enthalpy yields the total enthalpy (Eq. 2.8).

$$h_t = h + \frac{1}{2}c^2 \quad (2.8)$$

Using this and assuming that the flow can be considered as adiabatic, the common energy equation for a turbomachine can be expressed as

$$\dot{w} = \dot{m}(h_{t2} - h_{t1}) \quad (2.9)$$

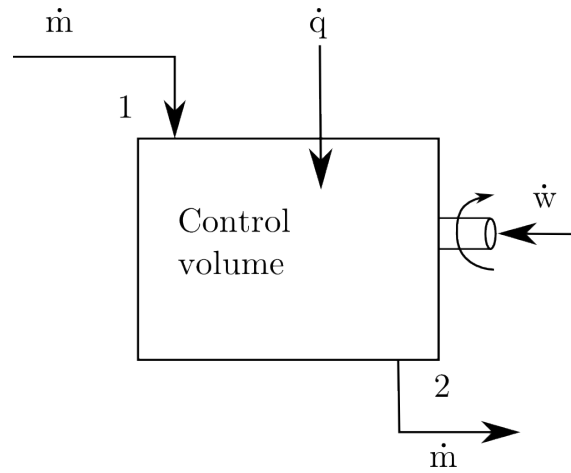


Figure 2.1: Control volume with heat, work and mass flow for a turbomachine

2.1.1.3 The Second Law of Thermodynamics

When the state of a system changes, this process is called reversible if the system can be returned to its initial state. Every real process involving heat transfer or losses like friction is irreversible. The second law of thermodynamics depicts this by connecting the amount of non-recoverable work with the entropy s . Equation 2.10 shows the second law for an infinitesimal change of state.

$$ds = \frac{dq_{rev}}{T} \quad (2.10)$$

If a process is adiabatic ($dq = 0$) then $ds > 0$. If the process is reversible as well, then it is called isentropic ($ds = 0$). As turbomachinery can usually assumed to be adiabatic, an isentropic change of state is the best process which can possibly be achieved. Therefore the amount of entropy has to be minimized to obtain a maximum of efficiency.

For a closed system undergoing a reversible process ($dq = dq_{rev} = Tds$ and $d\dot{w} = d\dot{w}_{rev} = pdv$) the first law of thermodynamics (2.4) can be written as

$$Tds = du + pdv \quad (2.11)$$

when no motion, gravity or other effects are present.

With $h = u + pv$ and $dh = du + pdv + vdp$ Eq. 2.11 becomes

$$Tds = dh + vdp \quad (2.12)$$

The version of the second law of thermodynamics given by Eq. 2.12 is especially useful as the entropy rise can be described only by properties of the system without taking any outer effects into account. Therefore, this equation can be applied to any system and process.

2.1.1.4 The Momentum Equation

Newton's second law of motion is one of the most fundamental principles of mechanics. When applied on a fluid element, the momentum equation (Eq. 2.13) gives a relation between the external forces F_i acting on the fluid and its rate of change of momentum in one direction.

$$\sum F_i = \frac{d}{dt} (mc_i) \quad (2.13)$$

In case of a one-dimensional control volume and steady flow, the momentum equation can be given as

$$\sum F_i = \dot{m} (c_{i2} - c_{i1}) \quad (2.14)$$

In a turbomachine energy is exchanged between a rotating impeller and the fluid. Therefore, the angular momentum rc_θ is of particular interest. For a control volume, the conservation of angular momentum defines the torque τ transferred between the fluid and the impeller (Eq. 2.15).

$$\tau = \dot{m} (rc_{\theta 2} - rc_{\theta 1}) \quad (2.15)$$

2.1.2 Gas Properties

Turbomachinery overall and centrifugal compressors in particular are used with a wide range of gases and gas mixtures. Many of these gases show a very non ideal behavior which would require the use of sophisticated real gas models. Still, one of the most commonly used flow media is air. Therefore, air is used as the flow medium in this work. Air is a mixture of different gases like nitrogen, oxygen, argon, carbon dioxide and many other components but, for temperatures between 160 to 2100K it can be treated like a pure substance. Within this range air obeys the ideal gas relationship

$$\begin{aligned} p &= \rho RT \text{ or} \\ pv &= RT \end{aligned} \quad (2.16)$$

where $R = C_p - C_v$ is the gas constant and C_p and C_v are the heat capacities at constant pressure respectively volume. When only a narrow range of temperatures is investigated, the heat capacities can be considered as constant values. For larger variations, the values of the heat capacities should be varied according to table values or correlation functions. In many flow equations the ratio of the heat capacities γ (Eq. 2.19) is an important parameter. Similar to the heat capacities, the heat capacity ratio is a function of temperature. In the typical range of pressures applicable for turbomachinery, the heat

capacities are predominantly dependent on the temperature, therefore the pressure influence is neglected.

The heat capacities C_p and C_v are connected to the specific enthalpy h and the inner energy u according to Eq. 2.17 and Eq.2.18.

$$dh = C_p \cdot dT \quad (2.17)$$

$$du = C_v \cdot dT \quad (2.18)$$

$$\gamma = \frac{C_p}{C_v} \quad (2.19)$$

2.1.3 Thermodynamic Processes

Figure 2.2 shows an enthalpy-entropy diagram for an arbitrary compressor stage. The point marked with “1” depicts the intake state with total pressure p_{ti} . If the compressor is operated as an ideal isentropic machine, the discharge pressure p_{td} can be reached at point “2_{is}”. This requires a work input equal to the isentropic enthalpy rise $\Delta h_{t,is}$ given by

$$\Delta h_{t,is} = \int_i^d v dp (s = const) \quad (2.20)$$

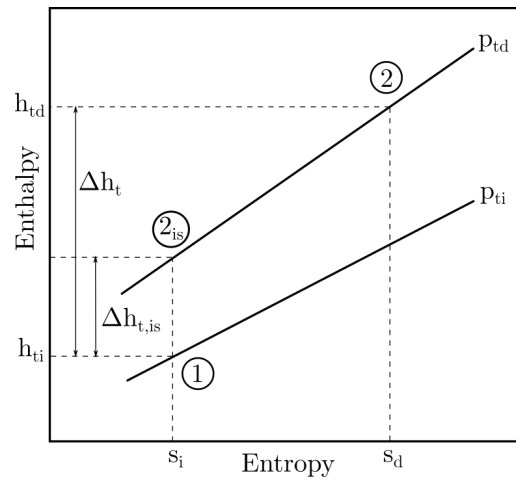


Figure 2.2: h-s Diagram for a compressor stage

The integration is carried out along a path between “1” and “2_{is}” defined by constant entropy.

In a real process though, the work input of Δh_t is required to produce the discharge pressure at point “2”. The ratio of isentropic and real work input is known as the total-to-

total isentropic efficiency η_{is} (Eq. 2.21). If an intake or discharge state is expressed in static conditions, the terminology changes accordingly. When comparing different compressor stages it is of particular importance to use uniform definitions of efficiency.

$$\eta_{is} = \frac{\Delta h_{t,is}}{\Delta h_t} \quad (2.21)$$

The isentropic efficiency is a well defined quantity but bears the disadvantage of undesirable thermodynamic effects when comparing different compressors. As the lines for constant pressure diverge in a h-s diagram as shown in Fig. 2.2, this quantity can not be used to compare stages of different pressure ratios.

To bypass this weakness, the polytropic enthalpy rise and the polytropic efficiency are used. For ideal gases, the polytropic enthalpy rise can be computed analogously to the isentropic enthalpy rise by using a path defined by $pv^n = const.$ where n is the polytropic index. Then the equation for the total-to-total polytropic efficiency yields

$$\eta_{pol} = \frac{\Delta h_{t,pol}}{\Delta h_t} \quad (2.22)$$

The total polytropic enthalpy rise¹ $\Delta h_{t,pol}$ is computed according to Eq. 2.23.

$$\Delta h_{t,pol} = \int_i^d v dp \quad (pv^n = const.) \quad (2.23)$$

When the ideal gas equation $pv = RT$ (Eq. 2.16) is combined with $pv^n = const.$, the following relations can be derived:

$$\begin{aligned} p_1 v_1^n &= p_2 v_2^n \\ \frac{p_1}{p_2} &= \left[\frac{v_2}{v_1} \right]^n \\ \frac{p_1}{p_2} &= \left[\frac{T_1}{T_2} \right]^{\frac{n}{n-1}} \\ \frac{T_1}{T_2} &= \left[\frac{p_1}{p_2} \right]^{\frac{n-1}{n}} \\ \frac{T_1}{T_2} &= \left[\frac{v_2}{v_1} \right]^{n-1} \end{aligned} \quad (2.24)$$

If the change of state is isentropic, the polytropic index n is replaced by the heat capacity

¹ In German literature, the quantity $\Delta h_{t,pol}$ is often denoted as y and called ‘‘Reversible Strömungsarbeit’’ (reversible flow work).

ratio γ of the respective fluid.

2.2 Fluid Dynamics

The fundamental equations of fluid dynamics are derived from the previously described laws of thermodynamics. This section gives an overview of the basic fluid dynamic equations. A brief introduction can be found in [Lec14] or [Oer11].

2.2.1 Bernoulli's Equation

For a steady, adiabatic flow the energy equation (2.7) takes the following form:

$$(h_2 - h_1) + \frac{1}{2} (c_2^2 - c_1^2) + g(z_2 - z_1) = 0 \quad (2.25)$$

Applied to an infinitesimal control volume this equation can be written in differential form.

$$dh + cdc + gdz = 0 \quad (2.26)$$

If the flow can be considered isentropic, Eq. 2.12 gives $dh = vdp = \frac{dp}{\rho}$. Combined with Eq. 2.26 this yields the one dimensional form of Euler's equation of motion.

$$\frac{1}{\rho} dp + cdc + gdz = 0 \quad (2.27)$$

Bernoulli's equation is obtained by integrating this equation in the stream direction.

$$\int_1^2 \frac{1}{\rho} dp + \frac{1}{2} (c_2^2 - c_1^2) + g(z_2 - z_1) \quad (2.28)$$

When Bernoulli's equation is combined with the conservation of mass and energy, one dimensional flow problems can be solved.

2.2.2 Navier Stokes Equations

Bernoulli's equation is valid only for isentropic flow, therefore no friction effects are taken into account. General flow can be computed by the Navier Stokes Equations which are given in the following sections. All equations are given in differential form for a volume element.

2.2.2.1 The Conservation of Mass

The mass flow through an infinitesimal volume element is shown in Fig. 2.3. The conservation of mass is defined by the summation of all mass flows entering and leaving the volume element and the temporal alteration $\frac{\partial}{\partial t} (m) = \frac{\partial}{\partial t} (\rho \cdot V) = \frac{\partial}{\partial t} (\rho \cdot dx \cdot dy \cdot dz)$ of the mass

in the element. Equation 2.29 gives the conservation of mass in differential form where x , y and z represent the directions in cartesian space.

$$\frac{\partial}{\partial t}(\rho) + \frac{\partial}{\partial x}(\rho \cdot c_x) + \frac{\partial}{\partial y}(\rho \cdot c_y) + \frac{\partial}{\partial z}(\rho \cdot c_z) = 0 \quad (2.29)$$

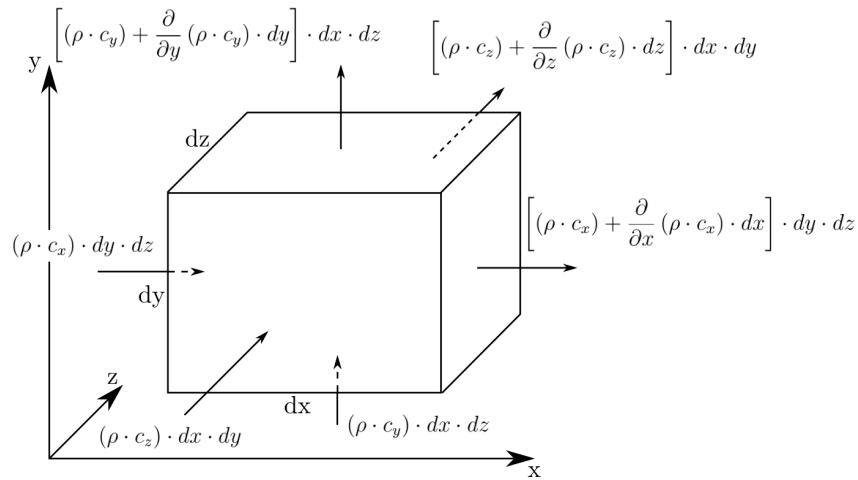


Figure 2.3: Mass flows entering and leaving an infinitesimal volume element

2.2.2.2 The Conservation of Momentum

Newton's first law of motion states that all forces acting on an object are in equilibrium ($\sum F_{i,x} = 0$). The balance of forces acting on a volume element in x-direction can be written as:

$$F_x = F_{shear,x} + F_{pressure,x} + F_{body,x} = m \cdot a_x \quad (2.30)$$

$F_{shear,i}$ are the forces resulting from friction at the surfaces of the volume element. $F_{pressure,i}$ depicts the pressure forces acting on the element's surfaces and $F_{body,i}$ are the external forces acting on the volume of the element like gravitation or electromagnetic force.

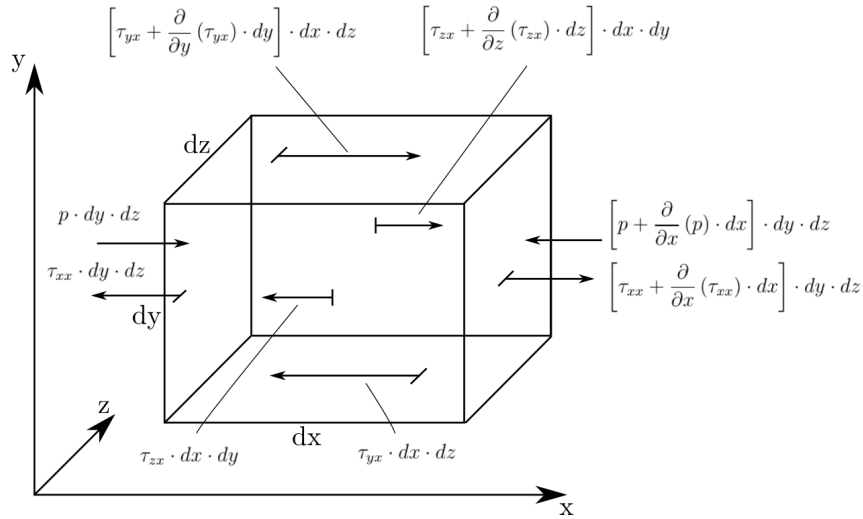


Figure 2.4: Forces in x direction for an infinitesimal volume element, shear stresses denoted as τ .

Figure 2.4 shows the forces acting on an infinitesimal volume element in x-direction. The summation of these forces gives the left hand side of the balance of forces:

$$F_x = \left[\frac{\partial}{\partial x} (\tau_{xx}) + \frac{\partial}{\partial y} (\tau_{yx}) + \frac{\partial}{\partial z} (\tau_{zx}) - \frac{\partial p}{\partial x} + \rho \cdot g_x \right] \cdot dx \cdot dy \cdot dz \quad (2.31)$$

The mass inside the element on the right hand side of Eq. 2.30 is given by

$$m = \rho \cdot dx \cdot dy \cdot dz \quad (2.32)$$

while the acceleration is computed by the total differential of the velocity:

$$a_x = \frac{dc_x}{dt} = \frac{\partial c_x}{\partial t} + c_x \cdot \frac{\partial c_x}{\partial x} + c_y \cdot \frac{\partial c_x}{\partial y} + c_z \cdot \frac{\partial c_x}{\partial z} \quad (2.33)$$

Combining equations Eq. 2.30, Eq. 2.31, Eq. 2.32 and Eq. 2.33, the differential form of the conservation of momentum in the x-direction can be written as

$$\frac{\partial}{\partial x} (\tau_{xx}) + \frac{\partial}{\partial y} (\tau_{yx}) + \frac{\partial}{\partial z} (\tau_{zx}) - \frac{\partial p}{\partial x} + \rho \cdot g_x = \rho \cdot \frac{\partial c_x}{\partial t} + \rho \cdot c_x \cdot \frac{\partial c_x}{\partial x} + \rho \cdot c_y \cdot \frac{\partial c_x}{\partial y} + \rho \cdot c_z \cdot \frac{\partial c_x}{\partial z} \quad (2.34)$$

This form of the momentum equation is also called “non-conservative“ form as the right hand side terms ρ , $\rho \cdot c_x$, $\rho \cdot c_y$, $\rho \cdot c_z$ are not part of the derivatives. From a mathematical point of view, a conservative derivative $\frac{\partial \rho \cdot c_x}{\partial x}$ can be split up into an identical non conservative derivative $\rho \cdot \frac{\partial c_x}{\partial x} + c_x \cdot \frac{\partial \rho}{\partial x}$. In the case of numerical differentiation, the first version could

be discretized by

$$\frac{\partial \rho \cdot c_x}{\partial x} \approx \frac{(\rho \cdot c_x)_i - (\rho \cdot c_x)_{i-1}}{\Delta x} \quad (2.35)$$

while the second version could be discretized as

$$\rho \cdot \frac{\partial c_x}{\partial x} + c_x \cdot \frac{\partial \rho}{\partial x} = \rho_i \frac{c_{x,i} - c_{x,i-1}}{\Delta x} + c_{x,i} \frac{\rho_i - \rho_{i-1}}{\Delta x} \quad (2.36)$$

While the conservative and non conservative differential are mathematically identical, the discretized versions are not the same. Of particular difficulty is the choice of the terms multiplying the derivative. This can lead to numerical errors when solving the momentum equation. To bypass this difficulty the right hand side of Eq. 2.34 can be transformed in a way that all terms are part of the derivatives. Equation 2.37 gives the conservative form of the balance of momentum in x direction. The details of the transformation can be found in standard text books on fluid dynamics.

$$\frac{\partial}{\partial t} (\rho \cdot c_x) + \frac{\partial}{\partial x} (\rho \cdot c_x^2 + p - \tau_{xx}) + \frac{\partial}{\partial y} (\rho \cdot c_x \cdot c_y - \tau_{yx}) + \frac{\partial}{\partial z} (\rho \cdot c_x \cdot c_z - \tau_{zx}) - \rho \cdot g_x = 0 \quad (2.37)$$

Analogously, the balance of momentum for the y and z direction are given by Eq. 2.38 and Eq. 2.39.

$$\frac{\partial}{\partial t} (\rho \cdot c_y) + \frac{\partial}{\partial x} (\rho \cdot c_y \cdot c_x - \tau_{xy}) + \frac{\partial}{\partial y} (\rho \cdot c_y^2 + p - \tau_{yy}) + \frac{\partial}{\partial z} (\rho \cdot c_y \cdot c_z - \tau_{zy}) - \rho \cdot g_y = 0 \quad (2.38)$$

$$\frac{\partial}{\partial t} (\rho \cdot c_z) + \frac{\partial}{\partial x} (\rho \cdot c_z \cdot c_x - \tau_{xz}) + \frac{\partial}{\partial y} (\rho \cdot c_z \cdot c_y - \tau_{yz}) + \frac{\partial}{\partial z} (\rho \cdot c_z^2 + p - \tau_{zz}) - \rho \cdot g_z = 0 \quad (2.39)$$

2.2.2.3 The Conservation of Energy

The conservation of energy is described by the first law of thermodynamics (Eq. 2.4) which balances the change of energy in the volume element with the work and the heat exchange.

$$\frac{dE}{dt} = \dot{w} + \dot{q} \quad (2.40)$$

The energy inside the element consists of three components:

- the inner energy $E_{inner} = m \cdot u = \rho \cdot dx \cdot dy \cdot dz \cdot u$
- the kinetic energy $E_{kinetic} = \frac{1}{2} \cdot m \cdot c^2 = \frac{1}{2} \cdot \rho \cdot dx \cdot dy \cdot dz \cdot (c_x^2 + c_y^2 + c_z^2)$
- the potential energy $E_{potential} = m \cdot g \cdot z$ which can be neglected for gases

With $E_{potential} = 0$, the energy inside a fluid element reads

$$E = E_{inner} + E_{kinetic} = \rho \cdot \left(u + \frac{1}{2} \cdot c^2 \right) \cdot dx \cdot dy \cdot dz \quad (2.41)$$

and the total differential of Eq. 2.41 gives the convective energy flows for an infinitesimal volume element.

$$\begin{aligned} \frac{dE}{dt} &= \frac{d}{dt} \left[\rho \cdot \left(u + \frac{1}{2} \cdot c^2 \right) \right] \cdot dx \cdot dy \cdot dz \\ &= \left\{ \frac{\partial}{\partial t} \left[\rho \cdot \left(u + \frac{1}{2} \cdot c^2 \right) \right] + \frac{\partial}{\partial x} \left[\rho \cdot c_x \cdot \left(u + \frac{1}{2} \cdot c^2 \right) \right] + \frac{\partial}{\partial y} \left[\rho \cdot c_y \cdot \left(u + \frac{1}{2} \cdot c^2 \right) \right] \right. \\ &\quad \left. + \frac{\partial}{\partial z} \left[\rho \cdot c_z \cdot \left(u + \frac{1}{2} \cdot c^2 \right) \right] \right\} \cdot dx \cdot dy \cdot dz \end{aligned} \quad (2.42)$$

The work input \dot{w} of the volume element is composed of three parts:

- the gravitation g acting on the element
- the pressure p on the elements surfaces
- the normal and shear stresses acting on the elements surfaces

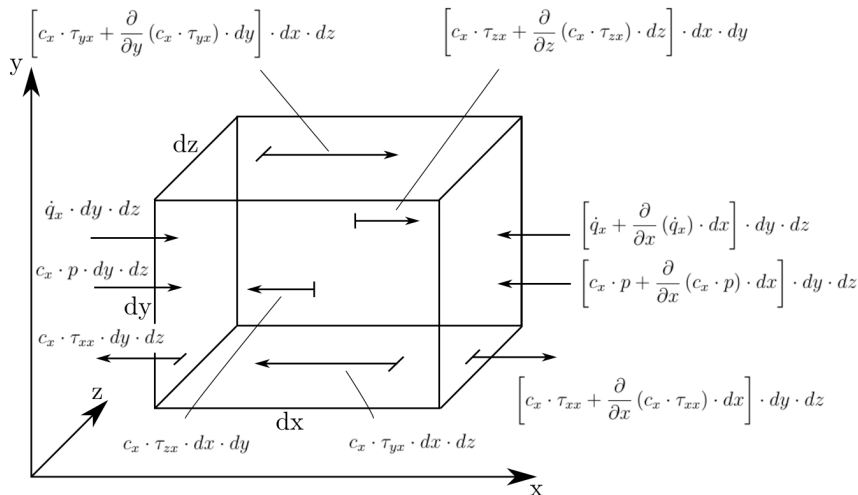


Figure 2.5: Energy flows for an infinitesimal volume element in x direction

The work input for the volume element is computed by the summation of the energy flows in x direction as shown in Fig. 2.5 and the respective flows in y and z direction.

$$\begin{aligned} \dot{w} = & \left[\rho \cdot (c_x \cdot g_x + c_y \cdot g_y + c_z \cdot g_z) - \frac{\partial}{\partial x} (c_x \cdot p) - \frac{\partial}{\partial y} (c_y \cdot p) - \frac{\partial}{\partial z} (c_z \cdot p) \right. \\ & - \frac{\partial}{\partial x} (c_x \cdot \tau_{xx} + c_y \cdot \tau_{xy} + c_z \cdot \tau_{xz}) - \frac{\partial}{\partial y} (c_x \cdot \tau_{yx} + c_y \cdot \tau_{yy} + c_z \cdot \tau_{yz}) \\ & \left. - \frac{\partial}{\partial z} (c_x \cdot \tau_{zx} + c_y \cdot \tau_{zy} + c_z \cdot \tau_{zz}) \right] \cdot dx \cdot dy \cdot dz \end{aligned} \quad (2.43)$$

The heat flux \dot{q} consists of two parts:

- the thermal radiation $\dot{q}_{radiation}$ acting on the volume element
- the heat flux through the volumes surfaces due to conduction $\dot{q}_{conduction}$

Together with Fourier's law ($\dot{q}_{conduction,i} = -\lambda \cdot \frac{\partial T}{\partial i}$), the heat flux is given as

$$\dot{q} = \left[\rho \cdot \dot{q}_{radiation} + \frac{\partial}{\partial x} \left(\lambda \frac{\partial T}{\partial x} \right) + \frac{\partial}{\partial y} \left(\lambda \frac{\partial T}{\partial y} \right) + \frac{\partial}{\partial z} \left(\lambda \frac{\partial T}{\partial z} \right) \right] \cdot dx \cdot dy \cdot dz \quad (2.44)$$

where λ is the thermal conductivity and i is an arbitrary direction.

Insertion of Eq. 2.42, Eq. 2.43 and Eq. 2.44 into Eq. 2.41 yields the conservation of energy for an infinitesimal fluid element. In this equation, the specific energy terms in the spacial derivatives have been replaced by the specific enthalpy $h = u + \frac{p}{\rho}$. This eliminates the pressure terms and simplifies the equation.

$$\begin{aligned} \frac{\partial}{\partial t} \left[\rho \left(u + \frac{1}{2} \cdot c^2 \right) \right] + \frac{\partial}{\partial x} \left[\rho \cdot c_x \cdot \left(h + \frac{1}{2} \cdot c^2 \right) - (c_x \cdot \tau_{xx} + c_y \cdot \tau_{xy} + c_z \cdot \tau_{xz}) - \lambda \cdot \frac{\partial T}{\partial x} \right] \\ + \frac{\partial}{\partial y} \left[\rho \cdot c_y \cdot \left(h + \frac{1}{2} \cdot c^2 \right) - (c_y \cdot \tau_{yx} + c_y \cdot \tau_{yy} + c_z \cdot \tau_{yz}) - \lambda \cdot \frac{\partial T}{\partial y} \right] \\ + \frac{\partial}{\partial z} \left[\rho \cdot c_z \cdot \left(h + \frac{1}{2} \cdot c^2 \right) - (c_z \cdot \tau_{zx} + c_y \cdot \tau_{zy} + c_z \cdot \tau_{zz}) - \lambda \cdot \frac{\partial T}{\partial z} \right] \\ - \rho \cdot (c_x \cdot g_x + c_y \cdot g_y + c_z \cdot g_z) - \rho \cdot \dot{q}_{radiation} = 0 \end{aligned} \quad (2.45)$$

2.2.2.4 Further Equations

The Navier-Stokes-Equations consisting of the five conservation equations for mass, energy and momentum can be used to describe the all flow phenomena inside a volume element. This set of equations includes 17 unknown variables ρ , c_x , c_y , c_z , p , u , h , T , τ_{xx} , τ_{yy} , τ_{zz} , τ_{xy} , τ_{yx} , τ_{xz} , τ_{zx} , τ_{yz} and τ_{zy} . Therefore, 12 additional equation are needed to obtain a solution. These are the three equations of state for the fluid and the 9 normal and shear stress relations of Stokes.

The fluid is described by the thermal equation of state Eq. 2.16 and the caloric equations Eq. 2.17 and Eq.2.18.

The Stokes's stress constitutive equations create a relation between the stresses τ and the velocity c . They are given by equations Eq. 2.46 to Eq. 2.54.

$$\tau_{xx} = -\frac{2}{3}\mu \cdot \left(\frac{\partial c_x}{\partial x} + \frac{\partial c_y}{\partial y} + \frac{\partial c_z}{\partial z} \right) + 2 \cdot \mu \cdot \frac{\partial c_x}{\partial x} \quad (2.46)$$

$$\tau_{yy} = -\frac{2}{3}\mu \cdot \left(\frac{\partial c_x}{\partial x} + \frac{\partial c_y}{\partial y} + \frac{\partial c_z}{\partial z} \right) + 2 \cdot \mu \cdot \frac{\partial c_y}{\partial y} \quad (2.47)$$

$$\tau_{zz} = -\frac{2}{3}\mu \cdot \left(\frac{\partial c_x}{\partial x} + \frac{\partial c_y}{\partial y} + \frac{\partial c_z}{\partial z} \right) + 2 \cdot \mu \cdot \frac{\partial c_z}{\partial z} \quad (2.48)$$

$$\tau_{xy} = \mu \cdot \left(\frac{\partial c_y}{\partial x} + \frac{\partial c_x}{\partial y} \right) \quad (2.49)$$

$$\tau_{xz} = \mu \cdot \left(\frac{\partial c_x}{\partial z} + \frac{\partial c_z}{\partial x} \right) \quad (2.50)$$

$$\tau_{yz} = \mu \cdot \left(\frac{\partial c_z}{\partial y} + \frac{\partial c_y}{\partial z} \right) \quad (2.51)$$

$$\tau_{yx} = \tau_{xy} \quad (2.52)$$

$$\tau_{zx} = \tau_{xz} \quad (2.53)$$

$$\tau_{zy} = \tau_{yz} \quad (2.54)$$

2.2.3 Turbulence

“I am an old man now, and when I die and go to heaven there are two matters on which I hope for enlightenment. One is quantumelectrodynamics and the other is the turbulent motion of fluids. About the former I am rather optimistic.“
Sir Horace Lamb (1849-1934)

A flow regime is considered laminar if the the fluid moves on parallel layers and no disruption is happening between the layers. If, by contrast, the flow includes chaotic fluctuations in pressure and flow velocity on a microscopic scale, the flow is considered as turbulent. The Reynolds number Re is used to predict if the flow is still laminar or has already changed to a turbulent flow. Equation 2.55 gives the definition of the Reynolds number where L_c is a characteristic length for the flow (e.g. the hydraulic diameter D_H for a pipe flow or the traveled length for traversal flow). The transition from laminar to turbulent flow starts at Reynolds numbers of about 1,800. For Reynolds numbers above 2,030 the flow is considered to be fully turbulent.

$$Re = \frac{\rho c L_c}{\mu} \quad (2.55)$$

The exact description of the behavior of a turbulent flow with all its internal structures remains one of the most important unsolved problems in physics. The previously introduced Navier-Stokes-Equations are believed to be capable of describing turbulent flow if the discretization of the flow is done by sufficiently small finite volumes to capture all internal flow structures. While this assumption can not be proven, the application on real flow problems is not possible at a reasonable computational expense due to the required fine discretization.

Modern CFD code bypass this problem by using the so called Reynolds averaged Navier-Stokes-Equations (RANS) which can depict the underlying physics with sufficient accuracy at a reasonable computational expense. This method does not compute the exact turbulent flow field of the fluid but approximates it by using so called turbulence models. This is achieved by substituting the time and location dependent flow variables ρ , c , u by their time invariant mean values $\bar{\rho}$, \bar{c} , \bar{u} and adding turbulent fluctuation ρ' , c' , u' depending on both time and location.

$$\begin{aligned} \rho(x,y,z,t) &= \bar{\rho}(x,y,z) + \rho'(x,y,z,t) \\ c(x,y,z,t) &= \bar{c}(x,y,z) + c'(x,y,z,t) \\ u(x,y,z,t) &= \bar{u}(x,y,z) + u'(x,y,z,t) \end{aligned} \quad (2.56)$$

The turbulent fluctuations can be modeled by different approaches reaching from simple algebraic expressions to complex systems of differential equation of order 2. In turbomachinery CFD applications, the common practice is using two equation algebraic turbulence models like the $k - \varepsilon$, $k - \omega$ - or Shear-Stress-Transport-model (SST-model). Therefore the rest of this section focuses on these models.

2.2.3.1 $k - \varepsilon$ Turbulence Model

The $k - \varepsilon$ model is the most widely used turbulence model for CFD. Turbulence is modeled by introducing two additional transport equations. This model was first proposed by Jones and Launder in 1972 [Jon72]. The version used in most modern CFD codes is based on the standard $k - \varepsilon$ model described by Launder and Spalding [Lau74].

The first equation is used to model the turbulent kinetic energy k which determines the amount of energy per mass unit associated with the turbulent eddies in the flow. The transport equation for the turbulent kinetic energy in x direction reads as follows:

$$\frac{\partial \rho \cdot k}{\partial t} + \frac{\partial \rho \cdot k \cdot c_x}{\partial x} = \frac{\partial}{\partial y} \left[\frac{\mu_t}{\sigma_k} \frac{\partial k}{\partial y} \right] + 2\mu_t \cdot \tau_{xy} \cdot \tau_{yx} - \rho \varepsilon \quad (2.57)$$

The dissipation ε of the turbulent kinetic energy in x direction is given by

$$\frac{\partial \rho \cdot \varepsilon}{\partial t} + \frac{\partial \rho \cdot \varepsilon \cdot c_x}{\partial x} = \frac{\partial}{\partial y} \left[\frac{\mu_t}{\sigma_\varepsilon} \frac{\partial \varepsilon}{\partial y} \right] + C_{1\varepsilon} \cdot \frac{\varepsilon}{k} \cdot 2\mu_t \cdot \tau_{xy} \cdot \tau_{yx} - C_{2\varepsilon} \cdot \rho \frac{\varepsilon^2}{k} \quad (2.58)$$

The equations for the other directions can be derived analogously.

$\mu_t = \rho \cdot C_\mu \frac{k^2}{\varepsilon}$ is the eddy viscosity which is used to model transport and dissipation of small scale turbulent eddies on a global scale. C_μ , $C_{1\varepsilon}$, $C_{2\varepsilon}$, σ_ε and σ_k are empirical constants fitted for a wide range of turbulent flows.

The $k - \varepsilon$ model is primary designed for free-shear flow and therefore gives good results in the core flow far from walls. For boundary layer interaction near walls a very fine discretization would be required.

2.2.3.2 $k - \omega$ Turbulence Model

The $k - \omega$ model is another commonly used two equation turbulence model for RANS computations. It is specifically developed for low Reynolds number computations near walls. On the downside, the results obtained by this model for free-shear flows are strongly dependent on initial conditions. The model was introduced by Wilcox in 1988 [Wil88].

The turbulent kinetic energy in the x direction is computed as

$$\frac{\partial \rho \cdot k}{\partial t} + \frac{\partial \rho \cdot k \cdot c_x}{\partial x} = \frac{\partial}{\partial y} \left[(\mu + \sigma_k \cdot \rho \cdot \mu_t) \frac{\partial k}{\partial y} \right] + \rho \cdot \tau_{xy} \frac{\partial c_x}{\partial y} - \beta \cdot \rho \cdot \omega \cdot k \quad (2.59)$$

The turbulent frequency ω is given by

$$\frac{\partial \rho \cdot \omega}{\partial t} + \frac{\partial \rho \cdot \omega \cdot c_x}{\partial x} = \frac{\partial}{\partial y} \left[(\mu + \sigma_\omega \cdot \rho \cdot \mu_t) \frac{\partial \omega}{\partial y} \right] + \frac{\gamma \omega}{k} \tau_{xy} \frac{\partial c_x}{\partial y} - \beta \cdot \rho \cdot \omega^2 + \frac{\rho \cdot \sigma_d}{\omega} \frac{\partial k}{\partial y} \frac{\partial \omega}{\partial y} \quad (2.60)$$

σ_k , σ_ω , σ_d , β and γ are the empirical constants of the model.

2.2.3.3 SST Turbulence Model

The Shear-Stress-Transport turbulence model combines the advantages of the $k - \varepsilon$ and $k - \omega$ models. The flow near the walls is described by the $k - \omega$ formulation, while the $k - \varepsilon$ model is used for the free-shear flow far from the walls. The $k - \varepsilon$ model has to be transformed to a version using the turbulent frequency ω instead of the dissipation ε for compatibility reasons. The $k - \omega$ and the transformed $k - \varepsilon$ model are then combined using a blending function which takes a value of one near the wall and becomes zero outside of the boundary layer. The SST turbulence model was first introduced by Menter in 1994 [Men94].

2.3 Computational Fluid Dynamics

Computational fluid dynamics (CFD) is a branch of fluid mechanics which uses numerical methods to analyze fluid flows. Depending on the intended application area and the needed level of detail, the flow can be modeled by the Navier-Stokes equations, Euler equations, Stokes equations, potential equations or Lattice Boltzmann equations, just to name the most popular. For internal flows with high Reynolds numbers, the RANS equations as introduced in 2.2.3 are used by most CFD codes. A summary of the basic principles of CFD can be found in [Hir07] or [Lec14].

2.3.1 Discretization by Finite Volumes

The finite volume method (FVM) is used to solve systems of partial differential equations. For this method, the geometry is discretized by a mesh and values are calculated at discrete places, similar to the finite differences or finite element method. In case of the FVM, small volumes are placed around each node of the mesh. When integrating the respective partial differential equation over the volume, these volume integrals can be converted to surface integrals by the divergence theorem. Then, the surface integrals are evaluated as fluxes through the volume's surfaces. As the flow into a given volume is equal to the flow leaving the volume, this method is conservative and therefore particularly suitable for solving conservation equations.

Equation 2.61 gives an arbitrary conservation law. In this partial differential equation $u(x,t)$ represents a vector of states while \mathbf{f} is the flux tensor.

$$\frac{\partial}{\partial t}u(x,t) + \operatorname{div}\mathbf{f}(u(x,t)) = 0 \quad (2.61)$$

When the flow domain is subdivided into finite volumes, Eq. 2.62 gives the volume integral for one particular cell i over the complete volume of the cell V_i .

$$\int_{V_i} \frac{\partial}{\partial t}u(x,t)dV + \int_{V_i} \operatorname{div}\mathbf{f}(u(x,t))dV = 0 \quad (2.62)$$

The volume average of $u(x,t)$ in V_i is obtained by integration of the first term. The second term can be transformed according to the divergence theorem. This yields

$$V_i \frac{\partial}{\partial t}\bar{u}_i(x,t) + \oint_{A_i} f(u(x,t)) \cdot n dA = 0 \quad (2.63)$$

where A_i describes the sum of all surfaces of V_i . n is the outward pointing unit normal vector of A_i . Further trivial transformations lead to Eq. 2.64 which shows that all changes of $u(x,t)$ in the cell depend exclusively on the fluxes through A_i .

$$\frac{\partial}{\partial t}\bar{u}_i(x,t) = -\frac{1}{V_i} \oint_{A_i} f(u(x,t)) \cdot n dA \quad (2.64)$$

2.4 Turbomachines

A machine which transfers energy between a rotor and a fluid is called a turbomachine. This class of machinery encompasses both compressors, which transfer energy from the rotor to the fluid, and turbines, which transfer energy from the fluid to the rotor. Both machine types obey the same basic physical relationships described by Newton's law of motion and Euler's turbomachinery equation. On top of that, turbines and compressors exist in open and closed forms. Examples for open machines are propellers, windmills or unshrouded fans. These machines act on an infinite extent of fluid. Closed machines, like for example steam and gas turbines or axial and centrifugal compressors, on the other hand work with a finite volume of fluid which enters the casing at the intake and is expelled at the discharge. As the subject of this research are centrifugal compressors, the rest of this section will focus on this type of machine.

2.4.1 Dimensionless Numbers for Turbomachines and Similitude

A great deal of the fundamental comprehension of turbomachines is obtained from dimensional analysis. Dimensional analysis is a formal procedure which takes the independent variables describing an arbitrary physical system and replaces these by a smaller set dimensionless variables. This enables the analysis of the relations between the influence of the variables on the systems performance by means of simple analytical methods. Applied to the field of turbomachinery, two further advantageous uses of dimensional analysis can be identified: firstly, two systems which are same in terms of the dimensionless variables are considered as similar. This can be used to relate tests on scale models to the real machine. Secondly, dimensional analysis of turbomachines is used to generate correlations for choosing the best suited machine design for a given area of application. A popular example for this approach is the Cordier diagram which was first published by Cordier [Cor53] in 1953. Cordier derived a relation between the non dimensional diameter δ and the non dimensional speed σ for machines of high efficiency. This relation is shown in Fig. 2.6. In addition to σ and δ , this version of the cordier diagram includes lines of constant flow coefficient φ and work coefficient Ψ . Both quantities are derived in the course of this chapter.

In the field of turbomachinery, dimensional analysis is in most cases carried out by the Buckingham *II* theorem [Buc14]. This theorem states that any physical meaningful equation of n physical variables can be rewritten by using $p = n - k$ dimensionless parameters $\pi_1, \pi_2, \dots, \pi_p$ where k is number of physical dimensions involved. To obtain a dimensionless number, a set of influencing parameters has to be chosen out of the available parameters. The number of influencing parameters is determined by the number physical dimension of the system. Table 2.1 lists the eligible systems and their dimensions. The chosen set of influencing parameters has to include each physical dimension at least once. Therefore, a great number of possible dimensionless numbers can be theoretically derived. In order to avoid a confusing variety of dimensionless numbers, standards have been defined for many fields of application (for example [VDI93]).

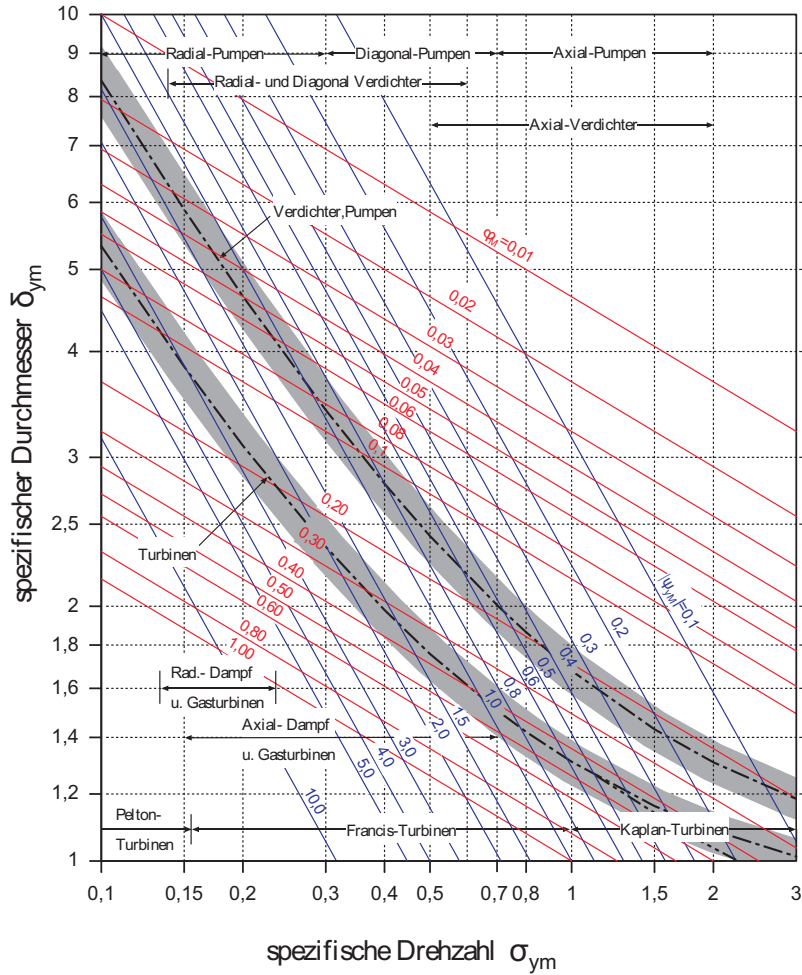


Figure 2.6: A modern version of the Cordier diagram taken from [Eng07]

Table 2.1: Dimensions and parameters of systems in dimensional analysis

Nature of the system	Physical dimensions	Number of required influencing parameters
Geometric	Length (L)	1
Kinematic	Length, time (T)	2
Dynamic	Length, time, mass (M)	3
Thermodynamic	Length, time, mass, temperature (Θ)	4
General physical system	Length, time, mass, temperature, electric charge (Q)	5

For the compressible flow through a turbomachine, a comprehensive analysis of the applicable dimensionless number has been carried out by Fister [Fis84]. In the following paragraphs the most important quantities are derived in a shortened form.

The influencing parameters applicable for turbomachinery and their physical dimensions are listed in Table 2.3. The system “turbomachine“ is of thermodynamic nature as only the dimensions L, M, T, Θ are observed. Therefore, four parameters have to be chosen which include these four dimensions at least once.

Table 2.2: Dimensions and parameters for dimensional analysis of turbomachines

Parameter	Physical dimensions
\dot{m} mass flow rate	MT^{-1}
Δh enthalpy rise	L^2T^{-2}
v_i specific volume at intake	L^3M^{-1}
T_i temperature at intake	Θ
T_d temperature at discharge	Θ
Ω rotational speed	T^{-1}
D diameter	L
A_i intake area	L^2
A_d discharge area	L^2
ν_i kinematic viscosity at intake	L^2T^{-1}
$c_{S,i}$ local speed of sound at intake	LT^{-1}
η_{pol} polytropic efficiency	—
γ heat capacity ratio	—

Out of these quantities, v_E , Ω , D and T_i are chosen as parameters to demonstrate the process of developing a dimensionless number $\Pi_{\dot{m}}$ for the mass flow rate \dot{m} . To derive this number, a product of exponentiations of the dimensions of the parameters has to be formed

in such a way that it is equal to the dimension of the mass flow rate. This is illustrated by Eq. 2.66:

$$\Pi_{\dot{m}} = \frac{\dot{m}}{(v_i)^\alpha (\Omega)^\beta (D)^\gamma (T_i)^\delta} \implies \frac{M^1 T^{-1}}{(L^3 M^{-1})^\alpha (T^{-1})^\beta (L^1)^\gamma (\Theta^1)^\delta} \quad (2.65)$$

A comparison of the exponents in the numerator and the denominator yields:

Table 2.3: Exponent comparison

Exponent	Comparison	Result
M	$-\alpha = 1$	$\alpha = -1$
T	$-\beta = -1$	$\beta = 1$
L	$3\alpha + \gamma = 0$	$\gamma = 3$
Θ	$\delta = 0$	$\delta = 0$

Applying these findings to Eq. 2.66 gives the dimensional number $\Pi_{\dot{m}}$.

$$\Pi_{\dot{m}} = \frac{\dot{m} v_i}{\Omega D^3} = \frac{\dot{V}_i}{\Omega D^3} \quad (2.66)$$

The quantity $\Pi_{\dot{m}}$ derived in this example is not used in practice as an other dimensionless number φ_D , also called ‘‘flow coefficient’’, is well established (see [Fis84]). φ_D is defined as

$$\varphi_D = \frac{c_D}{u_d} \quad (2.67)$$

where c_D (Eq. 2.68) is the theoretical velocity which is achieved if the intake flow rate \dot{V}_i passes through a circular area defined by the discharge diameter. u_d is the circumferential velocity at the discharge given by Eq. 2.69.

$$c_D = \frac{4\dot{V}_i}{D_d^2 \pi} \quad (2.68)$$

$$u_d = \pi \Omega D_d \quad (2.69)$$

The combination of Eq. 2.67, Eq. 2.68 and Eq. 2.69 yields

$$\varphi_D = \frac{4\dot{V}_i}{D_d^3 \pi^2 \Omega} \quad (2.70)$$

for the flow coefficient φ_D . This expression is equal to II_m except for a constant factor of $\frac{4}{\pi^2}$. The common version of the flow coefficient, which can also be considered as a dimensionless representation of the flow rate, is given by Eq. 2.71.

$$\varphi_d = \frac{4\dot{V}_i}{\pi D_d^2 U_d} \quad (2.71)$$

A further important quantity is the work coefficient Ψ given by Eq. 2.72 without derivation. This quantity relates the enthalpy rise needed to move the fluid from the intake to the discharge state to the amount of work delivered by the rotor. The work coefficient can be viewed as a dimensionless form of the pressure ratio. A detailed derivation can be found in [Fis84].

$$\Psi = \frac{\Delta h}{u_d^2} \quad (2.72)$$

The dimensionless numbers σ and δ , which are used in the Cordier digram 2.6, are given by Eq. 2.73 and Eq. 2.74. A derivation can be found in [Cor53]. σ is a dimensionless measure of the machines rotational speed Ω , δ is directly related to the outer diameter D_d .

$$\sigma = \frac{\Omega \sqrt{\dot{V}_i}}{|\Delta h|^{3/4}} (2\pi^2)^{1/4} \quad (2.73)$$

$$\delta = \frac{D_d |\Delta h|^{1/4}}{\sqrt{\dot{V}_i}} \left(\frac{\pi^2}{8} \right)^{1/4} \quad (2.74)$$

2.4.2 Coordinate Systems and Conventions

In the field of rotating machinery, a polar coordinate system (z, r, ϑ) is normally used. In case of a common z -axis, the polar coordinates r and ϑ can be converted to the Cartesian coordinated x and y according to Eq. 2.75.

$$\begin{aligned} x &= r \cos\vartheta \\ y &= r \sin\vartheta \end{aligned} \quad (2.75)$$

The reverse conversion is carried out by

$$\begin{aligned} r &= \sqrt{x^2 + y^2} \\ \vartheta &= \text{atan}\left(\frac{y}{x}\right) \end{aligned} \quad (2.76)$$

where the quadrant of the point defined by (x, y) has to be considered when computing the angle ϑ .

The commonly used coordinates (z, r, ϑ) , m and s are shown in Fig. 2.7.

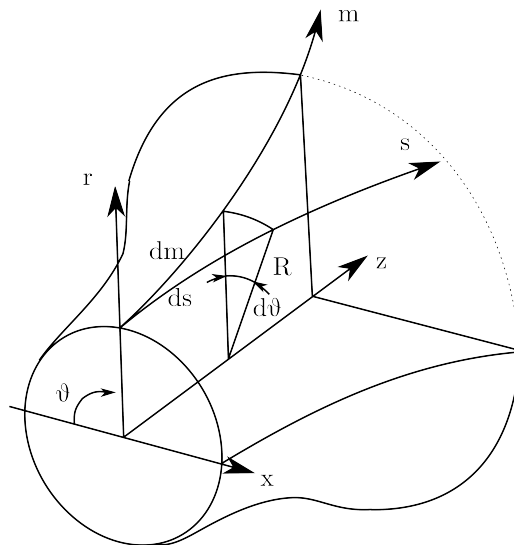


Figure 2.7: Coordinate systems of a centrifugal impeller.

A measure commonly used for describing turbomachinery is the meridional coordinate m . Its definition is illustrated in Fig. 2.8. The meridional coordinate measures the distance between the intake and a point on a two dimensional streamline in the meridional plane. It can be computed by summing up infinitesimal elements dm defined as $dm = \sqrt{r^2 + z^2}$. The normalization of the meridional coordinate is carried out by dividing by the value of the meridional coordinate at the discharge. This dimensionless meridional coordinate m' has a value of 0 at the intake and a value of 1 at the discharge.

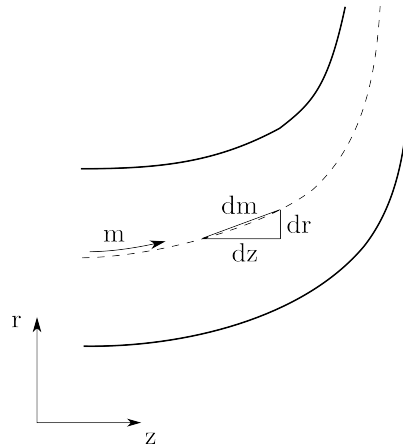


Figure 2.8: Definition of the meridional coordinate m .

The stream wise coordinate s is another measure commonly used in turbomachinery. Similar to the meridional coordinate, it measures the distance between a point on a streamline and the intake. In contrast to the meridional coordinate, the stream wise coordinate is computed on a three dimensional streamline by adding up infinitesimal elements ds defined as $ds = \sqrt{x^2 + y^2 + z^2}$. Analogously, it can be normalized by dividing by the value at the discharge.

A common method of representation in turbomachines is the blade to blade view. It is created by plotting values obtained on a rotation surface defined by a constant location between hub and shroud in a $m - \vartheta$ coordinate system. An example for a curve with a constant hub to shroud location which defines such a rotation surface is the dashed middle streamline shown in Fig. 2.8. The blade to blade view can be used to visualize the three dimensional flow in an impeller in a two dimensional way. Furthermore, it is used to determine the impellers throat area which is important for many one dimensional flow models.

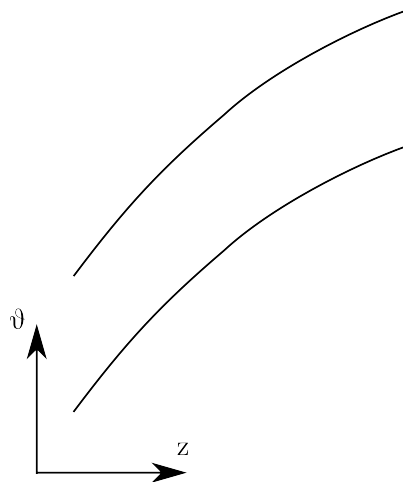


Figure 2.9: Blade to blade view of two adjacent impeller blades.

2.4.3 Centrifugal Compressors

Figure 2.10 shows the side view of a single stage centrifugal compressor. The heart of the compressor is the impeller which is responsible for the energy transfer. The flow enters the machine at the intake and is drawn towards the impeller. Therefore the first function of the impeller is to lower the static pressure at the eye of the impeller. This forces the fluid to flow into the impeller. As soon as the flow enters the impeller, the blades exert strong forces on the fluid and most of the fluid elements will follow a pseudo-helical pattern through the impeller. The efficiency of this process depends strongly on the shape of the impeller blades. If the blading is not matched with the flow field, losses will occur due to incidence or flow separation just to name two effects. After the impeller, the flow enters a diffuser which is used to convert a part of the kinetic energy in the fluid to pressure. Finally, the volute is used to collect the flow which leaves the diffuser through a cylindrical surface spanning 360° .

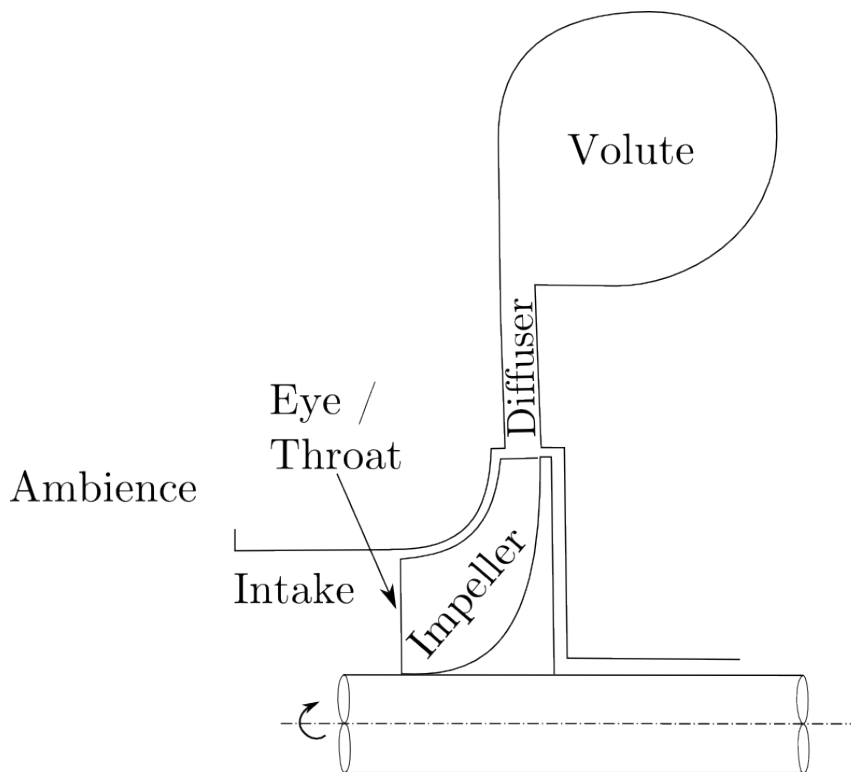


Figure 2.10: Side view of a single stage compressor

2.4.4 Operation Characteristics

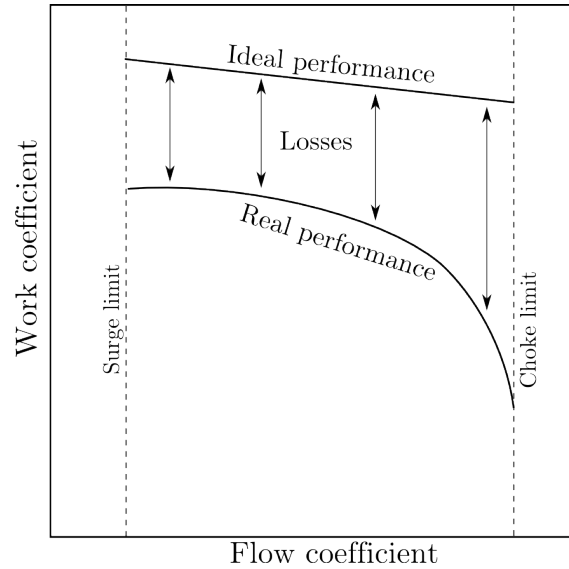


Figure 2.11: Characteristic curve plotted by flow and work coefficient

The term “operation characteristic“, “performance characteristic“ or “speedline“ is used in the field of turbomachinery for characteristic curves which connects points consisting of a measure flow rate and a value describing the state of operation of the machine at this flow rate. A detailed description of the thermodynamic and fluid dynamic processes in a centrifugal compressor can be found in [Aug00] and [Fis84]. Figure 2.11 shows a typical compressor characteristic illustrated by the variation of the work coefficient (2.72) as a function of the flow coefficient (2.71). The flow coefficient is directly related to the machines flow rate, the work coefficient is a dimensionless measure for the pressure ratio. This way, the performance of the compressor can be described non-dimensionally. The upper line in Fig. 2.11 depicts the performance of an ideal compressor. The difference between the ideal and the real performance is caused by losses occurring at different levels of intensity at each state of operation.

The working range of the machine is limited towards low flow rates by the surge limit. At low mass flow rates and high pressure ratios, the pressure in the components downstream of the impeller can become higher than the pressure the impeller can deliver causing the flow to change its direction until the downstream pressure is lower than the impeller outlet pressure. The pulsating reversal of the flow direction can cause heavy machine vibration and lead to severe damages. Therefore this kind of operation has to be avoided. Towards high mass flow rates, the characteristic is limited by the choke limit. Choke occurs at high mass flow rates when the Mach number of the relative inlet velocity of the impeller throat reaches unity over the whole flow area. This marks the maximum mass flow rate which the impeller can deliver.

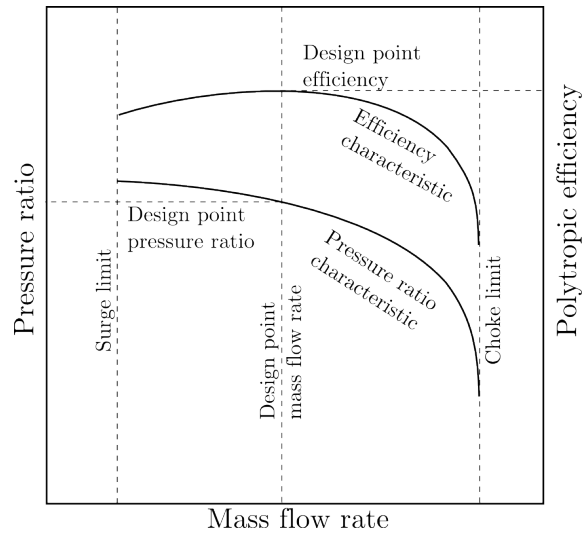


Figure 2.12: Characteristic curve plotted by mass flow rate and pressure ratio as well as polytropic efficiency

Figure 2.12 shows an alternative representation of a performance characteristic. Here, the pressure ratio and the polytropic efficiency are plotted as functions of the mass flow rate. Additionally, the design point is marked in terms of mass flow rate, pressure ratio and efficiency.

2.4.5 Flow in Centrifugal Compressors

The flow in a centrifugal compressor is highly complex and directly related to the three dimensional shape of the flow channel. [Jap96], [Aug00] and [Fis86] offer a multitude of methods to compute this flow. Generally, the flow can be divided into a primary flow which follows the impeller geometry from the inlet to the outlet and a secondary flow which deviates from the main flow direction. The generation of secondary vortices, and therefore losses, strongly depends on the shapes of the impeller blades and of the meridional contours. The three dimensional flow can be projected into the meridional plane and the crosswise or blade normal plane to analyze the flow by a simplified analytical approach. Another simplified approach is the mean line analysis. Here, the impeller is placed into a control volume whose boundaries match the inflow and outflow surfaces of the machine. Figure 2.13 shows a centrifugal compressor impeller with the boundaries of the control volume (green faces). The blue line marks the middle stream line placed at the center of the flow channel.

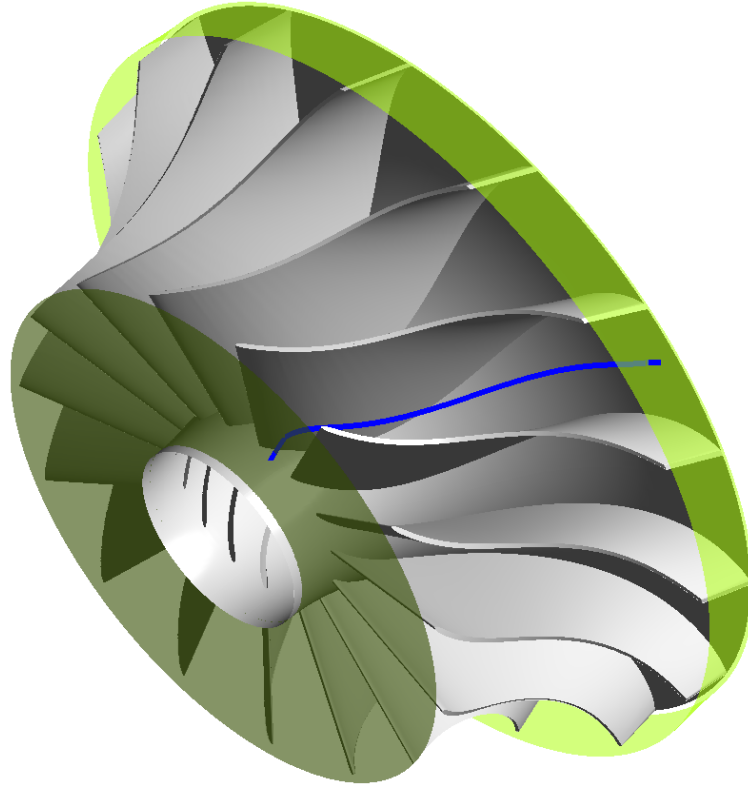


Figure 2.13: Centrifugal compressor impeller with boundaries for mean line computation. Boundaries depicted by green faces, mean filament marked as blue line.

2.4.5.1 Euler and Lagrange Description

Motion can be depicted in different ways depending on whether the observer has a fixed spacial position or follows the motion. The approach of a fixed observer is referred to as “Euler description“ while the approach of an observer following the motion is called “Lagrange description“. Figure 2.14 visualizes this by a simple flow through a pipe. Using the Euler description, the fluid properties like pressure, velocity or temperature are measured at “Location 1“. Therefore, each of this properties depends on the location and the time. In the Lagrange description, a fluid particle is labeled “A“ and is monitored as it flows through the pipe. Here, the fluid properties depend only on the time. If the location of the particles is know as a function of time, the Lagrange description can be transformed into the Euler description. In fluid mechanics the Euler description is primarily used.

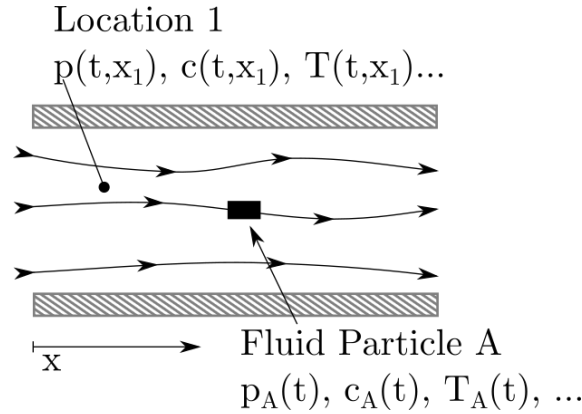


Figure 2.14: Observation of the fluid motion in a pipe by Euler and Lagrange description

2.4.5.2 Rotating Reference Frame

A centrifugal compressor consists of stationary and rotating parts. Therefore, the fluid flow inside the machine has to be observed in two frames of reference: a fixed inertial reference frame and a rotating reference frame. A detailed derivation of the underlying mathematics can be found in [Har05]. \vec{i} , \vec{j} and \vec{k} are the unit normal vectors in the inertial system representing the x , y and z direction. For a rotation with the angular velocity $\omega(t) = \Omega t$ about the z -axis, the transformed vectors are given by Eq. 2.77. The transformed vector representing the z direction is not changed for a rotation about the z -axis ($\vec{k} = \vec{k}$).

$$\begin{aligned}\vec{\hat{i}} &= (\cos(\Omega t), \sin(\Omega t))^T \\ \vec{\hat{j}} &= (-\sin(\Omega t), \cos(\Omega t))^T\end{aligned}\tag{2.77}$$

The time derivatives of the transformed unit vectors read as

$$\begin{aligned}\frac{d}{dt} \vec{\hat{i}} &= \Omega (-\sin(\Omega t), \cos(\Omega t))^T \\ \frac{d}{dt} \vec{\hat{j}} &= \Omega (-\cos(\Omega t), -\sin(\Omega t))^T\end{aligned}\tag{2.78}$$

With the vectorial notation of the angular velocity $\vec{\Omega} = (0, 0, \Omega)^T$, Eq. 2.78 can be written as

$$\begin{aligned}\frac{d}{dt} \vec{\hat{i}} &= \vec{\Omega} \times \vec{\hat{i}} \\ \frac{d}{dt} \vec{\hat{j}} &= \vec{\Omega} \times \vec{\hat{j}}\end{aligned}\tag{2.79}$$

An arbitrary vectorial valued function $f(t) = f_x(t) \vec{\hat{i}} + f_y(t) \vec{\hat{j}} + f_z(t) \vec{\hat{k}}$ in the rotating

frame of reference is derived with respect to time using the product rule according to Eq. 2.80.

$$\begin{aligned}
\frac{d}{dt}f &= \frac{df_x}{dt}\hat{i} + \frac{d\hat{i}}{dt}f_x + \frac{df_y}{dt}\hat{j} + \frac{d\hat{j}}{dt}f_y + \frac{df_z}{dt}\hat{k} + \frac{d\hat{k}}{dt}f_z \\
&= \frac{df_x}{dt}\hat{i} + \frac{df_y}{dt}\hat{j} + \frac{df_z}{dt}\hat{k} + \left[\Omega \times \left(f_x\hat{i} + f_y\hat{j} + f_z\hat{k} \right) \right] \\
&= \left(\frac{df}{dt} \right)_r + \Omega \times f(t)
\end{aligned} \tag{2.80}$$

The term $\left(\frac{df}{dt} \right)_r$ describes the temporal change of f as observed in the rotating frame of reference while $\Omega \times f(t)$ represents the change of f due to the rotation.

The velocity of any object is defined as the time derivative of the object's position ($c = \frac{dr}{dt}$). In the case of a rotating frame of reference, this position is denoted as $r(t)$. Analogously to Eq. 2.80, the velocities in the inertial reference frame (index i) and the rotating reference (index r) frame are connected by the equation

$$c_i = \frac{dr}{dt} = \left(\frac{dr}{dt} \right)_r + \Omega \times r = c_r + \Omega \times r \tag{2.81}$$

The velocity observed in the inertial frame of reference can be split into a velocity due to the motion of the object itself and a component resulting from the rotating frame's motion.

The acceleration is defined as the second time derivative of the object's position respectively as the first time derivative of the object's velocity. After carrying out the differentiations, the acceleration in the rotating frame of reference reads as

$$a_r = a_i - 2\Omega \times c_r - \Omega \times (\Omega \times r) - \frac{d\Omega}{dt} \times r \tag{2.82}$$

$a_r = \left(\frac{d^2r}{dt^2} \right)_r$ is the acceleration in the rotating frame, $a_i = \left(\frac{d^2r}{dt^2} \right)_i$ the acceleration in the inertial frame. The term $-\Omega \times (\Omega \times r)$ represents the centrifugal acceleration, $-2\Omega \times c_r$ is the Coriolis acceleration and the last term $\frac{d\Omega}{dt} \times r$ is the Euler acceleration which is zero in uniformly rotating frames.

According to Newton's second law of motion, force equals the product of mass and acceleration ($F = ma$). Multiplying Eq. 2.82 with the mass of the observed object yields

Newton's second law of motion in a rotating frame of reference as

$$ma_r = ma_i - 2m\Omega \times c_r - m\Omega \times (\Omega \times r) - m \frac{d\Omega}{dt} \times r \quad (2.83)$$

$$F_r = F_i + F_{centrifugal} + F_{Coriolis} + F_{Euler}$$

The forces $F_{centrifugal}$, $F_{Coriolis}$ and F_{Euler} are also called “fictious forces“ as they result solely from the rotation of the frame and not from any physical interaction between bodies. If the frame is not rotating, these forces become zero. The term $F_i = ma_i$ represents any externally impressed forces in the inertial system like for example gravitation or magnetism.

2.4.5.3 Velocity Triangles

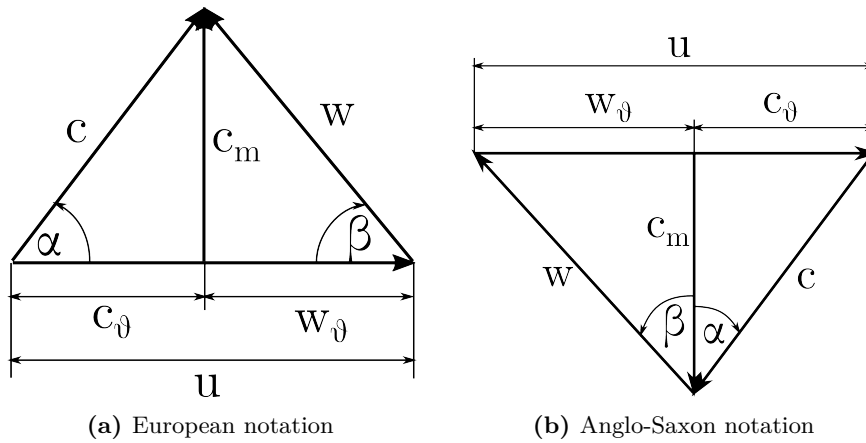


Figure 2.15: Velocity triangles for a centrifugal compressor.

The flow at any point of the streamline in Fig. 2.13 can be depicted by a velocity triangle ([Fis84], [Jap96]). The relative velocity \vec{w} represents the velocity of the flow in the rotating frame of reference as observed from the stationary frame (Eq. 2.84). This corresponds to the relation between the velocities in the inertial and rotating frame derived in Eq. 2.81. The meridional velocity \vec{c}_m is defined as the velocity tangential to the streamline. Furthermore, the centrifugal components of the absolute and the relative velocity can be read directly from the velocity triangles. The absolute and relative flow angles α and β can be read from the velocity triangles in different ways. In this work the European notation is used, where the absolute flow angle is located between \vec{c} and \vec{u} while the relative flow angle is located between \vec{w} and \vec{u} .

$$\vec{c} = \vec{w} + \vec{u} \quad (2.84)$$

2.4.5.4 Euler's Turbomachinery Equation

The angular momentum transferred between the impeller and the fluid is given by Eq. 2.15 as $\tau = \dot{m} (rc_{\theta 2} - rc_{\theta 1})$. The specific technical work \dot{w}_t , transferred between an impeller

rotating with Ω and the fluid, is given by

$$\dot{w}_t = \frac{\tau\Omega}{\dot{m}} \quad (2.85)$$

The combination of Eq. 2.15 and Eq. 2.85 together with the definition of the circumferential velocity $u = \Omega r$ yields

$$\dot{w}_t = u_2 c_{\theta 2} - u_1 c_{\theta 1} \quad (2.86)$$

This relation is known as Euler's turbomachinery equation. It gives the maximum amount of energy which can be transferred between the rotating blades and the fluid. In the case of a compressor \dot{w}_t takes a positive value, for a turbine its value is negative. In the case of a centrifugal compressor with a swirl free inflow, the absolute flow angle at the inlet α_1 becomes 90° , therefore $c_{\theta 1} = c \cdot \cos\alpha_1 = 0$. In this case, Euler's turbomachinery equation simplifies to

$$\dot{w}_t = u_2 c_{\theta 2} \quad (2.87)$$

A second form of Euler's turbomachinery equation can be derived from the trigonometric relations of the velocity triangles (Fig. 2.15a). The law of cosines yields

$$w^2 = c^2 + u^2 - 2c \cdot u \cdot \cos\alpha = c^2 + u^2 - 2c_{\theta}u \quad (2.88)$$

With Eq. 2.88 rearranged as $c_{\theta}u = \frac{1}{2}(c^2 + u^2 - w^2)$ Eq. 2.86 can be written as

$$\dot{w}_t = \frac{1}{2} [(c_2^2 - c_1^2) + (w_1^2 - w_2^2) + (u_2^2 - u_1^2)] \quad (2.89)$$

2.4.5.5 Flow in the Meridional Plane

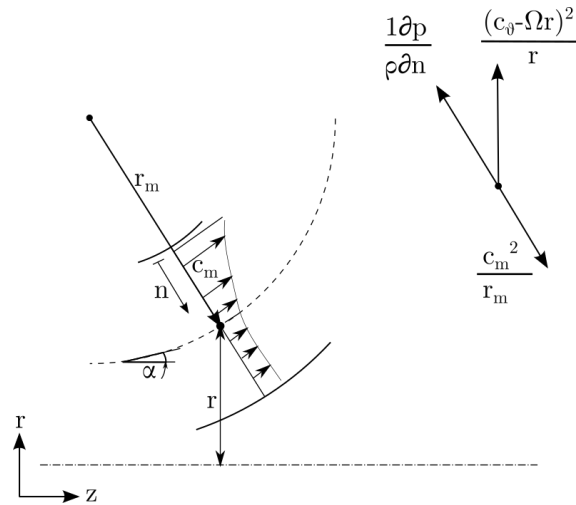


Figure 2.16: Simplified flow in the meridional plane

Figure 2.16 illustrates the flow in the meridional plane under the assumption of straight blades $\left(\frac{\partial \theta_{Blade}}{\partial n}\right)$. At every location on the meridional streamline defined by the curvature radius r_m , the local radius r and the meridional slope angle α , the pressure gradient from hub to shroud and the centrifugal forces are in equilibrium (Eq. 2.90).

$$\frac{1}{\rho} \frac{\partial p}{\partial n} = \frac{c_m^2}{r_m} - \frac{1}{\cos \alpha} \frac{(c_v - \Omega r)^2}{r} \quad (2.90)$$

The first right hand side term describes the centrifugal force due to the flow turning from the axial to the radial direction and depends on the meridional curvature. The second term depicts the centrifugal force induced by the rotation of the impeller (= motion on an axis symmetric surface in circumferential direction). This force is influenced by the meridional slope angle and the local radius.

2.4.5.6 Flow in the Crosswise Plane

The flow in the crosswise plane is primarily influenced by the pressure distributions in the hub to shroud and the blade to blade direction. The pressure distribution in a crosswise plane for blades with zero lean is shown schematically in Fig. 2.17 a-c. Areas of high pressure are labeled with a '+' sign while areas of low pressure are labeled with a '-' sign. The resulting pressure gradient (Fig. 2.17c) is caused by superimposition of two pressure gradients. The hub to shroud pressure gradient (Fig. 2.17a) originates from meridional curvature and centrifugal forces and is described by Eqn. 2.90. The blade to blade pressure gradient (Fig. 2.17b) is caused by the blade loading which increases the pressure on the pressure side (PS) and lowers it on the suction side (SS). The definition of the blade's pressure and suction sides is given in Fig. 2.18. Along the blades, the pressure remains constant from hub to shroud. Combining these two pressure fields yields a resulting pressure

field which has its maximum in the hub pressure side corner and its minimum in the shroud suction side corner.

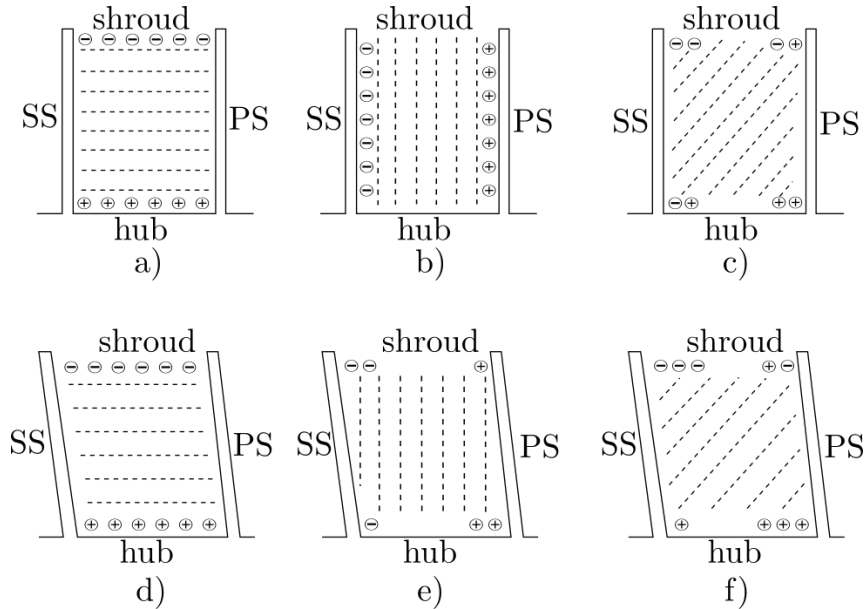


Figure 2.17: Pressure distribution in the crosswise plane for blades with zero lean (a-c) and blades with positive lean (d-f).

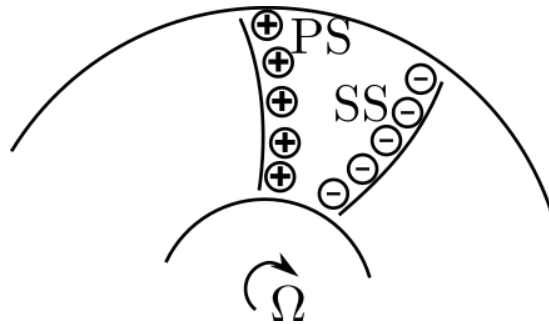


Figure 2.18: Definition of the pressure side (PS) and the suction side (SS) of the blade.

The same analysis is carried out again for a case with a positive blade lean (Fig. 2.17 d-f). As the blade lean does not influence the main factors of the hub to shroud pressure gradient (meridional slope angle and meridional curvature radius), this gradient remains almost unchanged (Fig. 2.17d). The pressure distribution from blade to blade and the span-wise pressure gradient along the blades show obvious changes compared to the zero lean case (Fig. 2.17b and Fig. 2.17e). Comparing the resulting pressure field (Fig. 2.17f) with the one for zero lean (Fig. 2.17c), a higher pressure in the hub pressure side corner and a lower pressure in shroud suction side corner can be observed. This results in a higher force on the flow towards the shroud and therefore in higher velocities near the shroud. These simple considerations already show that blade lean can strongly influence the flow field.

2.4.5.7 Secondary Flow

Preliminary predictions of the flow in turbomachinery are usually carried out assuming an inviscid flow. These methods can describe the global characteristics of the flow field or the primary flow. However, when observing real flow situations, the flow field diverges significantly from the predicted flow in both velocity and direction in certain regions. This effect can be described by superimposing a secondary flow on the primary flow.

The secondary flow in a centrifugal impeller redistributes low energy fluid and thereby influences both velocity and direction of the inviscid primary flow and the pressure by blockage. These effects are driven by the stream-wise vorticity. Smith [Smi57] derived equations to describe the build up of stream-wise vorticity along a relative streamline. A more practical version, used in this study, was presented by Hawthorn [Haw74]. This formulation, given by Eq. 2.91, expresses the rate of increase of stream-wise vorticity as a function of rotary stagnation pressure gradients.

$$\frac{\partial}{\partial s} \left[\frac{\omega_s}{w} \right] = \frac{2}{\rho w^2} \left[\frac{1}{r_m} \frac{\partial p_{t,r}}{\partial b} + \frac{1}{r_b} \frac{\partial p_{t,r}}{\partial n} + \frac{2\Omega}{w} \frac{\partial p_{t,r}}{\partial z} \right] \quad (2.91)$$

The rotary stagnation pressure is given by Eqn. 2.92. This quantity can be seen as a total pressure in the rotating frame of reference.

$$p_{t,r} = p + \frac{\rho w^2}{2} - \frac{\rho u^2}{2} \quad (2.92)$$

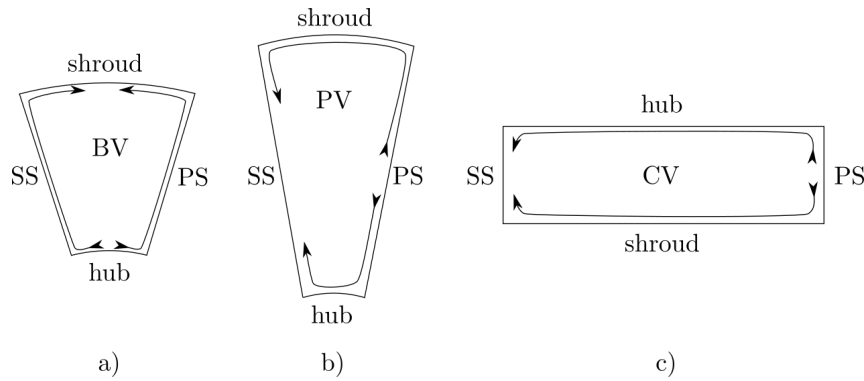


Figure 2.19: Schematic illustration of the different channel vortices

The terms on the right hand side of Eqn. 2.91 describe the different factors for the generation of stream-wise vorticity. The first two terms correspond to the vorticity generated by the turning of the flow in the meridional or the blade-to-blade planes. The third term describes the influence of the Coriolis force and is only relevant in the radial part of the impeller. Equation 2.91 can further be used to describe three typical secondary flow phenomena.

The first term on the right hand side describes the blade surface vortices (BV). This vortex is influenced by the meridional curvature and by the pressure gradient in blade-to-blade direction which again is influenced by the blade lean. It generates a circulation flow

along the blades from hub to shroud (Fig. 2.19a). The blade surface vortex develops when the flow changes from axial to radial direction and progressively becomes smaller in the radial part of the impeller towards the exit.

The second term on the right hand side generates the passage vortices (PV) which are mainly influenced by flow turning in the blade-to-blade plane. These vortices are driven by the radius of curvature of the blade (r_b) and the pressure gradient in hub to shroud direction which again is strongly influenced by the meridional curvature and the meridional slope angle. The passage vortices drive low energy fluid along the hub and shroud endwalls (Fig. 2.19b) and usually occur in the first half of the impeller as the radius of curvature of the blade decreases towards the impeller exit.

The third right hand side term describes the vortices generated by the Coriolis force (CV). These vortices are generated by a pressure gradient in the axial direction. This is the case in the radial part of the impeller where the Coriolis vortex will contribute to the passage vortex by driving low energy fluid from the pressure to the suction side (Fig. 2.19c).

2.4.5.8 Slip factor

Euler's turbomachinery equation for a compressor with swirl free inflow (Eq. 2.87) states that the amount of work transferred between the fluid and the impeller is related to the circumferential velocity u_2 and the circumferential components of the absolute velocity $c_{\vartheta 2}$, both taken at the impeller exit. In an impeller with an infinite number of infinitesimally thin blades, the relative flow angle at the trailing edge β_2 is equal to the blade's angle $\beta_{2,b}$. In a real impeller with a finite number of blades with a certain thickness however, the flow angle diverges from the blade angle. Figure 2.20 shows velocity triangles for both cases with a clear difference between the circumferential component of the absolute velocity for the blade and the flow angle. This results in a deviation between the theoretically possible amount of work transferred between the impeller and the fluid and the real amount. The ratio of the theoretical and the real amount of work can be computed according to Eq. 2.93.

$$\mu = \frac{\dot{w}_t}{\dot{w}_{t,theoretical}} = \frac{u_2 c_{\vartheta 2}}{u_2 c_{\vartheta 2,b}} = \frac{c_{\vartheta 2}}{c_{\vartheta 2,b}} \quad (2.93)$$

$$\sigma = \frac{u_2 - c_{SL}}{u_2} = 1 - \frac{c_{SL}}{u_2} \quad (2.94)$$

$$c_{SL} = c_{\vartheta 2,b} - c_{\vartheta 2} \quad (2.95)$$

$$\sigma = \mu + \varphi_2(\mu - 1)\cot(\beta_{2,b}) \quad (2.96)$$

The quantity μ is used mostly in the German literature and is called "Minderleistungsfaktor". The author was not able to determine an English name for μ . In the English language

area the “slip-factor“ σ is used (Eq. 2.94). It uses the slip velocity given by Eq. 2.95 to measure the deviation between a flow and the blade angle and rates this velocity against the circumferential velocity. μ and σ are connected by Eq. 2.96 where φ_2 is the meridional flow coefficient at the impeller exit given by $\varphi_2 = \frac{c_{m2}}{u_2}$. A derivation can be found in [Fis86].

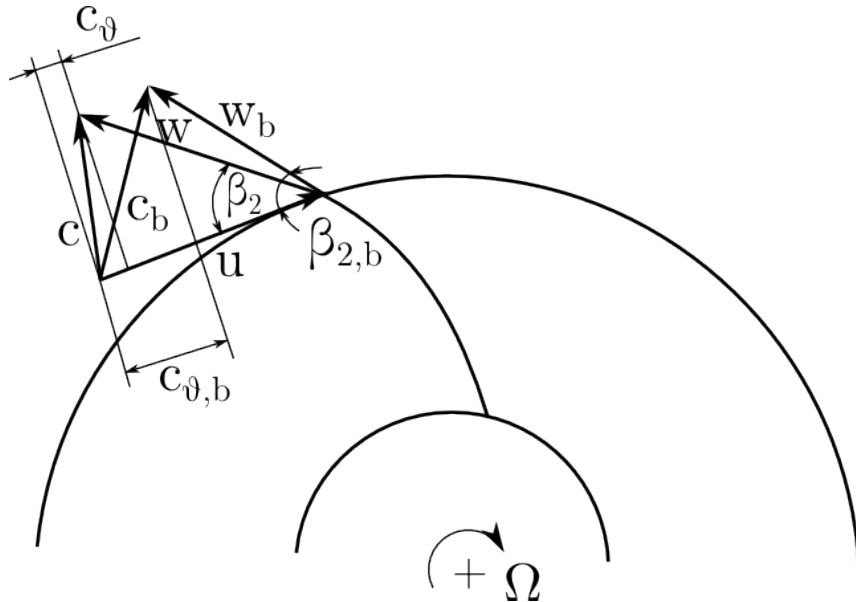


Figure 2.20: Exit velocity triangle for blade and real flow angle

2.5 Solid Mechanics

In this section a short overview of the fundamentals concerning continuum solid mechanics is given. In agreement with the standard textbooks on this subject, most equations are given in tensor notation. Tensors will be written as bold face letters. A brief introduction to tensor algebra can be found in [Hol00]. The theoretic fundamentals of continuum mechanics can be found in [Hol00], [Mar19] or [Alt12].

2.5.1 Cinematics of the Continuum

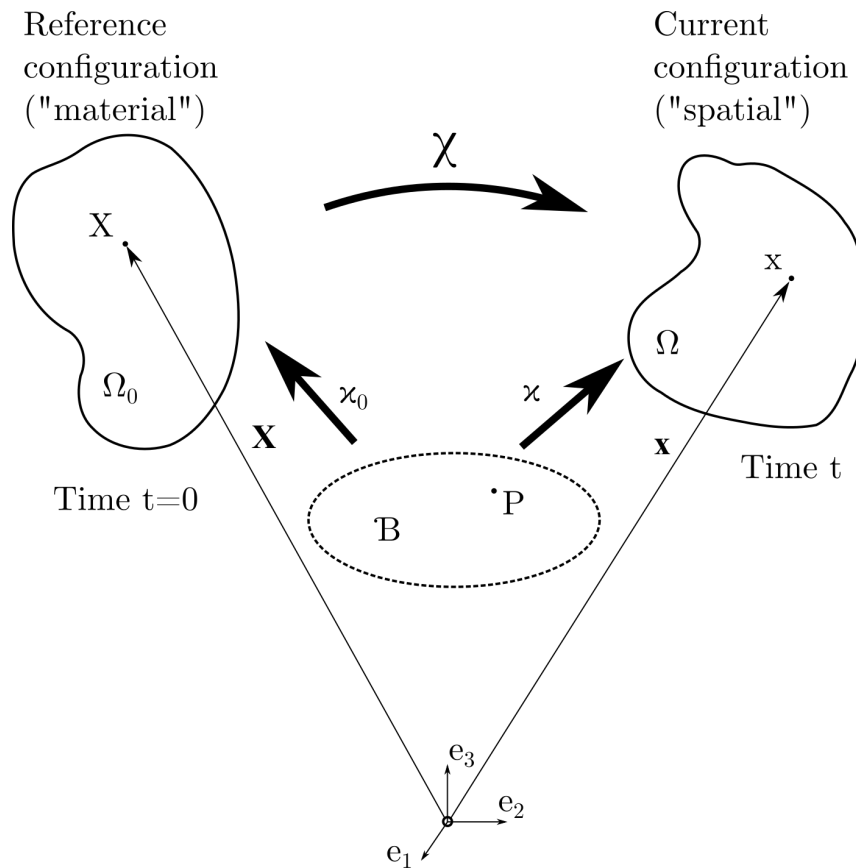


Figure 2.21: Deformation and motion of a continuum body

A body \mathcal{B} is described as a continuous set of material points P in continuum theory. Figure 2.21 depicts a continuum body \mathcal{B} in both the reference (also “undeformed“ or “material“) configuration Ω_0 at time $t = 0$ and the current (also “deformed“ or “spatial“) configuration Ω at time t . The particles P of \mathcal{B} are mapped to the points of reference configuration by κ_0 while κ maps the particles P to the points of the current configuration (Eq. 2.97).

$$\mathbf{X} = \kappa_0(P, t), \quad \mathbf{x} = \kappa(P, t) \quad (2.97)$$

By introduction of the inverse mapping $P = \kappa_0^{-1}(\mathbf{X}, t)$, a point in the current configuration can be expressed by Eq. 2.98 as function of its location in the reference configuration and the time by the motion $\chi(\mathbf{X}, t)$ which is assumed to be invertible ($\mathbf{X} = \chi^{-1}(\mathbf{x}, t)$).

$$\mathbf{x} = \kappa(P, t) = \kappa[\kappa_0^{-1}(\mathbf{X}, t)] = \chi(\mathbf{X}, t) \quad (2.98)$$

The displacement

$$\mathbf{U}(\mathbf{X}, t) = \mathbf{x}(\mathbf{X}, t) - \mathbf{X} \quad (2.99)$$

describes the change of position from \mathbf{X} to \mathbf{x} in Lagrangian or material form as it is a function of the reference position and the time. The spatial or Eulerian form is given by

$$\mathbf{u}(\mathbf{x}, t) = \mathbf{x} - \mathbf{X}(\mathbf{x}, t) \quad (2.100)$$

Both descriptions are related by the motion $\chi(\mathbf{X}, t)$ ($\mathbf{U}(\mathbf{X}, t) = \mathbf{U}[\chi^{-1}(\mathbf{x}, t), t] = \mathbf{u}(\mathbf{x}, t)$).

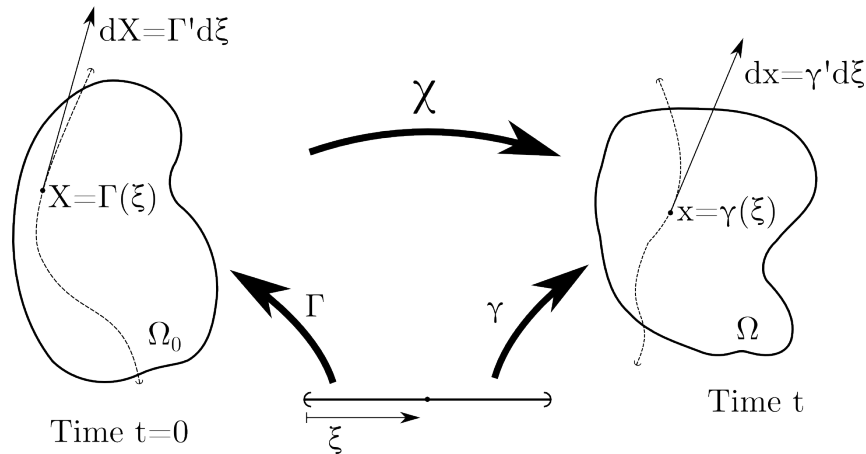


Figure 2.22: Deformation of a curve

A curve parametrized by χ is mapped to the reference configuration by $\mathbf{X} = \Gamma(\chi)$. If the body is deformed from the reference to the current configuration by the motion χ , the resulting curve can be described by $\mathbf{x} = \gamma(\mathbf{X}, t)$ (Fig. 2.22). The spatial curve \mathbf{x} at time t can then be described by

$$\mathbf{x} = \gamma(\mathbf{X}, t) = \chi[\Gamma(\chi), t] \quad (2.101)$$

The tangent vector to the material curve $d\mathbf{X}$ and the tangent vector to the spatial curve

$d\mathbf{x}$ are given as

$$d\mathbf{X} = \Gamma'(\chi)d\chi = \frac{\partial \Gamma(\chi)}{\partial \chi} d\chi, \quad d\mathbf{x} = \gamma'(\chi, t)d\chi = \frac{\partial \gamma(\chi, t)}{\partial \chi} d\chi \quad (2.102)$$

The combination of Eq. 2.101 and Eq. 2.102 yields

$$\gamma' = \frac{\partial \chi(\mathbf{X}, t)}{\partial \mathbf{X}} \Gamma' = \mathbf{F}(\mathbf{X}, t) d\mathbf{X} \quad (2.103)$$

where \mathbf{F} is the deformation gradient which is defined as

$$\mathbf{F}(\mathbf{X}, t) = \frac{\partial \chi(\mathbf{X}, t)}{\partial \mathbf{X}} = \text{Grad}\mathbf{x}(\mathbf{X}, t) \quad (2.104)$$

The deformation gradient is a fundamental quantity in continuum mechanics to measure the deformation. Furthermore it characterizes the behavior of motion in the neighborhood of a point. It is a second-order tensor with 9 time-dependent components and is called a two-point tensor as it includes points from two distinct configurations. Under the assumption that the inverse motion χ^{-1} is derivable, the inverse deformation gradient can be defined as

$$\mathbf{F}^{-1}(\mathbf{x}, t) = \frac{\partial \chi^{-1}(\mathbf{x}, t)}{\partial \mathbf{x}} = \text{grad}\mathbf{X}(\mathbf{x}, t) \quad (2.105)$$

In contrast to the deformation, the strain is a measure of the change in length between two neighboring points \mathbf{X} and \mathbf{Y} with regard to the reference configuration. Figure 2.23 shows two material points \mathbf{X} and \mathbf{Y} and the deformed points \mathbf{x} and \mathbf{y} in the spatial configuration.

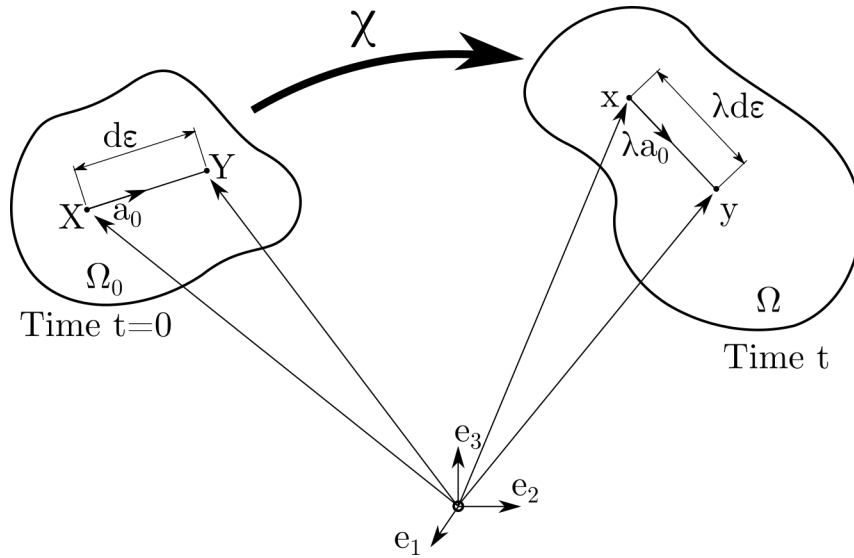


Figure 2.23: Deformation of a line element

The relations between the points in the reference configuration are given by

$$\begin{aligned} \mathbf{Y} &= \mathbf{X} + d\mathbf{X} & d\mathbf{X} &= d\varepsilon \mathbf{a}_0 \\ d\varepsilon &= |\mathbf{Y} - \mathbf{X}| & \mathbf{a}_0 &= \frac{\mathbf{Y} - \mathbf{X}}{|\mathbf{Y} - \mathbf{X}|} \end{aligned} \quad (2.106)$$

The corresponding points in the current configuration are written as

$$\begin{aligned} \mathbf{y} &= \mathbf{x} + d\mathbf{x} & d\mathbf{x} &= \lambda d\varepsilon \lambda \mathbf{a}_0(\mathbf{X}, t) \\ \lambda \mathbf{a}_0 &= \mathbf{F}(\mathbf{X}, t) \mathbf{a}_0 & \lambda d\varepsilon &= |\mathbf{y} - \mathbf{x}| = [(\mathbf{y} - \mathbf{x}) \cdot (\mathbf{y} - \mathbf{x})]^{\frac{1}{2}} \\ & & &= (\lambda \mathbf{a}_0 \cdot \lambda \mathbf{a}_0)^{\frac{1}{2}} d\varepsilon \end{aligned} \quad (2.107)$$

From Eq. 2.106, the squared distance in the reference configuration ($d\varepsilon^2$) can be derived as

$$d\varepsilon^2 = d\varepsilon \mathbf{a}_0 \cdot d\varepsilon \mathbf{a}_0 = d\mathbf{X} \cdot d\mathbf{X} \quad (2.108)$$

With Eq. 2.107, the square of λ can be computed as

$$\lambda^2 = \lambda \mathbf{a}_0 \cdot \lambda \mathbf{a}_0 = \mathbf{F} \mathbf{a}_0 \cdot \mathbf{F} \mathbf{a}_0 = \mathbf{a}_0 \cdot \mathbf{F}^T \mathbf{F} \mathbf{a}_0 = \mathbf{a}_0 \cdot \mathbf{C} \mathbf{a}_0 \quad (2.109)$$

The quantity \mathbf{C} is the right Cauchy-Green tensor (also ‘‘Green deformation tensor’’)

which measures the strain in material coordinates. \mathbf{C} is defined as

$$\mathbf{C} = \mathbf{F}^T \mathbf{F} \quad (2.110)$$

With this, the stretch of an arbitrary curve can be determined solely from the direction \mathbf{a}_0 and the tensor \mathbf{C} .

A further measure of the strain is the change in the squared length $(\lambda d\varepsilon)^2 - d\varepsilon^2$. Using Eq. 2.109 and Eq. 2.108 the change in squared length is given as

$$\begin{aligned} \frac{1}{2}[(\lambda d\varepsilon)^2 - d\varepsilon^2] &= \frac{1}{2}[(d\varepsilon \mathbf{a}_0) \cdot \mathbf{C}(d\varepsilon \mathbf{a}_0) - d\mathbf{X}^2] = \frac{1}{2}[d\mathbf{X} \cdot \mathbf{C}d\mathbf{X} - d\mathbf{X} \cdot d\mathbf{X}] \\ &= d\mathbf{X} \cdot \mathbf{E}d\mathbf{X} \end{aligned} \quad (2.111)$$

where \mathbf{E} is the Green-Lagrangian strain tensor which describes the strain in the direction \mathbf{a}_0 at a point \mathbf{X} in the reference configuration. The Green-Lagrangian tensor \mathbf{E} is defined as

$$\mathbf{E} = \frac{1}{2}(\mathbf{C} - \mathbf{I}) \quad (2.112)$$

where \mathbf{I} is the unit tensor.

2.5.2 Stress

In the preceding section the kinematic aspects of the motion and the deformation of a continuum body were introduced. Inside the body, motion and deformation result in stress. This section describes the concept of stress for a deformable body undergoing a finite motion.

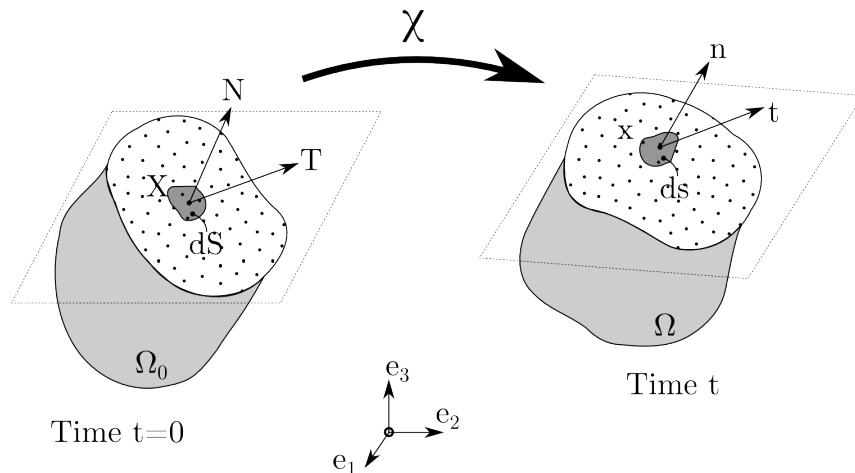


Figure 2.24: Traction vectors acting on an infinitesimal small surface element

Figure 2.24 depicts a continuum body which is cut by a plane that passes through the

point \mathbf{x} in spatial coordinates at the time t . If an arbitrary force acts on the body, the resulting traction vectors on the surface elements dS and ds can be computed as

$$\mathbf{T} = \frac{df}{dS}, \quad \mathbf{t} = \frac{df}{ds} \quad (2.113)$$

where df is the infinitesimal resultant force acting on the surface element. \mathbf{t} is the Cauchy traction vector which measures the force per unit surface area in the current configuration. \mathbf{T} is the first Piola-Kirchhoff traction vector which gives the force measured per unit surface area in the reference configuration. According to Cauchy's stress theorem, there exist two second-order tensor fields $\boldsymbol{\sigma}$ and \mathbf{P} which fulfill the relations

$$\mathbf{t}(\mathbf{x}, t, \mathbf{n}) = \boldsymbol{\sigma}(\mathbf{x}, t) \mathbf{n}, \quad \mathbf{T}(\mathbf{X}, t, \mathbf{N}) = \mathbf{P}(\mathbf{X}, t) \mathbf{N} \quad (2.114)$$

$\boldsymbol{\sigma}$ is the Cauchy stress tensor (or simply Cauchy stress), while \mathbf{P} is the first Piola-Kirchhoff stress tensor (or simply Piola stress). A more convenient form of Cauchy's stress theorem in matrix notation is given in Eq. 2.115.

$$[\mathbf{t}] = [\boldsymbol{\sigma}][\mathbf{n}], \text{ with} \quad (2.115)$$

$$[\mathbf{t}] = \begin{bmatrix} t_1 \\ t_2 \\ t_3 \end{bmatrix}, \quad [\boldsymbol{\sigma}] = \begin{bmatrix} \sigma_{11} & \sigma_{12} & \sigma_{13} \\ \sigma_{21} & \sigma_{22} & \sigma_{23} \\ \sigma_{31} & \sigma_{32} & \sigma_{33} \end{bmatrix}, \quad [\mathbf{n}] = \begin{bmatrix} n_1 \\ n_2 \\ n_3 \end{bmatrix}$$

2.5.3 Material Law

In the preceding chapters, the fundamental principles of motion, deformation, strain and stress are given. While motion, deformation and strain are connected by the kinematic equation presented in sections 2.5.1, a relation between stress and strain is needed. For small strains and under the assumption of a linear elastic material behavior, this relation can be described by Hooke's law (Eq. 2.116). \mathbb{C} is the stiffness tensor which linearly maps the elements of \mathbf{E} to the elements of $\boldsymbol{\sigma}$. As both the stress tensor $\boldsymbol{\sigma}$ and the strain tensor \mathbf{E} are second order tensors consisting of 9 elements, the stiffness tensor \mathbb{C} is a fourth order tensor containing 81 components (due to the symmetries of $\boldsymbol{\sigma}$, \mathbf{E} and \mathbb{C} only 21 of these components are independent). \mathbb{C} is a property of the material which in many cases depends on physical state variables like pressure or temperature.

$$\boldsymbol{\sigma} = \mathbb{C}\mathbf{E}, \text{ with} \quad (2.116)$$

$$[\boldsymbol{\sigma}] = \begin{bmatrix} \sigma_{11} & \sigma_{12} & \sigma_{13} \\ \sigma_{21} & \sigma_{22} & \sigma_{23} \\ \sigma_{31} & \sigma_{32} & \sigma_{33} \end{bmatrix}, \quad [\mathbf{E}] = \begin{bmatrix} \varepsilon_{11} & \varepsilon_{12} & \varepsilon_{13} \\ \varepsilon_{21} & \varepsilon_{22} & \varepsilon_{23} \\ \varepsilon_{31} & \varepsilon_{32} & \varepsilon_{33} \end{bmatrix}$$

For an isotropic material, \mathbb{C} can be described solely by the material's Young's modulus

E and its Poisson's ratio ν . Taking the symmetry of $\boldsymbol{\sigma}$, \mathbf{E} and \mathbb{C} into account, the relation from Eq. 2.116 can be written as

$$\boldsymbol{\sigma} = \mathbb{C}\mathbf{E}$$

$$\begin{bmatrix} \sigma_{11} \\ \sigma_{22} \\ \sigma_{33} \\ \sigma_{23} \\ \sigma_{13} \\ \sigma_{12} \end{bmatrix} = \frac{E}{(1+\nu)(1-2\nu)} \begin{bmatrix} 1-\nu & \nu & \nu & 0 & 0 & 0 \\ \nu & (1-\nu) & \nu & 0 & 0 & 0 \\ \nu & \nu & (1-\nu) & 0 & 0 & 0 \\ 0 & 0 & 0 & \frac{1-2\nu}{2} & 0 & 0 \\ 0 & 0 & 0 & 0 & \frac{1-2\nu}{2} & 0 \\ 0 & 0 & 0 & 0 & 0 & \frac{1-2\nu}{2} \end{bmatrix} \begin{bmatrix} \varepsilon_{11} \\ \varepsilon_{22} \\ \varepsilon_{33} \\ 2\varepsilon_{23} \\ 2\varepsilon_{13} \\ 2\varepsilon_{12} \end{bmatrix} \quad (2.117)$$

2.5.4 Governing equations

Based on the previously presented concepts, a stationary linear elastic problem is governed by the following set of equations:

$$\operatorname{div} \boldsymbol{\sigma} + F_B = 0 \quad (2.118)$$

$$\mathbf{E} = \frac{1}{2}(\mathbf{C} - \mathbf{I}) \quad (2.119)$$

$$\boldsymbol{\sigma} = \mathbb{C}\mathbf{E} \quad (2.120)$$

where Eq. 2.118 is the equation of motion derived from Newton's second law, Eq. 2.119 is the strain-displacement relation given by the Green-Lagrangian strain-tensor and Eq. 2.120 is Hooke's law which is used as the constitutive equation to relates the stresses to the strains. The equation of motion (Eq. 2.118) can be derived in a similar manner to the conservation of momentum presented in section 2.2.2.2. The term F_B represents an arbitrary body force like gravitation or magnetism. As the problem is considered to be stationary, no time derivatives are taken into account.

2.6 Statistics

The analysis of complex systems like centrifugal compressors requires tools which are able to detect correlations in high dimensional multi physic systems. While the relations between three, maybe four quantities can be analyzed visually, correlations in higher dimensional spaces can not be detected this way. This section gives a short introduction into the theoretical fundamentals of the applied statistical methods. The basic principles of statistics can be found in [Pap08], [Ras15] or [Wit85].

2.6.1 Sampling Methods

Random samples are the basis for all statistical analyses. These samples are generated by sampling methods. A set of random samples used for statistical analysis is often referred to as “Design of Experiments (DOE)“. This term will be used in the course of this work, too. Sampling methods can be divided into two major groups: systematic and stochastic sampling methods. In application areas with high dimensional spaces and costly design evaluations, a good coverage of the design space with a reasonable number of samples can only be achieved by stochastic methods. This is illustrated by Fig. 2.25. A sampling, done by central composite design for example, features samples with three different values for each parameter. Therefore only quadratic correlations can be observed. For a small scale example with 10 parameters over 1000 samples are generated. This fact disqualifies these methods for applications with numerically expensive CAE computations. Therefore this section focuses on these methods. A general overview of sampling methods can be found in [Rub11] or [Dyn13].

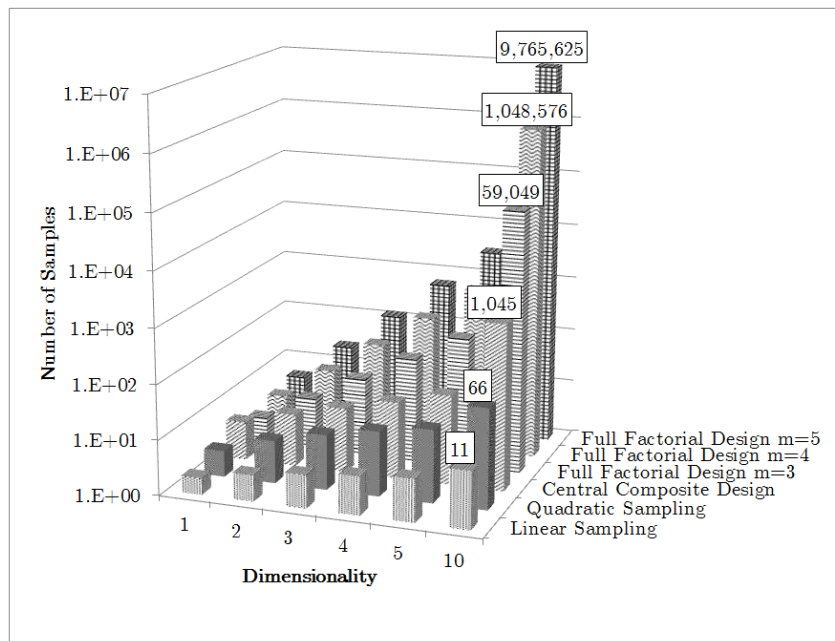


Figure 2.25: Number of samples for one- to ten-dimensional problems generated by systematic sampling methods (Linear sampling, quadratic sampling, central composite design, full factorial design with 3,4,5 values per dimension).

2.6.1.1 Monte Carlo Simulation

Monte Carlo simulation is a straight forward technique to generate stochastic design samples. This methods generates independent samples by drawing random numbers from a uniform distribution. The method was first proposed by Enrico Fermi in the 1930s to calculate neutron diffusion. The name “Monte Carlo“ refers to a casino in Monaco. The Monte Carlo method is particularly suitable for applications where the independence of the samples is the most important criterion for choosing the appropriate method. As it is a purely stochastic method, the spacial distribution of the samples can not be influenced. If a good coverage of the design space is desired, a large number of samples has to generated when using Monte Carlo sampling. Therefor other methods are more suitable in this case.

2.6.1.2 Latin Hypercube Sampling

Latin hypercube sampling (LHS) is a stochastic sampling method which generates nearly random independent samples with a focus on reducing the number of samples needed for a good spacial coverage of the design space. This method was proposed independently by McKay ([McK79]) and Eglājs ([Egl77]) in the 1970s. A sampling for two variables in a square grid is called a “Latin square“ only if the constrain is fulfilled that there is only one sample in each row and each column . The generalization of this rule to the n-dimensional space is called “Latin hypercube“.

A basic Latin hypercube sampling containing M samples of N variables is generated by the following algorithm:

1. Divide the range of each variable into M equal intervals.
2. Create a random sample $x_{n,m}$ for each variable n_i in each interval m_i . This will result in the following sampling matrix:

$$LHS = \begin{bmatrix} x_{1,1} & x_{2,1} & \dots & x_{N,1} \\ \vdots & & & \vdots \\ x_{1,M} & \dots & \dots & x_{N,M} \end{bmatrix} \quad (2.121)$$

Each column represents a variable while each row represents a sample.

3. Randomly permute the cells in each column.

The Latin hypercube algorithm is a stochastic simulation method. Therefore the resulting sampling can contain unwanted random correlations or uneven spacial distributions. Advanced versions of the algorithm try to minimize the correlations by optimizing the permutations in step 3. Alternatively the spacial distribution of the samples can be optimized by maximizing the minimal distance of the samples.

2.6.2 Metamodeling

In many cases CAE computations are costly in terms of computational expense. In these cases it is not possible to do stochastic or statistical analysis or optimizations by evaluating each design with a simulation. This problem can be bypassed by using a surrogate model which can deliver a fast prediction of the real problem's physics. These surrogate models are often called meta models. Popular approaches for meta modeling are for example polynomial least squares approximation or Kriging. The meta model is obtained by generating a set of samples with a suitable sampling method and fitting a regression defined by one of the previously mentioned methods to the data.

2.6.2.1 Least Squares Method

Least squares approximation is an established method to fit an arbitrary function to a given set of data. This method is often credited to Carl Friedrich Gauss, but it was first made public by Adrien-Marie Legendre ([Sti81]). Details and a derivation of this method can be found in standard texts on linear algebra like [Bre13]. As polynomials are used in many cases, this section focuses on these functions.

$y = f(x)$ is an arbitrary n -dimensional function. x is the n -dimensional vector of input parameters. The basis of the approximation is a DOE of y containing K samples. The k^{th} samples of y can be approximated by the following polynomial:

$$\hat{y}_k = \beta_0 + \beta_1 x_{1,k} + \beta_2 x_{2,k} + \dots + \beta_n x_{n,k} + \beta_{1,1} x_{1,k}^2 + \dots + \beta_{n,n} x_{n,k}^2 + \beta_{1,2} x_{1,k} x_{2,k} + \dots + \beta_{n-1,n} x_{n-1,k} x_{n,k} + \varepsilon_k \quad (2.122)$$

ε_k is the approximation error of the k^{th} sample defined as $\varepsilon_k = |y_k - \hat{y}_k|$, β_i are the regression coefficients. Writing Eq. 2.122 in matrix notation yields

$$y = X\beta + \varepsilon \quad (2.123)$$

with

$$\begin{aligned} y &= [y_1 \ y_2 \ \dots \ y_K]^T \\ \varepsilon &= [\varepsilon_1 \ \varepsilon_2 \ \dots \ \varepsilon_K]^T \\ \beta &= [\beta_0 \ \beta_1 \ \dots \ \beta_n \ \beta_{1,1} \ \dots \ \beta_{n,n} \ \beta_{1,2} \ \dots \ \beta_{n-1,n}]^T \end{aligned}$$

and

$$X = \begin{bmatrix} 1 & x_{1,1} & \dots & x_{n,1} & x_{1,1}^2 & \dots & x_{n,1}^2 & x_{1,1}x_{2,1} & \dots & x_{n-1,1}x_{n,1} \\ 1 & x_{1,2} & \dots & x_{n,2} & x_{1,2}^2 & \dots & x_{n,2}^2 & x_{1,2}x_{2,2} & \dots & x_{n-1,2}x_{n,2} \\ \vdots & \vdots & & \vdots & \vdots & & \vdots & \vdots & & \vdots \\ 1 & x_{1,K} & \dots & x_{n,K} & x_{1,K}^2 & \dots & x_{n,K}^2 & x_{1,K}x_{2,K} & \dots & x_{n-1,K}x_{n,K} \end{bmatrix}$$

The sum of square of errors S or least squares error is given by

$$S = \sum^K \varepsilon_K^2 = \varepsilon^T \varepsilon \rightarrow \min \quad (2.124)$$

and has to be minimized in order to obtain the best fit of the data. Combining Eq. 2.123 and Eq. 2.124 yields the least squares error as a function of the regression coefficients (Equation 2.125).

$$S(\beta) = (y - X\beta)^T (y - X\beta) \rightarrow \min \quad (2.125)$$

After expansion and simplification of the right hand side, Eq. 2.125 can be written as

$$S(\beta) = y^T y - 2\beta^T X^T y + \beta^T X^T X \beta \rightarrow \min \quad (2.126)$$

The minimum of the least squares error can be found by setting the partial gradient $\frac{\partial S(\beta)}{\partial \beta}$ to zero. The gradient is given by

$$\frac{\partial S(\beta)}{\partial \beta} = -2X^T y + 2(X^T X)\beta = 0 \quad (2.127)$$

If the matrix $X^T X$ is non-singular, the coefficients β can be obtained by solving Eq. 2.127 for β . This yields

$$\beta = (X^T X)^{-1} X^T y \quad (2.128)$$

The least squares approximation is given by

$$\hat{y} = X\beta \quad (2.129)$$

2.6.2.2 Moving Least Squares

The classical least squares method as described in the previous chapter is a global approximation method. Therefore, it is not suited to fit data with multiple local minima or discontinuities. The moving least squares (MLS) method eliminates this problem by using a local fit at every data point. This method was first introduced by Lancaster & Salkauskas in 1986 ([Lan86]). Inside the parametric space, n_S support points are placed at which a local approximation is performed. The MLS approximation at the i^{th} support point is written as

$$y(x, x_i) = X\beta_i + \varepsilon_i \quad (2.130)$$

where β_i represents the local approximation coefficients at the i^{th} support point and ε_i is the local approximation error. The approximation coefficients can be acquired in a way similar to the previously described least squares method. The least squares error is given by

$$S(x) = \sum_{i=1}^{n_s} w(x)\varepsilon_i^2 = \varepsilon_i^T w(x)\varepsilon_i = (X\beta(x) - y)^T w (X\beta(x) - y) \rightarrow \min \quad (2.131)$$

where $w(x)$ represents a weighting function to define the influence radius around the support points. Again, the minimum is found by setting the partial gradient $\frac{\partial S(x)}{\partial \beta(x)} = 0$. This yields the following formulation for the approximation coefficients

$$\beta(x) = (X^T w(x)X)^{-1} X^T w(x)y \quad (2.132)$$

2.6.2.3 Kriging

Kriging is a popular regression method for which the interpolated values in between the data points are modeled by a Gaussian process which is constrained by the prior covariances obtained from the data. In addition to the approximation of the function value for a parameter combination, this regression method delivers the prediction of the local uncertainty of the prediction in terms of the local variance. The method was first proposed by Daniel G. Krige [Kri51] and mathematically developed by Georges Matheron [Mat71]. The basic underlying mathematics are described in this section in a short manner.

The Kriging approximation for a n-dimensional real valued function $y(x)$ is given by

$$\hat{y}(x) = \mu(x) + Z(x) \quad (2.133)$$

The approximated value is split into a mean value given by the mean function $\mu(x)$ which is superimposed by a stationary Gaussian process $Z(x)$ with variance σ^2 . As the Gaussian process is stationary, the covariances $Cov(Z(x_i), Z(x_j))$ only depend on the distance $d_{ij} = x_i - x_j$ between x_i and x_j . Therefore the covariances can be denoted by

$$Cov(Z(x_i), Z(x_j)) = \sigma^2 \cdot R(d_{ij}) \quad (2.134)$$

where $R(\cdot)$ is an arbitrary kernel or covariance function and d_{ij} is the distance between x_i and x_j . If the mean function $\mu(x)$ is constant ($\mu(x) = \mu$) and known, the model is called a “simple Kriging“ model. A model with an unknown constant mean function is called “ordinary Kriging“. If the mean function varies depending on x , the model is referred to as “universal Kriging“. In many cases the mean function is given by a polynomial approach of the form $\mu(x) = X\beta$. The unknown coefficients β can be approximated by the least squares method.

2.6.2.4 Error Measurements

The usability of a metamodel relies heavily on the approximation quality which can be rated by several error measurements. The difference between the predicted and the actual value is often called residual. The maximal residual (Eq. 2.135) depicts the largest deviation between the approximation and the data while the mean residual (Eq. 2.136) uses the arithmetic average of all deviations to rate the approximation quality. The root mean square error (RMSE) uses the quadratic mean residual to assess the accuracy of the approximation (Eq. 2.137).

$$r_{max} = \max|y_i - \hat{y}_i| \quad (2.135)$$

$$r_{mean} = \frac{1}{N} \sum_{i=1}^N |y_i - \hat{y}_i| \quad (2.136)$$

$$RMSE = \sqrt{\frac{\sum_{i=1}^N (y_i - \hat{y}_i)^2}{N}} \quad (2.137)$$

The R^2 value is a measure which relates the variance of the approximation model to the variance of the data. Another common name for this value is ‘‘coefficient of determination (CoD)‘‘. R^2 can be computed as

$$R^2 = \frac{\sum_{i=1}^N (\hat{y}_i - \bar{y})^2}{\sum_{i=1}^N (y_i - \bar{y})^2} \quad (2.138)$$

where \bar{y} denotes the mean value of y . The CoD can take values between 0 and 1 and is dimensionless. It indicates how well the variance of the original data can be explained by the chosen regression. A high value of R^2 does not necessarily imply a highly accurate regression model as the value of R^2 increases with the number of model terms used for the regression. This problem is addressed by the adjusted coefficient of determination (Eq. 2.139) where n is the number of support points and p the number of regression model terms. This value does not increase with the number of model terms, but on the contrary does decrease for unnecessary model terms. If a comparison between R^2 and R_{adj}^2 shows a significant difference, the regression model most likely contains redundant terms.

$$R_{adj}^2 = 1 - \frac{n-1}{n-p} (1 - R^2) \quad (2.139)$$

2.6.2.5 Metamodel of Optimal Prognosis

The software optiSLang by Dynardo, which was used for the statistical analysis in this work, features an automated workflow to determine the best fitted metamodel for a set of data [Wil09]. This method uses cross validation to rate different metamodels. In a first step the data is divided into two subsets, one for metamodel generation and one for validation / testing. The metamodel is fitted to the data in the first subset. The responses of the samples in the testing subset are computed using the metamodel and compared against the original responses. This gives a trustworthy statement of the metamodel prediction quality. The prediction quality can be described by the ‘‘Coefficient of Prognosis (CoP)’’ (Eq. 2.140) which takes values between zero and one [Dyn13]. Furthermore the CoP can be used to derive sensitivity indices for single input variables which depict how much of the output variation can be explained by the respective input variable.

$$COP = \left(\frac{\sum_{i=1}^N (y_{Test,k} - \bar{y}_{Test}) (\hat{y}_{Test,k} - \bar{\hat{y}}_{Test})}{(N - 1) \sigma_{y_{Test}} \sigma_{\hat{y}_{Test}}} \right)^2 \quad (2.140)$$

2.7 Optimization

Optimization is the process of obtaining the best possible value of an objective function while fulfilling the given constraints. First approaches for both iterative and calculus based optimization methods were proposed by Newton, Gauss, Fermat or Lagrange. As of today a wide variety of optimization algorithms is known. [Sny18], [Noc06], [Boy06] or [Cor99] give an overview of these methods. Complex optimization tasks with many input variables and often multiple objectives can not be solved by manually changing the design and evaluating the outcome as the interactions between the individual variables are complex and non linear in many cases. Therefore, powerful optimization tools are required which are available in the form of mathematical optimization techniques. These techniques can be divided into two main categories:

- **Deterministic Optimization Techniques**

- Simplex algorithm
- Complex algorithm
- Hill climbing methods
- Gradient based algorithms
- ...

- **Stochastic Optimization Techniques**

- Nature inspired methods
 - * Physical process methods
 - * Artificial life methods
 - Evolutionary algorithms
 - Neural network methods
 - ...

The given problem of turbomachinery optimization features a high number of parameters, discrete parameters and multiple objectives. Deterministic optimizations techniques are unable to handle multiple objectives, constraints of discrete parameters. This limits the applicable optimization techniques to the group of nature inspired optimization methods.

2.7.1 Nature Inspired Optimization Methods

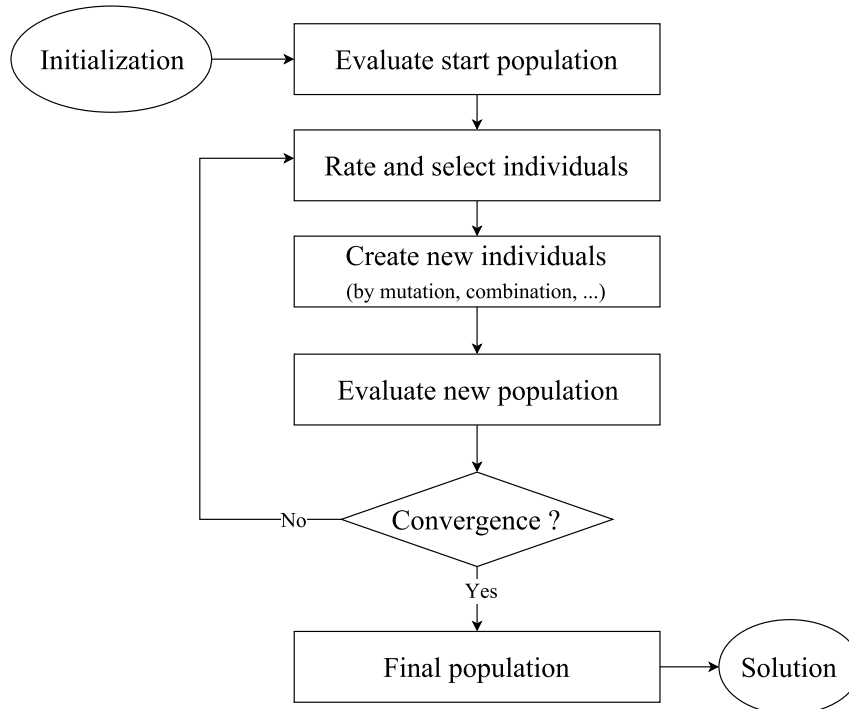


Figure 2.26: Generalized flowchart for nature inspired optimization.

In the course of this work, nature inspired optimization algorithms (NOA) based on evolutionary strategies and on animal swarm movement were used. Therefore, this section focuses on these two algorithms. A generalized flowchart for nature inspired optimization is given in Fig. 2.26. In all NOA methods a population of virtual individuals searches the parameter space for possible optima.

The typical flow of a NOA based optimization starts with a randomly generated initial population. For each of its individuals the objective function is evaluated. Based on this initialization, the actual optimization loop starts which generates a new generation of individuals in each iteration. At the beginning of the optimization loop, the individuals of the current generation are rated in terms of fitness and compliance to the constraints. The best designs are selected which are kept for the new generation. In the next step the new individuals are generated by an appropriate technique. Possible methods in this step are crossover or combination of existing individuals, mutation or swarm movement. Finally, the new population is evaluated in terms of the objective function. Afterwards the new generation again is rated in terms of fitness and compliance to the constraints. If the new best individual diverges significantly from the previous one, the algorithm returns to the selection step and continues with a new generation. Otherwise, convergence is assumed and the optimum is chosen from the final generation.

2.7.1.1 Evolutionary Algorithms

Evolutionary algorithms are optimization methods which originate from emulating mechanisms known from biological evolution like variation, adaption or selection. In this field of optimization algorithms the two main classes are genetic algorithms (GA) and evolutionary algorithms (EA). Generally, both strategies follow the flow as described before. The main differences lies in the creation of new individuals. While genetic algorithms combine successful individuals to obtain the new generation, evolutionary algorithms introduce variation into the new generation by modifying the fittest individual of the current generation by mutation. A good overview of GA is given by John Holland [Hol92], a description of EA can be found in [Sch81].

2.7.1.2 Particle Swarm Optimization

The particle swarm optimization (PSO) algorithm simulates a virtual swarm of animals in search for food. It was first proposed by Kennedy and Eberhart in 1995 [Ken95]. The simulated members of the swarm exchange information about beneficial regions of the parameter space and move into the direction in which the highest amount of food (=highest value of the objective function) is expected. The individual movement of the particles is influenced by the optimum presumed by the perception of the individual as well as the global optimum presumed by the swarm.

2.8 Computer Graphics

The mathematics used for the representation of geometries in Computer Aided Drawing (CAD) and all subsequent CAE processes is of complex nature and a details introduction would be going beyond the purpose of this chapter. One feature used frequently in this research are Bézier splines. Beside the use for geometric modeling Bézier splines will be used at many places to describe relations between parameters and as regression functions. Therefore, a short overview of the the underlying mathematics is given in this section.

2.8.1 Bézier Splines

A Bézier spline is a parametric curve which is used in computer graphics for the description of free form curves and surfaces. The basic concept was developed by de Casteljaeu in 1959 and Bézier in 1968 [Béz68] unknown from each other. Later, the concept was generalized in form of NURBS (Non Uniform Rational B-Spline). Detailed information about the mathematics used for representing curves and surfaces in computer graphics can be found in [Pie97].

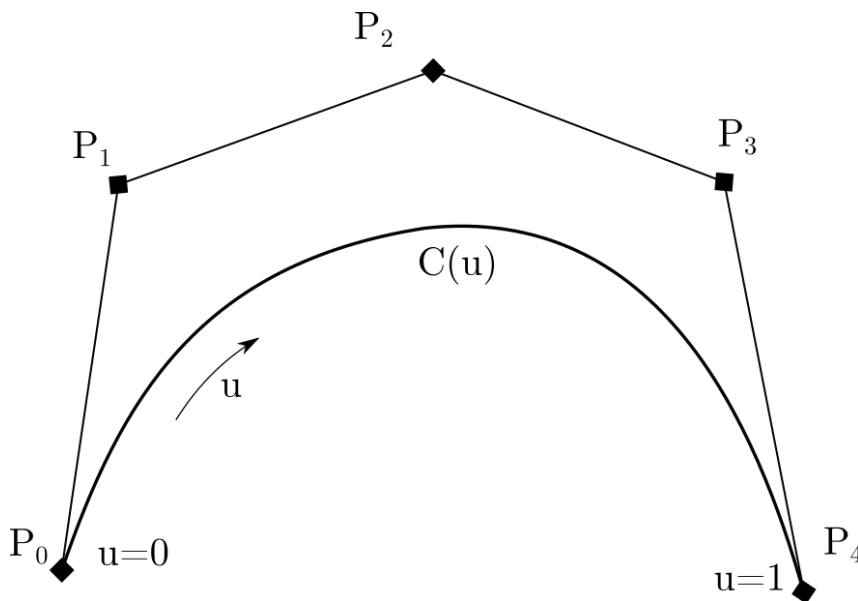


Figure 2.27: Bézier curve of degree 4.

A simple Bézier curve of degree 4 is shown in Fig. 2.27. The degree n of the curve is equal to the number of points in the control polygon minus one. The curve is defined by a set of control points P_i forming the control polygon and parametrized by the parameter u which can take values between zero and one. A value of $u = 0$ represents a point at the beginning of the curve at control point P_0 while a value of $u = 1$ represents the point at the end of the curve equal to control point P_4 . The first and last point of the control polygon are always on the Bézier spline while the other points lie outside the curve except for the special case of a straight line. Further beneficial properties of Bézier splines are steadiness and differentiability.

A Bézier curve of degree n is given by

$$C(u) = \sum_{i=0}^n B_{i,n}(u)P_i \quad (2.141)$$

where $B_{i,n}(u)$ represents the i th Bernstein polynomial of degree n at the position u [Ber12] which can be computed as

$$B_{i,n}(u) = \frac{n!}{i!(n-i)!} u^i (1-u)^{n-i} \quad (2.142)$$

$(\cdot)!$ defines the factorial given as $n! = 1 \cdot 2 \cdot 3 \cdot \dots \cdot (n-2) \cdot (n-1) \cdot n$.

Many applications require the derivatives of a curve. If the respective curve is given by a Bézier spline, the derivative at the location u can be computed by

$$\frac{\partial C(u)}{\partial u} = \frac{\partial \sum_{i=0}^n B_{i,n}(u)P_i}{\partial u} = \sum_{i=0}^n \frac{\partial B_{i,n}(u)}{\partial u} P_i \quad (2.143)$$

Analogously, the second derivative is defined by

$$\frac{\partial^2 C(u)}{\partial u^2} = \frac{\partial^2 \sum_{i=0}^n B_{i,n}(u)P_i}{\partial u^2} = \sum_{i=0}^n \frac{\partial^2 B_{i,n}(u)}{\partial u^2} P_i \quad (2.144)$$

Any derivative of a Bézier spline with respect to the parameter u can be computed by deriving the Bernstein polynomials.

CHAPTER 3

Preliminary Information and Low-fidelity Methods

In this chapter the possible sources of preliminary information to identify beneficial parameter regions are collected and reviewed. Based on this review the models used in this work are chosen.

3.1 Investigation of Available Information

A review of literature and published research works provides many methods to predict the aerodynamic performance of a compressor. These are:

- Empirical correlations
- Preliminary design methods
- One dimensional loss models
- Stream surface models

In contrast to the wide range of models for the aerodynamics, similar methods are not available to predict the structure mechanical performance of the compressor. Therefore a custom approach has to be developed.

3.1.1 Empirical Correlations

Empirical correlations enable the turbomachinery engineer to reuse experience from manufactured machines in the design process. This section gives an overview of the most important correlations found in literature.

3.1.1.1 The Cordier Diagram

A widely used correlation in turbomachinery is the Cordier diagram (Fig. 2.6) which relates the specific speed σ to the specific diameter δ . The Cordier diagram is typically used for the development of new machines from scratch. The specific diameter δ can be computed by Eq. 2.74 from the outer diameter of the impeller and the operation conditions given by the flow rate \dot{V} and the pressure ratio Π . Then the Cordier diagram delivers a specific speed σ as a function of δ for which a high efficiency can be expected. The rotational speed Ω can be computed according to Eq. 2.73. This makes the Cordier diagram an important tool at the start of the design process.

3.1.1.2 Slip Factor Correlations

The slip factor introduced in 2.4.5.8 has a major influence on the amount of work transferred between the impeller and the fluid. One of the earliest and simplest equations for approximating the slip has been derived by Stodola in 1927 [Sto27]. Stodola assumes a channel vortex described by a circle fitted into the channel which is generated by the non uniform distribution of the relative velocity along the direction normal to the flow as prescribed in Fig. 3.1. In this model, the slip velocity is calculated as the product of the vortex' speed and its diameter D_v ($c_{SL} = \pi\Omega D_v$). For a realistic number of blades z^1 , the diameter of the vortex can be approximated by $D_v \approx \left(\frac{\pi D_2}{z}\right) \beta_{2,b}$. Together with the definition of the circumferential velocity $u_2 = \pi\Omega D_2$, $c_{SL,Stodola}$ can be written according to Eq. 3.1.

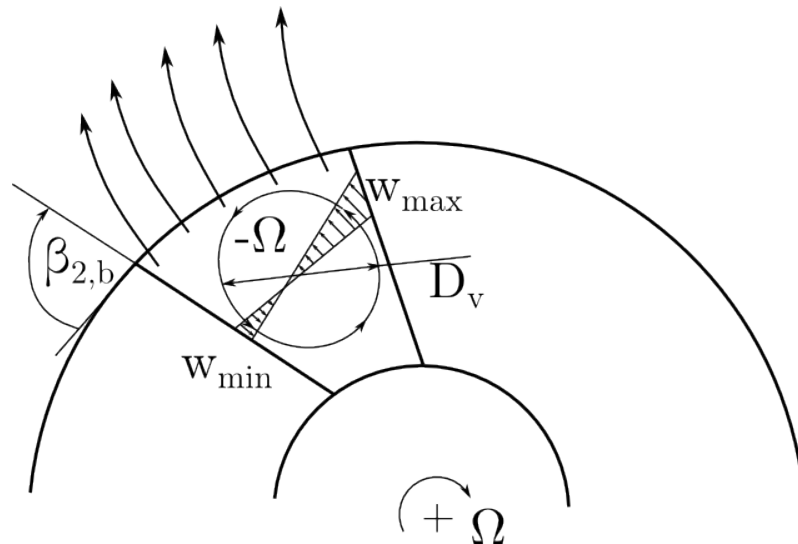


Figure 3.1: Flow model for the Stodola slip factor

¹ Typical blade numbers for centrifugal compressors are in the range of 7 to 19

$$c_{SL,Stodola} = \frac{\pi u_2}{z} \cos \beta_{2,b} \quad (3.1)$$

Combining Eq. 3.1 with the general definition of the slip factor (2.94) yields the Stodola slip factor as

$$\sigma_{Stodola} = 1 - \frac{\pi}{z} \cos \beta_{2,b} \quad (3.2)$$

The Stodola slip factor was developed for straight blades and therefore is not applicable for more complex blade shapes. A number of slip factor correlations have been developed to bypass this problem of which the one of Busemann is the most popular [Bus28]. The Busemann slip factor is given by an empirical correlation which is a function of the diameter ratio $\frac{D_2}{D_1}$, the blade angle and the blade number. The values of $\sigma_{Busemann}$ can be read from diagrams contained in [Bus28].

Subsequent to the works of Stodola and Busemann, further slip factor correlations have been developed by Eck, Pfeleiderer, Stanitz, Ferguson and others. In 1967 all currently available models were reviewed by Wiesner [Wie67] and compared against measurements. Wiesner found the Busemann model to be most generally applicable for centrifugal impellers and developed a simple empirical correlation for the slip velocity:

$$c_{SL,Wiesner} = \frac{u_2 \sqrt{\sin \beta_{2,b}}}{z^{0.7}} \quad (3.3)$$

Together with Eq. 2.94, the slip factor according to Wiesner can be written as

$$\sigma_{Wiesner} = 1 - \frac{\sqrt{\sin \beta_{2,b}}}{z^{0.7}} \quad (3.4)$$

This definition is applicable for impellers with a diameter ratio $\frac{D_1}{D_2}$ below a limit defined by

$$\varepsilon_{Limit} = \exp \left(\frac{-8.16 \sin \beta_{2,b}}{z} \right) \quad (3.5)$$

For impellers with a diameter ratio above this limit the slip factor can be obtained by the empirical equation

$$\sigma'_{Wiesner} = \sigma_{Wiesner} \cdot \left[1 - \left(\frac{\frac{D_1}{D_2} - \varepsilon_{Limit}}{1 - \varepsilon_{Limit}} \right)^3 \right] \quad (3.6)$$

This definition of the slip factor given by Wiesner is applicable for a wide range of impellers and does not rely on graphical methods. This makes it the favorable method to be used in applications requiring automation without user interaction.

An exact approximation of the slip is important for any performance prediction based on one dimensional fluid dynamic computations as it allows to incorporate the influence of the three dimensional blade shape into a mean line computation.

3.1.1.3 Efficiency Correlations

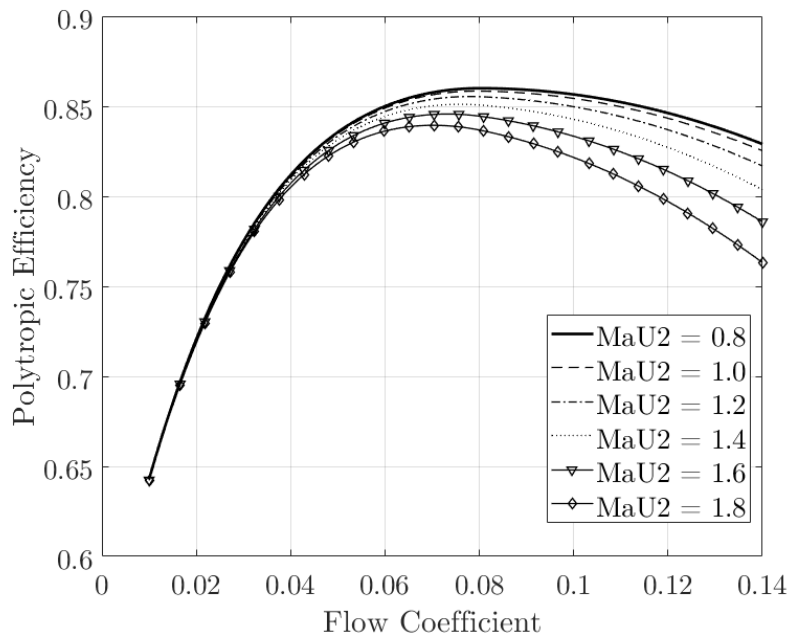


Figure 3.2: Prediction of the polytopic efficiency in dependence of flow coefficient and tip speed Mach number

The efficiency of a centrifugal compressor impeller relies on many different factors like the impeller geometry, the thermodynamic and fluid dynamic processes inside the impeller and the operation state of the machine. In many cases, these influences can not be taken into account in simplified analytical computations. Therefore, empirical correlations are used to get a course first guess of the efficiency. Rodgers has presented several correlations for the efficiency in dependence of the specific speed and global geometric quantities ([Rod79],[Rod91]). In [Cas12], Casey and Robinson generalized this approach by using further empirical correlations to derive a model for efficiency prediction which only relies on the flow coefficient and the tip speed Mach number $Ma_{u_2} = \frac{u_2}{\sqrt{\gamma RT}}$. The efficiency is

predicted according to Eq. 3.7.

$$\begin{aligned} \varphi < 0.08 : \eta_{pol} &= \eta_{max} \left[1 - k_1 (\varphi_{max} - \varphi)^2 - k_2 (\varphi_{max} - \varphi)^2 \right] \\ \varphi \geq 0.08 : \eta_{pol} &= \eta_{max} \left[1 - k_3 (\varphi - \varphi_{max})^2 \right] \end{aligned} \quad (3.7)$$

with the empirical constants $\eta_{max} = 0.86$, $\varphi_{max} = 0.08$, $k_1 = 27$, $k_2 = 5000$ and $k_3 = 10$ taken from [Cas12]. For tip speed Mach number above 0.8 a decrement in efficiency has to be considered. It is computed according to

$$\Delta\eta_{pol} = -k_4 P - k_5 P^2 \quad (3.8)$$

with the empirical constants $k_4 = 0.05$ and $k_5 = 3$ and the expression $P = \varphi (Ma_{u_2} - 0.8)$. The resulting efficiencies are plotted in Fig. 3.2 and can be used in early design stages when no detailed information about the machine performance is available.

3.1.2 Preliminary Design Methods

The preliminary design of a centrifugal compressor is based on mean line analysis. This is done by solving the conservation equations at the stations depicted in Fig. 3.3. The inputs and outputs of a preliminary design are given in Tab. 3.1. A comprehensive description of the complete process is given in standard text books on turbomachinery design like [Fis86]. The most important outcome of a preliminary design computation are the blade angles at the leading edge, the blade height at the leading and trailing edge and the pressure at the impeller outlet. The blade angles at the leading edge are of particular importance for the operation of the impeller as these angles are crucial for a blade congruent flow at the impeller throat. Beside that, no further information about the machine performance can be obtained.

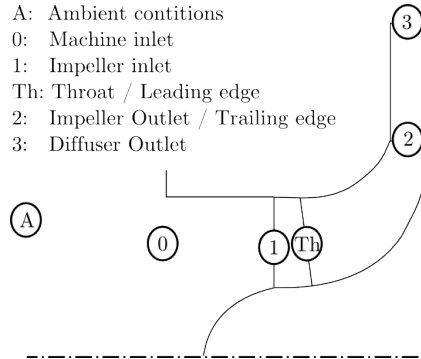


Figure 3.3: Side view of a single stage compressor with stations for mean line computation.

Table 3.1: Input and output quantities for preliminary compressor design

Quantity	Source
Input quantities	
Design flow rate	} Global machine specification
Design pressure ratio	
Gas properties	
Outer diameter	Cordier diagram
Rotational speed	Cordier diagram
Shaft diameter	Shaft design
Axial extent	Free design parameter
Trailing edge blade angle	Free design parameter
Stage polytropic efficiency	Correlation or experience
Output quantities	
Blade angles at the throat	Minimization of the relative Mach number at the throat tip
Leading edge blade height	Continuity equation and correlations
Trailing edge blade height	Continuity equation and correlations
Number of blades	Correlations
Outlet pressure	Energy and momentum equations

3.1.3 Loss Model Performance Prediction

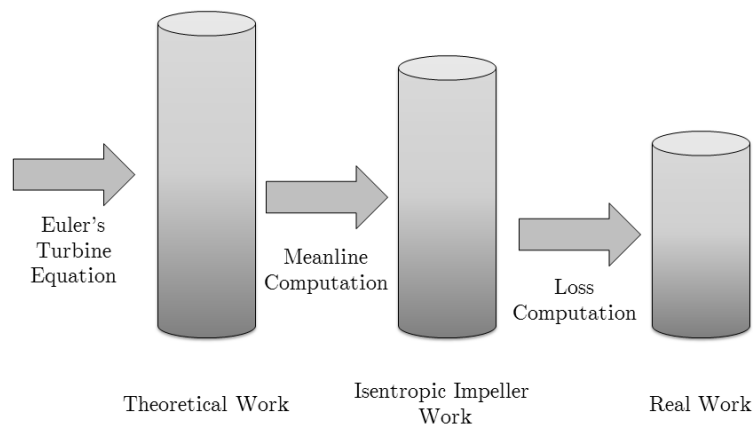


Figure 3.4: Fundamental principle of loss model performance prediction.

Loss modeling is an established technique to predict the aerodynamic performance of turbomachinery components at early design stages. Compared to three dimensional CFD it is considered a low-fidelity method. It uses one dimensional aerodynamic calculations to compute the ideal performance of the machine. The real performance is predicted by applying losses based on empirical correlations. This approach allows a fast prediction. The fundamental principal of performance prediction is depicted in Fig. 3.4. The theoretical maximum performance of the compressor is given by Euler's turbomachinery equation. The isentropic performance of the compressor can be obtained by a mean line computation. Finally the real performance is obtained by applying losses to the isentropic performance. If these steps are repeated for different mass flow rates, the complete characteristic of the compressor can be computed. An overview of the losses for centrifugal compressors is given in Fig. 3.5.

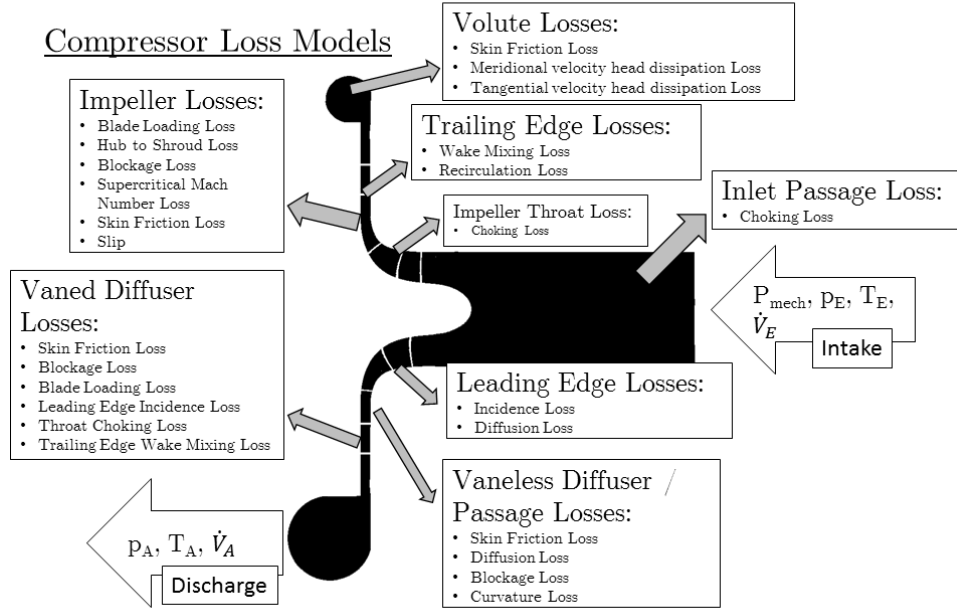


Figure 3.5: Overview of loss models for centrifugal compressor stages

3.1.4 Stream Surface Performance Prediction

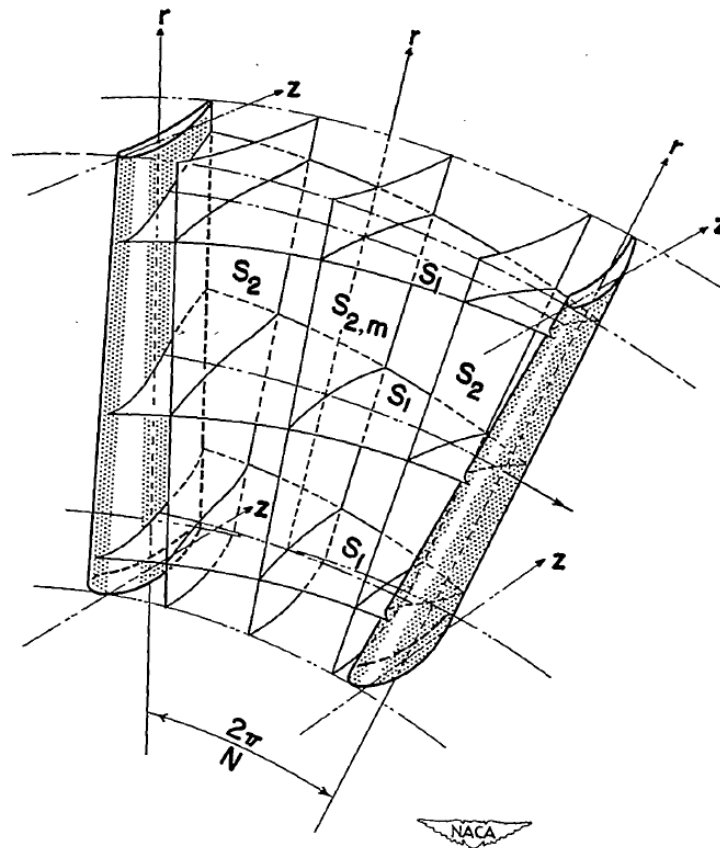


Figure 3.6: Placement of S1 and S2 stream surfaces in the flow channel of an axial machine. Image taken from [Wu52].

The performance prediction using stream surfaces is a pseudo three dimensional iterative flow computation method. The basic idea is to subdivide the flow channel into an infinite number of virtual blades of infinitesimal thickness in order to compute the three dimensional flow on two dimensional surfaces. This idea was first introduced by Lorenz in 1905 [Lor05]. The first successful implementation was published by Wu in 1952 [Wu52]. The placement of the S1 and S2 stream surfaces is shown in Fig. 3.6. The S1 surface is defined as a surface parallel to the flow direction between two adjacent blades. The S2 surface is a rotated version of the a blade surface. A S3 surface (not shown in Fig. 3.6) is defined as a surface perpendicular to the flow direction. The approach published by Wu uses a orthogonal mesh on the middle S2 surface. The nodes of the mesh are placed at the intersections of the streamlines (ξ direction) and the quasi-orthogonals (η direction) as shown in Fig. 3.7. In each node of this mesh the constitutive equations of mass and momentum are solved. This is done by obtaining a differential equation for the change in pressure in the local η and ξ directions from the combination of mass and momentum conservation. The effects of the circumferential variation of the flow field are incorporated by using values circumferentially

averaged on a S1 surface in each node of the two dimensional mesh. Details about the mathematical derivation and the implementation can be found in [Wu52]. A general problem of the S2 method using a pressure based approach is a unsteadiness that occurs when the Mach number reaches unity. Therefore, this method is not recommended for computations of modern high speed machines.

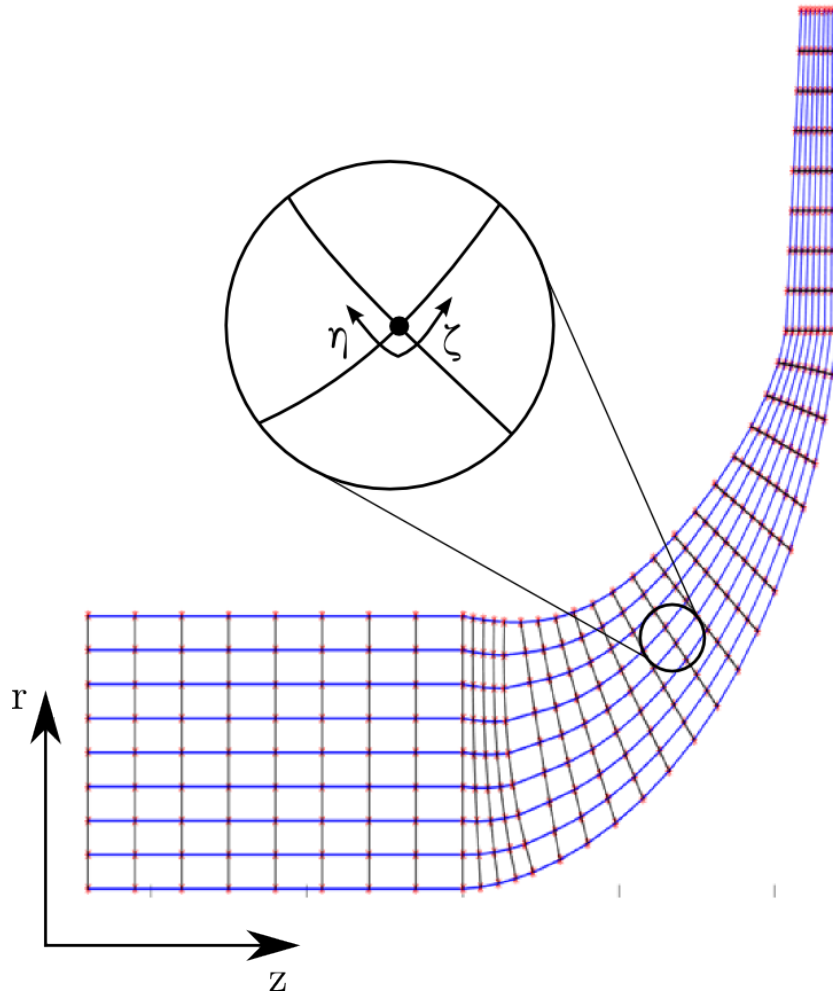


Figure 3.7: Mesh on a S2 surface with global r,z and local curvilinear η,ξ coordinate systems.

An alternative approach to compute three dimensional flow on a two dimensional stream surface is offered by Denton [Den78]. This approach uses a differential equation to describe the change of the meridional velocity in the hub to shroud direction (Eq. 3.9). The change of the meridional velocity c_m is computed by the summation of contributions resulting from the curvature of the streamlines, the energy equation solved for an equilibrium condition between hub and shroud (“radial equilibrium”) and the forces acting on the flow by friction (F_F) and the rotation of the blades (F_B). $r_{Streamline}$ is the local curvature radius of the streamline at the current node, r is the local radius of the node in the z,r -plane and ϑ is

the angular position of the node on the blade in a cylindrical coordinate system. In this method, no unsteadiness occurs due to Mach numbers of one. Therefore, modern high speed machines can be computed.

$$\frac{1}{2} \frac{\partial c_m^2}{\partial \eta} = \underbrace{c_m \frac{\partial c_m}{\partial \eta} \cos \vartheta + \frac{c_m^2}{r_{Streamline}} \sin \vartheta}_{\text{Terms resulting from streamline curvature}} + \underbrace{\frac{\partial h_t}{\partial \xi} - T \frac{\partial s}{\partial \xi} - \frac{1}{2r^2} \frac{\partial (rc_u)^2}{\partial \xi}}_{\text{Terms resulting from radial equilibrium}} + F_F + F_B \quad (3.9)$$

The solution of the meridional velocity differential equation is obtained numerically at each node of the mesh on the S2 surface. Therefore this method can not be considered as an analytical method. The solution algorithm is shown schematically in Fig. 3.8. In each iteration the spacing of the streamlines is adjusted in dependence of the mass flow through the streamline which is directly related to the meridional velocity by the equation of continuity (Eq. 2.1). The convergence of the solution depends strongly on detailed empirical correlations for the entropy generation in the impeller. Given this premise, a stream surface computation can obtain results orders of magnitude faster compared to a fully three dimensional CFD computation.

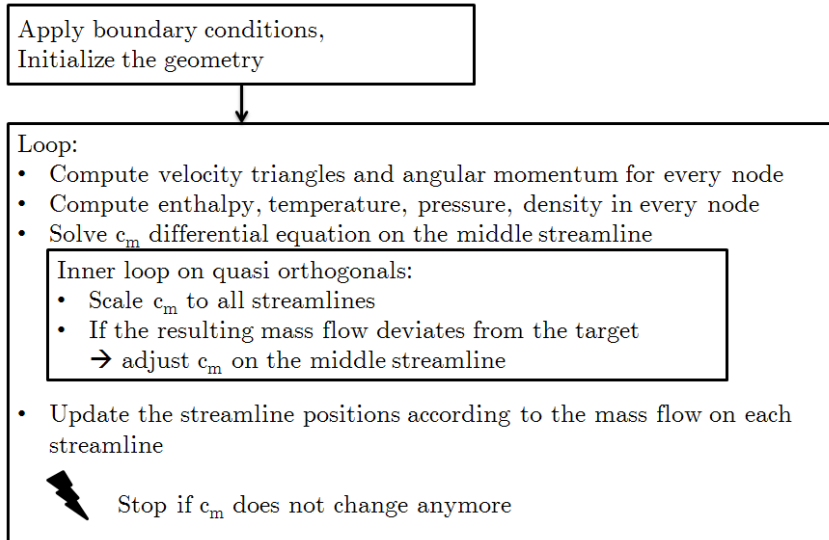


Figure 3.8: Flowchart of the stream surface algorithm.

3.1.5 Prediction of Structure Mechanical Performance

As mentioned before, the impeller of a centrifugal compressor is a highly stressed component. Thus, it is necessary to check every possible design for compliance to the structure mechanical constraints in terms of stress and deformation. In contrast to the diverse methods available for the fluid dynamic performance prediction, almost no comparable models can be found for the structure mechanic domain.

Biezeno and Grammel [Bie53] describe a simplified method to predict the deformation and stress of a rotating disc on a shaft. Furthermore an analytical model for the mechanical performance of axial turbine blades is given. These models are not suitable for modern centrifugal compressors as the complex three dimensional shape of the blades can not be considered.

Several studies have shown that the three dimensional blade shape has a major influence on the distribution and magnitude of stress in the impeller ([Loh00], [Wan06]). Therefore a method for predicting the structure mechanical performance has to be capable of taking three dimensional effects into account. A reliable prediction of stress and deformation can only be accomplished by FEA computations. The amount of computational resources necessary for rating each design by a three dimensional FEA simulation however conflicts with the requirement of having a fast prediction method.

An alternative approach is the use of a metamodel for the prediction of the structure mechanical performance. This method uses the techniques described in section 2.6.2 which are used to generate a regression model based on a DOE of FEA simulations to predict stress and deformation. While this approach still requires a certain amount of computation time, the result is a reusable for fast prediction of the structure mechanical performance in dependence of the three dimensional blade shape.

3.2 Review and Selection of Models

The methods introduced in the previous sections have to be reviewed in terms of applicability for rating designs in an optimization process in a fast way.

Empirical Correlations

The intended use of the Cordier diagram is delivering a matching “outer diameter”-“rotational speed”-pair for a new machine design with given pressure ratio and design flow rate. This data is useful at early design stages. In the case of optimizing an existing design, both the outer diameter and the rotational speed are kept constant as changes in these quantities would cause drastic changes of the operation characteristic of the machine. Furthermore modern impeller designs show deviations from the correlation observed by Cordier. Therefore, the Cordier diagram will not be used in this work.

Slip is an important effect which has a strong influence on the performance of the machine. When using one dimensional performance prediction methods, a model for predicting the slip is needed to depict the relation between the aerodynamic performance and the blade shape. In this work the slip model according to Wiesner (Eq. 3.6 and Eq. 3.5) will be used. This model has the advantage to cover a wide range of machines without the need of using graphical methods. Therefore, this method can be easily incorporated into an automated computation process.

Similar to the Cordier diagram, empirical correlations for the efficiency are typically used at early design stages when only little information on the performance of the machine is available. If the design of an existing machine is to be optimized, a great amount of data of the initial design is already available. Therefore efficiency correlations were used solely for the preliminary design method applied in the “Design-by-Optimization” approach.

Preliminary Design Methods

A preliminary design based on meanline computations provides values for the blade inlet angles and the blade height at leading and trailing edge (Tab. 3.1). If an optimization aims at the improvement of an existing design (“Design-Optimization”), these quantities are not changed in a pronounced way. Therefore no new preliminary design computations are needed in this case. If the optimization approach is applied to determine a new machine design from scratch (“Design-by-Optimization”), the leading edge blade angles and the inlet and outlet geometries should be determined by a preliminary design code. Otherwise, many designs are included in the sampling whose operation characteristics differ gravely from the intended operation range.

Therefore, a preliminary design code is implemented which can be used for the “Design-by-Optimization” case.

Loss Model Performance Prediction

Loss modeling offers a fast method to predict the performance of a machine in dependence of the geometric design. This makes loss models a useful tool to rate designs in an optimization process in a fast way. The implementation of the models is described in chapter 6.

Stream Surface Performance Prediction

In the course of this work, a flow solver based on the meridional velocity differential equation (Eq. 3.9) according to Denton has been developed. As described in section 3.1.4, this method relies strongly on empirical correlations for the entropy generation to achieve a sufficiently fast convergence. The solver developed in the course of this work showed a very slow convergence behavior and therefore can not be used for a fast rating of designs in an optimization process. As it seemed very unlikely to solve this problem within an acceptable development time, this prediction method has been discarded. The convergence problems were very likely caused by the used correlation for entropy generation. As no detailed empirical data was available the entropy generation has been predicted by a efficiency correlation according to Casey and Robinson (Eq. 3.7 and Eq. 3.8).

Structure Mechanical Performance Prediction

The structure mechanical performance is predicted by a metamodel in this work as no simplified computation method is capable of taking the three dimensional blade shape into account. The metamodel generation is described in detail in chapter 6.

CHAPTER 4

Statistical Model

Information acquired from the models introduced in the previous chapter shall be used to generate a sampling which clusters samples in potentially beneficial regions of the parameter space while assuring an even but sparse coverage of the remaining areas. For any given problem, the relation between input and output parameters can be described by some kind of distribution function. In this work, a distribution is required which describes the relation between the geometry of an impeller design and sample quality in terms of the aerodynamic and structure mechanical performance of the design. This distribution is, as in most real applications, not known in a mathematically closed way by a single formula but a value at each point can be computed from the preliminary information introduced in chapter 3. Therefore, the underlying distribution must be approximated numerically. In this chapter a literature research was conducted to generate an overview of the available methods. Finally, the method best suited to fulfill the given constraints is chosen.

4.1 Investigation of Available Methods

A research of available literature revealed two methods from the group of Monte Carlo Methods for sampling from an unknown distribution function. These are:

- Acceptance / Rejection Sampling
- Bayesian Updating / Metropolis Hastings Algorithm

The methods are evaluated by using high dimensional test functions to model the distribution of the sample quality. The resulting sampling is rated by two criteria:

1. Are the designs of the resulting sampling concentrated in areas with high sample quality?
2. Is the level of correlation between the input parameters at a low, acceptable level?

The applied method for rating the different methods is illustrated by a simple example. Figure 4.1 shows the histogram and the correlation matrix of a sampling of a 20 dimensional test function consisting of 100 samples generated by Latin hypercube sampling. The correlation matrix clearly shows that the input parameters are independent of each other. Under the aspect of input correlations, the sampling complies very well with the required criterion. The distribution of the samples in terms of sample quality as depicted by the histogram on the other hand shows a contrary tendency. The green curve in the histogram is the “desired“ or “ideal“ distribution function of a sampling with a clustering in regions with a high sample quality. The red curve is the distribution fitted to the data of the sampling. In the given example a strong discrepancy between the ideal and the fitted distribution can be observed. The generated sampling contains many samples of low quality which are unlikely to lead towards the optimum. This is due to the fact that the Latin hypercube algorithm aims at generating a sampling that evenly covers the whole parameter space with minimal input correlations. The values of the sample’s output quantities however are not taken into account. Therefore, a simple Latin hypercube sampling is not suited for this special case.

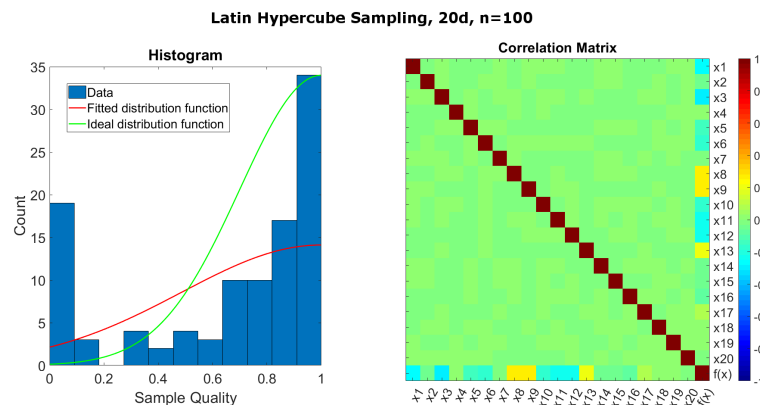


Figure 4.1: Histogram (left) and correlation matrix (right) for a Latin hypercube sampling of a 20 dimensional test function consisting of 100 samples.

4.1.1 Test Functions

Many popular test (or benchmark) functions for optimization algorithms have properties which are not observed in “real world“ problems and thus limit the significance of evaluation results obtained by optimizing these functions. These properties are in particular:

- **Symmetry and same parameter values of the optimum**

Many popular test functions are symmetrical around their global optimum. Ackley’s function, Griewanks’s function or Rastrigin’s function for example are symmetrical in respect to their global optimum at the origin. Additionally the global optimum of many popular benchmark functions has the same parameter value for all dimensions. Examples are Rosenbrock’s function with the global optimum at $[1,1,1,\dots,1]$ or Schwefel’s function ($[420.9687,420.9687,420.9687,\dots,420.9687]$). Both effects are unlikely to be found in real applications.

- **Global optimum at the origin**

The global optimum of many benchmark functions is located at the origin of the parameter space. This behavior is rarely observed in real world problems.

- **Global optimum at the center of the search range**

The combination of the two previously mentioned effects can often result in the effect that the global optimum is located at the center of the search range which again is not typical in real applications.

Liang et al. proposed a method for generating composed test functions which bypass those problems [Lia05]. The benchmark function is created by combining different test functions. Each single functions is shifted and rotated. The functions are combined using Gaussian functions to blur the individual functions and obtain a smooth composite function. The functional principle of the algorithm are given below:

Definitions:

- $F(x)$: The composed benchmark function.
- $f_i(x)$: i th basic test function.
- n : Number of basic test functions.
- D : Dimensionality.
- x_{min}, x_{max} : Search range of $F(x)$ (D dimensional vector).
- $x_{min,i}, x_{max,i}$: Search range of $f_i(x)$ (D dimensional vector).
- M_i : Rotation matrix for $f_i(x)$.
- o_i : New position of the shifted optimum of $f_i(x)$.
- $o_{i,old}$: Original position of the optimum of $f_i(x)$.

- w_i : Gaussian weighting function for $f_i(x)$.
 λ_i : Scaling factor for $f_i(x)$.
 $bias_i$: Sorting parameter to mark the function $f_i(x)$ whose optimum shall be used as the global optimum. The optimum of the function with the smallest value of $bias_i$ becomes the global optimum of the composed function.

The composed function is computed by the following equation:

$$F(x) = \sum_{i=1}^n \left\{ w_i \cdot \left[f_i \left(\frac{x - o_i + o_{i,old}}{\lambda_i} M_i \right) + bias_i \right] \right\} \quad (4.1)$$

The Gaussian weighting functions w_i are given by

$$w_i = \exp \left(\frac{\sum_{k=1}^D (x_k - o_{i,k} + o_{i,old,k})^2}{2D\sigma_i^2} \right) \quad (4.2)$$

$$w_i = \begin{cases} w_i & \text{for } w_i = \max(w_i) \\ w_i \cdot (1 - \max(w_i)^{10}) & \text{for } w_i \neq \max(w_i) \end{cases}$$

The Gaussian weighting functions are normalized by $w_i = \sum_{i=1}^n w_i$. The parameter σ_i controls the length of the Gaussians which influences the range around the individual optimum in which the function is used for the global composed function. When different functions $f_i(x)$ are used it is recommended to scale the values of all functions to the same interval to obtain a smooth composed function.

Figure 4.2 shows a multimodal two dimensional test function composed from 10 sphere, Ackley and Levy functions. Using the method described above, arbitrary functions with any number of dimensions and local optima can be constructed.

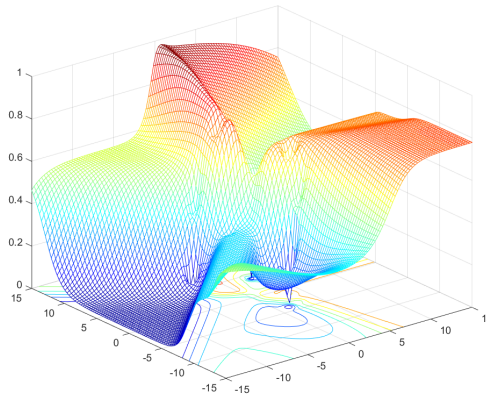


Figure 4.2: Composed two dimensional test function.

4.1.2 Acceptance / Rejection Sampling

Acceptance / rejection sampling is a technique which belongs to the class of Monte Carlo simulation methods. A general overview of this method can be found in [Cas04]. Acceptance / rejection sampling is used to generate samples from an arbitrary target distribution X whose density function $f(x)$ can not be written in a mathematically closed form. Therefore, samples cannot be generated directly from this distribution. This is the case for many real problems where the relation between the systems parameters and responses can be described by a complex multivariate distribution which can only be computed for single parameter configurations.

The general principle of the algorithm can be visualized by a simple example. The density function of a random variable is drawn on a rectangular board and darts are thrown at the board. The distribution of the darts around the board is assumed to be uniform. After throwing the darts, all which are not in the area under the curve are removed. Then the density at certain location on the x axis is depicted by the number of darts in the y direction at this location. For the algorithmic implementation of this principle, the acceptance / rejection sampling method uses a proposal distribution Y with a known density function $g(x)$ to generate samples from X . This is accomplished by drawing samples from Y and accepting these samples with the probability $f(x)/(Mg(x))$. M is a constant which has to satisfy the relation $f(x) \leq Mg(x)$ to ensure that the samples drawn from Y lie “below“ the density function $f(x)$ of X . The algorithm to obtain a sample from distribution X with density $f(x)$ by sampling from Y with density $g(x)$ works as follows:

- Draw sample y from distribution Y and u from $\mathcal{U}(0,1)$ (the uniform distribution over the unit interval).
- Compute $f(y)$.
- Check whether $u < f(y) / (Mg(y))$:
 - Yes: accept y as a sample generated from $f(x)$
 - No: reject y and return to the first step

This algorithm is repeated until the desired number of samples is generated from the target distribution X .

Figure 4.3 shows the histogram of a sampling generated by rejection sampling. This example uses a 2-dimensional multi modal test function as the density function $f(x)$ of the target distribution X and draws samples from a proposal distribution Y with uniform density. The red line in Fig. 4.3 depicts a probability density function fitted to the data of the simulated distribution while the green line shows the desired distribution for a sampling with a focus on high quality designs. In this case, the fitted probability density function is close to the ideal one. The result of the application of the acceptance rejection algorithm to a 20 dimensional case is shown in Fig. 4.4(a). Here, the positive effect decreases and the fitted density function shows a strong deviation from the ideal one. Therefore, this method does not fulfill the requirement of generating a sampling with a focus on high quality designs.

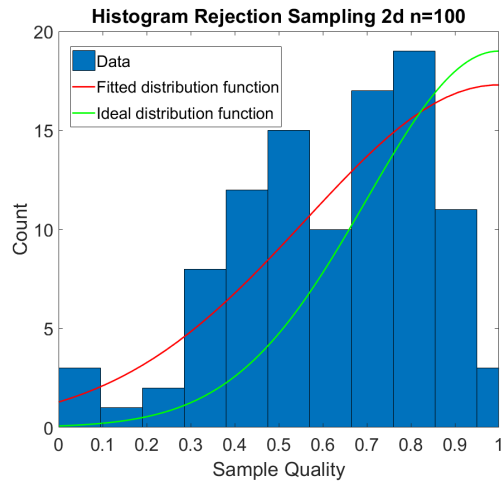
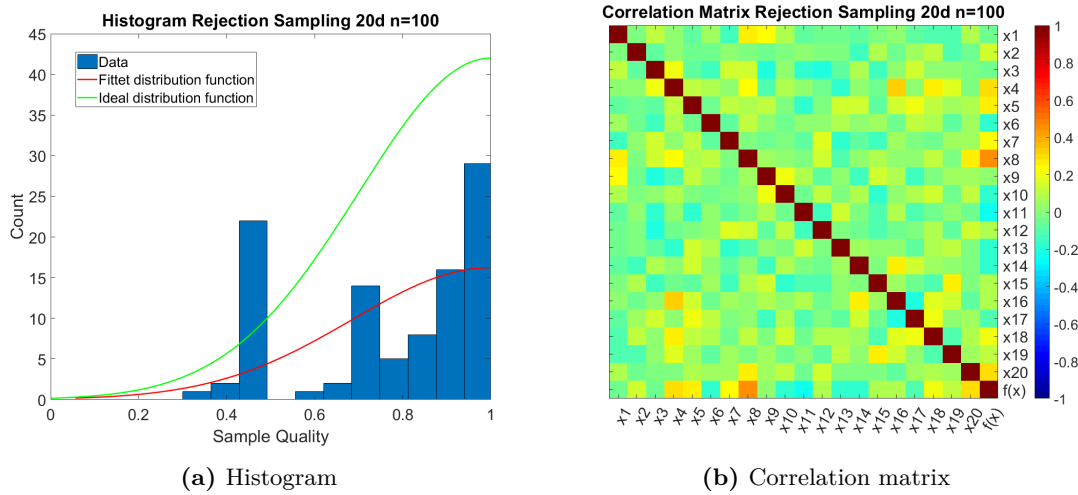


Figure 4.3: Histogram of a sampling generated by rejection sampling for a 2d test function.



(a) Histogram

(b) Correlation matrix

Figure 4.4: Histogram and correlation matrix for a sampling consisting of 100 samples generated by acceptance rejection sampling for a 20d test function.

The correlations generated by acceptance rejection sampling for the 20 dimensional case are shown in Fig. 4.4(b). While there are some correlations, the overall level of input correlations is within an acceptable range.

4.1.3 Bayesian Updating

Bayesian updating is a method used to update the probability of a hypotheses of the occurrence of an event as more information becomes available by using Bayes' rule (Eq. 4.3). Bayes' rule describes the occurrence of an event E under certain preconditions. The conditional probability $P(H|D)$ describes the probability of the hypothesis H given that the data D was observed and is also called the "posterior probability". The probability $P(H)$ is the "prior probability" of the hypothesis H , while $P(D)$ is the probability of observing D , which can be related to model or measurement errors. $P(D|H)$ is the probability of observing E under the condition of H .

$$P(H|D) = \frac{P(D|H)P(H)}{P(D)} \quad (4.3)$$

The process of updating a probability according to Bayes' rule can be modeled by a Markov chain. A Markov chain is a stochastic process whose future state can be predicted from it's present state. The sought after density function of probability X represents the future state of the chain while the proposal probability Y presents it's current state. Using algorithms from the class of Markov chain Monte Carlo methods, the unknown density function $f(x)$ of probability X can be estimated by sampling from a proposal probability Y with known density $g(x)$ under the condition that $f(x)$ can be evaluated at every point. Popular algorithms of this class are the Metropolis-Hastings algorithm, Gibbs sampling or slice sampling. A review of literature on this topic has revealed the Metropolis-Hastings algorithm as the most promising approach. Therefore the rest of this section focuses on the Metropolis-Hastings algorithm.

As a possible alternative to Bayes' updating, the principle of maximum entropy can be used to update a probability distribution based on observed data. A literature review on this topic has revealed no significant advantages over Markov chain Monte Carlo methods. Therefore, this path was not pursued any further.

4.1.3.1 Metropolis Hastings Algorithm

The Metropolis-Hastings algorithm is a Markov chain Monte Carlo method and was first proposed by Metropolis et al. [Met53]. It is used to generate a sequence of random samples from a probability distribution for which direct sampling is not possible. Similar to rejection sampling, it requires a density which is used to generate candidates. As the algorithm is used to simulate a Markov chain, the proposal density should depend only on the current state of the process. In the course of this research, a version of the Metropolis-Hastings algorithm according to Chib and Greenberg [Chi95] is used. A crucial decision with a grave effect on the algorithms efficiency is the choice of the proposal density $g(x_{i+1}|x_i)$ for a new candidate x_{i+1} based on the previous observation x_i . If no additional information about the system behavior is known, a proposal density has to be assumed. For every step the probability of moving to the new candidate point can be computed by Eqn. (4.4).

$$\alpha(x_{i+1}|x_i) = \min \left[\frac{f(x_{i+1})g(x_i|x_{i+1})}{f(x_i)g(x_{i+1}|x_i)}, 1 \right] \quad (4.4)$$

If the proposal density is symmetric, which is usually the case, the conditional probabilities $g(x_i|x_{i+1})$ and $g(x_{i+1}|x_i)$ are equal and therefore Eqn. (4.4) simplifies to:

$$\alpha(x_{i+1}|x_i) = \min \left[\frac{f(x_{i+1})}{f(x_i)}, 1 \right] \quad (4.5)$$

The Metropolis Hastings algorithm goes as follows :

Algorithm 1 Metropolis-Hastings algorithm

```

Start with initial sample  $x_0$ 
while  $n < N$  do
  Generate  $y$  from  $g(y|x_i)$ 
  Generate  $u$  from  $\mathcal{U}(0,1)$ 
  Calculate  $\alpha(y|x_i)$  according to Eqn. (4.5)
  if  $u \leq \alpha$  then
    Set  $x_{i+1} = y$ 
    Set  $n = n + 1$ 
  else
    Do nothing
  end if
end while

```

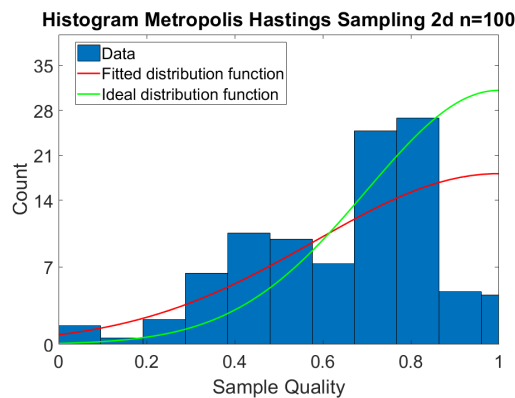


Figure 4.5: Histogram of a sampling generated by the Metropolis Hastings algorithm for a 2d test function.

Analogously to the acceptance / rejection sampling, the Metropolis Hastings algorithm is applied to sampling from a distribution whose density function is modeled by a test function. Figure 4.5 shows the histogram of a sampling generated by the Metropolis Hastings algorithm for a two dimensional test case. As no information about the proposal distribution is known in this case, new samples are drawn from a Gaussian distribution centered at the previous sample with a standard deviation of a third of the parameter range. The red line again marks the distribution function fitted to the data while the green line represents the desired, ideal distribution function. For the two dimensional case a

bias of the distribution towards designs with a high quality can be observed. For the 20 dimensional case however, this distribution shifts as most of the generated samples are located in areas of lower sample quality (see Fig. 4.6(a)).

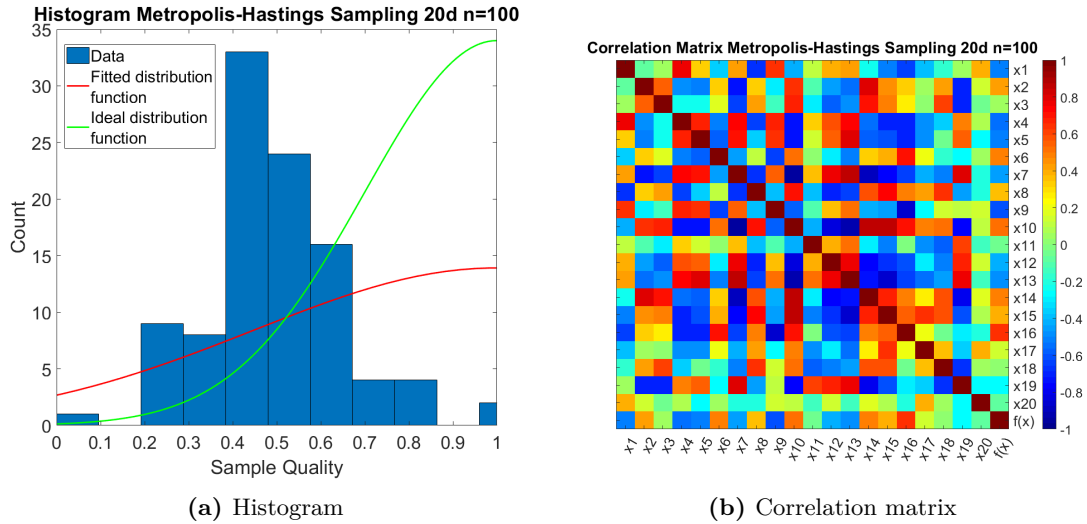


Figure 4.6: Histogram and correlation matrix for a sampling consisting of 100 samples generated by the Metropolis Hastings algorithm for a 20d test function.

Figure 4.6(b) shows the correlation matrix of the Metropolis Hastings sampling for the 20 dimensional case. A high level of input correlations can be observed for this sampling. Together with the non-ideal distribution of the designs in terms of sample quality this method does not meet the design goals.

4.1.3.2 Advanced Metropolis Hastings Algorithm

One potential problem of the Metropolis-Hastings Algorithm is that it may get stuck in one region of the parameter space which can lead to unwanted accumulation of samples and high input correlations. This problem could be bypassed by generating a higher number of samples. As the reduction of the numerical expense is a main goal of this research, an incrementation of the generated samples is not an option. Another approach is the inclusion of a mechanism which prevents the generation of new designs in areas of the parameter space which were already searched. Luersen et al.[Lue04] presented a method which uses a Gaussian-Parzen-window approach to determine restart points for a global optimization algorithm. The density of the points already placed in the parameter space is described by an additional probability $p(x_{i+1})$ which takes high values in sparsely populated areas of the parameter space and low values in areas which already contain a lot of samples. This probability is used in the Metropolis-Hastings-algorithm to additionally rate each sample. The step probability for the advanced Metropolis-Hastings-algorithm can be computed as

$$\alpha(x_{i+1}|x_i) = \min \left[\frac{f(x_{i+1})}{f(x_i)} \cdot p(x_{i+1}), 1 \right] \quad (4.6)$$

The probability $p(x_{i+1})$ is computed by

$$p(x_{i+1}) = \frac{1}{N} \sum_{j=1}^N p_j(x_{i+1}) \quad (4.7)$$

where N is the number of previously sampled points and p_j is the multi-dimensional Gaussian probability density function given by

$$p_j(x_{i+1}) = \frac{1}{(2\pi)^{\frac{n}{2}} (\det(\Sigma))^{\frac{1}{2}}} \cdot \exp \left(-\frac{1}{2} (x_{i+1} - x_j)^T \Sigma^{-1} (x_{i+1} - x_j) \right) \quad (4.8)$$

Here, n is the dimension and Σ is the covariance matrix given by Eqn. (4.9).

$$\Sigma = \begin{bmatrix} \sigma_1^2 & & 0 \\ & \ddots & \\ 0 & & \sigma_n^2 \end{bmatrix} \quad (4.9)$$

The variances are estimated by

$$\sigma_j^2 = a (x_j^{max} - x_j^{min})^2 \quad (4.10)$$

where a is a parameter which controls the length of the Gaussians and x_j^{min} and x_j^{max} are the bounds of the parameter range in the j th direction.

Figure 4.7a) shows a sampling generated by the advanced Metropolis Hastings algorithms for a 20 dimensional test function. While this result looks promising, the repetition of the algorithm in Fig. 4.7c)-d) reveals a strong stochastic component in this method. The correlations of a sampling generated by this method are shown in Fig. 4.8. Compared with acceptance rejection sampling (Fig. 4.4(b)) and the standard Metropolis Hastings algorithm (Fig. 4.6(b)), this method generates the highest level of input correlations. These correlations in combination with the uncertainty of the generated distribution rule out this method as a possible approach to fulfill the design goals of a sampling with a bias towards high quality designs and low input correlations.

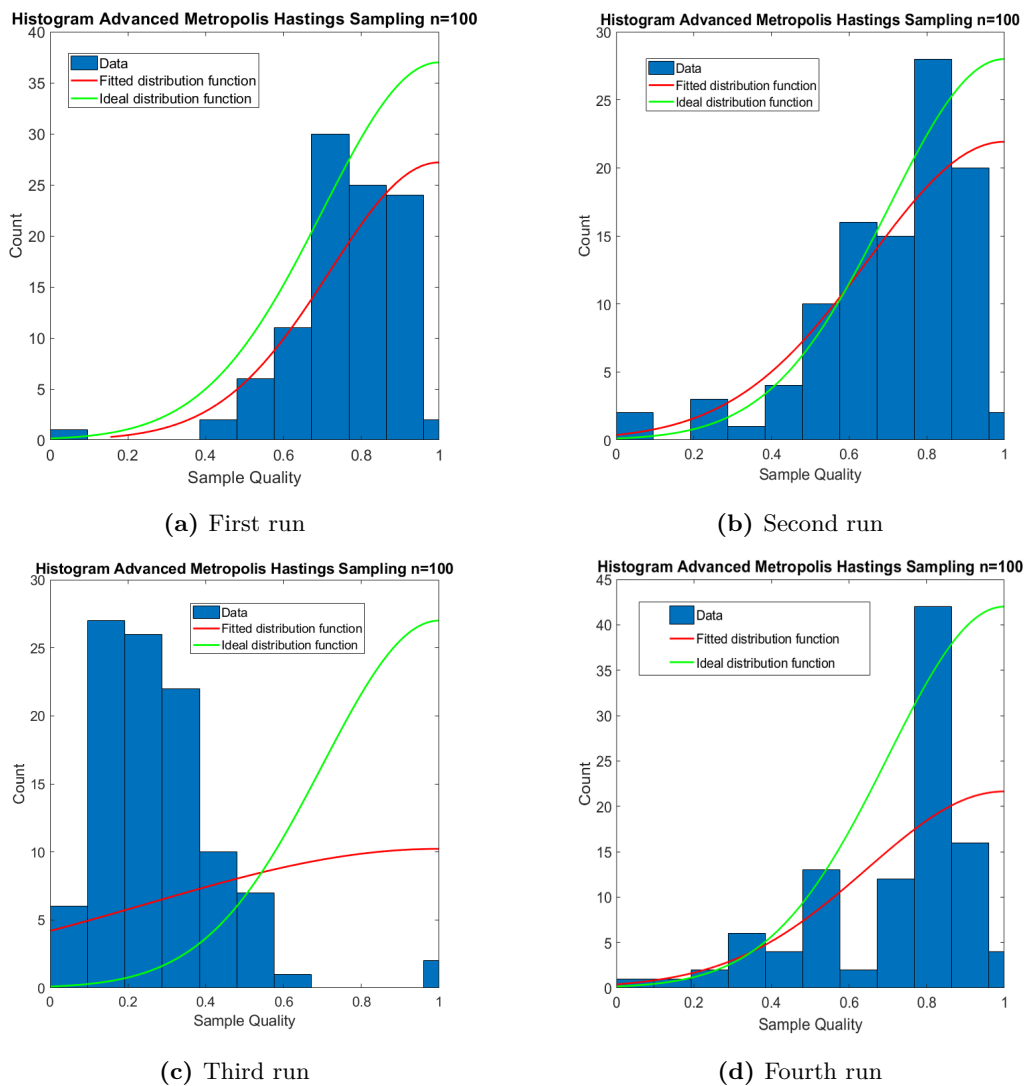


Figure 4.7: Histogram of four samplings generated by the advanced Metropolis Hastings algorithm for a 20d test function.

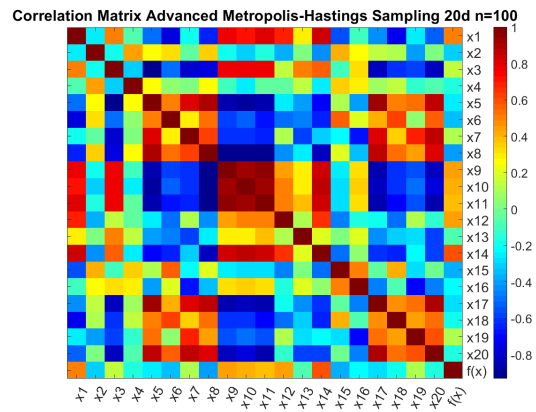


Figure 4.8: Correlation matrix of a sampling generated by the advanced Metropolis Hastings algorithm for a 20d test function.

4.2 Review and Rating

The review of the methods presented in the preceding sections shows that no method manages to meet the requirements of a sampling with a focus on high quality designs together with a low level of input correlation. Acceptance rejection sampling can satisfy the requirement of low input correlations but fails to generate a sampling with a bias towards high quality designs. The standard Metropolis Hastings algorithm fails to meet both the design goals of low correlations as well as the requirement of a sampling with many high quality designs. The advanced Metropolis Hastings algorithm is able to generate a sampling with the desired distribution but the results have a strong stochastic component. Therefore, they are not reliable. Additionally, the advanced Metropolis Hastings algorithm generates the strongest correlations of all tested methods. However, further investigations on the advanced Metropolis Hastings algorithm have shown that both the difference between the actual and ideal probability density function as well as the level of input correlation decrease with a higher number of generated samples (see Fig. 4.9). As the main motivation for this research is the reduction of costly numerical computations, a higher number of samples is clearly not an option. Therefore, in the case of higher sample numbers, it would be necessary to thin out the sampling while maintaining the spacial distribution of the samples. This consideration leads to the development of a novel sampling method.

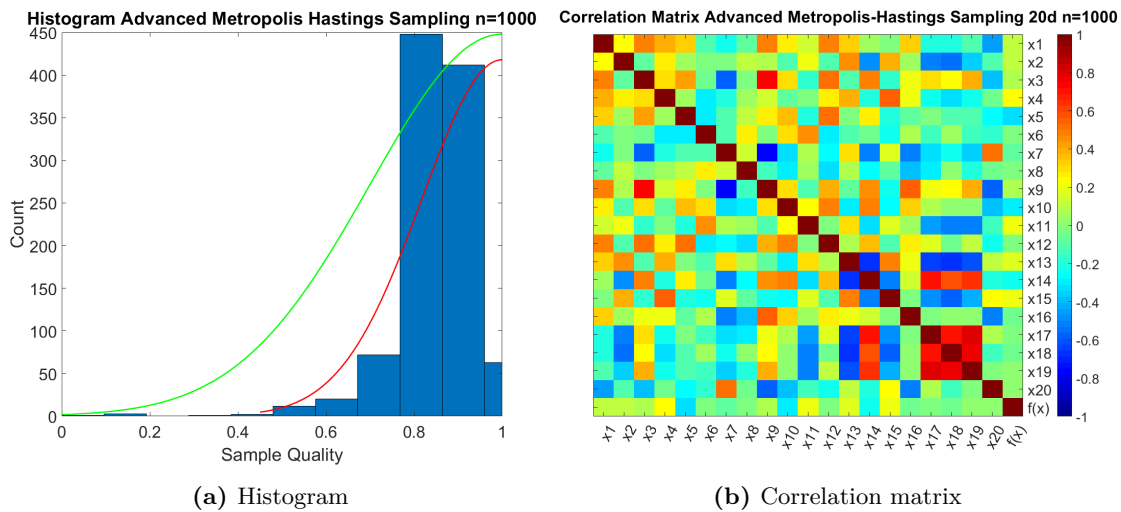


Figure 4.9: Histogram and correlation matrix for a sampling consisting of 1000 samples generated by the advanced Metropolis Hastings algorithm for a 20d test function.

CHAPTER 5

Filtered Sampling

The review at the end of the previous chapter revealed that the advanced Metropolis Hastings algorithms is capable of generating the desired sampling, if a high number of samples is created. This approach contrasts the aim of this research to reduce the numerical expense. Therefore, some kind of sample reduction would be needed. Based on these results, a novel, multi-fidelity sampling method called “Filtered Sampling“ is proposed. The considerations leading to this approach are:

- A sampling with a concentration of samples in areas of high sample quality can be generated by the advanced Metropolis Hastings algorithm, if a large number of samples is created.
- This sampling has to be thinned out to meet the design goal “minimize the numerical expense“. The thinning must retain the overall spacial distribution and the correlations of the samples.
- If the final sampling can only be acquired by thinning out an initial sampling, the initial sampling does not need to fulfill the requirements in terms of spacial distribution as the desired distribution can be generated by the thinning.

The “Filtered Sampling“ approach can be formulated as follows: generate a very detailed Latin hypercube sampling, which is thinned out until the desired number of samples is left and the quality of the samples is distributed in the desired way.

5.1 Method

The filtered sampling algorithm starts with a high-resolution latin hypercube sampling of the whole parameter space. A magnitude of ten times the target sample size has proven purposeful. Next, the quality of each sample is determined. According to its quality, each sample is assigned to a class defined by bounds in terms of sample quality. Figure 5.1 illustrates the classification of samples by a 2-dimensional test function. These classes are thinned out by removing samples in densely populated areas until the desired distribution of the sample quality is reached. This way, the spacial distribution of the samples stays nearly uniform and therefore only minor input correlations are introduced into the sampling.

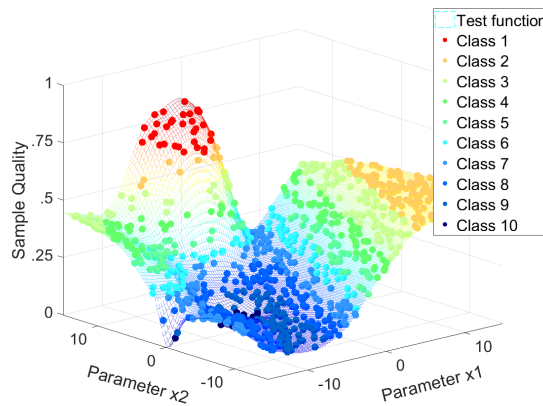


Figure 5.1: Sample classification of a 2-dimensional test function

5.1.1 Implementation

The algorithm for the filtered sampling approach is outlined in Fig. 5.2. The classification of the initial sampling is controlled by two weighting functions which control the size and the bounds of the classes. The choice of the weighting function is arbitrary. In this work Bézier splines are used. The algorithm iterates over the samples of one class and removes in each iteration the sample with lowest information value until the desired class size is achieved. The “information value“ of a sample is determined by looking at the population density of the parameter space in the neighborhood of the sample. The idea behind this is that another sample in an already densely populated area will not add much additional information to the sampling. The local density of the sampling at one sample ρ_{l,x_i} is determined by the minimum of the distances between this sample and the samples in the subset S according to Eq. 5.1. S is a subset of the complete sampling consisting of the class x_i belongs to and the adjacent classes. $dist(\cdot)$ is an arbitrary, normalized distance metric (e.g. Euclidean distance, Manhattan distance, Mahalanobis distance). The sample with the highest value of ρ_{l,x_i} has the nearest neighbor and is therefore removed. Rating the local density of high dimensional data by a distance measure can be dangerous as the dimensionality becomes a significant influence on the distance for high dimensions. This effect is known as the “curse of dimensionality“ [Bey99]. For data with strong correlations however, like in the case of classification by one dimension, this effect does not occur.

Similar observations have been made by Zimek et al. [Zim12].

$$\rho_{l,x_i} = \frac{1}{\min(\text{dist}(x_i, S))} \quad (5.1)$$

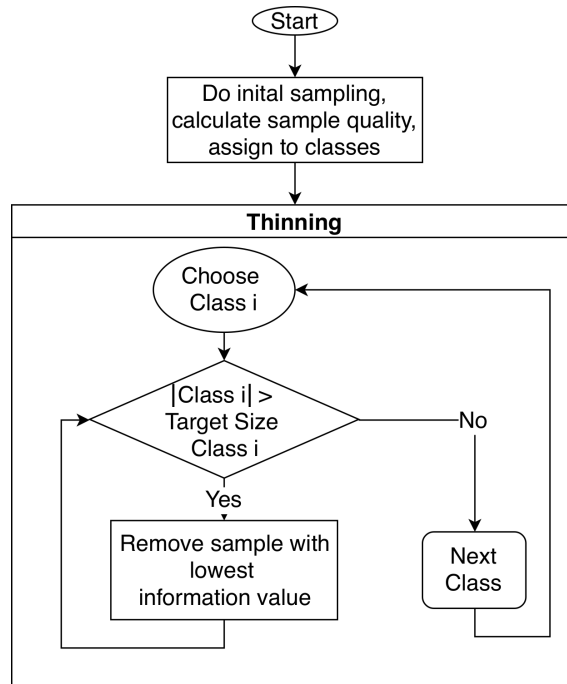


Figure 5.2: Flowchart of the filtered sampling algorithm

5.1.2 Distance Metrics

A metric (or “distance function“) is a function which computes the distance between elements of a set as a non-negative real number. This way, distance functions provide an instrument to measure how close the elements of a set are. These elements can be scalar numbers, vectors or arbitrary matrices. If the resulting distance of two elements is zero, those elements can be considered equivalent in terms of the applied metric. In this section, a short overview of some common distance metrics is given without the claim of completeness. Detailed derivations and additional metrics can be found in standard textbooks on mathematics like [Bro13].

5.1.2.1 Euclidean Distance

The most commonly know distance metric is the Euclidean distance (also know as “Pythagorean metric“, “ L^2 distance“ or “ L^2 norm“). The Euclidean distance of two points \vec{P} and \vec{Q} is given by the length of the line segment connecting these point (\overline{PQ}) .

In an n -dimensional Cartesian space it can be computed by the Pythagorean formula:

$$\begin{aligned} d_{Euclidean}(\vec{P}, \vec{Q}) &= \sqrt{(q_1 - p_1)^2 + (q_2 - p_2)^2 + \dots + (q_n - p_n)^2} \\ &= \sqrt{\sum_{i=1}^n (q_i - p_i)^2} \end{aligned} \quad (5.2)$$

5.1.2.2 Manhattan Distance

The Manhattan distance (also referred to as “taxicab metric“) was first considered by Hermann Minkowski in the 19th century¹. It measures the distance between two points as the sum of the absolute differences of their Cartesian coordinates. This principle is illustrated in Fig. 5.3 by the distance between two points \vec{P} and \vec{Q} on a rectangular grid in two dimensions.

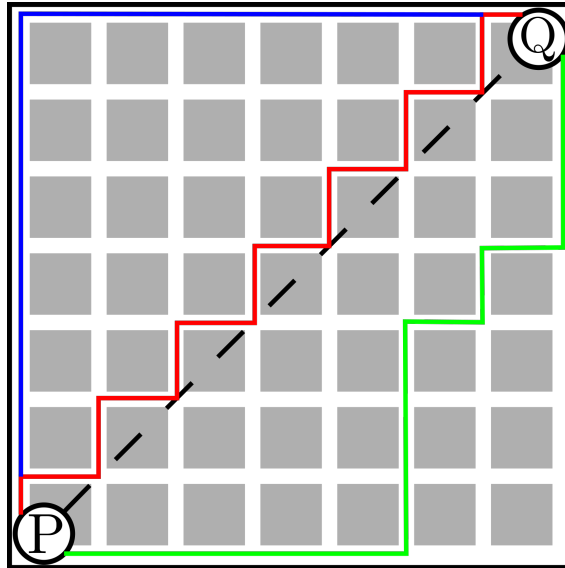


Figure 5.3: Schematic representation of the Manhattan distance (red, blue and green line) between two points “P“ and “Q“ in comparison with the Euclidean distance (dashed black line).

The shortest distance is given by the Euclidean distance depicted by a dashed black line. Possible path with the same length in terms of the Manhattan distance are depicted by the red, blue and green lines. The Manhattan distance can be computed for the n -dimensional

¹ The author was unable to find the original publication by Minkowski. A comprehensive discourse on this topic can be found in [Kra75].

case as

$$d_{Manhattan} = \sum_{i=1}^n |p_i - q_i| \quad (5.3)$$

5.1.2.3 Mahalanobis Distance

The Mahalanobis distance measures the distance between a point \vec{p} and a set of points \vec{P} in terms of standard deviations. It was introduced by P.C. Mahalanobis in 1936 [Mah36]. The distance of the point \vec{p} from a set of points \vec{P} with mean $\vec{\mu}$ and covariance matrix Σ is given by Eq.5.4. In contrast to the previously presented distance measures, the correlations of the data is taken into account.

$$d_{Mahalanobis}(\vec{p}, \vec{P}) = \sqrt{(\vec{p} - \vec{\mu})^T \Sigma^{-1} (\vec{p} - \vec{\mu})} \quad (5.4)$$

5.2 Example

The filtered sampling approach is applied to sampling from a target distribution X with a 20-dimensional multi-modal test function as the density function. The distances used for the thinning are obtained from the Mahalanobis distance. The weighting functions used for the classification of the samples are shown in Fig 5.4. The blue curve gives the size of the classes in percent. The minimum non-dimensional sample quality required for a sample to be assigned to a certain class is given by the red staircase function. For example, the first class includes all samples with a quality of 0.8 or greater, in the second class all samples have a quality between 0.6 and 0.8 and so on. Figure 5.5(a) shows the histogram of the generated sampling. The fitted probability density function (red line) is very similar to the ideal one (green line). Furthermore, the correlation matrix plotted in Fig. 5.5(b) shows only minor input correlations. Therefore, the filtered sampling method satisfies the requirements for a sampling method.

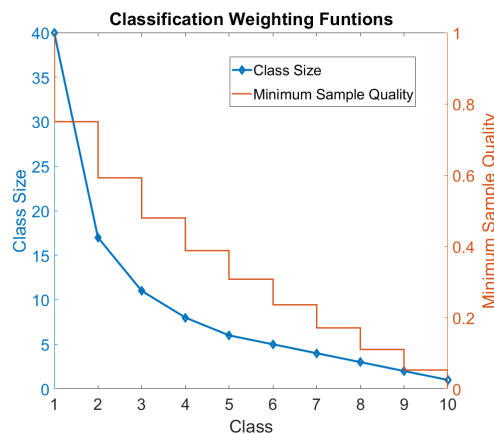


Figure 5.4: Weighting function used in the classification to control the class boundaries in terms of sample quality and the class sizes.

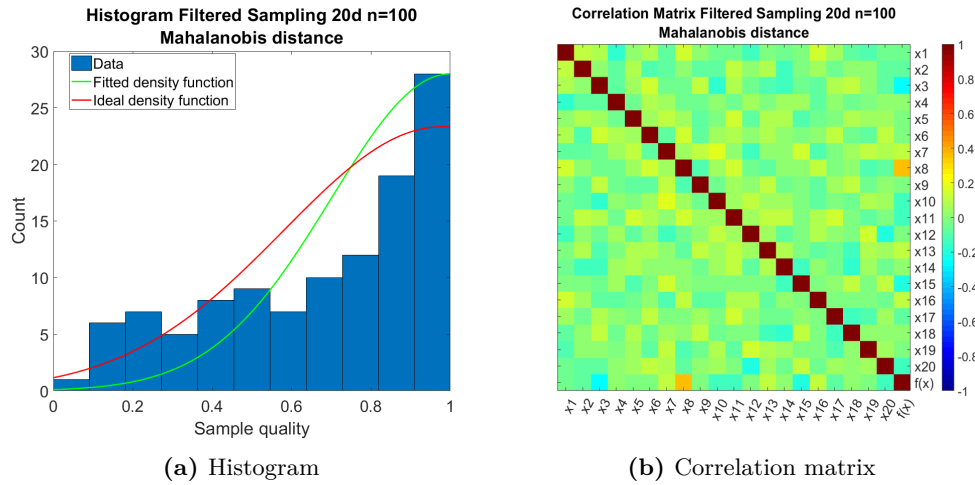
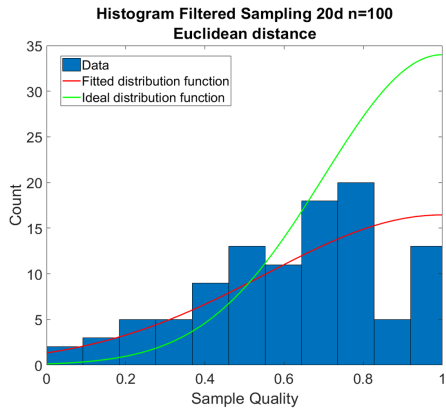


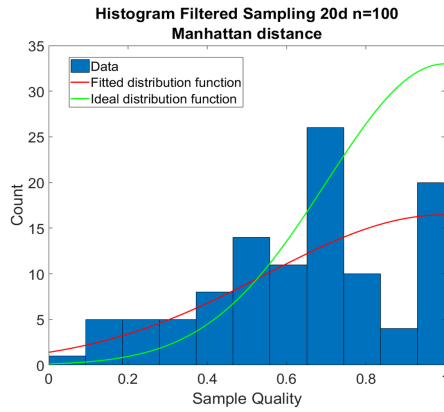
Figure 5.5: Histogram and correlation matrix for a sampling consisting of 100 samples generated by the filtered sampling algorithm for a 20d test function (Mahalanobis distance).

Figure 5.6 shows histograms and correlation matrices for samplings from the same target distribution X with a 20-dimensional multi-modal test function as the density function using different distance metrics. The histogram in Fig. 5.6(a) depicts a sampling generated by the filtered sampling algorithm using the Euclidean distance metric. When compared to the histogram in Fig. 5.5(a), a strong deviation from the desired distribution can be observed. The correlation matrices in Fig. 5.5(b) and Fig. 5.6(b) show no significant differences. A similar tendency can be observed when comparing the sampling using the Manhattan distance with the one using the Mahalanobis distance. While the histogram (Fig. 5.6(c)) shows a strong deviation between the fitted and the ideal distribution function, the observed level of input correlations is almost identical.

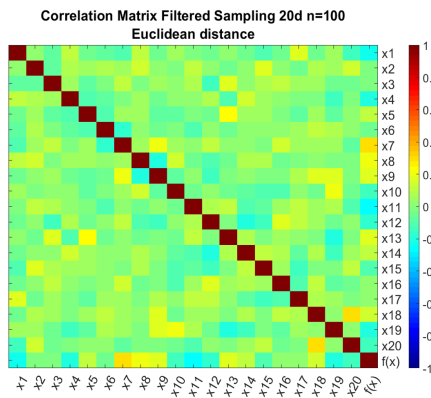
In summary, it can be stated based on this example and further test carried out in the course of this research that the Mahalanobis distance seems to be the best suited distance metric for use with the filtered sampling algorithm. Still, it is recommended to test different distance metrics depending on the respective field of application as firstly, the results may vary and, secondly, such a test can be carried out with little effort.



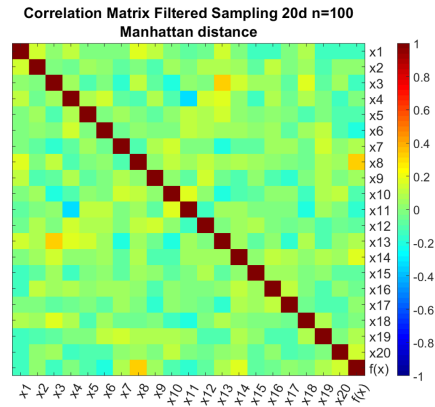
(a) Histogram using Euclidean distance



(b) Histogram using Manhattan distance



(c) Correlation matrix using Euclidean distance



(d) Correlation matrix using Manhattan distance

Figure 5.6: Histograms and correlation matrices for a samplings consisting of 100 samples generated by the filtered sampling algorithm for a 20d test function with different distance functions.

CHAPTER 6

Computational Model

In this chapter the computational model is described. This model encompasses the preliminary design method, the concept for geometry parametrization, the low-fidelity flow computation method based on one-dimensional loss models and the CAE models for fluid dynamics and structure mechanics. Special emphasis is put into the development of a geometry parametrization method, which takes fluid mechanic considerations into account to prevent physically inexpedient designs. Another central aspect is the calibration of the low-fidelity flow computation method. While the analytical models used for these aerodynamic computations are implemented according to literature sources, the models are not usable for the prediction of the performance of modern centrifugal compressors unless the model parameters are calibrated.

6.1 Preliminary Design

Preliminary design methods are used to determine global geometric features of the impeller like the dimensions of inlet and outlet areas or the blade angles at the leading edge. In addition, these methods allow a first check if the chosen design is capable of delivering the desired pressure ratio. The computations are based on stream filament theory. Therefore, only the geometries of the impeller inlet and outlet can be considered in the calculations. In this section, the applied analysis method is presented. If not stated otherwise, all equations in this section are taken from [Fis86].

The input parameters required for the preliminary design computations are given in Tab. 6.1.

Table 6.1: Input parameters for preliminary design

Quantity	Symbol	Unit
Global machine parameters		
Outer diameter	D_2	m
Tip speed	u_2	$\frac{m}{s}$
Trailing edge relative blade angle	β_2	$degree$
Leading edge hub diameter ratio	$\nu_{1,Hub}$	
Axial impeller extent	L_{Ax}	m
Number of blades	z	
Blade thickness	t_{Blade}	m
Meridional velocity ratio	μ_m	
Pressure ratio	$\Pi = \frac{p_3}{p_0}$	
Thermodynamic quantities		
Ambient pressure	p_A	Pa
Ambient temperature	T_A	K
Inlet flow ratio	\dot{V}_0	$\frac{m^3}{s}$
Gas constant	R	$\frac{J}{kg \cdot K}$
Heat capacity ratio	γ	

The basic idea behind the presented preliminary design strategy is the minimization of the inlet relative Mach number at the blade tip. High Mach numbers in this area can lead to shocks and aerodynamic blockage and therefore losses. Figure 6.1 illustrates the influence of the inlet shroud diameter on the velocity triangles for an otherwise identical impeller ($D_2, u_2, D_{1,Hub}, \dot{V}_1, \omega_2 = const.$). The inflow is assumed to be swirl free ($c_{\theta 1} = 0$). It is clearly evident that an optimal value of $D_{1,Shroud}$ exists for which $w_{1,Shroud}$ becomes minimal.

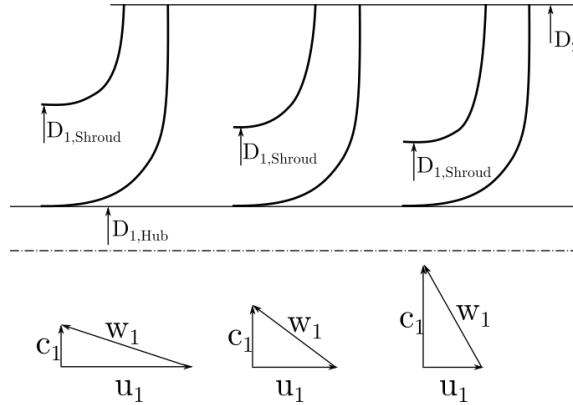


Figure 6.1: Influence of the inlet shroud diameter on the inlet velocity triangles at shroud.

The inlet and outlet geometries and the blade angles at the leading edge are obtained by iterating over equations Eq. 6.1 to Eq. 6.37. The indexes of the stations in the machine are chosen in accordance to Fig. 3.3 (“A” \Rightarrow ambient conditions, “0” \Rightarrow machine inlet, “1” \Rightarrow impeller inlet, “2” \Rightarrow impeller outlet / trailing edge, “3” \Rightarrow machine outlet). ν_x depicts a geometric quantity in relation to the outer diameter D_2 (Example: $\nu_{1,Hub} = \frac{D_{1,Hub}}{D_2}$). At the start of the iteration, the values of c_0 , c_1 , $\nu_{1,Shroud}$, $\eta_{pol,0-1}$, k_c and k_v have to be chosen. $\eta_{pol,0-1}$ is the efficiency of the pipe flow from “0” to “1”. The factor k_c is used to scale the absolute flow velocity along the leading edge, the factor k_v depicts the change in volume flow between “0” and “1”. Furthermore, the polytropic efficiency η_{pol} of the machine has to be guessed or determined by an empirical correlation (see section 3.1.1.3). The inflow is assumed to be swirl free which implies $c_{\theta 1} = 0 \Rightarrow c_{m1} = c_1$. The Iteration is considered as converged if the values of $\beta_{1,Hub}$, $\beta_{1,Shroud}$, $\nu_{1,Shroud}$ and o_2 change less then a given threshold from one iteration to the next.

The preliminary design method outlined by the equations listed above is based on a stream filament computation from the machine inlet (“0”) to the impeller outlet (“2”). The thermodynamic state of the flow at the machine inlet is computed in Eq.6.1 and Eq. 6.2. The temperature is determined by applying Bernoulli’s equation to the case that the flow is accelerated form a stationary state at ambient conditions T_A , p_A to the velocity c_0 . In the first iteration c_0 is guessed. For a know temperature T_0 , the pressure at the machine inlet p_0 is computed according to Eq. 6.2. The change of state between “A” and “0” is assumed to be isentropic, therefore the polytropic exponent n_{A-0} is set to γ . If both the temperature and the pressure at the machine inlet are known, the mass flow rate can be computed by Eq. 6.3.

$$T_0 = T_A - \frac{1}{2C_p} c_0^2 \quad (6.1)$$

$$p_0 = p_A \left[\frac{T_0}{T_A} \right]^{\frac{\gamma}{\gamma-1}} \quad (6.2)$$

$$\dot{m} = \frac{\dot{V}_0}{\rho_0} = \frac{\dot{V}_0 RT_0}{p_0} \quad (6.3)$$

The thermodynamic conditions at the impeller inlet (“1”) are computed in Eq. 6.4, Eq. 6.6 and Eq.6.7. The approach is analogous to the computation at state “0”, except that the change of state is polytropic. The polytropic index for this flow process is computed by Eq. 6.5 based on an assumed efficiency $\eta_{pol,0-1}$. For a known thermodynamic state of the flow at “0” and “1”, the velocities c_0 and c_1 can be computed based on the geometry (Eq. 6.8 and Eq. 6.9). These values are used to compute T_0 and T_1 in the next iteration.

$$T_1 = T_0 - \frac{1}{2C_p} (c_1^2 - c_0^2) \quad (6.4)$$

$$n_{0-1} = \frac{\eta_{pol,0-1}}{\eta_{pol,0-1} - \frac{\gamma-1}{\gamma}} \quad (6.5)$$

$$p_1 = p_0 * \left[\frac{T_1}{T_0} \right]^{\frac{n_{0-1}}{n_{0-1}-1}} \quad (6.6)$$

$$\dot{V}_1 = k_v \dot{V}_0 \quad (6.7)$$

$$c_0 = \frac{\dot{V}_0}{A_0} = \frac{\dot{V}_0}{\frac{\pi}{4} D_{1,Shroud}^2} \quad (6.8)$$

$$c_1 = \frac{\dot{V}_1}{A_1} = \frac{\dot{V}_1}{\frac{\pi}{4} (D_{1,Shroud}^2 - D_{1,Hub}^2)} \quad (6.9)$$

The velocity c_1 used in all computations up to this point is the averaged velocity at the middle stream line. The distribution of the absolute velocity c along the leading edge is assumed to be linear with slope k_c . The absolute velocities at shroud and hub can be computed by Eq. 6.10 and Eq. 6.11.

$$c_{1,Shroud} = \frac{\dot{V}_1 k_c}{\frac{\pi}{4} D_2 (\nu_{1,Shroud}^2 - \nu_{1,Hub}^2)} = c_1 k_c \quad (6.10)$$

$$c_{1,Hub} = \frac{c_1}{k_c} \quad (6.11)$$

If the absolute velocities are known along the leading edge, the relative blade angles for an incidence free flow can be computed according to Eq. 6.14.

$$\nu_{1,Mid} = \sqrt{\frac{1}{2} (\nu_{1,Shroud}^2 + \nu_{1,Hub}^2)} \quad (6.12)$$

$$u_{1,i} = \nu_{1,i} u_2 \text{ with } i=\text{Hub, Mid, Shroud} \quad (6.13)$$

$$\beta_{1,i} = \tan^{-1} \frac{c_{1,i}}{u_{1,i}} \text{ with } i=\text{Hub, Mid, Shroud} \quad (6.14)$$

The factor k_v , which describes the change in volume between stations “0“ and “1“, was guessed in the first iteration step. Therefore, the value of k_v , which represents the computed ratio of flow rates, is given in Eq. 6.16. This value is used in the next iteration for the computation of \dot{V}_1 .

$$a_0 = \sqrt{\gamma RT_0} \quad (6.15)$$

$$k_v = \frac{\dot{V}_1}{\dot{V}_0} = \frac{1}{\left(1 - \frac{\gamma-1}{2} \frac{c_1^2}{a_0^2}\right)^{\frac{1}{\gamma-1}}} \quad (6.16)$$

Analogous to the k_v factor, the factor k_c , which describes the distribution of the absolute velocity along the leading edge, has to be corrected according to Eq. 6.18. This value is used in the next iteration to compute $c_{1,Hub}$ and $c_{1,Shroud}$.

$$q = e^{\frac{\nu_{1,Shroud} + \nu_{1,Hub}}{4\nu_{Ax}} \left(1 + \frac{1}{\nu_{1,Shroud}}\right)} \quad (6.17)$$

$$k_c = \frac{c_{1,Shroud}}{c_1} = \frac{\nu_{1,Shroud} - \nu_{1,Hub}}{\nu_{1,Shroud} - \nu_{1,Hub} - (\nu_{1,Shroud} - \nu_{1,Mid}) \left(1 - \frac{1}{q}\right)} \quad (6.18)$$

In combination with the flow coefficient φ_d , Eq. 6.10 can be rewritten as

$$c_{1,Shroud} = \frac{\varphi_d k_c k_v}{\nu_{1,Shroud} - \nu_{1,Hub}} u_2 \quad (6.19)$$

The shroud relative velocity at the leading edge can be determined from the velocity triangle (Eq. 6.20). If the local speed of sound is assumed to be constant through the impeller ($a_0 = a_1 = a_2$), the Mach number at the leading and trailing edge are given by Eq. 6.21.

$$w_{1,Shroud}^2 = c_{1,Shroud}^2 + u_{1,Shroud}^2 = \left(\frac{\varphi_d k_c k_v}{\nu_{1,Shroud} - \nu_{1,Hub}} u_2 \right)^2 + (\nu_{1,Shroud} u_2)^2 \quad (6.20)$$

$$Ma_{w1,Shroud} = \frac{w_{1,Shroud}}{a_0} \text{ and } Ma_{u2} = \frac{u_2}{a_0} \quad (6.21)$$

The combination of Eq. 6.20 and Eq. 6.21 yields

$$Ma_{w1,Shroud}^2 = Ma_{u2}^2 \left[\left(\frac{\varphi_d k_c k_v}{\nu_{1,Shroud} - \nu_{1,Hub}} \right)^2 + \nu_{1,Shroud}^2 \right] \quad (6.22)$$

As the Mach number is always positive, $Ma_{w1,Shroud}^2$ and Ma_{u2} take a minimum value for the same optimal value of $\nu_{1,Shroud,Opt}$. This value can be determined by differentiating Eq. 6.22 for $\nu_{1,Shroud}$ and setting $\frac{\partial Ma_{w1,Shroud}^2}{\partial \nu_{1,Shroud}} = 0$. Solving for $\nu_{1,Shroud}$ gives

$$\nu_{1,Shroud} = \sqrt{\nu_{1,Hub}^2 + \left(2\varphi_D^2 (k_c k_v)^2 \right)^{\frac{1}{3}}} \quad (6.23)$$

The meridional velocity at the impeller outlet is computed from the meridional velocity ratio μ_m . If the flow at outlet follows the blade without any incidence, the amount of work transferred between the impeller and the flow is described by Eq. 6.25 (Euler's turbomachinery equation). As this is only the case if the impeller has an infinity number of infinitely thin blades, all quantities which rely on this assumption are marked by the subscript "inf". The flow incidence at the trailing edge can be described by a slip factor correlation. In this case, the correlation of Wiesner is used. The real amount of work transferred between the impeller and the fluid is computed according to Eq. 6.29. The incidence is accounted by the slip velocity $c_{\vartheta 2,SL}$ (Eq. 6.27).

$$c_{m2} = c_{m1} \mu_m = c_1 \mu_m \quad (6.24)$$

$$w_{t,inf} = c_{\vartheta 2,inf} u_2 = \left(u_2 - c_{m2} \frac{1}{\tan(\beta_2)} \right) u_2 \quad (6.25)$$

$$\sigma = \sigma_{Wiesner} \text{ see Eq. 3.4, Eq. 3.5 and Eq. 3.6} \quad (6.26)$$

$$c_{\vartheta 2,SL} = (1 - \sigma_{Wiesner}) u_2 \quad (6.27)$$

$$c_{\vartheta 2,inf} = \frac{w_{t,inf}}{u_2} \quad (6.28)$$

$$w_t = u_2 (c_{\vartheta 2,inf} - c_{\vartheta 2,SL}) \quad (6.29)$$

The amount of enthalpy needed to rise the pressure in the impeller from p_1 to p_2 is given by Eq. 6.30. The polytropic efficiency of the impeller is assumed to be 3% higher than the efficiency of the machine (Eq. 6.31). The polytropic index of the flow through the impeller can be computed according to Eq. 6.32. The pressure at the impeller outlet can be computed by solving Eq. 6.30 for p_2 .

$$\Delta h_{Impeller} = w_t = \frac{\gamma}{\gamma - 1} RT_1 \left[\frac{p_2^{\frac{n_{Impeller}-1}{n_{Impeller}}}}{p_1} - 1 \right] \quad (6.30)$$

$$\eta_{pol,Impeller} = \eta_{pol} + 0.03 \quad (6.31)$$

$$n_{Impeller} = \frac{\eta_{pol,Impeller}}{\eta_{pol,Impeller} - \frac{\gamma-1}{\gamma}} \quad (6.32)$$

$$p_2 = p_1 \left[\left(w_t \frac{\gamma-1}{\gamma RT_1} + 1 \right)^{\frac{n_{Impeller}}{n_{Impeller}-1}} \right] \quad (6.33)$$

With the pressure at the impeller outlet known, the temperature and volume flow can

be computed according to Eq. 6.34 and Eq. 6.35.

$$T_2 = T_1 \left(\frac{p_2}{p_1} \right)^{\frac{n_{Impeller}-1}{n_{Impeller}}} \quad (6.34)$$

$$\dot{V}_2 = \dot{m} \frac{RT_2}{p_2} \quad (6.35)$$

The trailing edge blade height is computed by Eq. 6.37. The amount of blockage introduced by the blades at the impeller outlet is taken into account by the blockage factor B_2 (Eq. 6.36).

$$B_2 = \frac{D_2}{D_2 - \frac{z_{tBlade}}{\pi \sin(\beta_2)}} \quad (6.36)$$

$$o_2 = \frac{\dot{V}_2 B_2}{\pi D_2 c_{m2}} \quad (6.37)$$

6.2 Geometric Modeling

The choice of the input parameters, which are used to describe the geometry, plays an important role for the quality of the metamodel. The metamodel has to relate the input parameters to the model responses. A parametrization concept, which describes the geometry by means of purely geometric concepts, like for example spline control point positions, results in a high number of completely independent parameters. Past research activities have shown that such parametrization concepts are contra productive when it come to metamodeling ([Böc09],[Ryb11]). Furthermore, a set of parameters which can be varied completely independently of each other complicates the exclusion of physically non-expedient designs from the sample set. In this research, a concept has been developed to avoid such problems.

Based on the findings presented in chapters 2 and 3, a set of parameters, which show a strong influence on the flow inside the impeller, has been identified. These parameters are:

Table 6.2: Fluid dynamically relevant geometric quantities

Quantity	Influence on	Reference
Meridional curvature	Hub to shroud pressure gradient, secondary flow	Eq. 2.90, Eq. 2.91
Meridional slope	Hub to shroud pressure gradient	Eq. 2.90
Blade high distribution	Meridional velocity distribution, hub to shroud pressure gradient	Eq. 2.90
Blade lean	Crosswise pressure distribution, secondary flow	Eq. 2.91, Fig. 2.17
Blade curvature	Secondary flow	Eq. 2.91
Blade angles at leading edge	Flow incidence, efficiency	Eq. 6.103
Blade angles at trailing edge	Slip, work	Eq. 2.96, Sec. 3.1.1.2
Flow area at inlet and exit	Flow velocity, work	Eq. 2.89

6.2.1 Definition of the Meridional Contours

Based on the fluid dynamic considerations made in the previous chapters, the meridional curvature, the meridional slope and the blade height distribution have a significant impact on the flow in the impeller. While intake and discharge geometries are given by preliminary design and constructional constraints, the shape of the contours in between can be designed freely. The hub contour is parametrized by the meridional curvature and the meridional slope. The shroud contour is defined by applying a blade height distribution to the hub contour. The distribution of the blade height has a direct influence on the variation of meridional velocity along the streamwise direction. As strong local gradients in the meridional velocity can cause losses due to flow separation, the blade height is parametrized in a way that enforces a monotonous decrease of blade height from hub to shroud. In

contrast to a parametrization concept which treats the shroud contour independently from the hub contour, this concept already minimizes one potential source of losses. A sketch of the meridional contour with all major parameters is shown in Fig. 6.2.

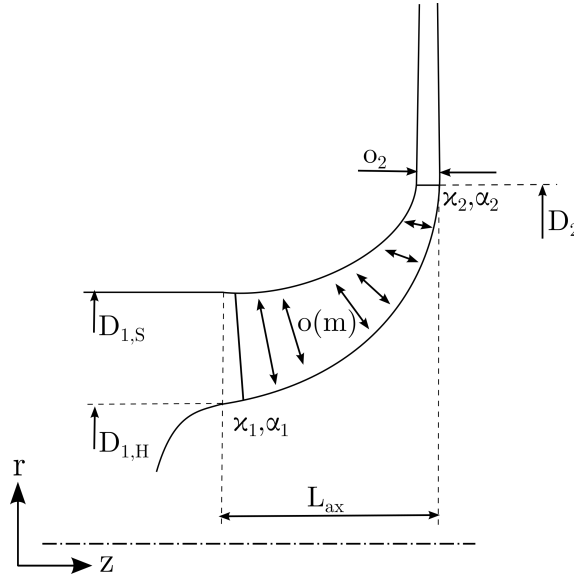


Figure 6.2: Meridional contours with relevant parameters.

6.2.1.1 Definition of the Hub Contour

The parameters defining the hub contour between the impeller inlet and outlet are shown in Fig. 6.3. The hub contour is represented by a Bézier spline with 5 control points of which the first and the last are fixed by global design choices. The second and fourth control point are described by the meridional slope angle and the the respective distance form the first or last control point. The middle control point's position can be computed from the meridional curvatures at the impeller inlet (κ_1) and the impeller outlet (κ_2).

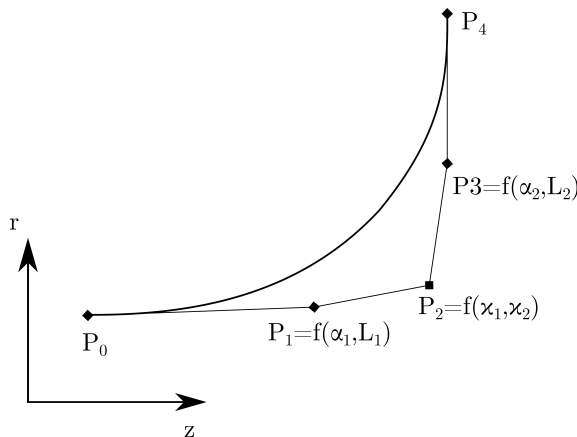


Figure 6.3: Parameters describing the hub contour.

The local curvature of a Bézier curve at the position u can be computed according to

Eq. 6.38. The first and second derivatives of Bézier splines can be computed according to Eq. 2.143 and Eq. 2.144.

$$\kappa(u) = \frac{\frac{\partial z(u)}{\partial u} \frac{\partial^2 r(u)}{\partial u^2} - \frac{\partial^2 z(u)}{\partial u^2} \frac{\partial r(u)}{\partial u}}{\left(\frac{\partial z(u)}{\partial u}^2 - \frac{\partial r(u)}{\partial u}^2 \right)^{3/2}} \quad (6.38)$$

The first and second derivatives of the Bernstein polynomials needed for the computation of the derivatives of the Bézier splines are given by

$$\begin{aligned} \frac{\partial B_{i,n}(u)}{\partial u} &= u^{i-1} i (1-u)^{n-i} - u^i (1-u)^{n-i-1} (n-1) \\ \frac{\partial^2 B_{i,n}(u)}{\partial u^2} &= \frac{u^i i^2 (1-u)^{n-1}}{u^2} - \frac{u^i i (1-u)^{n-1} (n-1)}{u^2} - \frac{2u^i i (1-u)^{n-1} (n-1)}{u(1-u)} + \\ &\quad \frac{u^i (1-u)^{n-1} (n-1)^2}{u(1-u)^2} - \frac{u^i (1-u)^{n-1} (n-1)}{u(1-u)^2} \end{aligned} \quad (6.39)$$

As only the curvature at the start ($u=0$) and the end of the curve ($u=1$) are of interest, the derivatives of the Bernstein polynomials are computed only for these cases. The resulting derivatives are given by Table 6.3.

Table 6.3: Derivatives of the Bernstein polynomials.

First derivative		
Control point i	Derivative at $u=0$	Derivative at $u=1$
0	$-n$	0
1	n	0
2	0	0
3	0	$-n$
4	0	n
Second derivative		
Control point i	Derivative at $u=0$	Derivative at $u=1$
0	$n(n-1)$	0
1	$-2n(n-1)$	0
2	$n(n-1)$	$n(n-1)$
3	0	$-2n(n-1)$
4	0	$n(n-1)$

By combining these simplified derivatives with Eq. 2.143 and Eq. 2.144, the first and

second derivative of the hub curve at the first and last point can be computed as

$$\begin{aligned}
\frac{\partial C(u=0)}{\partial u} &= \left(\frac{\frac{\partial z(u=0)}{\partial u}}{\frac{\partial r(u=0)}{\partial u}} \right) = \sum_{i=0}^n \frac{\partial B_{i,n}(u=0)}{\partial u} \begin{pmatrix} P_{i,z} \\ P_{i,r} \end{pmatrix} = -n \begin{pmatrix} P_{0,z} \\ P_{0,r} \end{pmatrix} + n \begin{pmatrix} P_{1,z} \\ P_{1,r} \end{pmatrix} \\
\frac{\partial C(u=1)}{\partial u} &= \left(\frac{\frac{\partial z(u=1)}{\partial u}}{\frac{\partial r(u=1)}{\partial u}} \right) = \sum_{i=0}^n \frac{\partial B_{i,n}(u=1)}{\partial u} \begin{pmatrix} P_{i,z} \\ P_{i,r} \end{pmatrix} = -n \begin{pmatrix} P_{3,z} \\ P_{3,r} \end{pmatrix} + n \begin{pmatrix} P_{4,z} \\ P_{4,r} \end{pmatrix} \\
\frac{\partial^2 C(u=0)}{\partial u^2} &= \left(\frac{\frac{\partial^2 z(u=0)}{\partial u^2}}{\frac{\partial^2 r(u=0)}{\partial u^2}} \right) = \sum_{i=0}^n \frac{\partial^2 B_{i,n}(u=0)}{\partial u^2} \begin{pmatrix} P_{i,z} \\ P_{i,r} \end{pmatrix} = n(n-1) \begin{pmatrix} P_{0,z} \\ P_{0,r} \end{pmatrix} - 2n(n-1) \begin{pmatrix} P_{1,z} \\ P_{1,r} \end{pmatrix} \\
&\quad + n(n-1) \begin{pmatrix} P_{2,z} \\ P_{2,r} \end{pmatrix} \\
\frac{\partial^2 C(u=1)}{\partial u^2} &= \left(\frac{\frac{\partial^2 z(u=1)}{\partial u^2}}{\frac{\partial^2 r(u=1)}{\partial u^2}} \right) = \sum_{i=0}^n \frac{\partial^2 B_{i,n}(u=1)}{\partial u^2} \begin{pmatrix} P_{i,z} \\ P_{i,r} \end{pmatrix} = n(n-1) \begin{pmatrix} P_{2,z} \\ P_{2,r} \end{pmatrix} - 2n(n-1) \begin{pmatrix} P_{3,z} \\ P_{3,r} \end{pmatrix} \\
&\quad + n(n-1) \begin{pmatrix} P_{4,z} \\ P_{4,r} \end{pmatrix}
\end{aligned} \tag{6.40}$$

The curvature at the start and end of the hub spline can be computed by combining the derivatives given by Eq. 6.40 with the formula for the local curvature (Eq. 6.38). (Due to the length of the equations, the numerator is written in two lines.)

$$\begin{aligned}
\kappa(u=0) &= \frac{(-nP_{0,z} + nP_{1,z})(n(n-1)P_{0,r} - 2n(n-1)P_{1,r} + n(n-1)P_{2,r}) - (n(n-1)P_{0,z} - 2n(n-1)P_{1,z} + n(n-1)P_{2,z})(-nP_{0,r} + nP_{1,r})}{\left[(-nP_{0,z} + nP_{1,z})^2 - (-nP_{0,r} + nP_{1,r})^2 \right]^{3/2}} \\
\kappa(u=1) &= \frac{(-nP_{3,z} + nP_{4,z})(n(n-1)P_{2,r} - 2n(n-1)P_{3,r} + n(n-1)P_{4,r}) - (n(n-1)P_{3,z} - 2n(n-1)P_{4,z} + n(n-1)P_{5,z})(-nP_{3,r} + nP_{4,r})}{\left[(-nP_{3,z} + nP_{4,z})^2 - (-nP_{3,r} + nP_{4,r})^2 \right]^{3/2}}
\end{aligned} \tag{6.41}$$

By solving Eq. 6.41 for $P_{2,r}$ and $P_{2,z}$, all control points of the hub spline are known.

$$P_{2,z} = \frac{P_{0,z}[-K_1 + P_{3,z}(P_{4,r} - P_{1,r})] + P_{1,z}[K_1 - P_{3,z}(P_{4,r} - P_{0,r} + P_{4,z}(P_{3,r} - P_{0,r}))] - K_0(P_{4,z} - P_{3,z})}{(P_{1,r} - P_{0,r})(P_{4,z} - P_{3,z}) - (P_{1,z} - P_{0,z})(P_{4,r} - P_{3,r})}$$

with $K_0 = \kappa(u = 0) \frac{n}{n-1} [(P_{1,z} - P_{0,z})^2 + (P_{1,r} - P_{0,r})^2]^{3/2}$
and $K_1 = \kappa(u = 1) \frac{n}{n-1} [(P_{4,z} - P_{3,z})^2 + (P_{4,r} - P_{3,r})^2]^{3/2}$

$$P_{2,r} = \frac{P_{0,z}P_{1,r} - P_{1,z}P_{0,r} + P_{2,z}P_{0,r} - P_{2,z}P_{1,r} - K_0}{P_{0,z} - P_{1,z}} \quad (6.42)$$

The final parametrization of the hub spline is given in Table 6.4.

Table 6.4: Parametrization of the hub spline.

Control point	Defined by
0	Inlet area definition from preliminary design
1	Meridional slope at inlet and distance from inlet
2	Meridional curvature at inlet and outlet
3	Meridional slope at outlet and distance from outlet
4	Fixed outer diameter and axial extent

6.2.1.2 Definition of the Shroud Contour

The shroud contour is connected to the hub contour by a distribution of blade height (see Fig. 6.4). The distribution is given by a Bézier spline with four control points. While the first and the last control points are constrained by the input and output areas taken from the preliminary design, the inner control points can be varied parametrically. The parameters of the inner control points are chosen in a way that ensures a monotonically decreasing blade height, which again prevents local decelerations of the meridional velocity. This way, one potential source of flow separation is excluded by the parametrization.

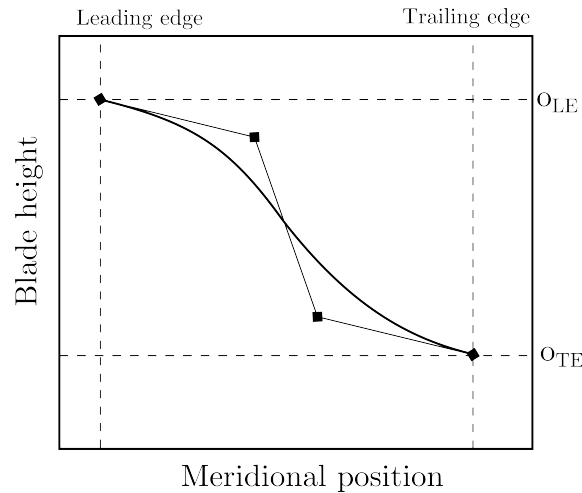


Figure 6.4: Definition of the blade height distribution.

The blade height is defined as the normal distance between the hub and the shroud curve in the meridional plane. If the shroud curve is defined by normals generated on the hub curve, these normals can intersect for certain forms of the hub curve which results in faulty shroud curves containing bumps or even loops. Therefore, circles are used to define the offset between the hub and the shroud curve. These circles are tangentially aligned on the hub curve and their diameter is equivalent to the blade height at the respective meridional position. Fig. 6.5 shows a circle \vec{C} of radius $\frac{c}{2}$ with center \vec{C}_0 tangentially aligned to the hub curve \vec{H} at the point \vec{T} . The circle at hub curve position $u = u_i$ is computed by

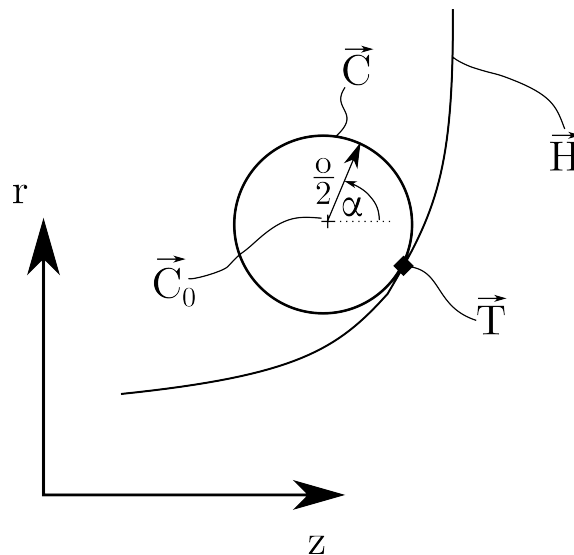


Figure 6.5: Alignment of a blade height circle on the hub curve.

$$\vec{C}(u_i) = \frac{o(u_i)}{2} \begin{pmatrix} \cos\alpha \\ \sin\alpha \end{pmatrix} \quad (6.43)$$

with $\alpha = 0 \dots 2\pi$. The diameter of the circle described by Eq. 6.43 equals the blade height at the meridional position $m = m_i$ but has to be aligned correctly to the hub curve. As the circles are tangentially aligned to the hub curve, the gradient of the circle and the hub curve is identical in the contact point $\vec{T} = C(m = m_i)$. This results in

$$\frac{\frac{\partial C(u_i)_r}{\partial m}}{\frac{\partial C(u_i)_z}{\partial u}} = \frac{\frac{\partial H(u_i)_r}{\partial m}}{\frac{\partial H(u_i)_z}{\partial u}} \quad (6.44)$$

Based on Eq. 6.44, the angle α_T in the contact point is given as

$$\alpha_T(u_i) = \arctan \left(-\frac{\frac{\partial C(u_i)_z}{\partial u}}{\frac{\partial C(u_i)_r}{\partial u}} \right) = \arctan \left(\frac{\frac{\partial H(u_i)_z}{\partial u}}{\frac{\partial H(u_i)_r}{\partial u}} \right) \quad (6.45)$$

The location of the circle's center in respect to the contact point can be determined by substituting α by α_T in Eq. 6.43. The location of the circle's center in the (z,r) coordinate system is obtained by translating it by the vector \vec{T} :

$$\vec{C}_0(u_i) = \vec{T} - \frac{o(u_i)}{2} \begin{pmatrix} \cos\alpha_T(u_i) \\ \sin\alpha_T(u_i) \end{pmatrix} \quad (6.46)$$

with $\vec{T} = \vec{H}(m_i)$. Finally, the aligned circle is given by

$$\vec{C}(u_i) = \vec{H}(u_i) - \frac{o(u_i)}{2} \begin{pmatrix} \cos\alpha_T(u_i) \\ \sin\alpha_T(u_i) \end{pmatrix} + \frac{o(u_i)}{2} \begin{pmatrix} \cos\alpha \\ \sin\alpha \end{pmatrix} \quad (6.47)$$

with $\alpha = 0 \dots 2\pi$.

The shroud curve is defined by fitting a curve to the circles (Fig. 6.6(a)).

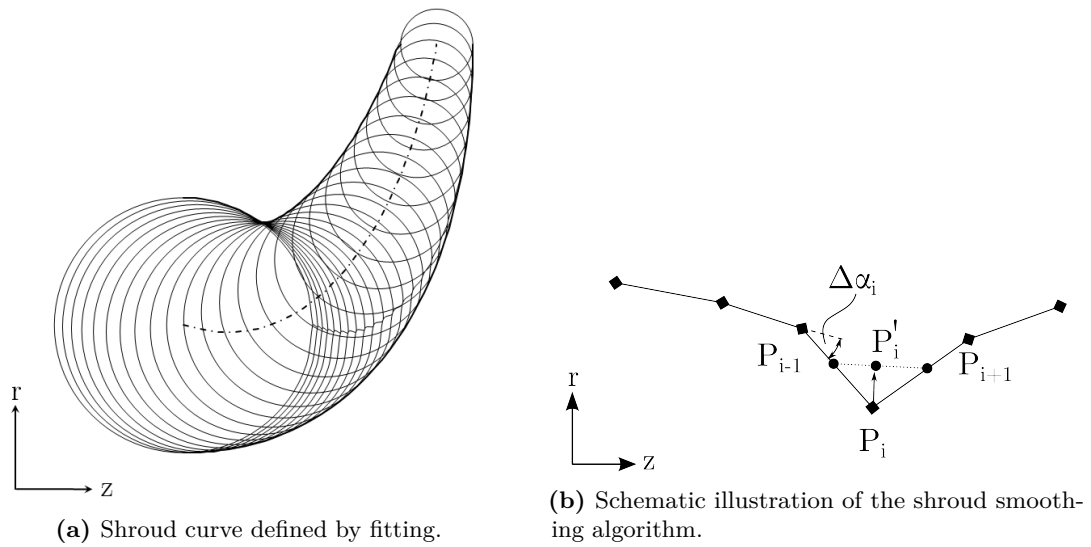


Figure 6.6: Definition of the shroud curve.

The fitting is carried out by choosing the point with the maximum r -coordinate for a given z -coordinate from all circles as the shroud point for this z -coordinate. In many cases, unwanted strong negative gradients of the fitted shroud contour in r -direction result from the combination of the hub curve with the chosen blade height distribution. Therefore, the resulting shroud curve has to be smoothed. Figure 6.6(b) illustrates the principle behind the smoothing algorithm: if the angle $\Delta\alpha_i$ exceeds a certain threshold, the point P_i is projected to a line defined by the connection of the midpoints of the lines $\overline{P_{i-1}P_i}$ and $\overline{P_iP_{i+1}}$ to create the new point P_i' . The algorithm is applied to all points of the shroud contour and repeated until the threshold angle is not exceeded at any point. The result of the smoothing is shown in Fig. 6.7. Finally, a Bézier spline is fitted to the smoothed shroud contour which will be used for all further computations.

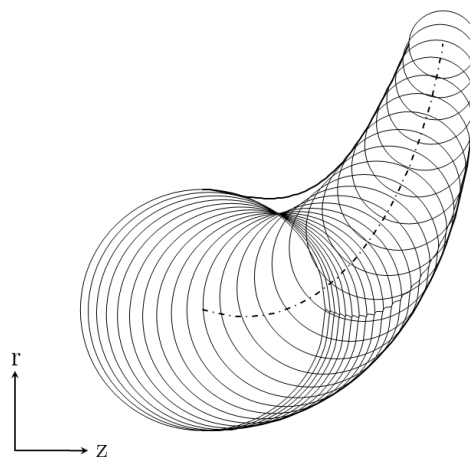


Figure 6.7: Smoothed shroud curve (Threshold angle 3°).

6.2.2 Definition of the Leading Edge

The meridional position of the leading edge is defined by two angles as depicted in Fig. 6.8. The leading edge hub position is defined by the angle $\alpha_{LE,Hub}$. Based on this point, a leading edge perpendicular to the hub contour is constructed. A second angle measured between the final leading edge and the priorly defined perpendicular leading edge ($\Delta\alpha_{LE,Shroud}$) then defines the leading edge position on the shroud curve.

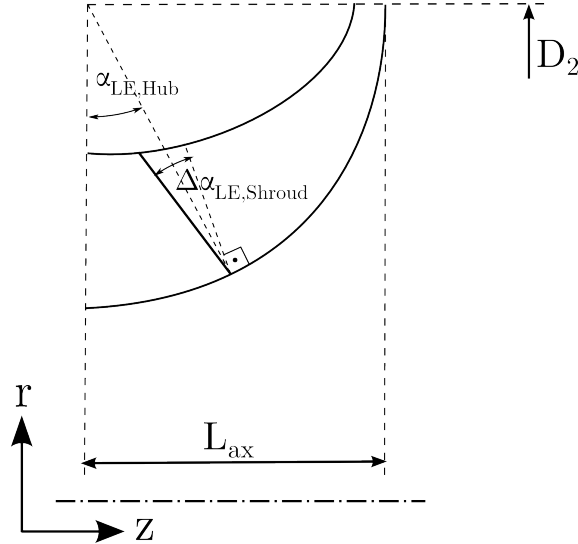


Figure 6.8: Definition of the leading edge in the meridional view.

6.2.3 Definition of the Blade

The shape of the blade can be defined by the distribution of either the relative blade angle β or the circumferential position ϑ . Both are connected by the relation

$$\tan\beta = \frac{1}{r} \frac{dm}{d\vartheta} \quad (6.48)$$

In this work, the blades are defined by the distribution of the circumferential blade angle at hub and shroud which is given as a Bézier spline. Figure. 6.9 shows a spline used for defining the distribution of the circumferential blade angle $\vartheta(m)$ for an arbitrary blade and the spline used for defining the distribution of the circumferential blade angle between the leading and the trailing edge. The dotted curve depicts the resulting distribution of the relative blade angle $\beta(m)$. The meridional position of the first and the last point of the spline's control polygon are defined by the locations of the leading and trailing edge in the meridional view. Their circumferential position is given by the circumferential blade lean at the leading and trailing edge (α_{Twist} and α_{Rake}) and by the global circumferential extent of the blade (ϑ_{Blade}). The second and fourth control points can vary their locations on straight lines defined by the angles $\alpha_{\vartheta,LE}$ and $\alpha_{\vartheta,TE}$. These angles are computed by rearranging Eq. 6.48 for $\frac{d\vartheta}{dm}$ for given values of β . This ensures that the resulting blade's relative angles at the leading and trailing edge match the desired values which are of

particular importance as the relative blade angles at the leading edge greatly influence the amount of losses due to incidence and therefore the impeller's efficiency. The relative blade angle at the trailing edge is directly related to the compressor's technical work by Euler's turbomachinery equation (Eq. 2.87) as the circumferential component of the discharge velocity computes as $c_{\vartheta 2} = \frac{c_{m2}}{\tan\beta_2}$. This makes the angle β_2 an important design parameter. The middle control point finally can be varied freely in both meridional and circumferential direction.

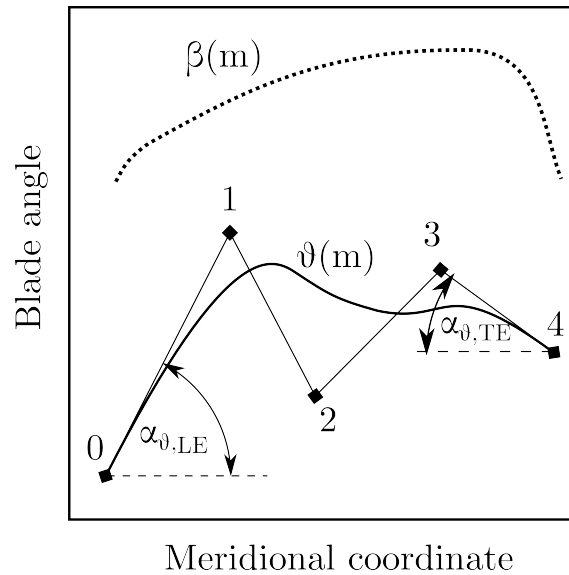


Figure 6.9: Parametrization of the circumferential blade angle distribution $\vartheta(m)$ and resulting relative blade angle distribution $\beta(m)$ (dotted).

The parameters which define the circumferential blade angle spline are summarized in Tab. 6.5.

Table 6.5: Parametrization of the circumferential blade angle spline.

Control point	Defined by	Parameters
0	Circumferential blade lean of leading edge	α_{Twist}
1	Relative blade angle at leading edge and meridional position	β_1, m_1
2	Meridional and circumferential position	ϑ_2, m_2
3	Relative blade angle at trailing edge and meridional position	β_2, m_3
4	Circumferential blade extent and circumferential blade lean at trailing edge	$\vartheta_{Blade}, \alpha_{Rake}$

While this parametrization concept integrates parameters of high fluid dynamic relevance like the relative blade angles at leading and trailing edge and design parameters with a strong influence on both fluid dynamic and structure mechanic performance (circumferential blade lean at trailing and leading edge, circumferential blade extent), the remaining free

parameters m_1 , m_2 , m_3 and ϑ_2 have proven to be problematic. When these parameters are varied independently, many parameter combinations can lead to circumferential blade angle curves which result in distributions of the relative blade angle with strong changes in gradient. While a relative blade angle distribution with strong changes in gradient can be beneficial in certain flow situations, it will cause flow separation in most cases, as the flow can not follow the blade. Therefore, an alternative approach has been developed. The free parameters m_1 , m_2 , m_3 and ϑ_2 are varied by an optimization algorithm which minimizes the curvature of the resulting relative blade angle distribution. This way, the resulting blades feature no strong changes in the gradient of the relative angle and will less likely cause flow separation. An additional advantage is the elimination of four free parameters for each circumferential blade angle distribution.

The points of the three dimensional blade in Cartesian coordinates are obtained according to Eq. 6.49. In this equation, the values of r and z are taken from the Bézier splines of the meridional contours and ϑ is obtained from the spline describing the circumferential blade angle, which is parametrized as stated above. Based on the resulting three dimensional blade contours at hub and shroud the blade is generated as a ruled surface. The final shape of the blade is obtained by applying a distribution of blade thickness to this surface. The blade thickness is given by the thickness at the hub point of the leading edge and two ratios describing the change of thickness in hub to shroud and leading to trailing edge direction.

$$\begin{pmatrix} x \\ y \\ z \end{pmatrix}_{Blade} = \begin{pmatrix} r \cdot \sin\phi \\ r \cdot \cos\phi \\ z \end{pmatrix} \quad (6.49)$$

The resulting parameters, which define the three dimensional shape of the blade, are given in Tab. 6.6.

Table 6.6: Parametrization of the blade.

Parameter	Description
$\beta_{1,Hub}$	Relative leading edge blade angle at hub
$\beta_{1,Shroud}$	Relative leading edge blade angle at shroud
β_2	Relative trailing edge blade angle at hub and shroud
α_{Twist}	Circumferential blade lean at leading edge
α_{Rake}	Circumferential blade lean at trailing edge
ϑ_{Blade}	Circumferential blade extent
$t_{LE,Hub}$	Blade thickness at leading edge hub point
$\nu_{t,Hub-Shroud}, \nu_{t,LE-TE}$	Blade thickness ratios

6.2.4 Definition of the Impeller Disc

The parametrization of the impeller disc is shown in Fig. 6.10. The shaft-hub connection is kept fixed, as this feature is prescribed by the structure mechanic design of the shaft and rotor-dynamic constraints. The general shape of the backside of the impeller disc is obtained by applying a disc thickness distribution t_{Disk} to the hub contour. The resulting contour is connected to the disc by a fillet defined by the radius $r_{Fillet,Disc}$. The transition between the blade and the impeller disc is carried out by another fillet.

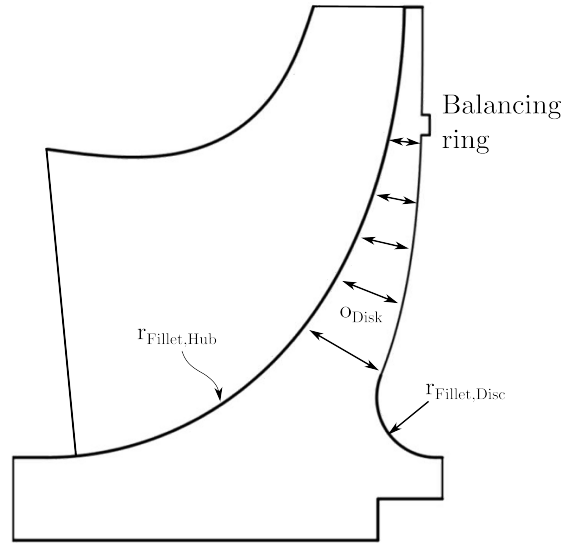


Figure 6.10: Parametrization of the impeller disc.

6.2.5 Overview of the Parametrization

A total of 27 parameters is used to parametrize the complete impeller. Table 6.7 gives an overview of the applied parametrization.

Table 6.7: Parametrization of the impeller.

Parameter	Description	Number of parameters
Meridional contours		
$D_{1,Hub}, D_{1,Shroud}$	Impeller inlet hub and shroud diameter	2
α_1, α_2	Meridional slope angle at inlet and outlet	2
κ_1, κ_2	Meridional curvature at inlet and outlet	2
L_1, L_2	Distance of the second and fourth control point from the inlet or outlet	2
o_2	Trailing edge blade height	1
$o(m)$	Blade height distribution	4
L_{ax}	Axial extent	1
Leading edge		
$\alpha_{LE,Hub}$	Angle defining the leading edge hub point	1
$\Delta\alpha_{LE,Shroud}$	Leading edge inclination	1
Blade shape		
$\beta_{1,Hub}, \beta_{1,Shroud}$	Leading edge relative blade angles	2
β_2	Trailing edge blade angle	1
$\alpha_{Twist}, \alpha_{Rake}$	Circumferential blade lean at leading and trailing edge	2
ϑ_{Blade}	Circumferential blade extent	1
$t_{LE,Hub}, \nu_{t,Hub-Shroud}, \nu_{t,LE-TE}$	Blade thickness	3
Impeller disc		
t_{Disc}	Disc thickness distribution	3
$r_{Fillet,Disc}$	Disc backside fillet radius	1
Further parameters		
$r_{Fillet,Hub}$	Blade hub fillet radius	1
z	Number of blades	1

6.3 One Dimensional Loss Modeling

The one dimensional model for computing the impeller's performance consists of three parts. At first, the performance of the ideal impeller is calculated by a mean line code. To obtain the performance of the real impeller, the losses are computed and applied onto the ideal impeller's performance. Finally, the speedline is computed by performing the mean line and loss calculations for different mass flow rates. The mass flow steps are controlled by an algorithm. Figure 6.11 illustrates the stations at which the thermodynamic conditions are computed.

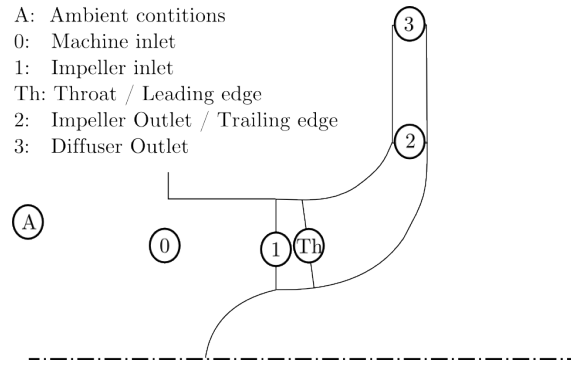


Figure 6.11: Side view of a single stage compressor with stations for mean line computation.

6.3.1 Consideration of Splitter Blades

Mean line based computation methods solve the fluid dynamic equations on the up- and downstream boundaries of the flow volume. Therefore, the following strategy is used to take splitter blades into account:

- The inducer and throat area is computed using the number of full blades z_{FB} .
- The discharge area is computed using the total number of blades $z_{FB} + z_{SB}$.
- All models used to compute the flow inside the blade channel use the effective number of blades $z_{Eff} = z_{FB} + \frac{L_{c,SB}}{L_{c,FB}} z_{SB}$ where $L_{c,i}$ marks the length of the mid-span camber line of the respective blade

If only full blades are used, z_{FB} is used for all computations.

6.3.2 Impeller Meanline Analysis

The first step of the impeller mean line analysis is the computation of the thermodynamic conditions at the impeller inlet from the idle conditions. This is accomplished by assuming a value for the meridional velocity at the impeller inlet and iterating over Eq. 6.50 to Eq. 6.58.

$$h_A = c_{p,A} \cdot T_A \quad (6.50)$$

$$\rho_A = \frac{p_A}{R \cdot T_A} \quad (6.51)$$

$$c_{m0} = \frac{\dot{m}}{\rho_A \cdot \pi/4 \cdot D_{0,Mid}^2} \quad (6.52)$$

$$\Delta p_{0-1} = \frac{L_{0-1}}{D_{0,Mid}} \cdot 4 \cdot c_f \cdot \frac{1}{2} \cdot \rho_A \cdot \left(\frac{1}{2} \cdot (c_{m1} + c_{m0}) \right)^2 \quad (6.53)$$

$$h_1 = h_0 + \frac{1}{2} \cdot (c_{m,1}^2 - c_{m,0}^2) \quad (6.54)$$

$$T_1 = \frac{h_1}{c_{p,1}} \quad (6.55)$$

$$p_1 = p_0 \cdot \left(\frac{T_1}{T_0} \right)^{\frac{\kappa}{\kappa-1}} - \Delta p_{0-1} \quad (6.56)$$

$$\rho_1 = \frac{p_1}{R \cdot T_1} \quad (6.57)$$

$$c_{m1} = \frac{\dot{m}}{\rho_1 \cdot A_1} \quad (6.58)$$

Based on the thermodynamic conditions at the impeller inlet, the values at the impeller throat can be computed. The throat is defined as the smallest area between the leading edge of one blade and the surface of the adjacent blade. Figure 6.12(a) shows the location of the throat area in the blade to blade plane at one span value. The throat area is of particular importance for the performance analysis as it plays an important role in the prediction of surge and choke and in the loss models. Therefore, an accurate determination is crucial for the performance analysis. This can be accomplished by calculating the throat width o_{Th} for many streamlines between hub and shroud. Then, the throat area can be computed as the sum of the products of throat width and the streamline distance. To achieve an acceptable accuracy, many streamlines and therefore a high computational expense is needed. In this work an alternative approach is used. For blades with constant curvature between hub and shroud, it is sufficient to use three streamlines at hub, mid span and shroud. Using these streamlines, the throat area can be defined by 8 points. The throat

surface is described by a 8-node serendipity planar element and it's area is determined by numerical integration along the non dimensional (ξ, η) coordinates (Fig. 6.12(b)). Any point on this surface can be computed according to

$$P = f(\xi, \eta) = \vec{N} \cdot \vec{P} \quad (6.59)$$

with the bi-quadratic shape functions \vec{N} and the vector of support points \vec{P} given by

$$\vec{N} = \begin{pmatrix} \frac{1}{4}(1-\xi)(1-\eta)(-\xi-\eta-1) \\ \frac{1}{2}(1-\xi^2)(1-\eta) \\ \frac{1}{4}(1+\xi)(1-\eta)\xi-\eta-1 \\ \frac{1}{2}(1-\xi)(1-\eta^2) \\ \frac{1}{2}(1+\xi)(1-\eta^2) \\ \frac{1}{4}(1-\xi)(1+\eta)(-\xi+\eta-1) \\ \frac{1}{2}(1-\xi^2)(1+\eta) \\ \frac{1}{4}(1+\xi)(1+\eta)(\xi+\eta-1) \end{pmatrix}, \quad \vec{P} = \begin{pmatrix} P_1 \\ P_2 \\ \vdots \\ P_8 \end{pmatrix} \quad (6.60)$$

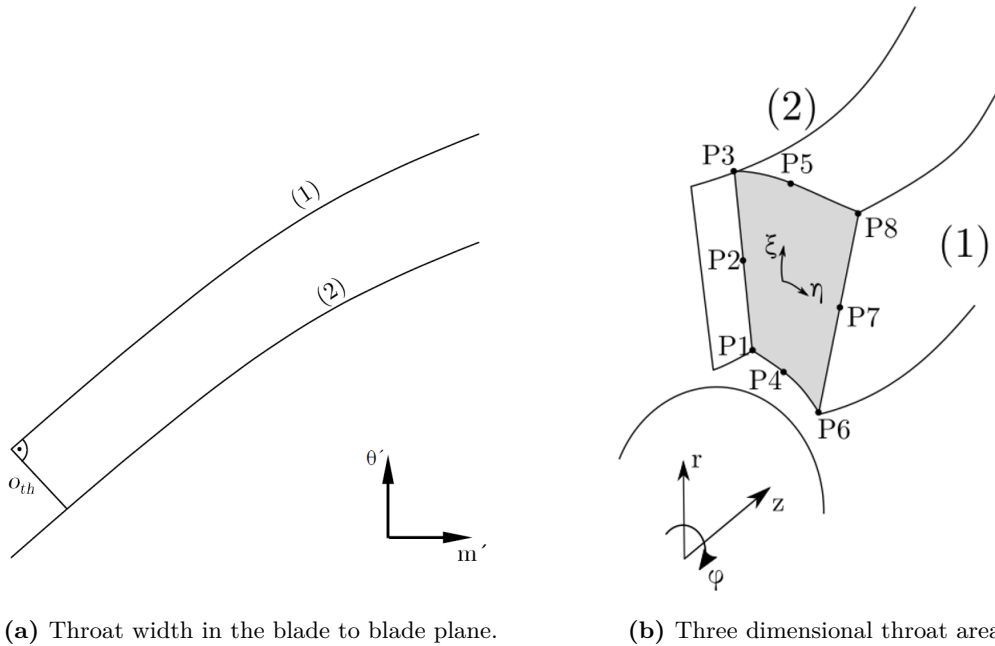


Figure 6.12: Definition of the throat width and throat area.

With the above formulation, any point on the throat area surface can be computed. The surface area is computed by subdividing the area into a finite number of arbitrary

quadrilaterals A_i whose area can be computed according to

$$A_i = \frac{1}{2} |(\vec{v}_i^3 - \vec{v}_i^1) \times (\vec{v}_i^4 - \vec{v}_i^2)| \quad (6.61)$$

where $\vec{v}_i^1 \dots \vec{v}_i^4$ are the position vectors of the vertices defining the i -th quadrilateral counted in counterclockwise direction starting from the bottom left corner. Finally, the throat area is determined by

$$\frac{A_{Th}}{z_{FB}} = \sum_{i=1}^{n_Q} A_i - A_{Blade} \quad (6.62)$$

where n_Q is the number of quadrilaterals and A_{Blade} is the area reduction caused by the blade thickness.

The thermodynamic conditions in the throat are computed by choosing a value for w_{Th} and iterating over Eq. 6.63 to Eq. 6.71.

$$h_{t,1} = h_0 + \frac{1}{2} \cdot c_{m0}^2 \quad (6.63)$$

$$R_{Th} = h_{t,1} - u_1 \cdot c_{\theta 1} \quad (6.64)$$

$$h_{t,rel,Th} = R_{Th} + \frac{1}{2} \cdot u_{Th}^2 \quad (6.65)$$

$$h_{Th} = h_{t,rel,Th} - \frac{1}{2} \cdot w_{Th}^2 \quad (6.66)$$

$$T_{Th} = T_0 + \frac{h_{Th} - h_0}{c_{p,0}} \quad (6.67)$$

$$p_{Th} = p_0 \cdot \left(\frac{T_{Th}}{T_0} \right)^{\frac{\kappa}{\kappa-1}} \quad (6.68)$$

$$\rho_{Th} = \frac{p_{Th}}{R \cdot T_{Th}} \quad (6.69)$$

$$cr_{Th} = \left(\frac{A_1 \cdot \sin(\beta_1)}{A_{Th}} \right)^{\frac{1}{2}} \quad (6.70)$$

$$w_{Th} = \frac{\dot{m}}{\rho_{Th} \cdot A_{Th} \cdot cr_{Th}} \quad (6.71)$$

The conditions at the impeller exit can be computed by choosing a value for ρ_2 and iterating over Eq. 6.72 to Eq. 6.77.

$$c_{m2} = \frac{\dot{m}}{\rho_2 \cdot A_2} \quad (6.72)$$

$$w_2 = \frac{c_{m2}}{\sin\beta_2} \quad (6.73)$$

$$h_2 = R_1 - \frac{1}{2} \cdot w_2^2 + \frac{1}{2} \cdot u_2^2 = h_{t,1} - \underbrace{u_1 \cdot c_{\theta 1}}_{=0} - \frac{1}{2} \cdot w_2^2 + \frac{1}{2} \cdot u_2^2 \quad (6.74)$$

$$T_2 = T_0 + \frac{h_2 - h_0}{c_{p,2}} \quad (6.75)$$

$$p_2 = p_0 \cdot \left(\frac{T_2}{T_0} \right)^{\frac{\kappa}{\kappa-1}} \quad (6.76)$$

$$\rho_2 = \frac{p_2}{R \cdot T_2} \quad (6.77)$$

The flow in the vaneless diffuser is computed by dividing the diffuser into n elements in radial direction and iterating over Eq. 6.78 to Eq. 6.84 for each element. The pressure in every element is computed by subtracting a pressure loss Δp_i from the pressure of the previous element p_{i-1} (equation 6.81). The computation of Δp_i is described later on.

$$\delta = \left(1 - \frac{rc_{\theta}}{(rc_{\theta})_{BL}} \right) \cdot 4.5 \cdot o_{Diffuser} \quad (6.78)$$

$$B = \frac{\delta}{8 \cdot o_{Diffuser}} \quad (6.79)$$

$$c_m = \frac{\dot{m}}{2 \cdot \pi \cdot R \cdot \rho \cdot O_{Diffuser} \cdot (1 - B)} \quad (6.80)$$

$$p_i = p_{i-1} - \Delta p_i \quad (6.81)$$

$$c = (c_m^2 + c_{\vartheta}^2)^{\frac{1}{2}} \quad (6.82)$$

$$T = \frac{1}{c_p} \cdot \left(h_{t,2} - \frac{1}{2} \cdot c^2 \right) \quad (6.83)$$

$$\rho = \frac{p}{R \cdot T} \quad (6.84)$$

With this simple set of basic equations all thermodynamic conditions for the ideal impeller are known.

6.3.3 Computation of Losses

In this section all applied loss models are described. The loss model correlation parameters λ_i are added to be used later on for the calibration of the models. Unless otherwise stated, all equations in this chapter are taken from [Aug00].

Impeller work coefficient

The maximum amount of mechanical energy to be transferred from the rotating blades to the fluid is described by Euler's turbine equation (2.86). However, this can only be accomplished by an impeller with an infinite number of infinitesimally thin blades. The amount of energy transferred to the fluid by a real impeller can be computed by the impeller work input coefficient I given in Eq. 6.85.

$$I = I_B + I_R \quad (6.85)$$

The impeller work input coefficient consists of the blade work input coefficient I_B and the recirculation work input coefficient I_R . The blade work input coefficient is given by Eq. 6.86.

$$I_B = \lambda_{Sigma} \cdot \sigma \cdot \left(1 - DF \cdot \varphi_2 \cdot \cot \beta_2 - \frac{u_1 \cdot c_{\vartheta 1}}{u_2^2} \right) \quad (6.86)$$

This equation depends on the slip factor σ , the distortion factor DF and the tip flow

coefficient φ_2 . The tip flow coefficient is given by Eq. 6.87.

$$\varphi_2 = \frac{\dot{m}}{\rho_2 \cdot A_2 \cdot u_2} \quad (6.87)$$

The slip factor is computed by a model presented by [Aug95] which combines the Busemann and Wiesner models to a more accurate model. The slip factor model is given by Eq. 6.88 to Eq. 6.91.

$$\sigma = \begin{cases} \sigma_{Wiesner} = 1 - \frac{\sqrt{\sin\beta_2}}{z^{0.7}} & , \varepsilon \leq \varepsilon_{Limit} \\ \sigma_{Augnier} = \sigma_{Wiesner} \cdot \left[1 - \left(\frac{\varepsilon - \varepsilon_{Limit}}{1 - \varepsilon_{Limit}} \right)^{\sqrt{0.1 \cdot \beta_2}} \right] & , \varepsilon > \varepsilon_{Limit} \end{cases} \quad (6.88)$$

$$\varepsilon_{Limit} = \frac{\sigma_{Wiesner} - \sigma^*}{1 - \sigma^*} \quad (6.89)$$

$$\sigma^* = \sin(19^\circ + 0.2\beta_2) \quad (6.90)$$

$$\varepsilon = \frac{D_1}{D_2} \quad (6.91)$$

The impeller distortion factor can be computed using Eq. 6.92 to Eq. 6.96.

$$DF = \frac{1}{1 - B_2} \quad (6.92)$$

$$B_2 = \bar{\omega}_{SF} \cdot \frac{p_1}{p_2} \cdot \sqrt{\frac{w_1 D_h}{w_2 o_2}} + \left[0.3 + \frac{o_2^2}{L_{Blade}^2} \right] \cdot A_R^2 \cdot \frac{\rho_2}{\rho_1} \cdot \frac{o_2}{L_B} \quad (6.93)$$

$$\bar{\omega}_{SF} = 4 \cdot c_f \cdot \left(\frac{w_{mean}}{w_1} \right)^2 \cdot \frac{L_B}{D_h} \quad (6.94)$$

$$D_h = 4 \cdot \frac{A_{Th} + A_2 \cdot \sin\beta_2}{P_{Th} + P_2} \quad (6.95)$$

$$A_R = \frac{A_2 \cdot \sin\beta_2}{A_{Th}} \quad (6.96)$$

The recirculation work input coefficient is given in Eq. 6.97.

$$I_R = \max \left[\left(\frac{D_{eq}}{2} - 1 \right) \left(\frac{w_{2,u}}{c_{2,m}} - 2 \cot \beta_2 \right), 0 \right] \quad (6.97)$$

This model is based on the equivalent diffusion factor D_{eq} which was developed for axial compressors by [Lie59] and generalized to centrifugal and mixed flow compressors by [Aug95]. The equivalent diffusion factor is computed according to Eq. 6.98 to Eq. 6.100.

$$D_{eq} = \frac{w_{max}}{w_2} \quad (6.98)$$

$$w_{max} = \frac{1}{2} (w_1 + w_2 + \Delta w) \quad (6.99)$$

$$\Delta w = \frac{2\pi \cdot D_2 \cdot u_2 \cdot I_B}{z \cdot L_{Blade}} \quad (6.100)$$

The equivalent diffusion factor can furthermore be used to predict surge. For ($D_{eq} > D_{eq, Surge}$) surge can be expected.

With the impeller work input coefficient I , the real total enthalpy at the impeller exit can be computed according to Eq. 6.101.

$$h_{t,2,real} = h_{t,1} + I \cdot u_2^2 \quad (6.101)$$

Impeller losses

Losses in the impeller are described by the impeller loss coefficient $\bar{\omega}$ (Eq. 6.102), which is the sum of all individual losses in the impeller. The individual losses are described in the following.

$$\bar{\omega} = \bar{\omega}_{Diff} + \bar{\omega}_{Ch} + \bar{\omega}_{SF} + \bar{\omega}_{BL} + \bar{\omega}_{HS} + \bar{\omega}_{Dist} + \bar{\omega}_{Mix} + \bar{\omega}_{Cr} \quad (6.102)$$

Incidence losses at the impeller entrance occur when the incoming flow is not perfectly matched by the leading edge blade angle, as well as due to the abrupt flow area contraction by the impeller blade's thickness. An incidence loss ($\bar{\omega}_{inc}$) (Eq. 6.103) is applied at the inner, mean and outer streamline, whereby the incidence loss for the mean streamline is weighted 10 times higher than for the inner and outer streamlines.

$$\bar{\omega}_{inc} = \lambda_{inc}^j \cdot \left[\left(1 - \frac{c_{1,m}^j}{w_1^j \cdot \sin \beta_1^j} \right)^2 + \left(\frac{z \cdot s_1^j}{\pi \cdot D_1^j \sin \beta_1^j} \right)^2 \right], j = i, m, o \quad (6.103)$$

A second and in many cases more significant entrance loss is caused by flow diffusion

between the leading edge and the throat. This occurs especially for lower flow rates due to inducer stall or even stage surge. A criterion for the beginning of this instable operation range is given by $w_1^0/w_{Th} \geq 1.75$. The diffusion loss coefficient is computed according to Eq. 6.104.

$$\bar{\omega}_{Diff} = \begin{cases} \max\left(\lambda_{Diff1} \cdot \left(1 - \frac{w_{Th}}{w_1}\right)^2 - \bar{\omega}_{inc}, 0\right) & , \frac{w_1^0}{w_{Th}} < 1.75 \\ \left(\frac{w_1^0 - \lambda_{Diff2} \cdot w_{Th}}{w_1}\right)^2 - \bar{\omega}_{inc} & , \frac{w_1^0}{w_{Th}} \geq 1.75 \end{cases} \quad (6.104)$$

At high mass flow rates, a choking loss can occur due to supersonic flow in the impeller. The choking parameter X determines if choke is occurring. It is calculated by Eq. 6.105.

$$X = 11 - 10 \cdot cr_{Th} \frac{A_{Th}}{A_{Ma}} \quad (6.105)$$

A_{Ma} is the area for which a supersonic flow occurs in the throat. The choking loss $\bar{\omega}_{Ch}$ can be computed according to Eq. 6.106.

$$\bar{\omega}_{Ch} = \begin{cases} 0 & , X \leq 0 \\ \frac{1}{2} (\lambda_{Ch} \cdot X - X^7) & , X > 0 \end{cases} \quad (6.106)$$

A further source of losses are pressure gradients in the blade to blade and hub to shroud directions. These are accounted by the loss coefficients $\bar{\omega}_{BL}$ and $\bar{\omega}_{HS}$ (Eq. 6.107 and Eq. 6.108).

$$\bar{\omega}_{BL} = \lambda_{BL} \cdot \frac{\Delta w^2}{w_1} \quad (6.107)$$

$$\bar{\omega}_{HS} = \lambda_{HS} \cdot \frac{\bar{\kappa}_{1,m} \cdot \frac{1}{2} (o_1 + o_2) \cdot \frac{1}{2} (w_1 + w_2)^2}{w_1} \quad (6.108)$$

When the distorted flow mixes with the free stream flow behind the impeller tip, a loss can be expected. This is modeled by the distortion loss coefficient $\bar{\omega}_{Dist}$, which depends on the distortion factor DF . This loss model is similar to the abrupt expansion loss by Benedict in [Ben66]. The distortion loss is given in Eq. 6.109.

$$\bar{\omega}_{Dist} = \left[(DF - 1) \frac{c_{m2}}{w_1} \right]^2 \quad (6.109)$$

The mixing of high energy fluid with low energy fluid is another source of losses. These losses are accounted by the wake mixing loss coefficient $\bar{\omega}_{Mix}$ (Eq. 6.110 to Eq. 6.113).

$$\bar{\omega}_{Mix} = \left(\frac{c_{m,Wake} - c_{m,Mix}}{w_1} \right)^2 \quad (6.110)$$

$$c_{m,Wake} = \sqrt{w_{Separation}^2 - w_u^2} \quad (6.111)$$

$$c_{m,Mix} = \frac{c_{m2} \cdot A_2}{\pi \cdot D_2 \cdot o_2} \quad (6.112)$$

$$w_{Separation} = \begin{cases} w_2 & , D_{eq} \leq D_{eq, Surge} \\ \frac{1}{2} w_2 \cdot D_{eq} & , D_{eq} > D_{eq, Surge} \end{cases} \quad (6.113)$$

Supersonic blade suction surface velocities cause shocks, boundary layer separation and therefore losses. These losses are modeled by the supercritical Mach number loss \bar{w}_{CR} (Eq. 6.114). The Mach numbers in Eq. 6.114 are calculated using the relative velocity w .

$$\bar{w}_{CR} = \lambda_{CR} \cdot \left((Ma_1 - Ma_{CR}) \frac{w_{max}}{w_1} \right)^2 \quad (6.114)$$

The global loss coefficient \bar{w} is used to compute the real total pressure rise in the impeller according to Eq. 6.115.

$$p_{t,2,real} = p_{t,2} - \frac{\rho_{t,2} \cdot T_{t,2}}{\rho_{t,1} \cdot T_{t,1}} \cdot (p_{t,1} - p_0) \cdot \bar{w} \quad (6.115)$$

Diffuser losses

The pressure loss in the diffuser is described by Eq. 6.116. This equation is based on conventional mean streamline analysis ([Joh66]) and was extended by [Aug00] by the two loss terms at the end of the right hand side.

$$\frac{1}{\rho} \frac{dp}{dm} = \frac{c_{\theta}^2 \cdot \sin(\alpha_{Diffuser})}{R} - c_m \cdot \frac{dc_m}{dm} - \frac{c \cdot c_m \cdot c_f}{O_{Diffuser}} - \frac{dI_D}{dm} - I_C \quad (6.116)$$

The diffusion loss is computed solving Eq. 6.116 numerically. This is accomplished by using the subdivision of the diffuser described in the previous section and solving Eq. 6.117 to Eq. 6.124 for each element. The subscript ‘‘upstream’’ in Eq. 6.119 is used to address the previous element.

$$I_D = \begin{cases} I_{D1}, & I_{D1} \geq I_{D2} \\ I_{D2}, & I_{D1} < I_{D2} \end{cases} \quad (6.117)$$

$$\frac{dI_D}{dm} = -2 \cdot (p_t - p) (1 - E) \cdot \frac{1}{\rho \cdot c} \frac{dc}{dm} \quad (6.118)$$

$$I_{D1} = \frac{dI_D}{dm} \cdot dm + I_{D1,upstream} \quad (6.119)$$

$$E = \begin{cases} 1 & , D \leq 0 \\ 1 - \lambda_{E1} \cdot \left(\frac{D}{D_{max}}\right)^2 & , 0 < D < D_{max} \\ \lambda_{E2} \cdot \sqrt{\frac{D}{D_{max}}} & , D \geq D_{max} \end{cases} \quad (6.120)$$

$$D = -\frac{o}{c} \frac{dc}{dm} \quad (6.121)$$

$$D_{max} = \lambda_{Dmax} \cdot \left(\frac{o}{L}\right)^{0.35} \frac{c_m}{c} \quad (6.122)$$

$$I_{D2} = \lambda_{ID2} \frac{p_t - p}{\rho} \left(1 - \frac{(rb)_{max}}{rb}\right) \quad (6.123)$$

$$(rb)_{max} = (rb) \left(1 + \lambda_{rbmax} \frac{m}{b}\right) \quad (6.124)$$

The term I_C describes a curvature loss. As this work uses only straight diffusers, this term can be neglected.

6.3.4 Characteristic Prediction

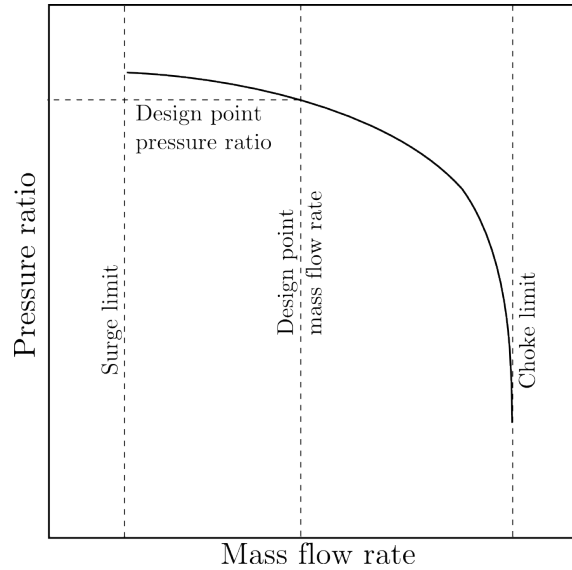


Figure 6.13: Schematic illustration of a compressor characteristic.

Figure 6.13 shows a schematic speedline. The characteristic is limited towards low mass flow rates by the surge limit. For low mass flow rates the delivery pressure of the compressor drops and reversed flow from the downstream components occurs. In the direction of high mass flow rates the characteristic is limited by the choke limit. Choke occurs at high mass flow rates when the Mach number of the relative inlet velocity of the impeller throat reaches unity over the whole flow area. Both phenomena are connected with highly unsteady flow conditions and severe machine vibrations. Therefore, the operation point of the compressor should always be chosen within a save margin from the stability limits. The computation of the compressor characteristic starts by calculating the impeller performance for a low mass flow rate in the surge region ($D_{eq} > D_{eq, Surge}$). Then, the mass flow is incrementally increased until a first non-surge point is found. The real surge mass flow is determined by linearly interpolating the mass flow value for $D_{eq} = D_{eq, Surge}$ between the last two points. The further points towards the choke limit are computed by using an adaptive mass flow increment (Eq. 6.125) based on the choke criterion (Eq. 6.126).

$$\dot{m}_{inc} = \min((C_{Choke} - 0.99) \cdot 1.5, 1) \cdot \dot{m} \quad (6.125)$$

$$C_{Choke} = cr_{Th} \frac{A_{Th}}{A_{Ma}} \quad (6.126)$$

A_{Ma} is the area for which supersonic flow occurs in the impeller throat. The above formulation allows a fine step size concerning mass flow rate towards choke. The choke limit is reached when the choke criterion exceeds unity.

6.3.5 Model Calibration

The previously presented loss models depend strongly on empirical correlations. Values for the parameters of these correlations can be found in literature [Aug00]. Using these parameter values, a reliable prediction of the operation characteristic of modern compressor impellers is not possible (Fig. 6.14). Therefore, it is crucial to adjust these models by finding the right parameters for a reliable prediction. The fitting of the parameters of an arbitrary model to existing data can be accomplished in different ways. If the model is of low complexity, it can be calibrated by manually changing the model parameters until the model's predictions meet the data. This method can be applied as long as the model features only few parameters and there are no strong cross interactions between the model's parameters. For models of high complexity, more sophisticated methods of parameter identification have to be used. A commonly used practice is the use of automated optimization algorithms to calibrate the parameters of the model. The optimization algorithm varies the model's parameters and minimizes the difference between the model's predictions and the existing data.

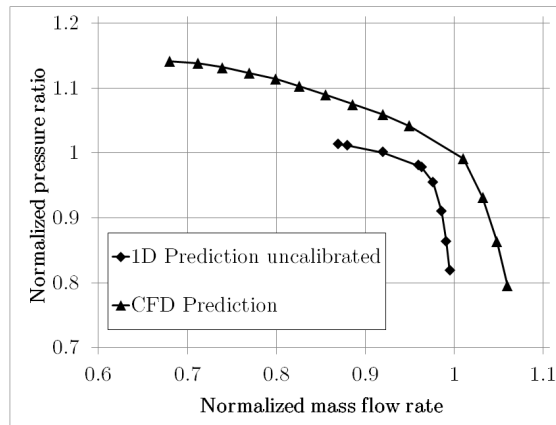


Figure 6.14: Comparison of an operation characteristic predicted by one dimensional loss model and three dimensional CFD computations.

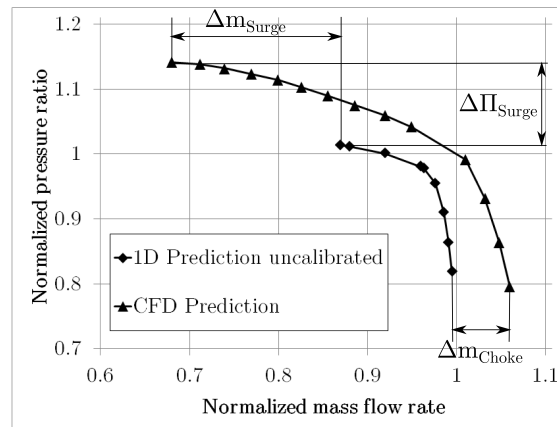
The loss models are calibrated using data available from numerous CFD studies conducted in the past. The calibration is carried out by a multicriterial evolutionary optimization algorithm offered by the software optiSLang version 6. The optimization algorithm minimizes the deviation between the speedline computed by one the dimensional loss model and by three dimensional CFD calculations by varying the loss model correlation coefficients λ_i . Table 6.8 lists the used coefficients. The following sections describe the calibration workflow.

Table 6.8: List of loss model parameters.

Loss model	Coefficients	Equations
Leading edge incidence	λ_{inc}^j	Eq. 6.103
Leading edge flow separation	$\lambda_{Diff1}, \lambda_{Diff2}$	Eq. 6.104
Impeller aerodynamic blockage	$\lambda_{Ch}, \lambda_{Cr}$	Eq. 6.106, Eq. 6.114
Impeller blade loading	λ_{BL}	Eq. 6.107
Impeller flow distortion	λ_{HS}	Eq. 6.108
Slip	λ_{Sigma}	Eq. 6.86
Diffuser diffusion losses	$\lambda_{E1}, \lambda_{E2}, \lambda_{Dmax}, \lambda_{ID2}, \lambda_{rbmax}$	Eq. 6.120, Eq. 6.122 , Eq. 6.123 , Eq. 6.124

6.3.5.1 Problem Definition

Characteristics of centrifugal compressors always have a similar shape. Therefore, it is not necessary to compare the characteristics in each point. In the course of this research, several different approaches to compare the speedlines predicted by loss models and CFD have been tested. Figure 6.15 shows the set of target values which has shown to deliver the best results and therefore was chosen for all further calculations. This set consists of the difference in mass flow rate near the choke limit $\Delta\dot{m}_{Choke}$, the difference in mass flow rate at the surge limit $\Delta\dot{m}_{Surge}$ and the difference in pressure ratio at the surge limit $\Delta\Pi_{Surge}$. For the last quantity, an average pressure ratio near the surge limit is used.

**Figure 6.15:** Definition of the target values for the loss model calibration.

6.3.5.2 Methodology

One dimensional loss model computations are fast compared to full three dimensional CFD calculations. Still, a loss model calculation of a complete characteristic takes 30 seconds on average for one design¹. Computing the deviations for all designs in the CFD dataset would take over one hour for each optimization step and thus would be highly inefficient. Therefore, a method for a fast and reliable testing of the loss model coefficients was developed. Below the tested methods are listed.

1 fixed design

The first tests were run by using a single geometric design to calibrate the loss model coefficients. While a fast convergence of the optimization algorithm and a good agreement between 1d and CFD prediction could be achieved, the resulting coefficients were only valid for very small geometric variations.

10 fixed designs

The first approach was improved by using 10 fixed designs in each optimization step. The mean deviations for all 10 designs were used as the objective functions for the optimization algorithm. This slightly increased the numeric expense but still offered a fast solution. However, the resulting coefficients still could not be used reliably for the whole geometric parameter space.

10, 20, and 40 random designs

Based on the findings of the previous attempts, a novel strategy was proposed. For each optimization step a set of designs was randomly chosen and the mean deviations were used as objective functions for the optimization algorithm. This approach was tested for 10, 20 and 40 randomly chosen designs. Using 40 randomly chosen designs finally delivered sufficiently exact results for the whole geometric parameter space, which could be obtained at a reasonable numerical expense.

Assessment of potential optima

An optimization with $n_{Obj} > 1$ competing objective functions yields not one best solution but a hyperplane of dimensionality n_{Obj} containing possible compromise solutions. This hyperplane is called pareto front. As no solution is perfect in all objective functions, the solution offering the best compromise for the given problem has to be chosen. Figure 6.16 shows the pareto front of one optimization run.

¹ Intel Core-i7-3840M quad core.

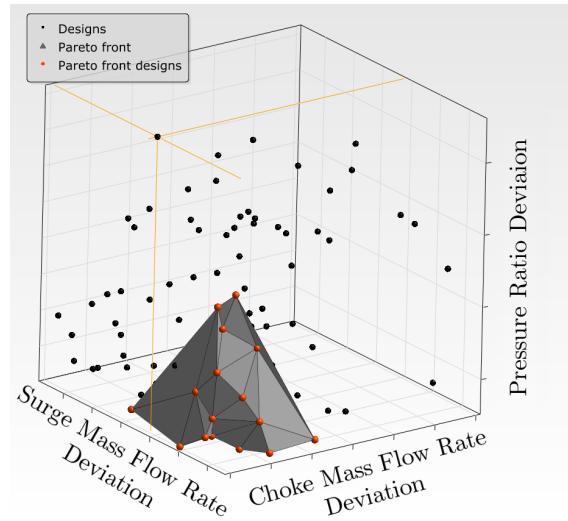


Figure 6.16: Pareto front for one optimization run.

The quality of each possible optimum on the pareto front is assessed by using this combination of loss model coefficients to compute the characteristics of all geometric designs in the CFD dataset. The optimum is then rated by calculating the sigma level for each deviation in respect to a maximum allowed deviation. The definition of the sigma level is given in Fig. 6.17 by the example of the surge mass flow rate deviation. The red line marks the maximum allowed deviation.

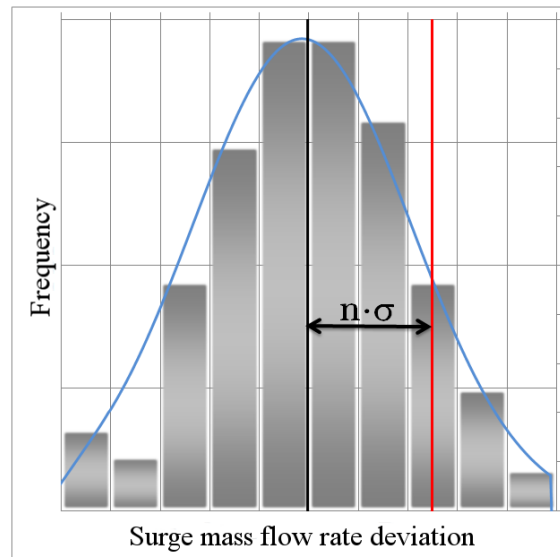


Figure 6.17: Definition of the sigma level for the rating of optima on the pareto front.

6.3.5.3 Optimization

The optimization was carried out using a global search evolutionary optimization algorithm implemented in optiSLang (see section 2.7.1). The settings of the optimization algorithm are given by Tab. 6.9. An optimization run was considered successful, if it converges towards an optimum before the maximum number of generations is reached.

Table 6.9: Settings of the evolutionary optimization algorithm.

Parameter	Value
Start population size	10
Maximum number of generations	60
Stop after generation of stagnation	20
Selection scheme	Pareto ranking, Tournament selection
Crossover method	Multipoint
Mutation scheme	Self addaptive

The optimization is subject to several objective functions and constraints. These are listed in Tab. 6.10. The optimization features two constraints. Firstly, the surge mass flow rate predicted by the loss model may not differ from the CFD prediction for more than 2.5% of the design mass flow rate. Secondly, no failed 1d calculations are tolerated for the randomly chosen geometric designs. These constraints are based on the following assumption: If any of the randomly chosen designs fails to meet these criteria, it is very likely that there will be several failing designs in whole set.

Table 6.10: Settings of the evolutionary optimization algorithm.

Parameter	Name	Expression
Objective functions:		
Surge mass flow rate deviation	DiffSu	min(DiffSu)
Choke mass flow rate deviation	DiffCh	min(DiffCh)
Surge pressure ratio deviation	DiffPI	min(DiffPI)
Constraints:		
Maximum allowed surge mass flow rate deviation	maxDiffSu	DiffSu<0.025
Number of failed characteristic computations	Failed	nFailed==0

6.3.5.4 Results

The calibration was carried out for two distinct classes of centrifugal compressor impellers, a mid-pressure impeller and a high-pressure impeller. In both cases, a set of 200 speedlines, evaluated by CFD computations, was available. The calibration results are presented below.

Calibration Results Mid-Pressure Impeller

The four most promising pareto-optimal results were chosen as possible optima. For each set of loss model coefficients the performance characteristics for all 200 geometric designs were predicted and compared to the CFD results. Table 6.11 lists the sigma levels for the individual deviations for each potential optimum. Furthermore, the values for the uncalibrated start design are given. Based on this data, the fourth result is chosen as the optimum.

Table 6.11: Sigma levels of the pareto-optimal designs and uncalibrated start design.

Pareto Optimum No.	Sigma Surge	Sigma Choke	Sigma PI
1	2.9	3.5	5
2	2.8	4	2.4
3	2.8	3.7	3.9
4	2.7	3.8	7
Uncalibrated	0	1.2	1.4

Figure 6.18 compares the operation characteristics of uncalibrated 1d, calibrated 1d and CFD calculations for two randomly chosen impeller geometries. Both results show good correspondence between the computation methods. Compared with the results for the uncalibrated loss models, a distinct improvement can be observed.

As the pure visual comparison of the predicted characteristics is not a reliable way to determine the quality of the optimum, histograms of each deviation were generated for the optimum and the uncalibrated model. Figure 6.19 shows distribution functions fitted to these histograms. For all deviations, a distinct shift towards a narrow distribution with a mean of zero can be observed. This further indicates the good prediction quality of the calibrated models.

These results show that the calibrated loss model is sufficiently exact to identify promising regions in the design space.

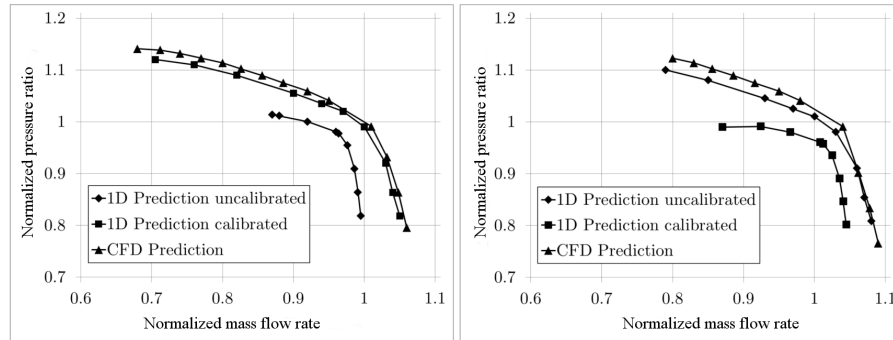


Figure 6.18: Comparison of one dimensional loss model and three dimensional CFD results for two arbitrary mid pressure impellers.

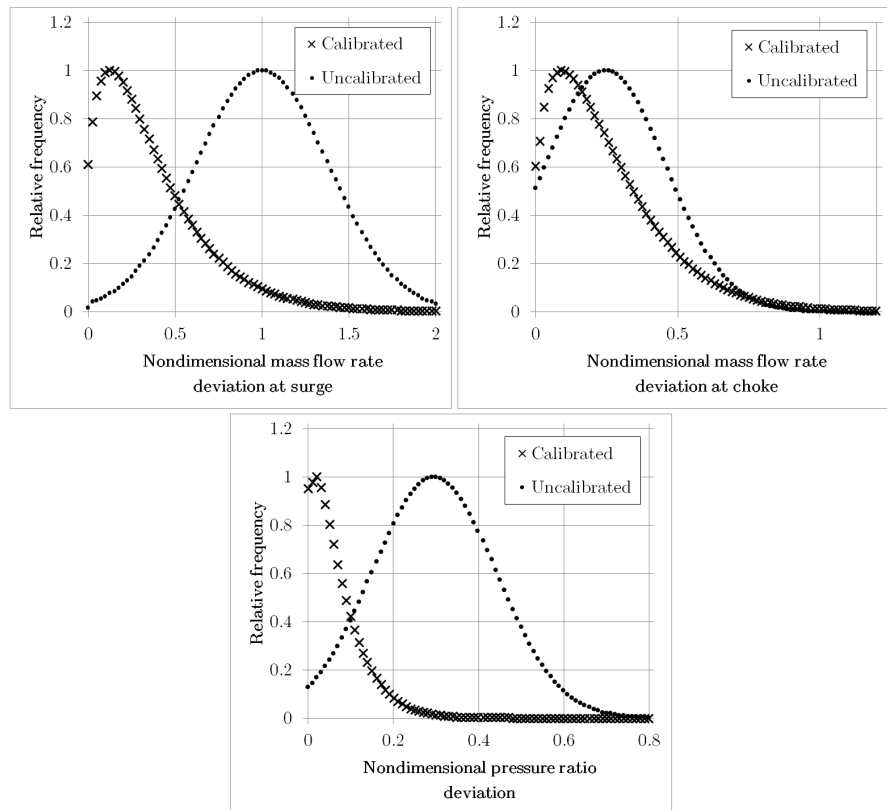


Figure 6.19: Distributions of the deviations between loss model and CFD prediction for the calibrated and the uncalibrated model (mid-pressure impeller).

Calibration Results High-Pressure Impeller

Analogous to the calibration of the loss models for the mid-pressure impeller, the four most promising pareto-optimal designs are chosen and rated based on the prediction quality for the complete CFD data set. Table 6.12 lists the sigma levels for the individual deviations for each potential optimum. Furthermore, the values for the uncalibrated start design are given. Based on this data, the second result is chosen as the optimum.

Table 6.12: Sigma levels of the pareto-optimal designs and uncalibrated start design.

Pareto Optimum No.	Sigma Surge	Sigma Choke	Sigma PI
1	2.3	3.3	3.7
2	3.1	2.7	3.7
3	2.7	2.7	3.6
4	2.7	2.0	3.77
Uncalibrated	1.7	0.1	2.0

Figure 6.20 shows the comparison of the operation characteristics between uncalibrated 1d, calibrated 1d and CFD calculations for two randomly chosen impeller geometries. Both results show good correspondence between the computational methods. Compared with the results for uncalibrated loss models, a distinct improvement can be observed.

As the pure visual comparison of the predicted characteristics is not a reliable way to determine the quality of the optimum, again histograms of each deviation were generated for the optimum and the uncalibrated model. Figure 6.21 shows distribution functions fitted to these histograms. For all deviations, a shift towards a narrow distribution with a mean of zero can be observed. This further indicates the increase in prediction quality achieved by the calibration of the models.

While the calibration results are not as good for the high pressure impeller as for the mid-pressure impeller, the the calibrated loss model can still be used to identify promising regions in the design space.

Possible reasons for the lower prediction quality are:

- This impeller operates in a performance range which is located at the boundaries of the range which Augnier recommends for the use of the loss models.
- The splitter blades, which show a strong influence on the impeller's performance, are taken into account only rudimentary.
- CFD computations of impellers in this performance range are difficult and include a certain amount of uncertainty due to convergence problems. Therefore, the reference data used for the calibration already includes uncertainty.

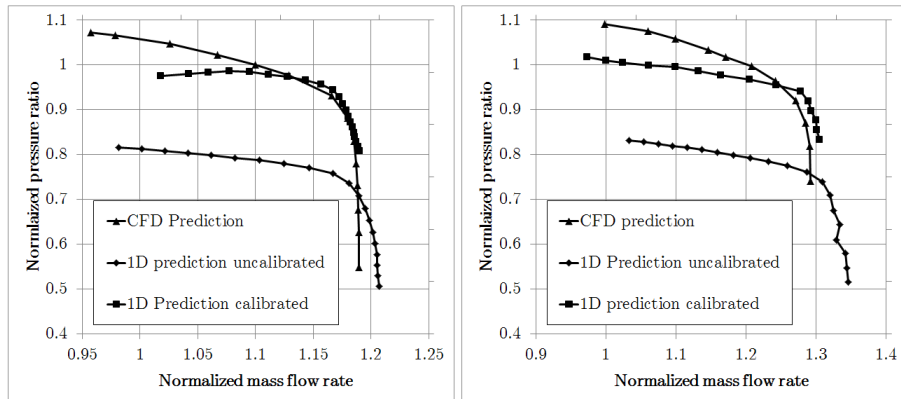


Figure 6.20: Comparison of one dimensional loss model and three dimensional CFD results for two arbitrary high pressure impellers.

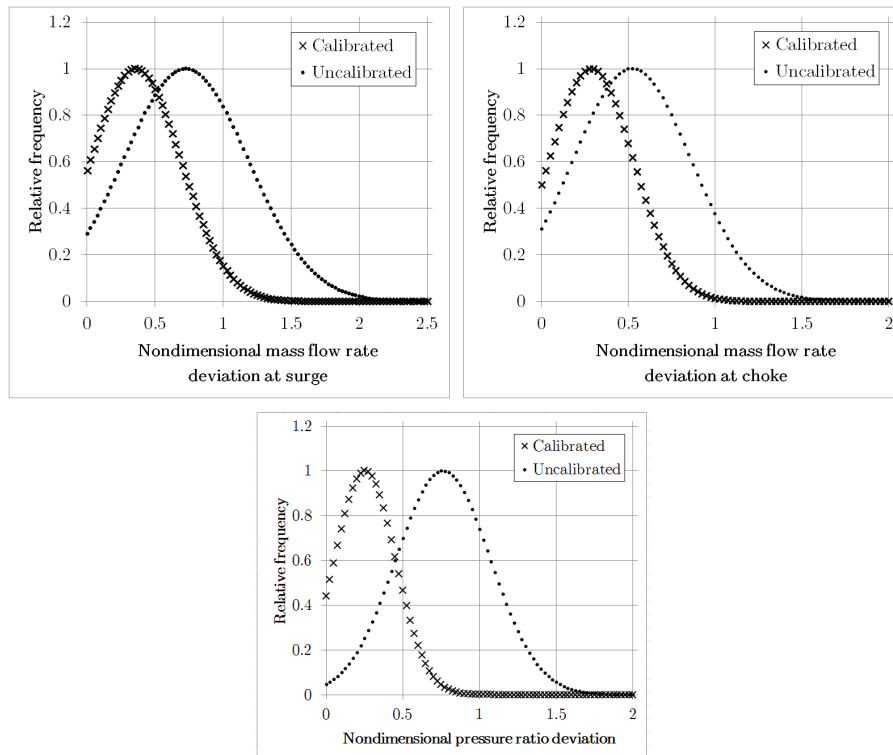


Figure 6.21: Distributions of the deviations between loss model and CFD prediction for the calibrated and the uncalibrated model (high pressure impeller).

6.4 Computational Fluid Dynamics Model

The CFD computations in this work were carried out in ANSYS CFX v.17.2. This section describes the applied computational workflow.

6.4.1 Grid Generation and Grid Independence

All grids for the CFD computations are generated in ANSYS TurboGrid. TurboGrid is an automated meshing application specialized on generating hexahedral CFD meshes of turbomachinery components. The meshes are based on predefined topologies which are adjusted to the respective geometric design. As the impeller features a rotational periodicity, only one blade-row has to be meshed. Figure 6.22 shows an example for a mesh of an impeller with splitter blades generated with TurboGrid.

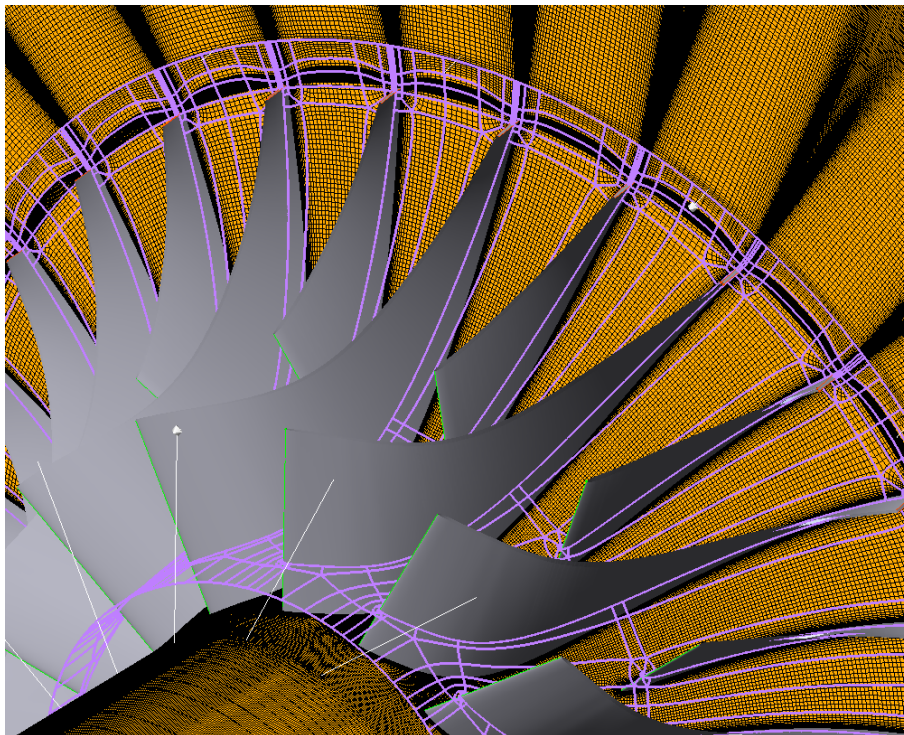
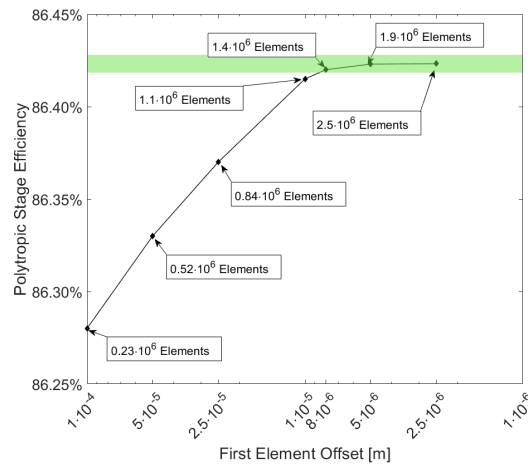


Figure 6.22: Mesh of an impeller with splitter blades in TurboGrid visualized on a surface of constant span (yellow). The mesh topology is visualized by purple lines.

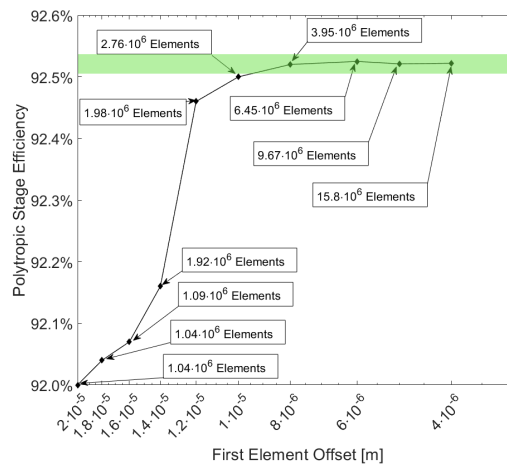
The mesh quality and size required for trustworthy CFD computations is determined by a mesh sensitivity test. The parameter used to define the different grids is the first element offset. This parameter is of particular importance as the wall resolution directly influences how well the near wall velocity gradient is depicted in the simulation. Therefore, the first element offset has a strong influence on the computation of the interactions between the impeller and the flow. After defining the first element offset, the remaining mesh parameters are set in a way which ensures a smooth transition of the element size in the whole computational domain. The results of the grid independence test are shown in Fig. 6.23. The choice of the first element offset is based on the deviation from the

efficiency computed by the largest of the examined grids. A bandwidth for a deviation of 0.5% is marked in the plots by a green area. Based on this, a grid with a first element offset of $8 \cdot 10^{-6}m$ consisting of $1.4 \cdot 10^6$ elements is chosen for the mid-pressure impeller while a grid with a first element offset of $7 \cdot 10^{-6}m$ consisting of $3.95 \cdot 10^6$ elements is chosen for the high-pressure impeller. As the high-pressure impeller features a splitter blade, one passage features two blades and a circumferential extent twice as big as for the mid-pressure impeller. Furthermore, the high-pressure impeller's outer diameter is bigger. Therefore, a significantly larger mesh is required to obtain mesh qualities comparable to the mid-pressure impeller.



(a) Mid-pressure impeller

Figure 6.23: Result of the mesh sensitivity test.



(b) High-pressure impeller

Figure 6.23: Result of the mesh sensitivity test (continued).

6.4.2 Boundary Conditions

Figure 6.24 gives an overview of the CFD boundary conditions. The simulations make use of the rotational periodicity by using only one sector with a circumferential extent of $\frac{2\pi}{\text{Number of blades}}$ to simulate the complete impeller. The simulation model consists of two stationary domains for the inlet and outlet, which are connected to the rotating impeller domain by frame change interfaces. Table 6.13 lists the details of the applied setup.

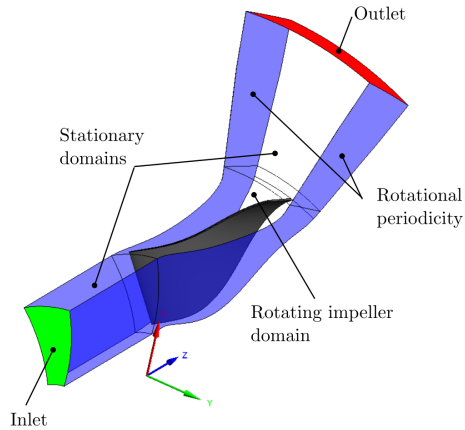


Figure 6.24: Overview of the CFD boundary conditions.

Table 6.13: CFD setup and boundary conditions.

Global settings	
Simulation type	Steady state
Material model	Air ideal gas
Turbulence model	SST
Inlet domain	
Frame type	Stationary
Inlet boundary	Total pressure (ambient)
Impeller domain	
Frame type	Rotating (nominal speed)
Outlet domain	
Frame type	Stationary
Outlet boundary	Static pressure or mass flow rate
Domain interfaces	
Inlet to impeller	Stage
Impeller to outlet	Stage

6.4.3 Characteristics Computation

The computation of the compressor's characteristic curve or speed line is a central aspect of the CFD workflow. The complete computation of an operation characteristic is a time consuming manual process, as each new design point has to be chosen carefully based on the previous points. Figure 6.25 shows a generic compressor characteristic. To compute the speedline, the first operation point is usually placed near the choke limit by using a pressure outlet boundary and a low outlet pressure ("1" in Fig. 6.25). From there, the pressure at the outlet is gradually increased for each new point "moving up" on the characteristic. Towards higher pressures and lower mass flow rates, the change in pressure between each point decreases and it can become difficult to obtain a constant step size in terms of mass flow by changing the pressure. Furthermore, it is possible that the pressure ratio starts to decrease near the surge limit which can not be computed by increasing the outlet pressure. At this point, the outlet boundary condition has to be changed to a mass flow type boundary ("2" in Fig. 6.25). Then, the last operation points towards the surge limit can be computed. Convergence is difficult of achieve towards the surge limit. If a new operation point does not converge ("3" in Fig. 6.25), the mass flow step size is lowered until a last converged point is found ("4" in Fig. 6.25). This point is considered as a fair prediction of the surge limit. As surge is a transient phenomenon which results from the interaction of all components of the whole system (compressor \leftrightarrow piping \leftrightarrow consumers), it cannot be predicted exactly by steady state simulations of just the compressor. Still, the surge limit obtained from this kind of simulations can be used in an optimization to identify parameter combinations which move the surge limit in one direction or the other.

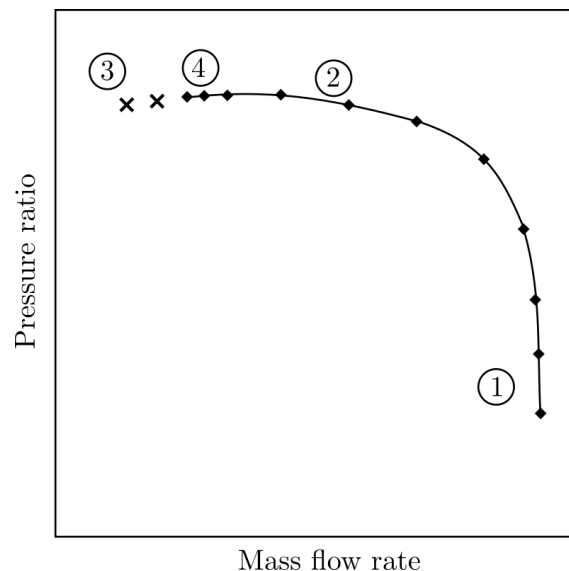


Figure 6.25: Principle of the computation of a speedline illustrated on a generic compressor characteristic ("1" - Start, "2" - Switch to mass flow outlet, "3" - Failed designs near surge, "4" - Approximated surge margin).

To evaluate a large number of operation characteristics in an optimization process, the computation strategy described above has to be automated. This is achieved by an

automation software which takes only the static outlet pressure of the first and second points in the choke area as an user input. From there, the software predicts the next operations point based on the previously computed points. This prediction is done by interpolating a spline through the previous operation points and extrapolating the next point from this spline. To prevent the spline from oscillating and thereby falsifying the prediction, it has proven beneficial to use no more than three points for the interpolation. For each predicted point, the software checks the gradient of pressure ratio over mass flow rate. If this gradient drops below a certain threshold, the outlet boundary condition is switched from a pressure type to a mass flow type for the further calculations. Towards the surge limit, the software automatically decreases the step size if a simulation does not converge and iteratively finds an estimation of the surge point. Typically, a complete operation characteristic consists of 8 to 15 operation points.

The convergence of each operation point is controlled by different means. First of all, the global residuals of the governing equations for impulse, energy, continuity and turbulence are monitored. A more sophisticated statement about the convergence of a CFD calculation can be given by looking at the most significant output quantities for the particular case. For a compressor impeller these are the velocities, temperatures, pressures and flow rates at the inlet and outlet as well as the polytropic efficiency. These quantities and their standard deviations are monitored at each operation point and are used to decide if a calculation has reached convergence. In this manner it can be assured that all CFD calculations have converged without manual interaction.

6.4.4 Post Processing

The operation characteristic of one design consists of an arbitrary number of operation points. This curve has to be represented by scalar variables which can then be used as objectives or constraints in an optimization workflow. Available values to rate the operation characteristic are the global maximum polytropic efficiency $\eta_{pol,max}$, the efficiency in the design point $\eta_{pol,DP} = \eta_{pol}(\dot{m} = \dot{m}_{DP})$, the pressure ratio in the design point $\Pi_{DP} = \Pi(\dot{m} = \dot{m}_{DP})$ and the mass flow rates at the surge and choke margins (\dot{m}_{Surge} and \dot{m}_{Choke}). In addition to these quantities, further coefficients can be developed. A first approach is to look at the areas below the pressure ratio respectively efficiency curves. These are computed according to Eq. 6.127 and Eq. 6.128. The values of λ_{Π} and λ_{η} rate the extent of the characteristic in both mass flow rate and pressure ratio respectively efficiency direction. A drawback of this approach is the missing relation to the desired design point for which the impeller is optimized. Therefore, an impeller with a wide operation range and a high pressure ratio / efficiency receives a high rating even if its operation characteristic does not include the desired operation point.

$$\lambda_{\Pi} = \frac{1}{\dot{m}_{Choke}} \int_{\dot{m}_{Surge}}^{\dot{m}_{Choke}} \frac{\Pi(\dot{m})}{\Pi_{max}} d\dot{m} \quad (6.127)$$

$$\lambda_{\eta} = \frac{1}{\dot{m}_{Choke}} \int_{\dot{m}_{Surge}}^{\dot{m}_{Choke}} \frac{\eta(\dot{m})}{\eta_{max}} d\dot{m} \quad (6.128)$$

Figure 6.26 shows three arbitrary characteristic curves which are rated by a characteristic number λ_{DP} (Eq. 6.129). A characteristic curve which includes the operation point receives a rating of $\lambda_{DP} = 1$. λ_{DP} is computed by applying a Gaussian centered at the design point to all points of the characteristic curve both in mass flow rate and pressure ratio direction (these Gaussians are depicted as dashed lines in Fig. 6.26). The resulting values are summed up and normalized by the maximum possible value which can be achieved for the given design point.

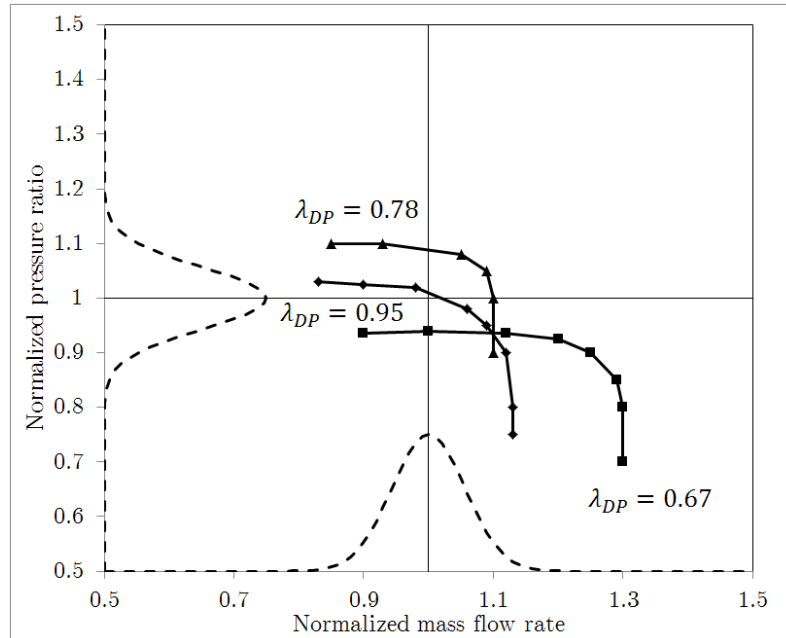


Figure 6.26: Rating of the operation characteristic in terms of the design point.

$$\lambda_{DP} = \frac{\sum_{i=1}^{N_{OP}} e^{-\frac{(\dot{m}_i - \dot{m}_{DP})^2}{2\sigma_m^2}} + \sum_{i=1}^{N_{OP}} e^{-\frac{(\Pi_i - \Pi_{DP})^2}{2\sigma_{\Pi}^2}}}{\lambda_{DP,max}} \quad (6.129)$$

6.5 Finite Elements Modeling

The FEA computations in this work were carried out in ANSYS v.17.2. This section describes the applied computational workflow.

6.5.1 Boundary Conditions

Figure 6.27 shows the simulation model and the applied boundary conditions. The complete impeller is depicted by a sector model which makes use of the rotational periodicity to reduce the amount of grid cells. The simulations are carried out as steady state simulations consisting of a single loadstep using a linear elastic material formulation. As the loads resulting from fluid pressure are negligibly small when compared to the loads resulting from centrifugal force, the impeller is solely loaded by a rotational velocity. The model is constrained by the rotational periodicity and a fixed displacement in axial and tangential direction of a single node at the shaft-hub connection. This way, the impeller can be deformed freely by the centrifugal force while rigid body movement is prevented. An overview of the FEA boundary conditions is given in Tab. 6.14.

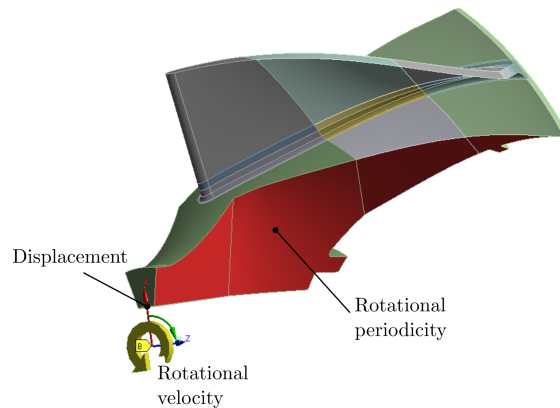


Figure 6.27: Boundary conditions for the FEA computations.

Table 6.14: FEA setup and boundary conditions.

Global settings	
Simulation type	Steady state
Number of load steps	1
Material model	Linear elastic
Constraints	
Rotational periodicity	
Nodal displacement at shaft	Axial and tangentially fixed, radial free
Loads	
Rotational velocity	

6.5.2 Post Processing

Past research activities like Boecker [Böc09], Rybacki [Ryb11] or Zangeneh [Zan14] have shown that the location of the maximum stress can change drastically for different compressor designs. This can lead to bad prediction qualities, if metamodeling approaches are applied to analyze the stresses, as the maximum stress can not be related to certain geometric features. Therefore, alternative approaches for rating the mechanical loading solely by the maximum stress value have to be found.

A first approach to analyze the stresses in a more local form is the partitioning of the impeller volume. Then, the stresses can be evaluated on the individual sub-volumes. An example for the subdivision of the impeller volume is shown in Fig. 6.27. This approach was tested by Senge [Sen15]. Senge showed that the prediction of the stresses by a metamodel is problematic due to the grave deviations between the FEA and metamodel predictions. The evaluation of the stresses on sub-volumes does not increase prediction quality significantly. One possible explanation for this behavior is the large bandwidth of stresses which are computed when the geometry parameters are changed in large bounds. In many cases the stress levels lie outside the linear elastic regime. Therefore, the applied material model is not able to depict the existing physics. The use of a higher quality, non-linear material model was not considered for two main reasons: firstly plastic deformations are not allowed in an impeller design and secondly the computational expense would drastically increase. Therefore, an alternative approach has to be found.

This alternative approach is the analysis of the elastic strain energy (Eq. 6.130). A derivation of the elastic strain energy can be found in [Kel18]. The elastic strain energy is defined as the volume integral of the elastic strain energy densities e . This quantity is robust against local peaks as it is integrated over the complete volume. Figure 6.28 compares the metamodel residuals for the normalized maximum stress (Fig. 6.28(a)) and the elastic strain energy (Fig. 6.28(b)). The red lines mark a bandwidth of 5% deviation between the FEA and the metamodel prediction. In the case of the maximum stress, over 30% of the predictions have a deviation greater than 5%. In the case of the elastic strain energy, the deviation limit is exceeded by only 3% of the predictions. While the elastic strain energy can not be compared against a material dependent limit like the yield stress to ensure the structural integrity of the impeller, it can be used to compare different designs and determine a low stress design as it is directly correlated to the stresses (Eq. 6.130).

$$E_{Strain,elastic} = \int_V e dV \text{ with } e = \frac{1}{2} (\sigma_{11}\varepsilon_{11} + \sigma_{22}\varepsilon_{22} + \sigma_{33}\varepsilon_{33}) + (\sigma_{12}\varepsilon_{12} + \sigma_{23}\varepsilon_{23} + \sigma_{31}\varepsilon_{31}) \quad (6.130)$$

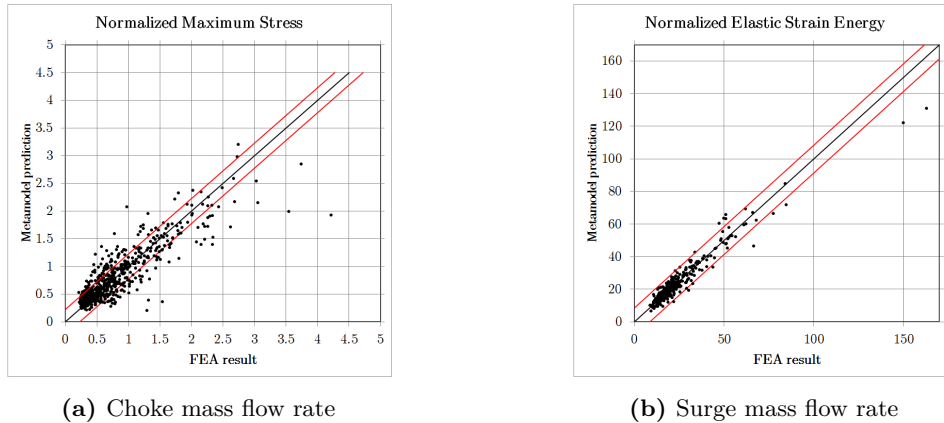


Figure 6.28

6.5.3 Structure Mechanical Metamodel

The review of available models carried out in section 3.1.5 revealed no analytical or empirical model for the prediction of the structure mechanical performance of an impeller. Therefore, a metamodel based on FEA computations will be used to obtain a fast prediction of the structure mechanic behavior of an impeller design.

The DOE on which the metamodel is based on uses the geometry parametrization which is described in section 6.2 and the FEA workflow from this section. The designs of the DOE are taken from the work of Senge [Sen15] and were extended by the analysis of the elastic strain energy. The DoE features a constant outer diameter D_2 and a constant tip speed u_2 . The deformations and stresses can be scaled for variations of D_2 and u_2 according to Eq. 6.131 and Eq. 6.132 (with the materials Young's modulus E). These relations are based on similitude. A derivation is given by Geller ([Gel85]). The structure mechanic metamodel is generated by the "Metamodel of Optimal Prognosis" workflow in optiSLang. The elastic strain energy is depicted by a Kriging regression with a high prediction accuracy (CoP=0.93). The metamodel is used in the sampling workflow to optimize those parameters of the impeller, which are not relevant for the aerodynamic performance, towards a mechanically low loaded design.

$$\varepsilon \propto \frac{\rho u_2^2 D_2}{E} \quad (6.131)$$

$$\sigma \propto \rho u_2^2 \quad (6.132)$$

6.6 Workflow

This section focuses on the optimization workflow which combines all previously described parts of the computational model with the filtered sampling method to generate a DOE. This DOE is used to build a metamodel on which the optimum is determined.

The workflow starts by defining the global parameters pressure ratio Π and flow rate \dot{V}_E , which determine the overall type of the machine. Furthermore, the ambient thermodynamic properties p_A and T_A and the fluid have to be set. In addition to these global quantities, the parameter ranges of the geometric model need to be chosen. The DOE is generated by the filtered sampling method. Before the algorithm can run, the parameters which control the classification and sample quality distribution, the size of the initial sampling and the size of the resulting DOE have to be stated. The actual sampling algorithm starts with the generation of an initial DOE. At this point, the application cases “Design-Optimization“ and “Design-by-Optimization“ have to be distinguished. In the case of a “Design-Optimization“, the applied changes of the inlet and outlet geometries are small when compared to the start design. Therefore, all parameters can be freely sampled by Latin hypercube sampling. In the case of the “Design-by-Optimization“ approach on the other hand, the inlet and outlet geometries may change drastically. If these changes are made in an independent way, many geometries would feature mismatched inlet and outlet geometries which would lead to a low aerodynamic performance. As a result, these dimensions are computed by the previously described preliminary design method. The remaining parameters are varied by Latin hypercube sampling. If the initial DOE is created, the geometries for all design points are generated. The aerodynamic performance of each design is predicted by a loss model computation. The rating is carried out by the characteristic number λ_{DP} (Eq. 6.129) which assigns a high rating to a design if it delivers the required pressure ratio at the design mass flow rate. Additionally, the distance between the stability limits and the design mass flow rate is taken into account. As previously stated, the prediction of the structural performance by a metamodel has proven difficult. Therefore, the parameters of the impeller with no or with only a low fluid dynamic relevance are optimized to minimize the elastic strain energy by using the previously described metamodel. These parameters are the shape of the impeller disc, the blade thicknesses and the blade hub fillet. By this approach, the average mechanical loading of the DOE designs can be reduced. The designs in the initial DOE are rated based on the predicted aerodynamic performance and assigned to the previously defined classes. These classes are thinned out until the desired number of samples and the distribution of sample quality is reached. The CAE responses of the designs in the resulting DOE are computed by the previously described CFD and FEA workflows. Based on these responses, a metamodel is generated in optiSLang using the MOP method. The optimization is carried out on this metamodel. If the optimum found on the metamodel can be successfully verified by one additional CAE computation, the optimization is finished. Figure 6.29 visualizes the workflow by a flow chart.

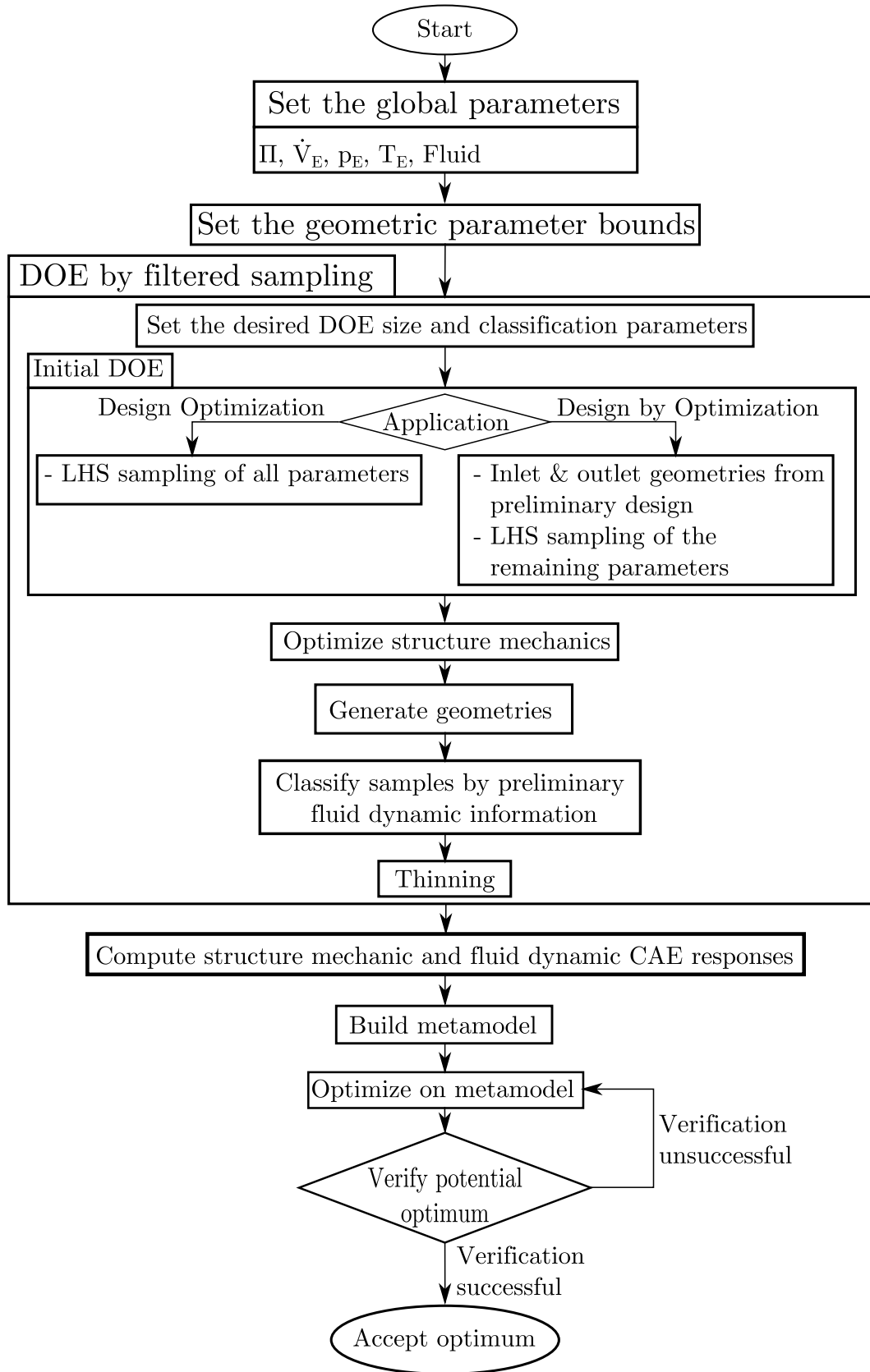


Figure 6.29: Workflow of the optimization method.

CHAPTER 7

Application and Proof-of-Concept

The methods described in the previous chapters are applied to optimize two existing centrifugal compressors (“Design-Optimization“). These compressors differ in terms of design pressure ratio, tip speed and outer diameter. The optimization is carried out by a particle swarm algorithm which seeks the optimum on a metamodel based on a DOE consisting of 100 samples created by the filtered sampling algorithm. The optima proposed by the algorithm are verified by CFD and FEA computations. The results and performance of the optimization are checked against an optimization which uses a metamodel based on a DOE consisting of 200 samples created by Latin hypercube sampling without taking preliminary information into account. For both DOEs the same parameters were used which were varied within the same bounds. This comparative data was available as results from two master theses ([Küp15] and [Lat18]).

In addition to these optimizations a new compressor impeller is designed by using a “Design-by-Optimization“ approach. In this application only the fluid dynamic behavior of the compressor is taken into account. The metamodel is based on a DOE consisting of 75 samples created by the filtered sampling algorithm. In contrast to the previously conducted “Design-Optimization“ cases, the outer diameter of the compressor is varied significantly in the optimization.

7.1 Testcase 1: Mid-Pressure Impeller Design-Optimization

The global dimensions and the performance data of the mid-pressure impeller are given in Tab. 7.1. Figure 7.1 gives the characteristic of the baseline impeller. The mass flow rate and the pressure ratio are normalized by their respective values at the design point ($\dot{m}_{norm}(\dot{m} = \dot{m}_{DP}) = 1$, $\Pi_{norm}(\Pi = \Pi_{DP}) = 1$). The baseline design delivers the desired pressure ratio at the design point ($\Pi(\dot{m}_{norm} = 1) = 1$). The efficiency at the design point has a value of 85.9%. Furthermore, the safety margin between the design point and the choke limit is 7% of the design mass flow rate, the distance between the design point and the surge limit has a value 25% of the design mass flow rate. This combination classifies the baseline design as a fluid dynamically good design with potential for further optimization.

Table 7.1: Global dimensions and performance data of the mid-pressure impeller.

Parameter	Symbol	Value
Outer diameter	D_2	300mm
Flow coefficient	φ_D	0.12
Work coefficient	Ψ	0.62
Pressure ratio	Π	2.5
Tip speed	u_2	$380 \frac{m}{s}$
Tip gap height	o_{TG}	0.5mm
Number of blades	z	15
Material	Titanium alloy	
Yield strength	σ_y	930MPa

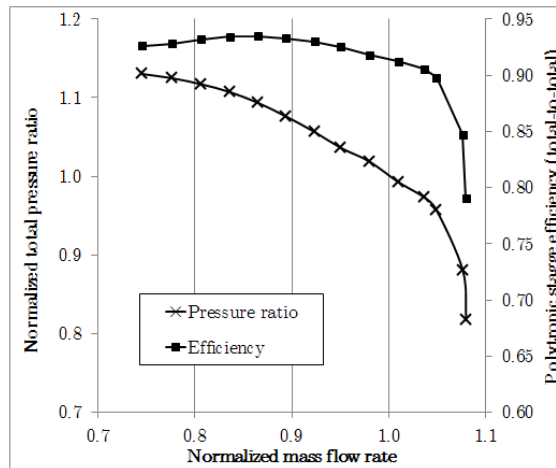


Figure 7.1: Characteristic of the baseline mid-pressure impeller.

A more detailed portrayal of the flow in the baseline impeller is given by Fig. 7.2. For this figure, the flow field is analyzed in the design point ($\dot{m}_{norm} = 1$). On the left hand side

of Fig. 7.2, the three-dimensional flow is visualized by Mach number streamlines. Apart from a small vortex originating from the tip gap, the flow is well aligned to the blade. The visualization of the Mach number distribution at mid-span given on the right hand side of the figure shows a similar picture, as no notable areas of low energy fluid and therefore no strong dissipation can be observed. In conclusion, the flow in the baseline impeller at the design point can be considered as nearly ideal. This further qualifies the initial design as a design of high fluid dynamic quality.

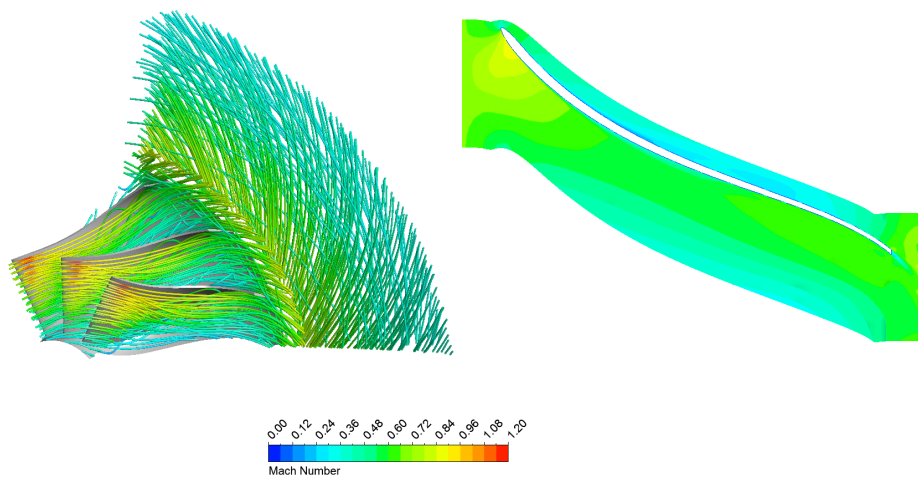


Figure 7.2: Flow in the baseline impeller (left: 3d streamlines colored by Mach number, right: blade to blade visualization of the Mach number distribution at mid-span).

The structure mechanic performance of the baseline impeller in terms of the Van Mises stresses is given in Fig. 7.3. The maximum of the stresses has a value of 1190MPa and is located at the leading edge of the blade near the hub. This value exceeds the yield limit by 25%. In addition to the stresses, Fig. 7.3 depicts the direction vectors which are used to measure the deformations of the blade tip at the leading and trailing edge. These deformations must be smaller than the tip gap as otherwise the blades will touch the casing. In case of the base line impeller, the deformation of the leading edge bears a value of 0.13mm , the deformation at the trailing edge has a value of 1.3mm which exceeds the tip gap height by 160%. The values of the maximum stresses and the trailing edge deformation disqualify the baseline design as a possible optimum.

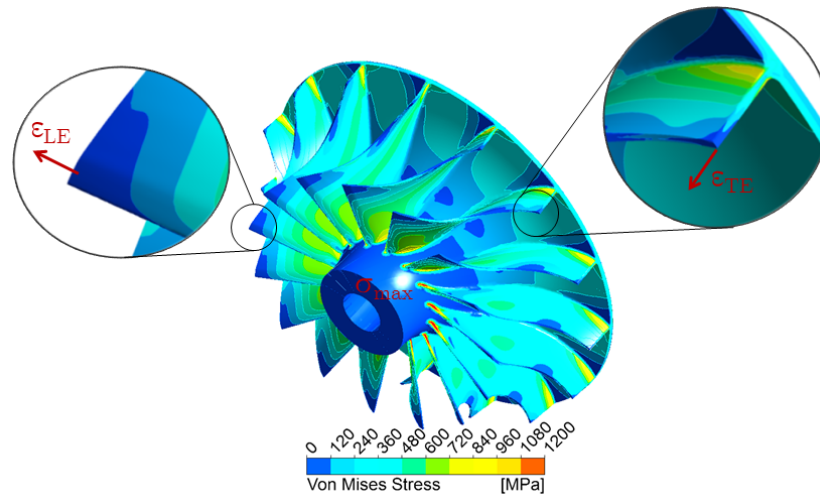


Figure 7.3: Structure mechanic loading of the baseline mid-pressure impeller.

In summary, it can be stated that the baseline geometry shows a good fluid dynamic performance with potential for optimization but is infeasible in terms of the structure mechanic constraints.

The parameters of this optimization are listed below. A total of 19 parameters are varied.

- **Constant parameters:**
 - Outer diameter
 - Inlet hub diameter
 - Blade count
- **Parameters varied in relation to the baseline design:**
 - Leading edge relative blade angles at hub and shroud ($\pm 10\%$)
 - Inlet shroud diameter ($\pm 5\%$)
 - Trailing edge blade height ($\pm 5\%$)
- **Free parameters:**
 - Axial extent
 - Hub contour shape (curvature and curvature influence length)
 - Blade height distribution between leading and trailing edge
 - Relative blade angle at trailing edge
 - Circumferential blade extent
 - Leading and trailing edge blade lean
 - Leading edge position

- **Parameters determined by optimization on the structure mechanic meta-model:**
 - Blade thicknesses
 - Hub blade fillet radius
 - Impeller disc contour

The DOE, on which the metamodel used for the optimization is based, is generated by the filtered sampling algorithm. As the intended use in this case is the optimization of an existing design, no preliminary design is used in the sampling process. The loss models calibrated for mid-pressure impellers presented in section 6.3 are used as preliminary information to rate the quality of the samples in the initial design. A high rating is assigned to a design if the desired pressure ratio is delivered when operating at the design point and if the distance between the stability limits and the design mass flow rate is greater than 10% of the design mass flow rate. The parameters with a low fluid dynamic relevance of each design are optimized using the structure mechanic metamodel (section 6.5.3) to minimize the elastic strain energy.

7.1.1 DOE results

The DOE consisting of 100 samples created by the filtered sampling algorithm is rated by the distribution of the responses of the fluid dynamic and structure mechanic simulation models. These results are compared against the DOE based on Latin hypercube sampling which contains 200 samples which was generated by Küppers [Küp15]. For the generation of this DOE no preliminary information was taken into account.

Figure 7.4(a) shows histograms of the choke mass flow rates of both DOEs. The mass flow rates are normalized by the design mass flow rate. This chart clearly indicates that the designs generated by the filtered sampling algorithm reach the choke margin at mass flow rates higher than the design mass flow rate ($\dot{m}_{choke,norm} > 1$). In the case of the Latin hypercube sampling, 50% of the samples feature a choke mass flow rate below the design mass flow rate and therefore fail to operate in the desired design point. Conversely, this means that this half of the designs is located in regions of the parameter space where no potential optima are to be found. Therefore, these designs can offer only a minor gain of information in regard of optimal designs and can be considered as wasted computational expense.

In Fig. 7.4(b), the distributions of the mass flow rates at the surge margin are compared for both DOEs. In contrast to the histogram of the choke mass flow rates, the surge mass flow rate are distributed in a similar way for both sample sets.

Histograms of the distribution of the design point polytropic stage efficiency are compared in Fig. 7.5(a). In the case of the DOE based on Latin hypercube sampling, only 15% of the samples reach design point efficiencies in the magnitude of 90% to 92% (highest stage efficiencies observed in this parameter space). The majority of the samples in this DOE (approx. 45%) achieve efficiencies between 89% and 90%. In comparison, 65% of the samples in the DOE generated by the filtered sampling algorithm feature an efficiency in the region of the highest efficiencies achievable in this parameter space (90%-92%). This

distribution indicates that the DOE based on the filtered sampling has a high sample density in parameter regions where highly efficient designs can be found.

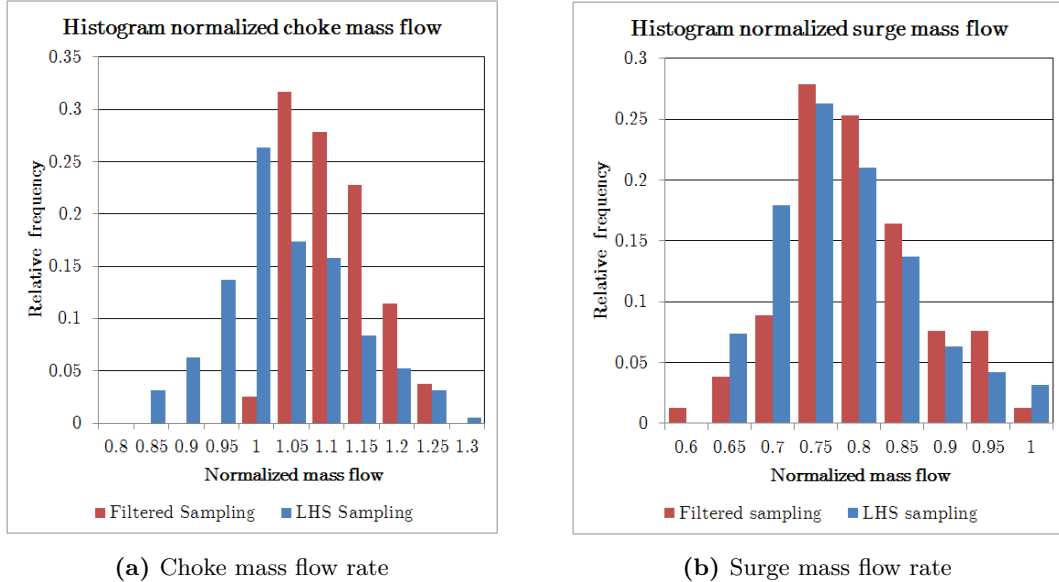


Figure 7.4: Distribution of the normalized mass flow rates at the stability limits for both DOEs.

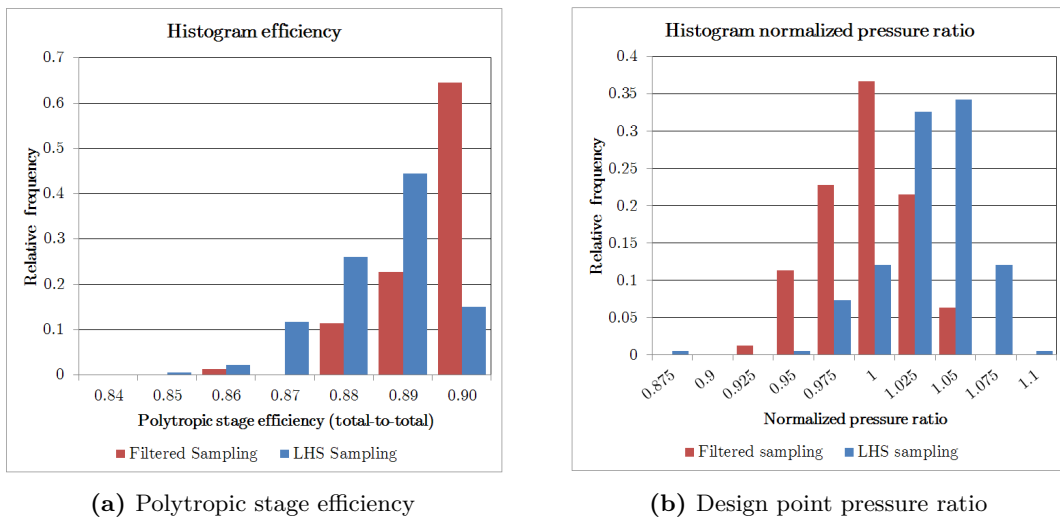


Figure 7.5: Distribution of the polytropic stage efficiencies and the pressure ratios at the design point for both DOEs.

Figure 7.5(b) shows histograms of the design point total pressure ratio for both DOEs. The pressure ratios are normalized by the design pressure ratio. The mean pressure ratio of the designs generated by the filtered sampling algorithm equals the desired design pressure ratio ($mean(\Pi_{norm}) = 1$). 36% of the samples produce the desired pressure ratio in the

design point while the remaining samples are approximately normal distributed. In the case of the Latin hypercube sampling, the mean pressure ratio of all samples is shifted towards higher pressure ratios. Only 12% of the samples produce the desired pressure ratio while nearly 80% of the samples exceed the design pressure ratio by 2.5% to 7.5%. This indicates, similarly to the results for the choke mass flow rate, that a high number of designs generated by the Latin hypercube sampling feature a characteristic which does not include the required design point. This disqualifies these designs as potential optima.

The distribution of the maximum stresses for both DOEs is shown in Fig. 7.6. The stresses are normalized by the material's yield strength. Both DOEs include a significant amount of samples which exceed the yield strength ($\sigma_{max,norm} > 1$). In the case of the DOE based on Latin hypercube sampling, 74% of the samples feature maximum stresses above the yield limit while this is the case for only 40% of the samples generated by the filtered sampling algorithm. Additionally, the highest stresses found in the LHS DOE are in the order of 5 times the yield limit while the highest stresses found in the DOE based in filtered sampling take values of 2.5 times the yield limit. Based on these findings it can be summarized that in the DOE based on filtered sampling the majority of the samples are feasible in terms of maximum stress.

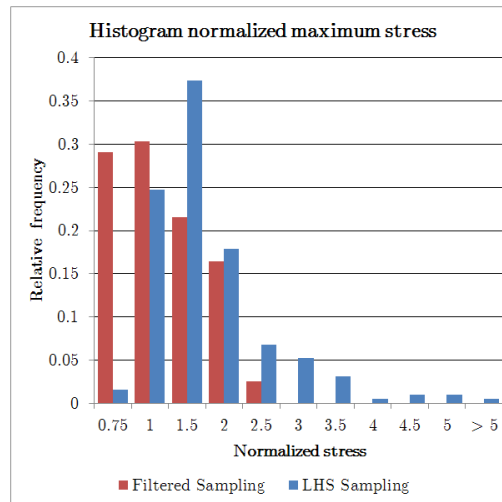
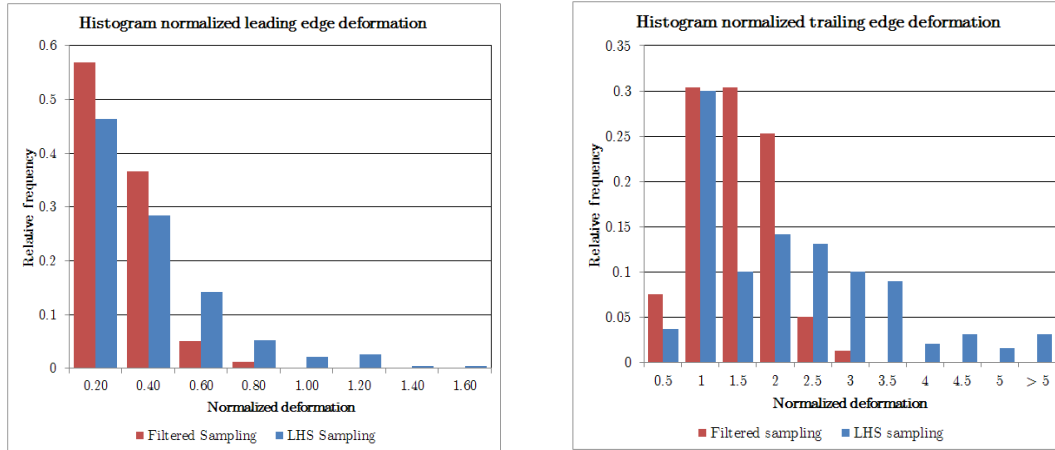


Figure 7.6: Distribution of the normalized maximum stress for both DOEs.

Figure 7.7(a) shows the histogram of the leading edge deformation for both DOEs. The deformations are measured as depicted in Fig. 7.3 and normalized by the tip gap height. All leading edge deformations observed in the DOE based on filtered sampling are smaller than the tip gap size and therefore uncritical. Only 3% of the deformations observed in the DOE based on Latin hypercube sampling exceed the tip gap height, the majority of the samples features uncritical leading edge deformations, too.

The histograms of the normalized trailing edge deformations are shown in Fig. 7.7(b). Both DOEs feature designs which exceed the tip gap high but in the case of the filtered sampling it can be observed that to mean trailing edge deformation has a value of 1.2 times tip gap high while the LHS sampling features a mean trailing edge deformation of 2 times the tip

gap height.



(a) Normalized leading edge deformation

(b) Normalized trailing edge deformation

Figure 7.7: Distribution of the normalized deformations for both DOEs.

Summary of the DOE results

The characteristics of all designs proposed by the filtered sampling algorithm fulfill the design-point criterion in terms of including the design mass flow rate. Furthermore, the mean pressure ratio of the designs equals the required design pressure ratio. These properties are of particular importance as a design, whose characteristic does not include the design point, can not be considered for an optimization. In addition, the filtered sampling includes a high number of designs which reach the highest efficiencies observed in the parameter space. Therefore, the DOE has a high information density in regions of the parameter space where optimal designs can be found. Finally, the designs are subject to lower structure mechanical loads when compared to the designs generated by Latin hypercube sampling. The histograms of the responses displayed in this section show a smaller range of variance for most responses. This can be a possible advantage for metamodeling.

7.1.2 Metamodel results

Both DOEs described and analyzed in the preceding section are used to generate metamodels. The global prediction qualities of the metamodels are compared Fig. 7.8, the respective CoP values are given in Table 7.2. The quality of the metamodel's prediction of each response is assessed by the Coefficient of Prognosis (CoP) as defined in Eq. 2.140. In addition to the global CoP, which rates the prediction quality over the complete parameter space, the local CoP values at the optimum of the responses are given. The local CoP rates the prediction quality on a local subset of the parameter space. The value of this parameter in the area of the optimal response values is of particular importance if the metamodel is used for optimization. Both metamodels are able to predict the responses relevant for an optimization with comparable accuracy. This indicates that a metamodel based on a DOE generated by filtered sampling can be used to optimize the impeller while only half the

samples are needed. Solely the surge mass flow rate shows a lower prediction quality which can be explained by the overall numeric problems encountered at the computation of the surge margin (see section 6.4.3).

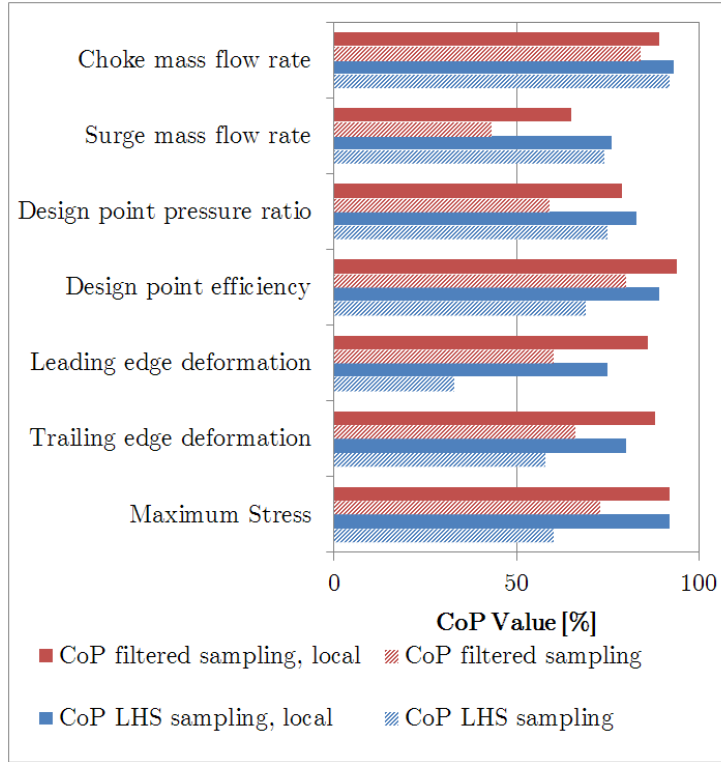


Figure 7.8: Prediction qualities of both metamodells.

Table 7.2: Comparison of the CoP values for both metamodells.

Response	$CoP_{filtered}$	$CoP_{filtered,local}$	CoP_{LHS}	$CoP_{LHS,local}$
Choke mass flow rate	84%	89%	92%	93%
Surge mass flow rate	43%	65%	74%	76%
Design point pressure ratio	59%	79%	75%	83%
Design point efficiency	80%	94%	69%	89%
Leading edge deformation	60%	86%	33%	75%
Trailing edge deformation	66%	88%	58%	80%
Maximum stress	73%	92%	60%	92%

In addition to the CoP values, the metamodel's prediction quality can be rated by the residual plots shown in Fig. 7.9. These plots compare the prediction of the CAE model to the prediction of the metamodel for each design point. A perfect prediction is indicated by the thin black diagonal line. The thick black lines indicate a bandwidth defined by a

deviation of 5% between the CAE and the metamodel prediction.

The metamodel residuals for the choke and surge mass flow rates (Fig. 7.9(a) and Fig. 7.9(b)), the efficiency (Fig. 7.9(c)) and the pressure ratio (Fig. 7.9(d)) show a similarly good prediction quality. As both metamodels are able to predict the locations of the stability limits and the design point pressure ratio with acceptable accuracy, these quantities will be used in the optimization.

In Fig. 7.9(e) the residuals for the metamodel prediction of the leading edge deformation are shown. The metamodel based on Latin hypercube sampling shows strong deviations between the finite element and the regression based predictions. The deviation observed for 67% of the samples exceeds the 5% margin. In the case of the metamodel based on filtered sampling, the leading edge deformation predicted by the metamodel deviates from the FEA results by more than 5% at only 20% of the samples. This result correlates with the prediction qualities for the leading edge deformation rated by the CoP value in Tab. 7.2. The residuals of the prediction of the trailing edge deformation are given in Fig. 7.9(f). Both metamodels show strong deviations, for the LHS based metamodel the deviations between the predictions exceed the 5% limit in 85% of the cases while the metamodel based on the filtered sampling fails to predict with the required accuracy for 42% of the samples. When only the samples in the feasible domain of the parameter space are taken into account (normalized deformation less than 1), only 23% of the predictions by the metamodel based on filtered sampling exceed the deviation limit of 5% while the prediction quality for the LHS based metamodel does not change. As the metamodel will be used for optimization, only the feasible domain of the parameter space is of interest.

The residuals of the metamodels for the prediction of the maximum stress are given in Fig. 7.9(g). Both metamodels show strong deviations. In the case of the metamodel based on LHS sampling, the 5% deviation margin is exceeded by 52% of the predictions. In comparison, 39% of the predictions by the metamodel based on the filtered sampling fail to meet this criterion. For the prediction of the maximum stress the same effect as for the prediction of the deformations can be observed: when only the structure mechanically feasible domain is taken into account, the number of inaccurate predictions is strongly reduced. For the case of maximum stresses below the yield stress (normalized stress smaller unity), the number of predictions which exceed the 5% deviation limit decreases to 19% for the metamodel based on filtered sampling and to 36% for the metamodel based on LHS sampling. As the metamodel is able to predict the deformations and stresses in the feasible domain with a good prediction quality, there is no need to analyze the elastic strain energy in this case. Therefore, these quantities will be used for the optimization. One possible explanation for the high deviations in the structure mechanically infeasible domain is the applied material model. All simulation are carried out using a linear elastic material model. This model will predict false stresses and deformations outside the elastic range of the material. Therefore, all results with stresses above the yield stress include a large numerical error (“solver noise”). Solver noise is known to impede the prediction of a response by a metamodel. Similar effects were noted by van Keulen et al. [Keu00].

In summary, both metamodels show a fair prediction quality for all major objectives needed for an optimization. This indicates that the filtered sampling approach can be

utilized to minimize the numerical expense required to generate a metamodel suited for optimization.

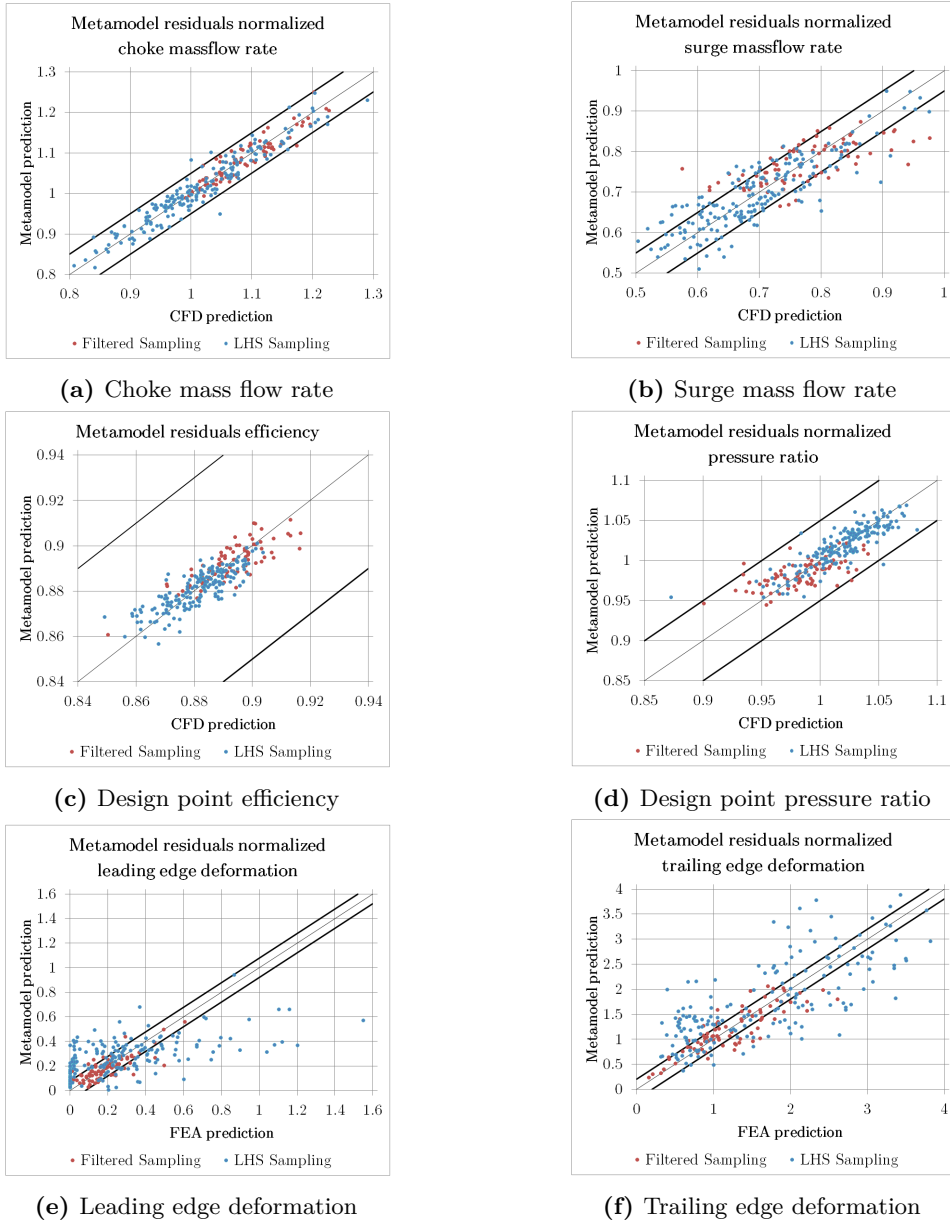
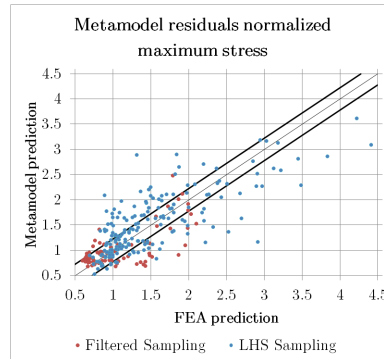


Figure 7.9: Residuals for metamodels based on both DOEs.



(g) Maximum stress

Figure 7.9: Residuals for metamodels based on both DOEs (continued).

7.1.3 Optimization results

The intended use of the previously created metamodels is optimization. Therefore, two optimization tasks are carried out using both metamodels. Concluding, the optimization results are compared to rate the metamodels. The objectives and constraints of both optimization scenarios are given in Table 7.3.

Table 7.3: Objectives and constraints of the optimization scenarios.

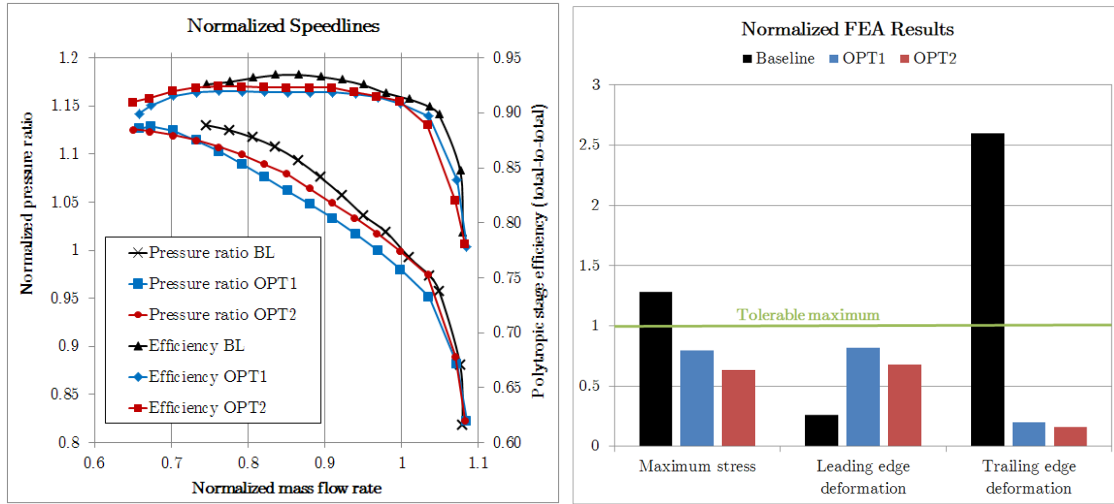
Scenario	I	II
Objectives	<ul style="list-style-type: none"> • Decrease the surge mass flow rate • Maximize the design point efficiency 	<ul style="list-style-type: none"> • Increase the choke mass flow rate • Maximize the design point efficiency
Constraints	<ul style="list-style-type: none"> • Deliver the design pressure ratio at the design mass flow rate • Retain the initial choke mass flow rate • Maximum stress below the yield stress • Leading and trailing edge deformation smaller than the tip gap height 	<ul style="list-style-type: none"> • Deliver the design pressure ratio at the design mass flow rate • Maximum stress below the yield stress • Leading and trailing edge deformation smaller than the tip gap height

The optimizations are carried out using a particle swarm optimization algorithm available in optiSLang.

Results of optimization scenario I

The results of the optimization in terms of the operation characteristic are given in Fig. 7.10(a). The characteristic resulting from an optimization carried out on the metamodel based on LHS sampling is labeled “OPT1“, the optimization carried out on the metamodel based on filtered sampling is labeled “OPT2“. In both cases, the optimized speedlines fulfill the optimization’s objectives: the surge margin is moved towards lower mass flow rates and the design point efficiency could be improved (85.9% → 87.3% for “OPT1“ and 85.9% → 88.1% for “OPT2“). Both optimal designs deliver the required pressure ratio

when operating at the design mass flow rate and the initial choke mass flow rate could be preserved. As the flow field in the initial design (Fig. 7.2) already showed nearly no dissipation, no further improvement could be expected and therefore no visualization of the flow field is given for the optimum.



(a) Operation characteristics for baseline and optimized impeller geometries.

(b) Normalized stresses and deformations for baseline and optimized impeller geometries.

Figure 7.10: Results of the first optimization scenario for the mid-pressure impeller.

The structure mechanic results are given in Fig. 7.10(b). The exact values of the stresses and deformations are listed in Table 7.4. Both optimized impellers are able to meet the requirements as the maximum stress is lower than the yield stress and the leading and trailing edge deformations do not exceed the tip gap height.

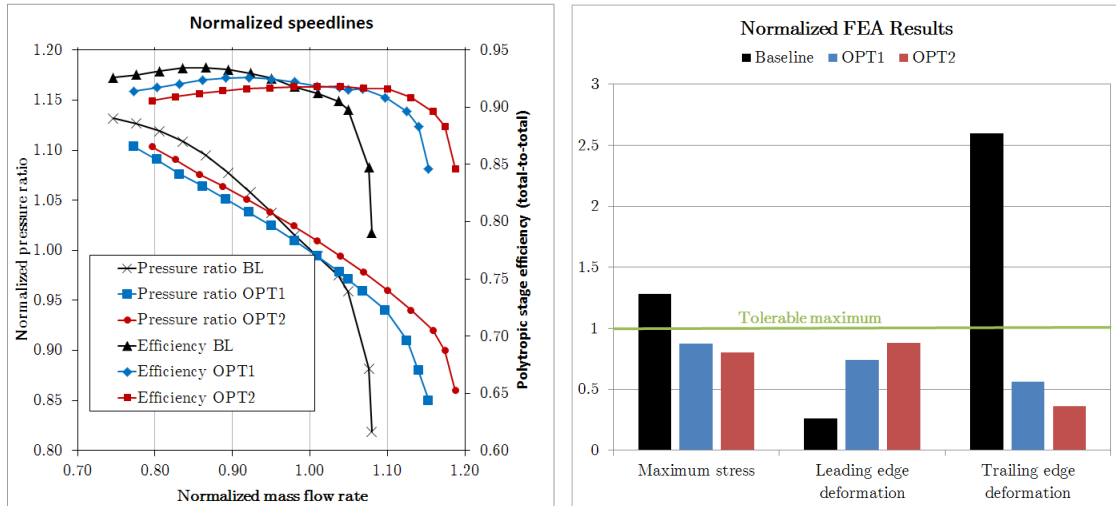
Table 7.4: Structure mechanic results of baseline and optimized impeller.

Quantity	Baseline	OPT1	OPT2
Maximum stress	1190MPa	743MPa	588MPa
Leading edge deformation	0.13mm	0.41mm	0.34mm
Trailing edge deformation	1.3mm	0.1mm	0.08mm

Results of optimization scenario II

Figure 7.11(a) shows the results of the second optimization in terms of the operation characteristic. Again, the characteristic resulting from an optimization carried out on the metamodel based on LHS sampling is labeled “OPT1“, the optimization carried out on the metamodel based on filtered sampling is labeled “OPT2“. Both optimized characteristic curves fulfill the objectives: the choke margin is extended towards higher mass flow rates and the efficiency in the design point is increased (85.8% → 86.8% for both optimizations). In both cases the impeller delivers the required pressure ratio when operating at the design mass flow rate. As a trade-off, the surge mass flow rate is slightly increased. As the

flow field in the initial design (Fig. 7.2) already showed nearly no dissipation, no further improvement could be expected and therefore no visualization of the flow field is given for the optimum.



(a) Operation characteristics for baseline and optimized impeller geometries.

(b) Normalized stresses and deformations for baseline and optimized impeller geometries.

Figure 7.11: Results of the second optimization scenario for the mid-pressure impeller.

Figure 7.11(b) summarizes the structure mechanic results. The exact values of stress and deformation are given in Tab. 7.5. Both optimized impellers are able to meet the requirements as the maximum stress is lower than the yield stress and the leading and trailing edge deformations do not exceed the tip gap height.

Table 7.5: Structure mechanic results of baseline and optimized impeller.

Quantity	Baseline	OPT1	OPT2
Maximum stress	1190MPa	812MPa	744MPa
Leading edge deformation	0.13mm	0.37mm	0.44mm
Trailing edge deformation	1.3mm	0.28mm	0.18mm

7.2 Testcase 2: High-Pressure Impeller Design-Optimization

Table 7.6 lists the global dimensions and the performance data of the high-pressure impeller design. The operation characteristic of the baseline design is given in Fig. 7.12. The mass flow rate and the pressure ratio are normalized by their respective values at the design point ($\dot{m}_{norm}(\dot{m} = \dot{m}_{DP}) = 1$, $II_{norm}(II = II_{DP}) = 1$). In contrast to the mid-pressure impeller, the baseline design of the high pressure impeller fails to meet the desired design point both in terms of mass flow rate and pressure ratio. Therefore, the baseline design has to be improved drastically to meet the design goals.

Table 7.6: Global dimensions and performance data of the high-pressure impeller.

Parameter	Symbol	Value
Outer diameter	D_2	350mm
Flow coefficient	φ_D	0.098
Work coefficient	Ψ	0.47
Pressure ratio	II	4
Tip speed	u_2	$480 \frac{m}{s}$
Tip gap height	o_{TG}	0.5mm
Number of full blades	z_{FB}	14
Number of splitter blades	z_{SB}	14
Material	High-strength aluminum alloy	
Yield strength	σ_y	430MPa

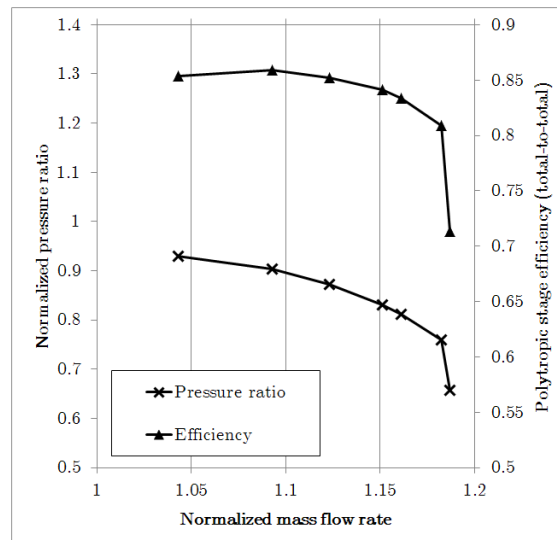


Figure 7.12: Characteristic of the baseline high-pressure impeller.

Figure 7.13 gives a more detailed portrayal of the flow in the baseline impeller. As the speedline of the baseline impeller fails to include the desired design point, the flow field is analyzed in the point which shows the smallest distance to the design point ($\dot{m}_{norm} = 1.03$). On the left hand side of Fig. 7.13, the three-dimensional flow is visualized as streamlines colored by the Mach number. The flow-field includes strong vortices and high Mach number gradients. The visualization of the Mach number distribution at mid-span given in the right hand side of the figure shows a similar picture, as several sources of dissipation can be observed. Firstly, the flow at the main blade's leading edge has strong incidence which shows in the form of a region with high Mach numbers right upstream of the leading edge on the suction side. This causes strong aerodynamic blockage in the impeller throat. Secondly, a region of low energy fluid can be observed at the main blade's pressure side about 30% into the passage. Finally, the flow at the splitter blade's leading edge again shows strong incidence which causes even further dissipation. In conclusion, the flow in the baseline impeller near the design point can be considered as far from ideal. This further indicates the strong need for aerodynamic improvement.

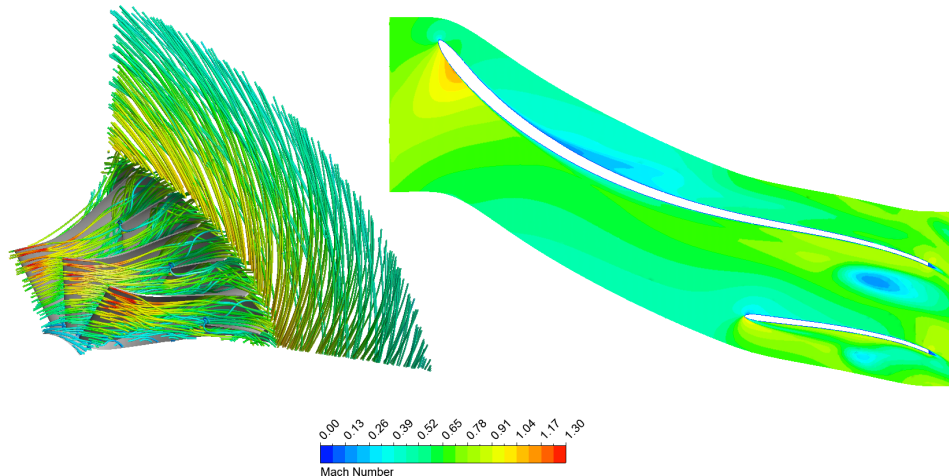


Figure 7.13: Flow in the baseline impeller (left: 3d streamlines colored by Mach number, right: blade to blade visualization of the Mach number distribution at mid-span).

The structure mechanic loading of the baseline impeller is given in Fig. 7.14 by a plot of the Van Mises stresses. The maximum stress takes a value of 1092MPa and is located at the hub fillet of the splitter blade. This value exceeds the yield strength by over 200%. Analogous to the mid-pressure impeller, the deformations are evaluated at the leading and trailing edge of the blades in direction of the tip gap. The leading edge of the full blades of the baseline impeller shows a deformation of 0.98mm which corresponds to approximately 200% of the tip gap height. The deformations of the splitter blade's leading edge (1.07mm) and the splitter blade's trailing edge (1.08mm) are of nearly the same magnitude. Only the deformation of the full blade's trailing edge (0.37mm) complies with the constraint of being smaller than the tip gap height of 0.5mm . Additionally to the bad aerodynamic performance, the values of the maximum stresses and the deformations disqualify the baseline impeller as a potentially optimal design.

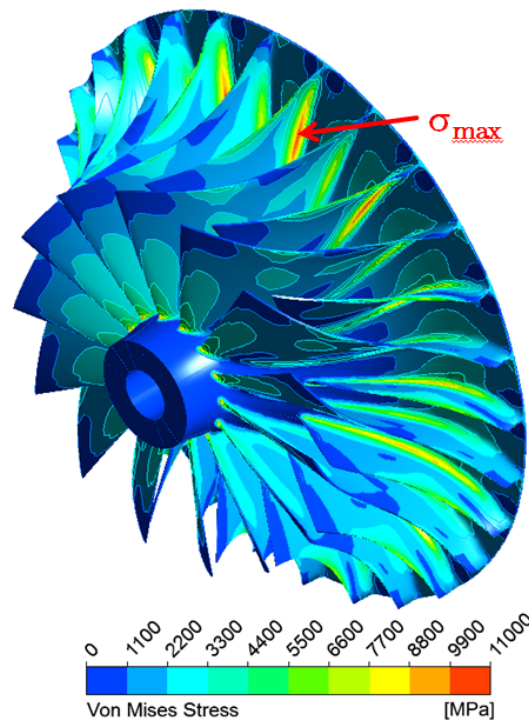


Figure 7.14: Structure mechanic loading of the baseline high-pressure impeller.

Summarizing, the baseline design requires a high amount of optimization in both the aerodynamic and the structure mechanic domain.

The parameters of this optimization are listed below. A total of 18 parameters are varied.

- **Constant parameters:**
 - Outer diameter
 - Inlet hub diameter
 - Inlet shroud diameter
 - Blade count
- **Parameters varied in relation to the baseline design:**
 - Leading edge relative blade angles at hub and shroud ($\pm 10\%$)
 - Trailing edge blade height ($\pm 5\%$)
- **Free parameters:**
 - Axial extent
 - Hub contour shape (curvature and curvature influence length)
 - Blade height distribution between leading and trailing edge
 - Relative blade angle at trailing edge
 - Circumferential blade extent
 - Leading and trailing edge blade lean
 - Leading edge position
- **Parameters determined by optimization on the structure mechanic meta-model:**
 - Blade thickness
 - Hub blade fillet radius
 - Impeller disc contour

As for the mid-pressure impeller optimization, the DOE, on which the metamodel used for the optimization is based, is generated by the filtered sampling algorithm. The intended use in this case is the optimization of an existing design. Therefore, no preliminary design is used in the sampling process. The loss models calibrated for high-pressure impellers presented in section 6.3 are used as preliminary information to rate the quality of the samples in the initial design. A high rating is assigned to a design if the desired pressure ratio is delivered when operating at the design point and if the distance between the stability limits and the design mass flow rate is greater than 10% of the design mass flow rate. Additionally, the parameters with a low fluid dynamic relevance of each design are optimized using the structure mechanic metamodel (section 6.5.3) to minimize the elastic strain energy.

7.2.1 DOE results

Analogous to the optimization of the mid-pressure impeller, a DOE consisting of 100 samples is generated by the filtered sampling algorithm. This DOE is compared to a DOE based on Latin hypercube sampling generated by Lattner [Lat18] consisting of 200 samples for which no preliminary information was taken into account. Both DOEs are rated in terms of the distributions of the fluid dynamic and structure mechanic responses.

Histograms of the choke mass flow rates for both DOEs are given in Fig. 7.15(a). The mass flow rates are normalized by the design mass flow rate. Both sample sets show similar distributions in terms of the choke mass flow rate.

Figure 7.15(b) shows the distribution of the mass flow rates at the surge margin. In contrast to the choke margin, significant differences are observable. Firstly, the distribution of the surge mass flow rate in the DOE based on filtered sampling is shifted towards lower mass flow rates when compared to the DOE based on Latin hypercube sampling. Secondly and more important, the DOE based on filtered sampling features no designs with a normalized surge mass flow rate greater than 1, which would indicate a characteristic curve which does not include the desired operation point. In the case of the DOE based on Latin hypercube sampling, 40% of the samples feature a surge mass flow rate higher than the design mass flow rate. Therefore, these designs are located in regions of the parameter space where no potential optimum can be found and can contribute only a minor gain of information in regard of optimal designs.

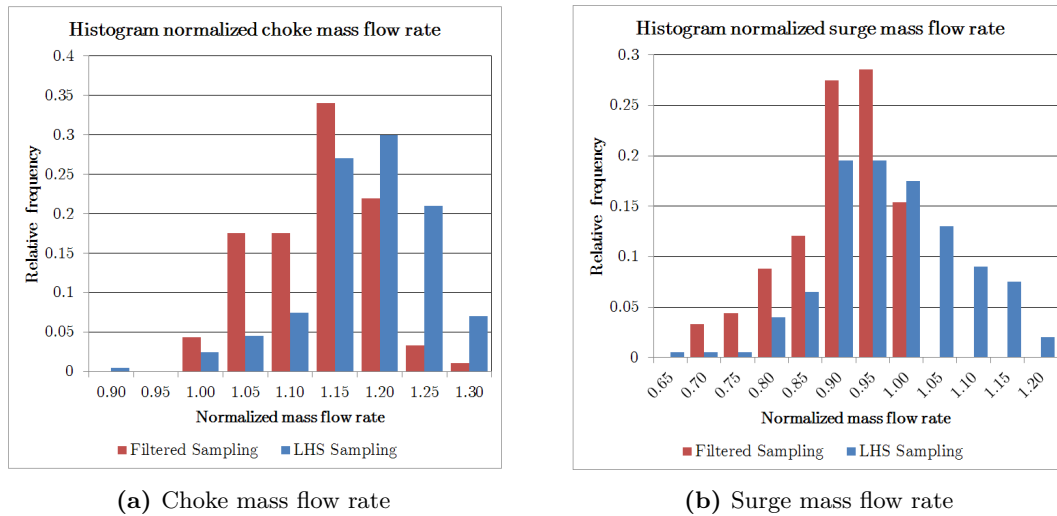


Figure 7.15: Distribution of the normalized mass flow rates at the stability limits for both DOEs.

Figure 7.16(a) shows histograms of the distribution of the design point polytropic stage efficiency for both DOEs. In the case of the DOE based on Latin hypercube sampling, only 15% of the samples reach design point efficiencies between 89% and 91% (highest efficiencies observed in both DOEs). In the case of the DOE based on filtered sampling, over 75% of the samples feature efficiencies in this order of magnitude. This indicates that the DOE based on filtered sampling has a high sample density in regions where highly efficient

designs can be found.

The distributions of the design point pressure ratio are depicted by histograms in Fig. 7.16(b). The pressure ratios are normalized by the desired design pressure ratio. For both DOEs, the mean of the distribution is greater than 1, which indicates that these designs fail to deliver the desired pressure ratio at the design point. In the case of the DOE based on filtered sampling, the majority of the samples feature design point pressure ratios which exceed the desired pressure ratio by 5% while the majority of the designs in the DOE generated by Latin hypercube sampling show a pressure ratio at the design point which is 10% higher than desired. While the mean design point pressure ratio is shifted away from the desired value for both DOEs, the DOE based on filtered sampling still includes more designs with a design point pressure ratio close to the required value. This indicates, similar to the distribution of the surge mass flow rate, that the DOE based on filtered sampling features a higher information density in potentially beneficial regions of the parameter space.

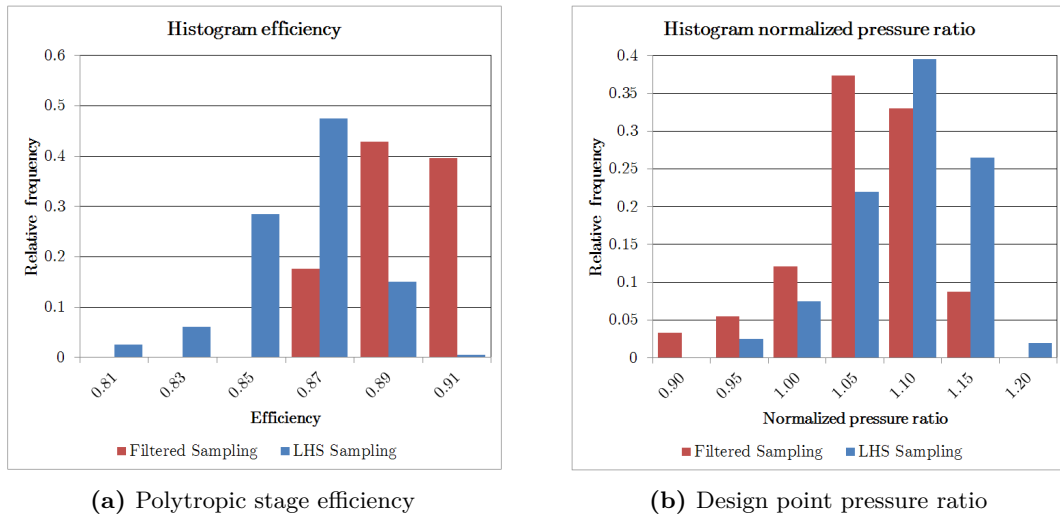


Figure 7.16: Distribution of the polytropic efficiency and the design point pressure ratio for both DOEs.

Figure 7.17 gives the distributions of the normalized stresses for both DOEs in form of histograms. The stresses are normalized by the material's yield limit. Both DOEs include a significant amount of designs which exceed the yield strength ($\sigma_{max,norm} > 1$). While the DOE based on filtered sampling shows a distribution which is shifted towards smaller values when compared to the DOE based on Latin hypercube sampling, still the majority of designs in both sets are outside of the mechanically feasible domain. Previous research activities ([Küs18]) have shown that the structure mechanic responses of designs with a high tip speed react very sensitive to even small geometric changes. Therefore, a high number of designs with stresses above the yield limit was expected. In this case the filtered sampling algorithm was unable to improve the distribution in a significant way. This is due to the fact that the metamodel used to optimize the aerodynamic irrelevant geometric quantities neglects the splitter blade.

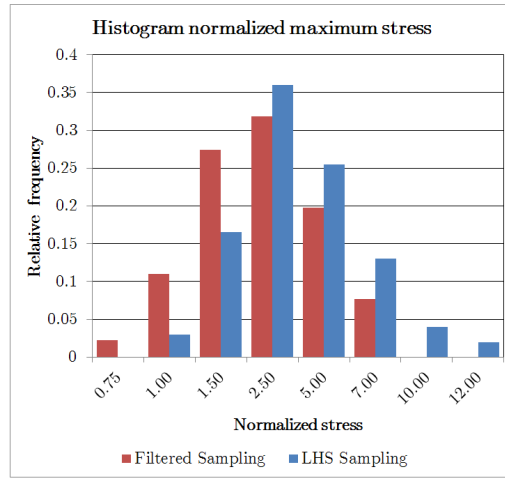
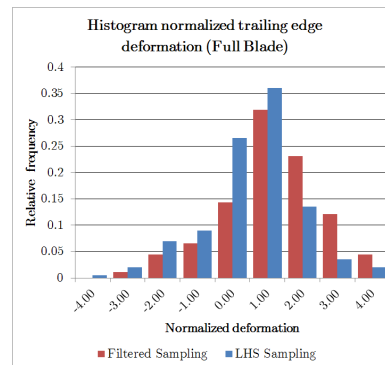
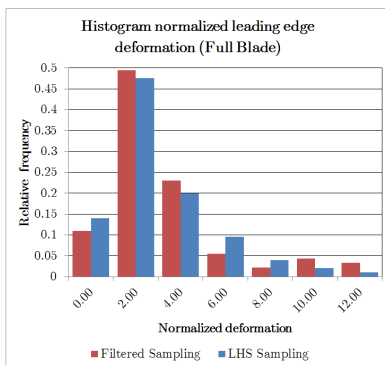


Figure 7.17: Distribution of the normalized maximum stress for both DOEs.

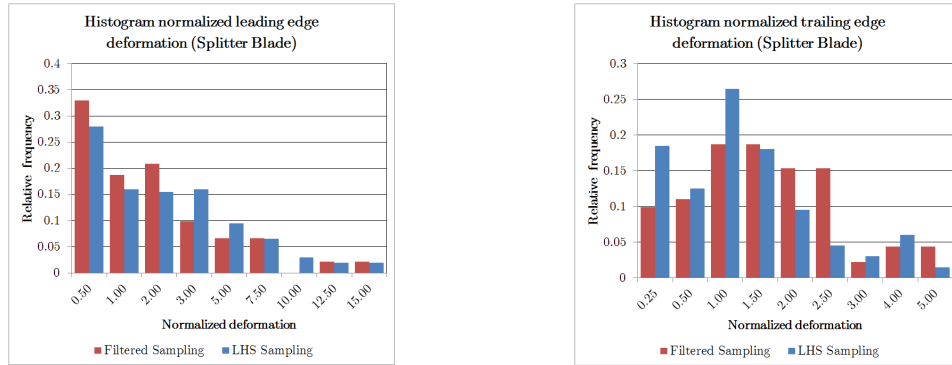
The distributions of the leading and trailing edges of the full and the splitter blades are depicted by histograms in Fig. 7.18. All deformations are normalized by the tip gap height. Similar to the maximum stresses, both DOEs feature a significant amount of designs which lie outside the feasible domain (normalized deformation > 1). Furthermore, no distinct improvement by the use of the filtered sampling method can be observed. This is again attributable to the high sensibility of the structure mechanic responses of highly loaded designs towards geometric changes and the metamodel used to optimize the designs for the filtered sampling.



(a) Normalized leading edge deformation (full blade)

(b) Normalized trailing edge deformation (full blade)

Figure 7.18: Distributions of the normalized deformations for both DOEs.



(c) Normalized leading edge deformation (splitter blade)

(d) Normalized trailing edge deformation (splitter blade)

Figure 7.18: Distributions of the normalized deformations for both DOEs (continued).

Summary of the DOE results

In summary, it can be stated that the filtered sampling approach is able to concentrate samples in areas of the parameter space where high quality designs in terms of the aerodynamics can be found. All designs proposed by the filtered sampling algorithm feature an operation characteristic which includes the design mass flow rate. Furthermore, the mean design point pressure ratio of the designs in the DOE generated by the filtered sampling algorithm is close to the desired design pressure ratio. In addition, the DOE generated by filtered sampling features a higher mean design point efficiency than the DOE generated by Latin hypercube sampling. This indicates that the DOE based on filtered sampling has a high sample density in areas of the parameter space where high quality designs can be found. The histograms shown in this section show a smaller variance for most aerodynamic responses in the case of the filtered sampling. This can be considered as a potential advantage for metamodeling. In the case of the structure mechanic responses on the other hand, no significant improvement can be recognized. This is due to the metamodel used as preliminary information, which was not able to predict the impellers structure mechanic behavior in a reliable way.

7.2.2 Metamodel results

The DOEs presented and analyzed in the previous section are used to generate metamodels. These metamodels are compared in Fig. 7.19 in terms of their prediction quality rated by the Coefficient of Prognosis (CoP). The respective CoP values are given in Tab. 7.7. In addition to the global CoP, which rates the prediction quality over the complete parameter space, the local CoP values at the optimum of the responses are given. This value is of particular importance if the metamodel is used for optimization. The results presented in Tab. 7.7 clearly indicate that the metamodel based on the DOE generated by filtered sampling shows high prediction qualities in areas of the parameters space which feature highly efficient designs while reducing the required computational expense by 50%.

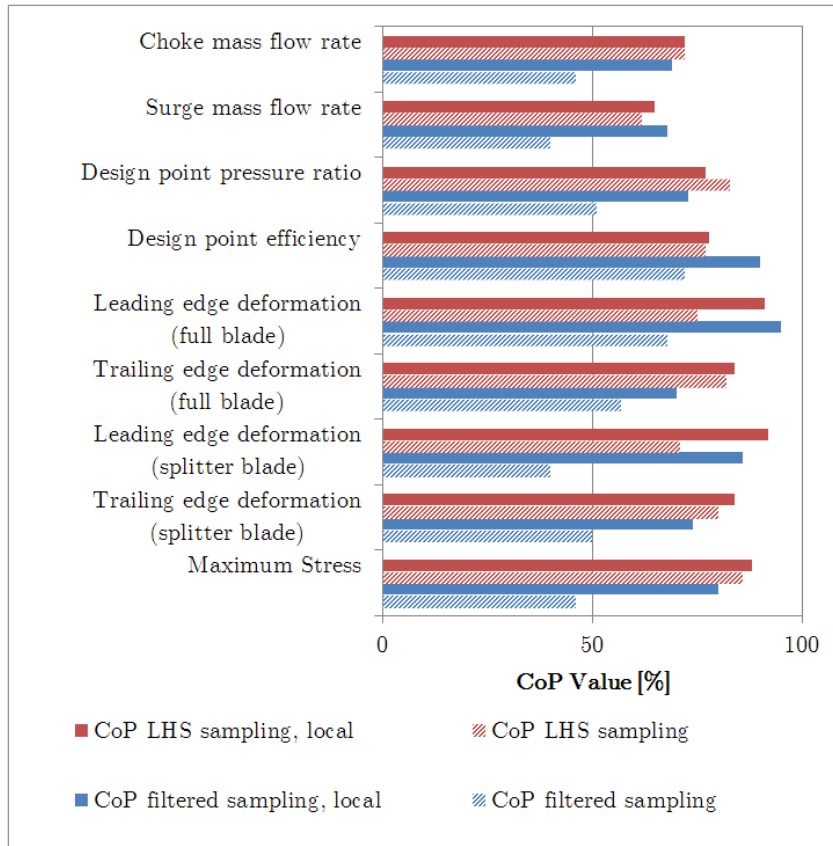


Figure 7.19: Prediction qualities of both metamodels.

The metamodel residuals for both models are compared in Fig. 7.20. These diagrams are generated by plotting the values predicted by the metamodel over the values computed by the CAE simulations and can be used to rate the prediction quality. The thin black, diagonal line indicates a perfect prediction which occurs if both the metamodel and the CAE workflow deliver the same response for one set of input parameters. The thick black lines describe a deviation bandwidth of 5% between the metamodel and the CAE prediction.

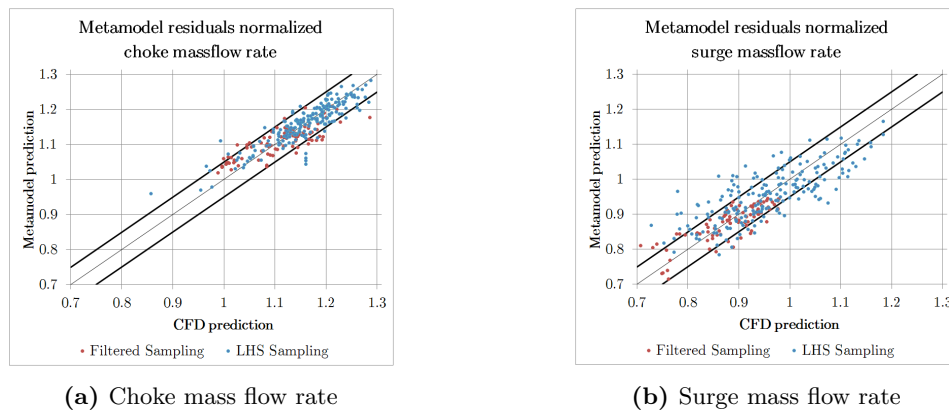
The choke and surge mass flow rates (Fig. 7.20(a) and Fig. 7.20(b)), the design point pressure ratio (Fig. 7.20(c)) and the design point efficiency (Fig. 7.20(d)) show comparable good prediction qualities.

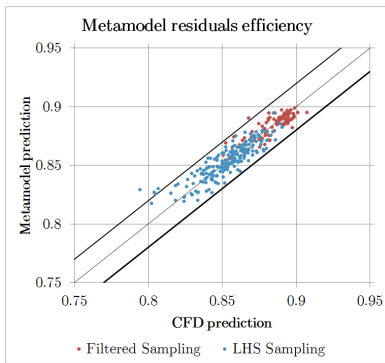
The residual plots of the deformations (Fig. 7.20(e) to Fig. 7.20(h)) show large spread widths and strong deviations for both metamodels. The pronounced scatter in the deformations is typical for impellers with a high tip speed as small geometry changes often result in strong variations of the deformations (see [Küs18]). If only the samples which feature deformations below the tip gap height are taken into account, the deviations of the predictions of the metamodel based on filtered sampling decrease. This is in good agreement with the global and local CoP values observed for the deformations in Tab. 7.7.

Table 7.7: Comparison of the CoP values for both metamodels.

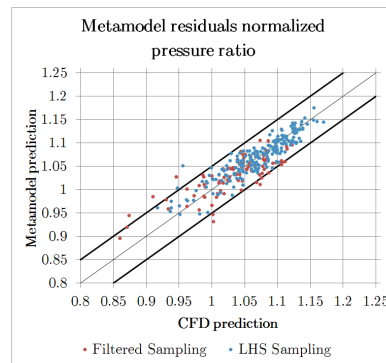
Response	$CoP_{filtered}$	$CoP_{filtered,local}$	CoP_{LHS}	$CoP_{LHS,local}$
Choke mass flow rate	46%	69%	72%	72%
Surge mass flow rate	40%	68%	62%	65%
Design point pressure ratio	51%	73%	83%	77%
Design point efficiency	72%	90%	77%	78%
Leading edge deformation (full blade)	68%	95%	75%	91%
Trailing edge deformation (full blade)	57%	70%	82%	84%
Leading edge deformation (splitter blade)	40%	86%	71%	92%
Trailing edge deformation (splitter blade)	50%	74%	80%	84%
Maximum stress	46%	80%	86%	88%

As already indicated by the local CoP values in Tab. 7.7, both metamodels are able to predict the maximum stress with acceptable accuracy for low stresses. This can be observed in the residual plot (Fig. 7.20(i)), too: while globally 75% of the LHS samples and 25% of the filtered samples are predicted with a deviation greater than 5%, the stresses are predicted correctly for all samples which belong to the feasible domain ($\sigma_{norm} < 1$). As the minimization of the stress is a typical requirement in every optimization, the prediction quality in regions with high stresses is not relevant. Both the stress as well as the deformations can be predicted with acceptable accuracy in the feasible domain. Therefore, these quantities can be used in the optimization.

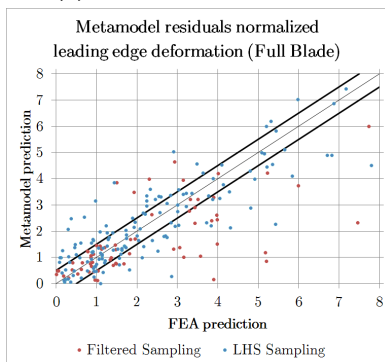
**Figure 7.20:** Residuals for metamodels based on both DOEs.



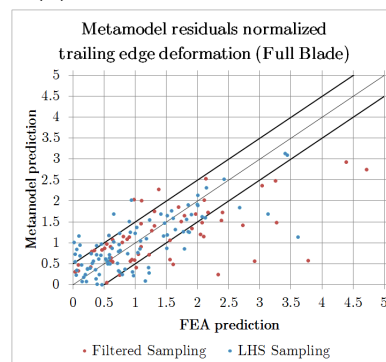
(c) Design point efficiency



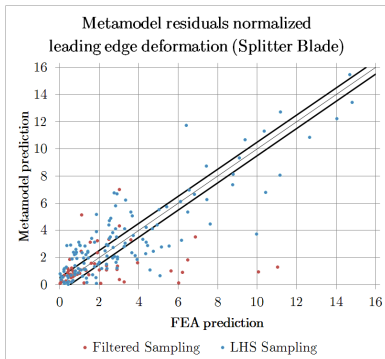
(d) Design point pressure ratio



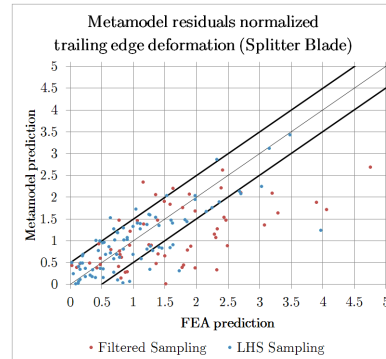
(e) Leading edge deformation (full blade)



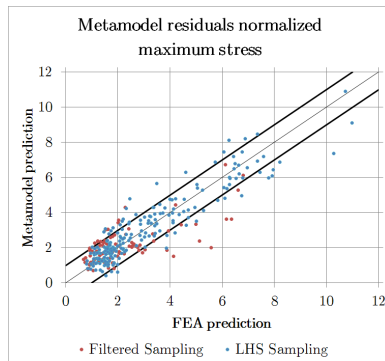
(f) Trailing edge deformation (full blade)



(g) Leading edge deformation (splitter blade)



(h) Trailing edge deformation (splitter blade)



(i) Maximum stress

Figure 7.20: Residuals for metamodels based on both DOEs (continued).

In summary, it can be stated that both metamodels are well suited for optimization as all relevant responses can be predicted with good accuracy. This shows that the filtered sampling approach allows the generation of a metamodel for optimization at a reduced numerical expense.

7.2.3 Optimization results

The intended use of the previously created metamodels is optimization. Therefore, an optimization is carried out using both metamodels. As stated before, the baseline impeller fails to reach the desired design mass flow rate and to deliver the design pressure ratio. Therefore, the objective of the optimization is the determination of an impeller design whose operation characteristic includes the desired design point and features a high efficiency in the design point. Furthermore, a defined width of the speed line is required. Concluding, the optimization results are compared to rate the metamodels. The objectives and constraints of the optimization are given in Table 7.8.

Table 7.8: Objectives and constraints.

Objectives	<ul style="list-style-type: none"> • Design point is part of the operation characteristic • Maximize the design point efficiency
Constraints	<ul style="list-style-type: none"> • Deliver the design pressure ratio at the design mass flow rate • Width of the operation characteristic at least 20% design mass flow rate • Maximum stress is below the yield stress • Leading and trailing edge deformation is smaller then the tip gap height

The optimization is carried out using a particle swarm optimization algorithm available in optiSLang.

Results of the optimization

The results of the optimization in terms of the operation characteristic are given in Fig. 7.22(a). The characteristic resulting from an optimization carried out on the metamodel based on LHS sampling is labeled “OPT1“, the optimization carried out on the metamodel based on filtered sampling is labeled “OPT2“. In both cases, the optimized speedlines fulfill the optimization’s objectives: the design mass flow rate is part of the speed line and the machine operates with high efficiency at the design point (“OPT1“: 86.92%, “OPT2“: 86.89%). Both optimal designs deliver the required pressure ratio when operating at the design mass flow rate and feature a width of the operation characteristic of 20% of the design mass flow rate.

A detailed comparison of the flow in the baseline impeller and the impeller optimized using the metamodel based on filtered sampling is given in Fig. 7.21. The flow field of the baseline design is analyzed at the point with the lowest distance to the desired design

point ($\dot{m}_{norm} = 1.03$), while the flow in the optimized design is analyzed at the desired design point ($\dot{m}_{norm} = 1$). The Mach number stream lines on the left hand side show a significant improvement of the flow in the optimized design, as the flow is mostly aligned to the blade and shows only minor vortices. Similar observations can be made when comparing the Mach number distributions in the blade to blade plots on the right hand side. The aerodynamic blockage at the throat is strongly reduced, the low energy region at the pressure side nearly vanishes and the flow at the splitter blades leading edge is aligned to the blade. The combination of these effects indicates, that a strong improvement of the aerodynamic quality is achieved by the optimization.

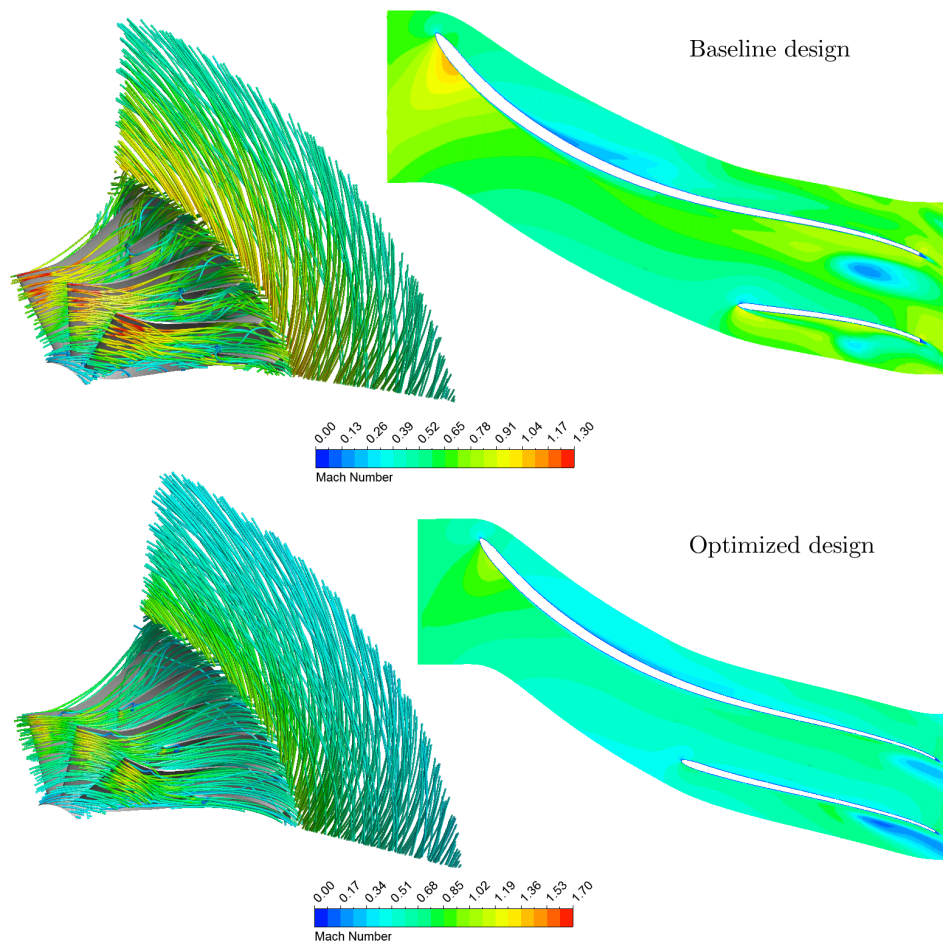
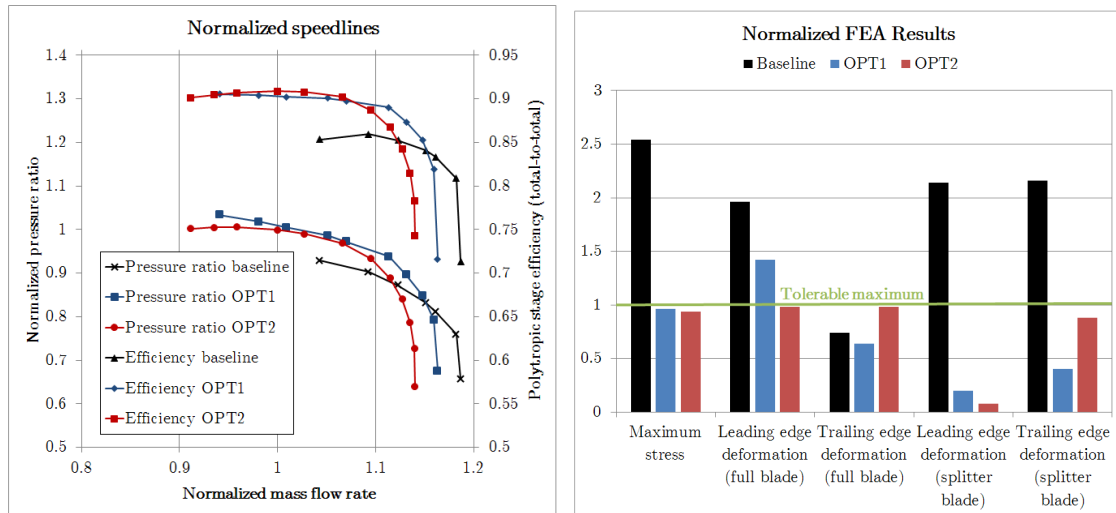


Figure 7.21: Flow in the baseline (top) and optimized impeller (bottom) (left: 3d streamlines colored by Mach number, right: blade to blade visualization of the Mach number distribution at mid-span). The optimized impeller is generated by an optimization carried out on the metamodel based on filtered sampling.

Figure 7.22(b) summarizes the structure mechanic results. The exact values of the stresses and deformations are given in Tab. 7.9. Both optimized impellers are able to

meet the requirements as the maximum stress is lower than the yield stress. In the case of the optimization carried out on the metamodel based on Latin hypercube sampling, only the deformation of the full blade's leading edge slightly exceeds the tip gap height. In the case of the optimization carried out on the metamodel based on filtered sampling, all deformations are inside the tolerable bounds.



(a) Operation characteristics for baseline and optimized impeller geometries.

(b) Normalized structure mechanic loading of the baseline and optimized impeller geometries.

Figure 7.22: Results of the optimization for the high-pressure impeller.

Table 7.9: Structure mechanic results of baseline and optimized impeller.

Quantity	Baseline	OPT1	OPT2
Maximum stress	1092MPa	415MPa	403MPa
Leading edge deformation (full blade)	0.98mm	0.71mm	0.49mm
Trailing edge deformation (full blade)	0.37mm	0.32mm	0.49mm
Leading edge deformation (splitter blade)	1.07mm	0.10mm	0.04mm
Trailing edge deformation (splitter blade)	1.08mm	0.20mm	0.44mm

7.3 Testcase 3: Design by Optimization of a Mid-Pressure Impeller

Table 7.10 lists the global dimensions and the performance data of the mid-pressure impeller. In contrast to the two previous examples, in this case the aim of the optimization is the design of a new impeller instead of the improvement of an existing design. Therefore, no initial design and no reference DOE exist in this case. With this example it is intended to demonstrate that the developed workflow is not only capable of optimizing an existing design with small changes to the blade design but can be used to generate a new design by optimization with strong global design changes, too. In addition, the loss models used to predict the aerodynamic performance were calibrated for fixed global impeller dimensions. Thus, this testcase is used to verify the ability of the loss models to predict the speedlines of impellers, which diverge from the calibration dataset.

The key challenge in this case is the strong variation of the global design parameters outer diameter and rotational speed. Thereby, the DOE consist of fundamentally different impeller designs. The amount of variation in the global design of the impellers is illustrated in Fig. 7.23. The range of impellers considered in this DOE is visualized by red dots in a Cordier diagram. These dots are close to the line which correlates the the non dimensional diameter δ and the non dimensional speed σ for machines of high efficiency (marked by “Verdichter,Pumpen“) in the range typical for centrifugal and diagonal compressors (marked by “Radial- und Diagonal Verdichter“). In contrast to this, the impeller designs considered in the previous examples are marked by a single blue dot for the mid-pressure design optimization and a green dot for the high-pressure design optimization. The slight deviations of the impeller designs from the original Cordier line are typical for modern compressor designs.

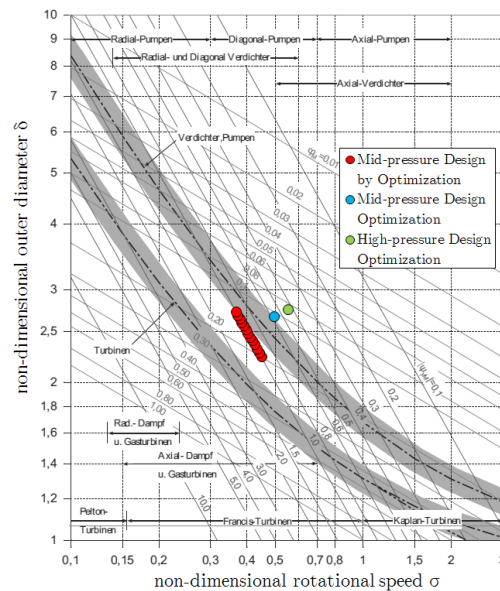


Figure 7.23: Location of the designs in the Cordier diagram (underlying diagram taken from [Eng07]).

This optimization focuses on the development of a new design which has to fulfill certain aerodynamic constraints. Thus, structure mechanics are not considered. The aerodynamic constraints of the new design are:

- Deliver the design pressure ratio when operating at the design mass flow rate.
- Operate at a high efficiency in the design point.
- Distance between stability limits and design point in mass flow direction: at least 20% of the design mass flow rate.

Table 7.10: Global dimensions and performance data for the Design-by-Optimization Impeller.

Parameter	Symbol	Value
Outer diameter	D_2	270-330mm
Flow coefficient	φ_D	0.12
Work coefficient	Ψ	0.78
Pressure ratio	Π	2.25
Tip speed	u_2	$384 \frac{m}{s}$
Number of blades	z	15

For this optimization the preliminary design approach is applied to determine the inlet and outlet geometries of each design. This results in the following set of parameters:

- **Constant parameters:**
 - Inlet hub diameter
- **Parameters with values obtained from preliminary design:**
 - Leading edge relative blade angles at hub and shroud
 - Leading edge blade height
 - Trailing edge blade height
- **Free parameters:**
 - Outer diameter
 - Axial extent
 - Hub contour shape (curvature and curvature influence length)
 - Blade height distribution between leading and trailing edge
 - Relative blade angle at trailing edge
 - Circumferential blade extent
 - Leading and trailing edge blade lean
 - Leading edge position

In summary, a total of 16 free parameters is varied in this optimization.

Analogous to the previous examples, the DOE, on which the metamodel used for the optimization is based, is generated by the filtered sampling algorithm. The loss models calibrated for mid-pressure impellers presented in section 6.3 are used as preliminary information to rate the quality of the samples in the initial design. A high rating is assigned to a design if the desired pressure ratio is delivered when operating at the design point and if the distance between the stability limits and the design mass flow rate is greater than 10% of the design mass flow rate.

7.3.1 DOE results

The DOE consisting of 75 samples created by the filtered sampling algorithm is rated by the distribution of the responses of the fluid dynamic simulation models.

Figure 7.24 shows the distributions of the choke and surge mass flow rates. All mass flow rates are normalized by the design mass flow rate. The distribution of the choke mass flow rates is given in Fig. 7.24(a). All designs feature a choke mass flow rate greater than the design mass flow rate. The mean choke mass flow rate has a value of 130% of the design mass flow rate. This indicates that the DOE offers a variety of design with a reasonable distance between the design point and the choke margin.

The distribution of the surge margin for all designs is given by Fig. 7.24(b). All surge mass flow rates observed in the DOE are smaller than the design mass flow rate. In combination with the distribution of the choke mass flow rates it can be stated that the speed lines of all design include the design point in terms of mass flow rate. Furthermore, the majority of the surge mass flow rates show up in the range of 70 to 90% of the design mass flow rate. As observed for the choke mass flow rate, this results in a DOE which includes a variety of designs with a reasonable distance between the surge margin and the design point.

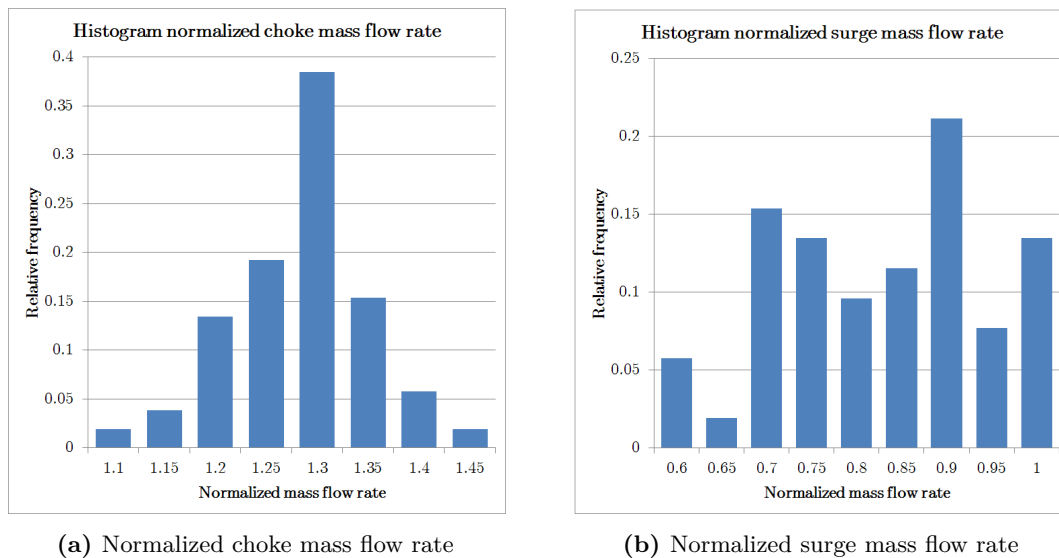


Figure 7.24: Distribution of the surge and choke mass flow rates.

The distributions of the design point pressure ratio and the polytropic stage efficiency are depicted by histograms in Fig. 7.25. The majority of designs in the DOE features high polytropic stage efficiencies above 90% in the design point as shown in Fig. 7.25(a). The histogram of the pressure ratios at the design mass flow rate is shown in Fig. 7.25(b). All pressure ratios are normalized by the desired design point pressure ratio. The mean pressure ratio of all designs equals the desired pressure ratio ($\Pi_{norm} = 1$). The design point pressure ratios of the majority of the impellers are scattered densely around a value of 1. Only 2% of the designs feature a pressure ratio in the area of 90% of the design point pressure ratio. This indicates that nearly all designs in the DOE are feasible in terms of pressure ratio.

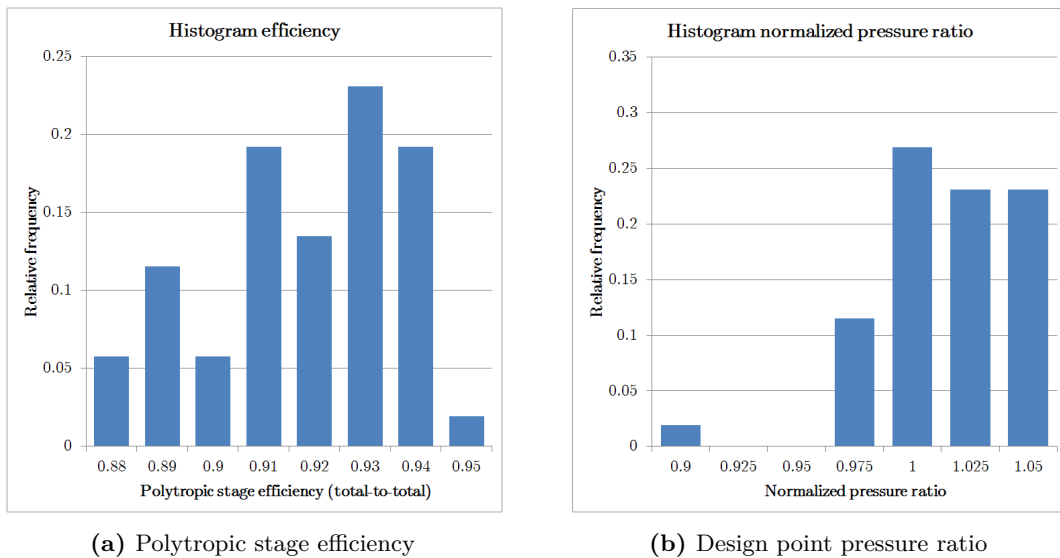


Figure 7.25: Distribution of the polytropic efficiency and the design point pressure ratio.

In summary it can be stated that the DOE generated by the filtered sampling algorithm is well suited for generating a metamodel usable to generate a new compressor design by optimization.

7.3.2 Metamodel Results

Based on the DOE presented and analyzed in the previous section, a metamodel is generated. The prediction qualities of the stability limits, the design point pressure ratio and the design point polytropic stage efficiency are shown in Fig. 7.26. The respective CoP values are listed in Tab. 7.11. In addition to the global CoP values, the local values at the optimal response values are given. Except for the surge mass flow rate, all responses can be predicted at high qualities both globally and locally. The lower prediction quality of the surge mass flow rate is related to the numeric problems which are known to be encountered in CFD computations near the surge limit. Still, the local prediction quality in the desired region of the surge mass flow rate (80% of the design mass flow rate) can be considered as sufficient.

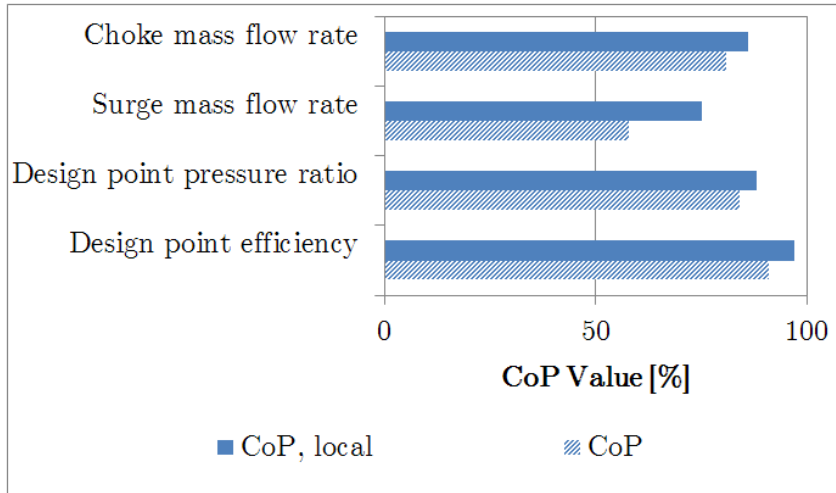


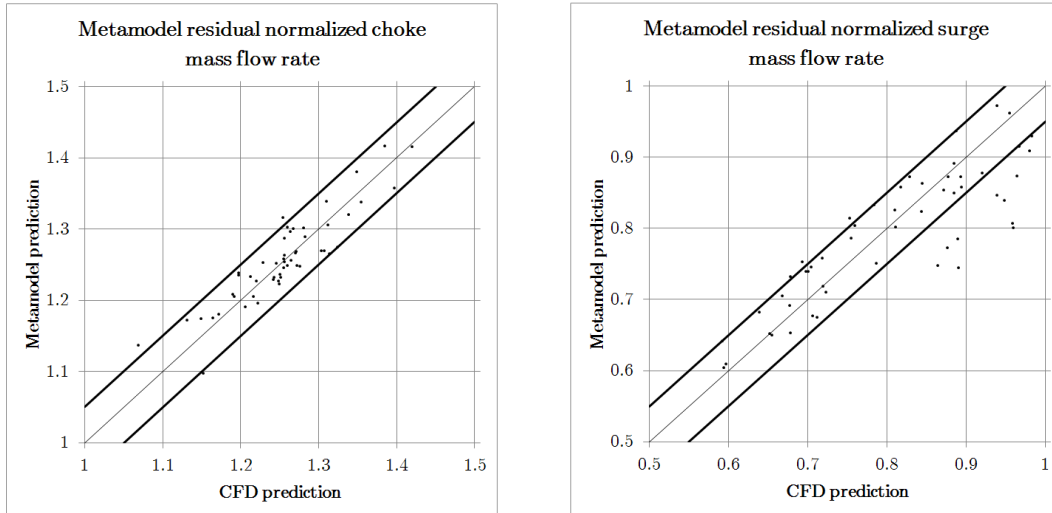
Figure 7.26: Prediction qualities the metamodel.

Table 7.11: CoP values of the metamodel.

Response	CoP	CoP_{local}
Choke mass flow rate	81%	86%
Surge mass flow rate	58%	75%
Design point pressure ratio	84%	88%
Design point efficiency	91%	97%

In addition to the CoP values, the metamodel's prediction quality can be rated by the residual plots shown in Fig. 7.27 and Fig. 7.28. These plots compare the prediction of the CAE model to the prediction of the metamodel for each design point. A perfect prediction is indicated by a thin black diagonal line. The thick black lines indicate a bandwidth defined by a deviation of 5% between the CAE and the metamodel prediction.

Figure 7.27(a) shows the metamodel residuals for the prediction of the surge mass flow rate. While large deviations can be observed for large surge mass flow rates (above 85% of the design mass flow rate), the predictions of the surge mass flow rate in the desired range (80% to 60% of the design mass flow rate) show only little deviation. The predictions of the choke mass flow rate (Fig. 7.27(b)) show only minor deviation across the whole range of choke mass flow rates observed in the DOE.

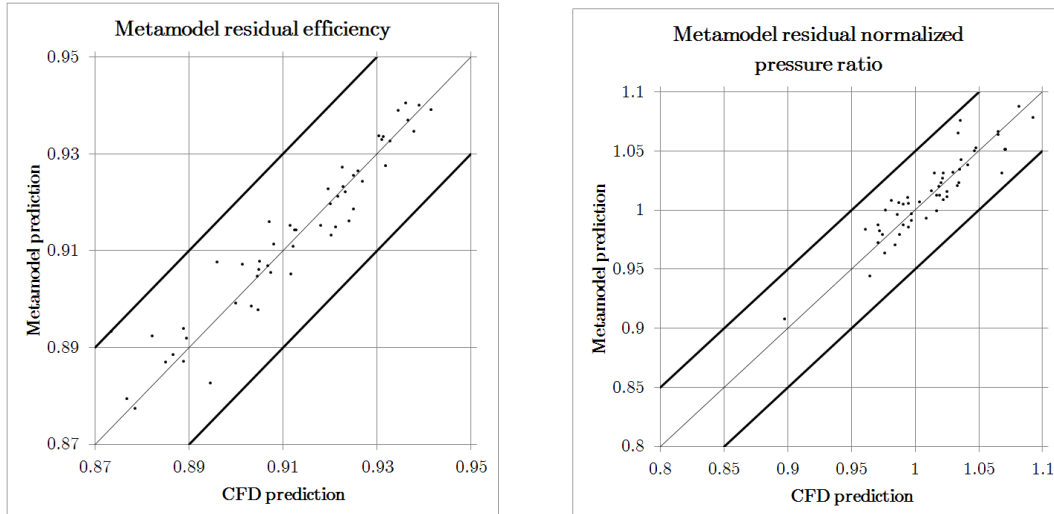


(a) Normalized choke mass flow rate

(b) Normalized surge mass flow rate

Figure 7.27: Metamodel residuals of the normalized choke and surge mass flow rates.

In accordance to the CoP values listed in Tab. 7.11, the residual plot for the prediction of the design point polytropic efficiency and pressure ratio given in Fig. 7.28 show a high prediction quality.



(a) Design point polytropic stage efficiency

(b) Design point stage pressure ratio

Figure 7.28: Metamodel residuals of the normalized pressure ratio and the polytropic stage efficiency.

In summary, the metamodel shows a high prediction quality for all major objectives needed for the optimization.

7.3.3 Optimization results

The intended use of the previously created metamodel is the design of a novel impeller by optimization. As stated before, this impeller design has to fulfill certain aerodynamic constraints. Based on these constraints the boundary conditions of the optimization are given in Tab. 7.12.

Table 7.12: Objectives and constraints.

Objectives	<ul style="list-style-type: none"> • Design mass flow rate included in the operation characteristic • Maximize the design point efficiency
Constraints	<ul style="list-style-type: none"> • Deliver the design pressure ratio at the design mass flow rate • Surge mass flow rate 80% of the design mass flow rate or less • Choke mass flow rate 120% of the design mass flow rate or more

The optimization is carried out using a particle swarm optimization algorithm available in optiSLang.

Results of the optimization

The results of the optimization in terms of the operation characteristic are given in Fig. 7.29 (the mass flow rate is normalized by the design mass flow rate and the pressure ratio is normalized by the required design point pressure ratio). The optimized operation characteristic fulfills all previously defined design goals: the impeller delivers the required pressure ratio when operating at the design mass flow rate ($\Pi_{norm}(\dot{m}_{norm} = 1) = 1$) and shows a high design point efficiency ($\eta(\dot{m}_{norm} = 1) = 0.93$). Furthermore, the impeller reaches the surge margin at 66% of the design mass flow rate and the choke margin at 128% of the design mass flow rate. Summarizing, it can be stated that all design goals are fulfilled by the optimized impeller design.

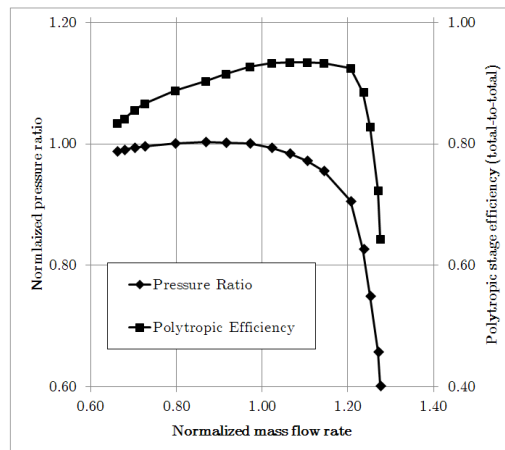


Figure 7.29: Operation characteristic of the mid-pressure impeller.

A more detailed portrayal of the flow in the optimized impeller is given by Fig. 7.30. For this figure, the flow field is analyzed in the design point ($\dot{m}_{norm} = 1$). In the left hand side of Fig. 7.30, the three-dimensional flow is visualized by Mach number streamlines. The flow is well aligned to the blade in the complete impeller channel. The visualization of the Mach number distribution at mid-span given in the right hand side of the figure shows a similar picture as no notable areas of low energy fluid and therefore no strong dissipation can be observed. In conclusion, the flow in the optimized impeller at the design point can be considered as nearly ideal.

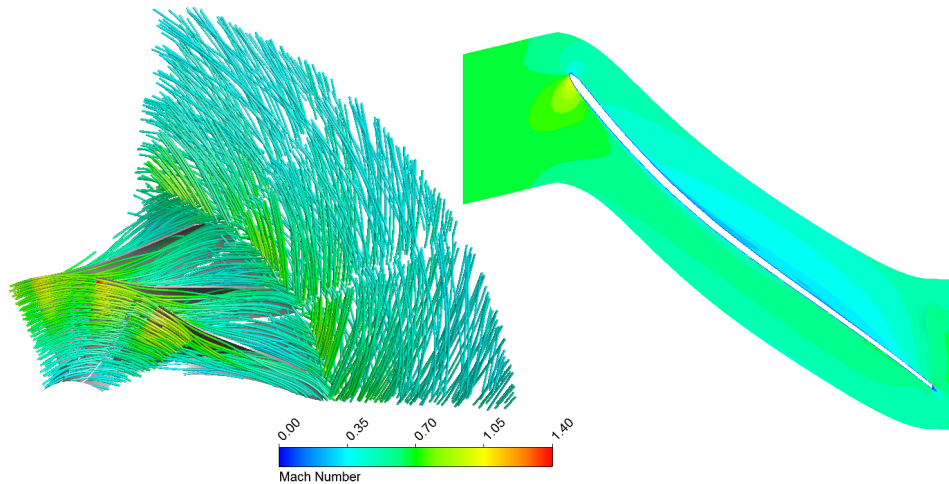


Figure 7.30: Flow in the optimized impeller (left: 3d streamlines colored by Mach number, right: blade to blade visualization of the Mach number distribution at mid-span).

CHAPTER 8

Conclusions

The goal of this research activity was the development of an efficient strategy for the metamodel based optimization of centrifugal compressor impellers with the main focus on the reduction of the required computational expense. The central idea followed in this work was the utilization of preliminary information from analytical models and empirical sources to identify promising regions in the parameter space and then concentrate the generation of samples in these areas. From this goals, three main tasks were derived: firstly the research, rating and implementation of sources of preliminary information, secondly the development of a suitable sampling method and finally the automated computational workflow. Concluding, the optimization strategy was applied to three examples.

The research for suitable models to rate the aerodynamic quality of an impeller design has revealed several potential methods. Out of these, one-dimensional loss modeling has been chosen to predict the aerodynamic performance of an arbitrary impeller geometry. The tested loss modeling approaches available in literature have shown strong deviation in the predicted speedlines when compared to fully 3-dimensional CFD computations. This problem was solved by calibrating the model parameters. The calibration was carried out by an optimization algorithm with the objective of minimizing the deviations between the loss model and the CFD prediction. The calibrated loss models are able to predict the aerodynamic performance of the impeller based on it's geometric design at a sufficient level of accuracy. This way, a first impression of the aerodynamic quality of the sample can be obtained. While a fully 3-dimensional CFD prediction of the compressor's speedline can take up to 300 core hours on a HPC CPU (Intel XEON E5, 2.9 GHz), the loss model prediction takes 30 core seconds in maximum on a desktop CPU (Intel i7-3840, 2.8GHz). Therefore, this method is well suited to quickly rate large sample numbers in order to identify promising regions of the parameter space.

In the case of the prediction of the structure mechanical loading of the impeller, a literature research has revealed no applicable analytical or empirical methods. Therefore, a metamodeling approach based on FEA computations has been chosen to obtain a fast prediction of the structure mechanical loading. This approach, however, was not able to predict the maximum stresses and the deformations reliably for the complete parameter space. A closer analysis of the metamodel's residuals indicated that the strongest deviations between the metamodel and the FEA prediction were mostly found for designs which featured extreme values of stress and deformation far beyond the linear elastic domain. For designs featuring maximum stresses below the yield limit on the other hand, acceptable

prediction qualities could be observed. Therefore, an alternative approach was used: for each design the parameters with low or no influence on the fluid mechanic performance were optimized to obtain a design with a low structure mechanic loading. To carry out these optimizations in an efficient way, the elastic strain energy was introduced as an additional output in the metamodel. This step had two advantages: firstly, the usage of an integral quantity reduced the influence of local stress peaks and secondly, only one optimization objective was needed to identify designs with low stresses and low deformations.

With the calibrated loss models and the metamodel for minimizing the structure mechanical loading, the required tools to identify promising regions of the parameter space were available.

In order to take advantage of the potentially beneficial regions of the parameter space identified by preliminary information, a sampling method is needed which concentrates designs in these areas while a good but coarser coverage of the complete design space is still ensured. Additionally, the amount of input correlation present in the sampling should be at the lowest possible level. A literature research revealed approaches like “Acceptance / Rejection Sampling“ or Markov chain Monte Carlo methods like the “Metropolis-Hastings algorithm“. These methods were tested to generate a sampling with a focus on high quality designs while the distribution of the sample quality was modeled by multi-modal test functions. These tests showed that none of the observed methods was able to generate a sampling which met the set goals of a bias towards high quality designs and low input correlations. Further tests however revealed that a DOE with the desired properties in terms of sample distribution and correlations could be created if a significantly higher number of samples was generated. A high sample number on the other hand was contrary to the global goal of the reduction of the numerical expense. Therefore, this DOE would have to be thinned out while retaining it’s beneficial properties.

Based on this finding, a new sampling method called “filtered sampling“ was developed which starts with following assumption: if a sampling that features the desired properties can only be generated by thinning out an initial sampling, the initial sampling can be generated by a Latin hypercube method which covers the complete parameter space evenly at a high resolution. Then, each sample in the initial DOE is assigned a measure of sample quality computed by the preliminary information. Based on this rating, the samples are sorted into classes. The desired distribution of sample quality in the sampling is set by the size and the limits of these classes. Based on this information, the sampling is thinned out by removing samples in densely populated areas of the parameter space until the desired distribution is achieved. This method was successfully tested for high dimensional multi-modal test function.

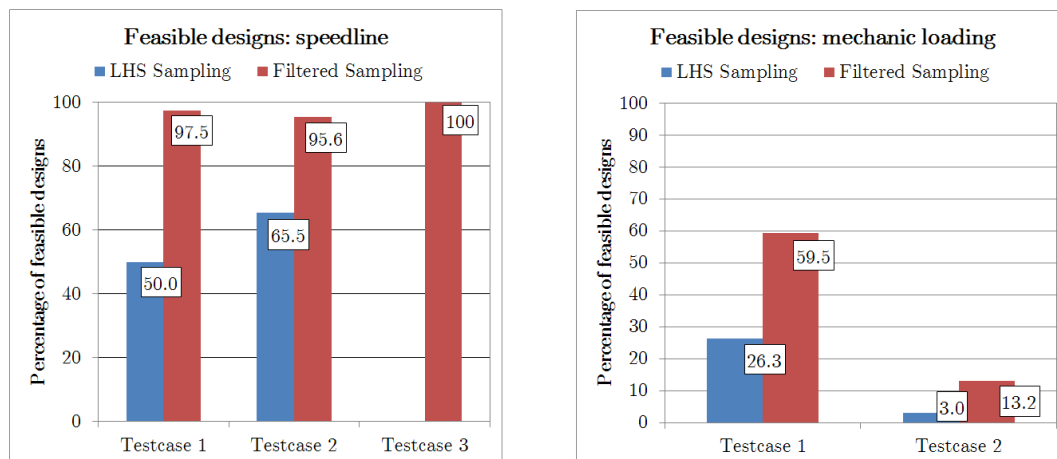
Based on these results, “filtered sampling“ was selected as the sampling method of choice for the optimization strategy to be developed.

A crucial part of every CAE based optimization is the applied computational workflow which has to work in a robust and reliable way. In this context, this means that no failed design occur and that no impellers are generated with aerodynamically disadvantageous parameter combinations. This challenge was solved by a strategy for geometry parametriza-

tion based on turbomachinery flow considerations. The parametrization concept was used in all further components of the computational workflow. These components were the preliminary design method, the one dimensional loss models, the metamodel for predicting the structure mechanic loading and the CFD and FEA models.

The optimization strategy was successfully tested on three optimization problems. In each case the workflow starts with a sampling generated by the “filtered sampling” method. The samples of the DOE are computed by the automated CAE workflow. Based on the DOE, a metamodel was generated by the MOP workflow in optiSLang and used for the optimization. In the case of the first and the second optimization problem, all results were compared against an optimization using a conventional Latin hypercube sampling without taking any preliminary information into account.

Figure 8.1 compares the global characteristics of the samplings in terms of the percentage of feasible designs. In the case of the samplings generated by the “filtered sampling” algorithm, nearly no failed designs in terms of the speedline (Fig. 8.1(a)) and in terms of the structure mechanic loading (Fig. 8.1(b)) were generated. Therefore, these DOEs contain a notable higher amount of information in subspaces where potentially optimal designs can be found.



(a) Percentage of feasible designs in terms of the speedline.

(b) Percentage of feasible designs in terms of the mechanic loading.

Figure 8.1: Comparison of the testcases in terms of feasible designs.

Testcase 1: Mid-Pressure Impeller Design-Optimization

The first example was the optimization of an existing mid-pressure impeller ($II = 2.5$). The DOE used for the metamodel consisted of 100 samples. In this case, the baseline design already showed a satisfactory aerodynamic performance but there was still potential for optimization. The structure mechanic loading on the other hand exceeded the material’s yield limit by 25% and showed deformations outside the feasible range. With respect to the baseline design, two optimization tasks were defined for this impeller. In both cases, the structure mechanic loading of the impeller had to be reduced to comply to the allowed

maximum values for both stress and deformation. On the aerodynamic side, the first optimization task demanded an extension of the surge margin towards smaller mass flow rates while maintaining the choke mass flow rate, the second task was the extension of the choke limit towards higher mass flow rates. In both cases, a further objective was the maximization of the design point efficiency. Additionally, the design point in terms of pressure ratio and mass flow had to be part of the speed line. The optimization was able to fulfill all constraints and determine an optimal solution in both cases. The results of the DOE, of the metamodel and of the optimization were compared to an optimization which did not take any preliminary information into account. For this optimization, the DOE consisted of 200 samples. Both optimizations were able to deliver optima of comparable quality. Thus, it can be stated that the optimization strategy based on the “filtered sampling” method is able to drastically reduce the computational expense needed for the optimization of a mid-pressure impeller.

Testcase 2: High-Pressure Impeller Design-Optimization

The second example was another optimization of an existing impeller. In this case, the task was the optimization of a high-pressure impeller ($II = 4$). The DOE used for the metamodel consisted of 100 samples. In contrast to the first example, the baseline impeller was not usable in terms of the aerodynamic performance: the surge mass flow rate had a value of 106% of the design mass flow rate while the maximum pressure ratio observed was 93% of the required design pressure ratio. Therefore, the intended design point was missed both in terms of pressure ratio and flow rate. In addition to the insufficient aerodynamic performance, the baseline impeller featured stresses and deformations outside of the feasible domain. This situation defined the optimization task: firstly, the speedline had to be shifted in a way that the impeller delivers the required pressure ratio when operating at the design mass flow rate while maintaining a safety distance between the operating point and the stability limits. Secondly, the polytropic stage efficiency in the design point was to be optimized. Finally, the optimal impeller had to comply to the structure mechanic constraints in terms of maximum stress and deformation. The optimization was able to determine an optimum and fulfill all constraints. The results in terms of the DOE, the metamodel and the optimization were benchmarked against an optimization using a metamodel based on a DOE consisting of 200 samples which were generated by Latin Hypercube sampling without taking preliminary information into account. Since both optimizations could provide comparable optima, in turn, it could be stated that the developed optimization strategy is able to minimize the amount of CAE computations required to obtain an optimum for a high-pressure impeller.

Testcase 3: Design by Optimization of a Mid-Pressure Impeller

In contrast to the previous examples, the third examples used the optimization strategy to design a new mid-pressure impeller ($II = 2.25$) which had to comply to a set of constraints in terms of the flow rate, the pressure ratio and the shape of the speedline. The first two examples focused on the optimization of the blade and meridional geometries without modifying the outer diameter and the speed of rotation. In this third example however, these quantities were modified in a pronounced way. Thus, this testcase was used to verify if the optimization strategy works for strong variations of the impeller’s global parameters, too. Furthermore, the ability of the loss models to predict the performance of impeller

designs which differ from the designs used for calibration in terms of global dimensions was tested. The DOE used for this optimization was generated by the “filtered sampling” method and consisted of 75 samples. The resulting impeller design had to comply to the following constraints: firstly, the impeller had to deliver the required pressure ratio when operating at the design mass flow rate. Secondly, a high efficiency in the design point was required. Finally, the distance between the stability limits and the design point should be at least 20% of the design mass flow rate or more. The optimization did successfully determine an optimal design which fulfilled all given constraints. This indicated, that the optimization strategy is capable of dealing with strong variations of global geometric variations and that the loss models can be used for impellers with global dimensions deviating from ones of the calibration designs.

In summary, it can be stated that the developed optimization strategy provides equally good results as the established methods while requiring a significantly smaller numerical expense.

With the presented method, the numerical expense required for optimizing a centrifugal compressor impeller could be drastically reduced. This reduction was achieved by using preliminary information gathered from fast, low-fidelity analytical or empirical methods to identify beneficial regions of the parameter space. These regions were then observed at a higher resolution by high fidelity CAE simulations. Low- and high-fidelity computation methods can be found in many fields of engineering. Based on the encouraging results obtained for centrifugal compressors, the method could be transferred to other engineering applications.

Bibliography

- [Alt12] ALTENBACH, HOLM: *Kontinuumsmechanik*. Springer Berlin Heidelberg, 2012 (cit. on p. 42).
- [Aug95] AUGNIER, RONALD H.: ‘Centrifugal Compressor Preliminary Aerodynamic Design and Component Sizing’. *ASME paper* (1995), vol. (95-GT-78) (cit. on pp. 124, 125).
- [Aug00] AUGNIER, RONALD H.: *Centrifugal Compressors - A Strategy for Aerodynamic Design and Analysis*. ASME Press, 2000 (cit. on pp. 5, 30, 31, 123, 127, 130).
- [Ben66] BENEDICT, R.P., CARLUCCI, N. A., and SWETZ, S. D.: ‘Flow Losses in Abrupt Enlargements and Contractions’. *Transactions ASME, Journal of Engineering for Power* (1966), vol. 88(1): pp. 73–81 (cit. on p. 126).
- [Ber12] BERNSTEIN, S.: ‘Démonstration du théorème de Weierstrass fondée sur le calcul des probabilités’. *Communications of the Kharkov Mathematical Society* (1912), vol. 12(2): pp. 1–2 (cit. on p. 60).
- [Bey99] BEYER, KEVIN, JONATHAN GOLDSTEIN, RAGHU RAMAKRISHNAN, and URI SHAFT: ‘When Is “Nearest Neighbor” Meaningful?’ *Database Theory — ICDT’99: 7th International Conference Jerusalem, Israel, January 10–12, 1999 Proceedings*. Ed. by BEERI, CATRIEL and PETER BUNEMAN. Berlin, Heidelberg: Springer Berlin Heidelberg, 1999: pp. 217–235 (cit. on p. 90).
- [Béz68] BÉZIER, P.: ‘Procédé de définition numérique des courbes et surfaces non mathématiques: Systeme UNISURF’. *Automatisme* (1968), vol. 13(5): pp. 189–196 (cit. on p. 59).
- [Bie53] BIEZENO, C. B. and R. GRAMMEL: *Technische Dynamik, Zweiter Band Dampfturbinen und Brennkraftmaschinen*. Springer Berlin Heidelberg, 1953 (cit. on p. 72).
- [Böc09] BÖCKER, MARKUS: ‘Automatische Optimierung eines parametrisch konstruierten Laufrades (unpublished)’. MA thesis. Dortmund University of Applied Sciences and Arts, 2009 (cit. on pp. 105, 146).
- [Boy06] BOYD, STEPHEN P. and LIEVEN VANDENBERGHE: *Convex optimization*. eng. Repr. with corr. Cambridge [u.a.]: Cambridge Univ. Press, 2006: XIII, 716 S. (Cit. on p. 56).
- [Bre13] BRETSCHER, OTTO: *Linear Algebra with Applications*. Pearson, 2013 (cit. on p. 51).

- [Bro13] BRONSTEIN, ILIJA N. ET AL.: *Taschenbuch der Mathematik*. Haan-Gruiten : Verl. Europa-Lehrmittel Nourney, Vollmer, 2013 (cit. on p. 91).
- [Buc14] BUCKINGHAM, E.: ‘On physically similar systems; illustrations of the use of dimensional equations’. *Physical Review* (1914), vol. 4 (cit. on p. 22).
- [Bus28] BUSEMANN, A.: ‘Das Förderhöhenverhältnis radialer Kreiselpumpen mit logarithmisch spiraligen Schaufeln’. *ZAMM - Journal of Applied Mathematics and Mechanics Zeitschrift für Angewandte Mathematik und Mechanik* (1928), vol. 8(5): pp. 372–384 (cit. on p. 63).
- [Cas04] CASELLA, GEORGE, CHRISTIAN P. ROBERT, and MARTIN T. WELLS: ‘Generalized Accept-Reject sampling schemes’. *Institute of Mathematical Statistics Lecture Notes - Monograph Series*. Institute of Mathematical Statistics, 2004: pp. 342–347 (cit. on p. 79).
- [Cas12] CASEY M., RUSCH. D.: ‘The Design Space Boundaries For High Flow Capacity Centrifugal Compressors’. *Proceedings of ASME Turbo Expo 2012 GT2012, June 11-15, 2012, Copenhagen, Denmark*. 2012 (cit. on pp. 64, 65).
- [Chi95] CHIB, SIDDHARTHA and EDWARD GREENBERG: ‘Understanding the Metropolis-Hastings Algorithm’. *The American Statistician* (1995), vol. 49(4): pp. 327–335 (cit. on p. 81).
- [Cor53] CORDIER, O.: ‘Ähnlichkeitsbedingungen für Strömungsmaschinen’. *BWK Zeitschrift* (1953), vol. 5(10): pp. 337–340 (cit. on pp. 22, 26).
- [Cor99] CORNE, DAVID: *New Ideas in Optimisation*. Advanced Topics in Computer Science. McGraw-Hill Inc.,US, 1999 (cit. on p. 56).
- [Den78] DENTON, J. D.: ‘Throughflow Calculations for Transonic Axial Flow Turbines’. *Journal of Engineering for Power* (1978), vol. 100(2): pp. 212–218 (cit. on p. 70).
- [Dix10] DIXON, S.L. and C.A. HALL: *Fluid Mechanics and Thermodynamics of Turbomachinery*. Elsevier, 2010 (cit. on p. 5).
- [Dyn13] DYNARDO: *optiSLang Documentation, Version 3.2.3*. Dynardo, dynamic software and engineering, 2013 (cit. on pp. 49, 55).
- [Egl77] EGLAJS V., AUDZE P.: ‘New approach to the design of multifactor experiments’. *Problems of Dynamics and Strengths* (1977), vol. (35): pp. 104–107 (cit. on p. 50).
- [Eng07] ENGEL, CHRISTOPH: ‘Untersuchung der Laufradströmung in einem Radialventilator mittels Particle Image Velocimetry (PIV)’. PhD thesis. Universität Duisburg-Essen, 2007 (cit. on pp. 23, 179).
- [Fis84] FISTER, WERNER: *Fluidenergiemaschinen Band 1*. Springer Verlag, 1984 (cit. on pp. 24–26, 30, 35).
- [Fis86] FISTER, WERNER: *Fluidenergiemaschinen Band 2*. Springer Verlag, 1986 (cit. on pp. 31, 41, 65, 98).

-
- [Gel85] GELLER, M.: ‘Festigkeitsanalyse von Radiallaufrädern beliebiger Bauform unter mechanischer und thermischer Beanspruchung’. PhD thesis. Ruhruniversität Bochum, 1985 (cit. on p. 147).
- [Har05] HARRISON, H. R.: *Classical Mechanics* J.R. Taylor. University Science Books, Sausalito, CA. 2004. Distributed by Macmillan Distribution, Houndmills, Basingstoke, Hampshire RG21 6XS, UK. 786pp. Illustrated. £41.99. ISBN 1-891389-22-X. Vol. 109. 1094. Cambridge University Press (CUP), Apr. 2005: p. 201 (cit. on p. 33).
- [Haw74] HAWTHORN, W.: *Secondary Vorticity in Stratified Compressible Fluids in Rotating Systems*. Tech. rep. CUED/A-Turbo/TR 63. Cambridge Univ. Eng. Dept., June 1974 (cit. on p. 39).
- [Hir07] HIRSCH, CHARLES: *Numerical Computation of Internal and External Flows*. Elsevier, 2007 (cit. on p. 21).
- [Hol92] HOLLAND, JOHN H.: *Adaptation in Natural and Artificial Systems*. MIT Press, 1992 (cit. on p. 58).
- [Hol00] HOLZAPFEL, GERHARD A.: *Nonlinear Solid Mechanics: A Continuum Approach for Engineering*. John Wiley & Sons, 2000 (cit. on p. 42).
- [Jap96] JAPIKSE, D.: *Centrifugal Compressor Design and Performance*. Concepts ETL, 1996 (cit. on pp. 31, 35).
- [Joh66] JOHNSTON, J.P. and DEAN R.C.: ‘Losses in Vaneless Diffusers of Centrifugal Compressors and Pumps’. *Transactions ASME, Journal of Engineering Power* (1966), vol. 88(1): pp. 49–62 (cit. on p. 127).
- [Jon72] JONES, W. P. and BRIAN LAUNDER: ‘The prediction of laminarization with a two-equation model of turbulence’. *International Journal of Heat and Mass Transfer* (Feb. 1972), vol. 15: pp. 301–314 (cit. on p. 19).
- [Kel18] KELLY, PIARAS: *Mechanics Lecture Notes: An introduction to Solid Mechanics*. University of Auckland, available at: <http://homepages.engineering.auckland.ac.nz/%7Epkel015/SolidMechanicsBooks/>, 2018 (cit. on p. 146).
- [Ken95] KENNEDY, J. and R. EBERHART: ‘Particle swarm optimization’. *Proceedings of ICNN’95 - International Conference on Neural Networks*. IEEE, 1995 (cit. on p. 58).
- [Keu00] KEULEN, F. van, B. LIU, and R. HAFTKA: ‘Noise and discontinuity issues in response surfaces based on functions and derivatives’. *41st Structures, Structural Dynamics, and Materials Conference and Exhibit*. American Institute of Aeronautics and Astronautics, Apr. 2000 (cit. on p. 160).
- [Kra75] KRAUSE, E.F.: *Taxicab Geometry: An Adventure in Non-Euclidean Geometry*. Dover Books on Mathematics Series. Dover Publications, 1975 (cit. on p. 92).
- [Kri51] KRIGE, DANIEL G.: ‘A statistical approach to some basic mine valuation problems on the Witwatersrand’. *Journal of the Chemical, Metal and Mining Society of South Africa* (1951), vol. 52(6): pp. 119–139 (cit. on p. 53).

- [Küp15] KÜPPERS, JAN-PHILIPP: ‘Entwicklung eines Metamodells zur automatisierten Optimierung eines hochbelasteten Radialkompressorlaufrades im Hinblick auf die Betriebskennlinie mittels CFD und FEM’. MA thesis. Dortmund University of Applied Sciences and Arts, 2015 (cit. on pp. 151, 155).
- [Küs18] KÜSTER, LASZLO: ‘Geometrieoptimierung einer höchstbelasteten Radialverdichterstufe im OFF-Design unter Berücksichtigung sowohl strömungstechnischer als auch festigkeitsgetriebener Gesichtspunkte (unpublished)’. MA thesis. Dortmund University of Applied Sciences and Arts, 2018 (cit. on pp. 170, 173).
- [Lan86] LANCASTER, PETER and KESTUTIS SALKAUSKAS: *Curve and surface fitting: an introduction*. English. London; Orlando: Academic Press, 1986 (cit. on p. 52).
- [Lat18] LATTNER, YANNICK: ‘Metamodellbasierte Optimierung der Betriebskennlinie hochbelasteter radialer Turboverdichterlaufräder unter Verwendung eines automatisierten, multidisziplinären CAE-Workflows und evolutionären Algorithmen’. MA thesis. Dortmund University of Applied Sciences and Arts, 2018 (cit. on pp. 151, 169).
- [Lau74] LAUNDER, B. E. and D. B. SPALDING: ‘The numerical computation of turbulent flows’. *Computer Methods in Applied Mechanics and Engineering* (Mar. 1974), vol. 3(2): pp. 269–289 (cit. on p. 19).
- [Lec14] LECHERER, STEFAN: *Numerische Strömungsberechnung*. Springer Fachmedien Wiesbaden, 2014 (cit. on pp. 11, 21).
- [Lia05] LIANG, J. J., P. N. SUGANTHAN, and K. DEB: ‘Novel composition test functions for numerical global optimization’. *Proceedings 2005 IEEE Swarm Intelligence Symposium, 2005. SIS 2005*. 2005: pp. 68–75 (cit. on p. 77).
- [Lie59] LIEBLEIN, S.: ‘Loss and Stall Analysis of Compressor Cascades’. *Transactions ASME, Journal of Basic Engineering* (1959), vol. 81: pp. 387–400 (cit. on p. 125).
- [Loh00] LOHMBERG, ANDREAS: ‘Strömungsbeeinflussung in Laufrädern von Radialverdichtern durch Neigung der Beschaufelung in Umfangsrichtung’. PhD thesis. Ruhruniversität Bochum, 2000 (cit. on p. 72).
- [Lor05] LORENZ, H.: ‘Theorie und Berechnung der Vollturbinen und Kreiselpumpen’. *V.D.I. Zeitschrift* (Oct. 1905), vol. 49(41): pp. 1670–1675 (cit. on p. 69).
- [Lue04] LUERSEN, M.A., R. LE RICHE, and F. GUYON: ‘A constrained, globalized, and bounded Nelder–Mead method for engineering optimization’. *Structural and Multidisciplinary Optimization* (June 2004), vol. 27(1): pp. 43–54 (cit. on p. 84).
- [Mah36] MAHALANOBIS, PRASANTA CHANDRA: ‘On the generalised distance in statistics’. *Proceedings of the National Institute of Sciences of India* (1936), vol. 2(1): pp. 49–55 (cit. on p. 93).
- [Mar19] MARTINEC, ZDENĚK: *Principles of Continuum Mechanics*. Springer International Publishing, 2019 (cit. on p. 42).

-
- [Mat71] MATHERON, G: ‘The theory of regionalized variables and its applications’. *Les Cahiers du Centre de Morphologie Mathématique, Fascicule 5. Ecole Nationale Supérieure des Mines de Paris* (1971), vol.: p. 211 (cit. on p. 53).
- [McK79] MCKAY, M. D., R. J. BECKMAN, and W. J. CONOVER: ‘A Comparison of Three Methods for Selecting Values of Input Variables in the Analysis of Output from a Computer Code’. *Technometrics* (1979), vol. 21(2): pp. 239–245 (cit. on p. 50).
- [Men94] MENTER, F. R.: ‘Two-equation eddy-viscosity turbulence models for engineering applications’. *AIAA Journal* (Aug. 1994), vol. 32(8): pp. 1598–1605 (cit. on p. 20).
- [Met53] METROPOLIS, NICHOLAS, ARIANNA W. ROSENBLUTH, MARSHALL N. ROSENBLUTH, AUGUSTA H. TELLER, and EDWARD TELLER: ‘Equation of State Calculations by Fast Computing Machines’. *The Journal of Chemical Physics* (1953), vol. 21(6): pp. 1087–1092 (cit. on p. 81).
- [Noc06] NOCEDAL, JORGE: *Numerical Optimization*. Springer New York, 2006 (cit. on p. 56).
- [Oer11] OERTEL, HERBERT, MARTIN BÖHLE, and THOMAS REVIOL: *Strömungsmechanik*. Vieweg+Teubner, 2011 (cit. on p. 11).
- [Pap08] PAPULA, LOTHAR: *Wahrscheinlichkeitsrechnung*. Vieweg+Teubner, 2008: pp. 249–464 (cit. on p. 49).
- [Pie97] PIEGL, LES and WAYNE TILLER: *The NURBS Book*. Springer Berlin Heidelberg, 1997 (cit. on p. 59).
- [Ras15] RASCH, D. and D. SCHOTT: *Mathematische Statistik: Für Mathematiker, Natur- und Ingenieurwissenschaftler*. Wiley, 2015 (cit. on p. 49).
- [Rod79] RODGERS, C.: ‘Specific speed and efficiency of centrifugal impellers’. *Performance Prediction of Centrifugal Pumps and Compressors*. Ed. by GOPALAKRISHNAN, S., P. COOPER, C. GRENNAN, and J. SWITZER. Vol. 4. 1979: pp. 191–200 (cit. on p. 64).
- [Rod91] RODGERS, C.: ‘The Efficiencies of Single-Stage Centrifugal Compressors for Aircraft Applications’. *International Gas Turbine and Aeroengine Congress and Exposition Orlando, FL June 3-6. 1991* (cit. on p. 64).
- [Rub11] RUBINSTEIN, R.Y. and D.P. KROESE: *Simulation and the Monte Carlo Method*. Wiley Series in Probability and Statistics. Wiley, 2011 (cit. on p. 49).
- [Ryb11] RYBACKI, ANNA: ‘Automatisierte Geometrieoptimierung eines Radialkompressorlauffrades unter Betrachtung von FEM- und CFD-relevanten Zielgrößen (unpublished)’. MA thesis. Dortmund University of Applied Sciences and Arts, 2011 (cit. on pp. 105, 146).
- [Sch81] SCHWEFEL, HANS-PAUL: *Numerical Optimization of Computer Models*. Wiley, 1981 (cit. on p. 58).

- [Sen15] SENGE, ANDREAS: ‘Entwicklung eines Metamodells zur Prognose des strukturemechanischen Verhaltens hochbelasteter Radialverdichter-laufräder unter Verwendung der FEM und eines automatisierten CAE-Workflows Thesis’. MA thesis. Dortmund University of Applied Sciences and Arts, 2015 (cit. on pp. 146, 147).
- [Smi57] SMITH, A.: ‘On the generation of the Streamwise Component of Vorticity for Flows in a Rotating Passage’. *Aeronautical Quarterly* (1957), vol. 8(4): pp. 369–383 (cit. on p. 39).
- [Sny18] SNYMAN, JAN A and DANIEL N WILKE: *Practical Mathematical Optimization*. Springer International Publishing, 2018 (cit. on p. 56).
- [Sti81] STIGLER, STEPHEN M.: ‘Gauss and the Invention of Least Squares’. *Ann. Statist.* (May 1981), vol. 9(3): pp. 465–474 (cit. on p. 51).
- [Sto27] STODOLA, AUREL: *Steam and gas turbines*. Springer Verlag, 1927 (cit. on p. 62).
- [VDI93] VDI: *VDI-Richtlinie: VDI 2045 Blatt 1 Abnahme- und Leistungsversuche an Verdichtern (VDI-Verdichterregeln); Versuchsdurchführung und Garantievergleich*. VDI-Gesellschaft Energietechnik. 1993 (cit. on p. 22).
- [Wan06] WANIEK, H.: ‘Geometrieoptimierung einer hochbelasteten Turbokompressorstufe anhand von CFD- und FEM-Analysen durch gezielte Parametervariation der Schaufelverwindung’. MA thesis. Fachhochschule Dortmund, 2006 (cit. on p. 72).
- [Wie67] WIESNER, F. J.: ‘A Review of Slip Factors for Centrifugal Impellers’. *Journal of Engineering for Power* (Oct. 1967), vol. 89(4): pp. 558–566 (cit. on p. 63).
- [Wil88] WILCOX, DAVID: ‘Reassessment of the scale-determining equation for advanced turbulence models’. *AIAA Journal* (Nov. 1988), vol. 26(11): pp. 1299–1310 (cit. on p. 19).
- [Wil09] WILL, J. and T. MOST: ‘Metamodell of optimized Prognosis MoP - an Automatic Approach for User Friendly Parameter Optimization’. *Proceedings of ANSYS Conference & 27th CADFEM Users Meeting*. Nov. 2009 (cit. on p. 55).
- [Wit85] WITTING, HERMANN: *Mathematische Statistik I*. Vieweg+Teubner Verlag, 1985 (cit. on p. 49).
- [Wu52] WU, CHUNG-HUA: ‘A General Theory of Three-Dimensional Flow in Subsonic and Supersonic Turbomachines of Axial-, Radial, and Mixed-Flow Types’. *National Advisory Committee for Aeronautics Technical Notes* (1952), vol. (2604) (cit. on pp. 69, 70).
- [Zan14] ZANGENEH, MEHRDAD, FRED MENDONÇA, YOUNGWON HAHN, and JACK COFER: ‘3D Multi-Disciplinary Inverse Design Based Optimization of a Centrifugal Compressor Impeller’. *ASME Turbo Expo 2014: Turbine Technical Conference and Exposition Volume 2B: Turbomachinery*. GT2014-26961. 2014 (cit. on p. 146).

- [Zim12] ZIMEK, ARTHUR, ERICH SCHUBERT, and HANS-PETER KRIEGEL: ‘A survey on unsupervised outlier detection in high-dimensional numerical data’. *Statistical Analysis and Data Mining* (Aug. 2012), vol. 5(5): pp. 363–387 (cit. on p. 91).

List of Figures

2.1	Control volume with heat, work and mass flow for a turbomachine	7
2.2	h-s Diagram for a compressor stage	9
2.3	Mass flows entering and leaving an infinitesimal volume element	12
2.4	Forces in x direction for an infinitesimal volume element, sheer stresses denoted as τ	13
2.5	Energy flows for an infinitesimal volume element in x direction	15
2.6	A modern version of the Cordier diagram taken from [Eng07]	23
2.7	Coordinate systems of a centrifugal impeller.	27
2.8	Definition of the meridional coordinate m.	28
2.9	Blade to blade view of two adjacent impeller blades.	28
2.10	Side view of a single stage compressor	29
2.11	Characteristic curve plotted by flow and work coefficient	30
2.12	Characteristic curve plotted by mass flow rate and pressure ratio as well as polytropic efficiency	31
2.13	Centrifugal compressor impeller with boundaries for mean line computation. Boundaries depicted by green faces, mean filament marked as blue line. . .	32
2.14	Observation of the fluid motion in a pipe by Euler and Lagrange description	33
2.15	Velocity triangles for a centrifugal compressor.	35
2.16	Simplified flow in the meridional plane	37
2.17	Pressure distribution in the crosswise plane for blades with zero lean (a-c) and blades with positive lean (d-f).	38
2.18	Definition of the pressure side (PS) and the suction side (SS) of the blade. .	38
2.19	Schematic illustration of the different channel vortices	39
2.20	Exit velocity triangle for blade and real flow angle	41
2.21	Deformation and motion of a continuum body	42
2.22	Deformation of a curve	43
2.23	Deformation of a line element	45
2.24	Traction vectors acting on an infinitesimal small surface element	46
2.25	Number of samples for one- to ten-dimensional problems generated by systematic sampling methods (Linear sampling, quadratic sampling, central composite design, full factorial design with 3,4,5 values per dimension. . . .	49
2.26	Generalized flowchart for nature inspired optimization.	57
2.27	Bézier curve of degree 4.	59
3.1	Flow model for the Stodola slip factor	62

3.2	Prediction of the polytropic efficiency in dependence of flow coefficient and tip speed Mach number	64
3.3	Side view of a single stage compressor with stations for mean line computation.	65
3.4	Fundamental principle of loss model performance prediction.	67
3.5	Overview of loss models for centrifugal compressor stages	68
3.6	Placement of S1 and S2 stream surfaces in the flow channel of an axial machine. Image taken from [Wu52].	69
3.7	Mesh on a S2 surface with global r,z and local curvilinear η,ξ coordinate systems.	70
3.8	Flowchart of the stream surface algorithm.	71
4.1	Histogram (left) and correlation matrix (right) for a Latin hypercube sampling of a 20 dimensional test function consisting of 100 samples.	76
4.2	Composed two dimensional test function.	78
4.3	Histogram of a sampling generated by rejection sampling for a 2d test function.	80
4.4	Histogram and correlation matrix for a sampling consisting of 100 samples generated by acceptance rejection sampling for a 20d test function.	80
4.5	Histogram of a sampling generated by the Metropolis Hastings algorithm for a 2d test function.	82
4.6	Histogram and correlation matrix for a sampling consisting of 100 samples generated by the Metropolis Hastings algorithm for a 20d test function.	83
4.7	Histogram of four samplings generated by the advanced Metropolis Hastings algorithm for a 20d test function.	85
4.8	Correlation matrix of a sampling generated by the advanced Metropolis Hastings algorithm for a 20d test function.	86
4.9	Histogram and correlation matrix for a sampling consisting of 1000 samples generated by the advanced Metropolis Hastings algorithm for a 20d test function.	87
5.1	Sample classification of a 2-dimensional test function	90
5.2	Flowchart of the filtered sampling algorithm	91
5.3	Schematic representation of the Manhattan distance (red, blue and green line) between two points “P“ and “Q“ in comparison with the Euclidean distance (dashed black line).	92
5.4	Weighting function used in the classification to control the class boundaries in terms of sample quality and the class sizes.	93
5.5	Histogram and correlation matrix for a sampling consisting of 100 samples generated by the filtered sampling algorithm for a 20d test function (Mahalanobis distance).	94
5.6	Histograms and correlation matrices for a samplings consisting of 100 samples generated by the filtered sampling algorithm for a 20d test function with different distance functions.	95

6.1	Influence of the inlet shroud diameter on the inlet velocity triangles at shroud.	99
6.2	Meridional contours with relevant parameters.	106
6.3	Parameters describing the hub contour.	106
6.4	Definition of the blade height distribution.	110
6.5	Alignment of a blade height circle on the hub curve.	110
6.6	Definition of the shroud curve.	112
6.7	Smoothed shroud curve (Threshold angle 3°).	112
6.8	Definition of the leading edge in the meridional view.	113
6.9	Parametrization of the circumferential blade angle distribution $\vartheta(m)$ and resulting relative blade angle distribution $\beta(m)$ (dotted).	114
6.10	Parametrization of the impeller disc.	116
6.11	Side view of a single stage compressor with stations for mean line computation.	118
6.12	Definition of the throat width and throat area.	120
6.13	Schematic illustration of a compressor characteristic.	129
6.14	Comparison of an operation characteristic predicted by one dimensional loss model and three dimensional CFD computations.	130
6.15	Definition of the target values for the loss model calibration.	131
6.16	Pareto front for one optimization run.	133
6.17	Definition of the sigma level for the rating of optima on the pareto front.	133
6.18	Comparison of one dimensional loss model and three dimensional CFD results for two arbitrary mid pressure impellers.	136
6.19	Distributions of the deviations between loss model and CFD prediction for the calibrated and the uncalibrated model (mid-pressure impeller).	136
6.20	Comparison of one dimensional loss model and three dimensional CFD results for two arbitrary high pressure impellers.	138
6.21	Distributions of the deviations between loss model and CFD prediction for the calibrated and the uncalibrated model (high pressure impeller).	138
6.22	Mesh of an impeller with splitter blades in TurboGrid visualized on a surface of constant span (yellow). The mesh topology is visualized by purple lines.	139
6.23	Result of the mesh sensitivity test.	140
6.23	Result of the mesh sensitivity test (continued).	140
6.24	Overview of the CFD boundary conditions.	141
6.25	Principle of the computation of a speedline illustrated on a generic compressor characteristic (“1” - Start, “2” - Switch to mass flow outlet, “3” - Failed designs near surge, “4” - Approximated surge margin).	142
6.26	Rating of the operation characteristic in terms of the design point.	144
6.27	Boundary conditions for the FEA computations.	145
6.28		147
6.29	Workflow of the optimization method.	149
7.1	Characteristic of the baseline mid-pressure impeller.	152

7.2	Flow in the baseline impeller (left: 3d streamlines colored by Mach number, right: blade to blade visualization of the Mach number distribution at mid-span).	153
7.3	Structure mechanic loading of the baseline mid-pressure impeller.	154
7.4	Distribution of the normalized mass flow rates at the stability limits for both DOEs.	156
7.5	Distribution of the polytropic stage efficiencies and the pressure ratios at the design point for both DOEs.	156
7.6	Distribution of the normalized maximum stress for both DOEs.	157
7.7	Distribution of the normalized deformations for both DOEs.	158
7.8	Prediction qualities of both metamodels.	159
7.9	Residuals for metamodels based on both DOEs.	161
7.9	Residuals for metamodels based on both DOEs (continued).	162
7.10	Results of the first optimization scenario for the mid-pressure impeller.	163
7.11	Results of the second optimization scenario for the mid-pressure impeller.	164
7.12	Characteristic of the baseline high-pressure impeller.	165
7.13	Flow in the baseline impeller (left: 3d streamlines colored by Mach number, right: blade to blade visualization of the Mach number distribution at mid-span).	166
7.14	Structure mechanic loading of the baseline high-pressure impeller.	167
7.15	Distribution of the normalized mass flow rates at the stability limits for both DOEs.	169
7.16	Distribution of the polytropic efficiency and the design point pressure ratio for both DOEs.	170
7.17	Distribution of the normalized maximum stress for both DOEs.	171
7.18	Distributions of the normalized deformations for both DOEs.	171
7.18	Distributions of the normalized deformations for both DOEs (continued).	172
7.19	Prediction qualities of both metamodels.	173
7.20	Residuals for metamodels based on both DOEs.	174
7.20	Residuals for metamodels based on both DOEs (continued).	175
7.21	Flow in the baseline (top) and optimized impeller (bottom) (left: 3d streamlines colored by Mach number, right: blade to blade visualization of the Mach number distribution at mid-span). The optimized impeller is generated by an optimization carried out on the metamodel based on filtered sampling.	177
7.22	Results of the optimization for the high-pressure impeller.	178
7.23	Location of the designs in the Cordier diagram (underlying diagram taken from [Eng07]).	179
7.24	Distribution of the surge and choke mass flow rates.	181
7.25	Distribution of the polytropic efficiency and the design point pressure ratio.	182
7.26	Prediction qualities the metamodel.	183
7.27	Metamodel residuals of the normalized choke and surge mass flow rates.	184
7.28	Metamodel residuals of the normalized pressure ratio and the polytropic stage efficiency.	184
7.29	Operation characteristic of the mid-pressure impeller.	185

7.30	Flow in the optimized impeller (left: 3d streamlines colored by Mach number, right: blade to blade visualization of the Mach number distribution at mid-span).	186
8.1	Comparison of the testcases in terms of feasible designs.	189

List of Tables

2.1	Dimensions and parameters of systems in dimensional analysis	24
2.2	Dimensions and parameters for dimensional analysis of turbomachines . . .	24
2.3	Exponent comparison	25
3.1	Input and output quantities for preliminary compressor design	66
6.1	Input parameters for preliminary design	98
6.2	Fluid dynamically relevant geometric quantities	105
6.3	Derivatives of the Bernstein polynomials.	107
6.4	Parametrization of the hub spline.	109
6.5	Parametrization of the circumferential blade angle spline.	114
6.6	Parametrization of the blade.	115
6.7	Parametrization of the impeller.	117
6.8	List of loss model parameters.	131
6.9	Settings of the evolutionary optimization algorithm.	134
6.10	Settings of the evolutionary optimization algorithm.	134
6.11	Sigma levels of the pareto-optimal designs and uncalibrated start design. . .	135
6.12	Sigma levels of the pareto-optimal designs and uncalibrated start design. . .	137
6.13	CFD setup and boundary conditions.	141
6.14	FEA setup and boundary conditions.	145
7.1	Global dimensions and performance data of the mid-pressure impeller. . . .	152
7.2	Comparison of the CoP values for both metamodels.	159
7.3	Objectives and constraints of the optimization scenarios.	162
7.4	Structure mechanic results of baseline and optimized impeller.	163
7.5	Structure mechanic results of baseline and optimized impeller.	164
7.6	Global dimensions and performance data of the high-pressure impeller. . . .	165
7.7	Comparison of the CoP values for both metamodels.	174
7.8	Objectives and constraints.	176
7.9	Structure mechanic results of baseline and optimized impeller.	178
7.10	Global dimensions and performance data for the Design-by-Optimization Impeller.	180
7.11	CoP values of the metamodel.	183
7.12	Objectives and constraints.	185

Academic Curriculum Vitae

Christoph Schemmann

Research Center “Computer simulation in mechanical engineering“
Dortmund University of Applied Sciences and Arts
Sonnenstr. 96, 44139 Dortmund, Germany
Email: schemmann@fh-dortmund.de
Date of Birth: July 20th, 1982
Place of Birth: Hagen, Germany
Citizenship: German

Education

- Ph.D: Computational Mechanics, Institute of Structural Mechanics, Bauhaus-Universität Weimar, Germany, 2012-2018.
- M.Eng: Product Design and Simulation, Dortmund University of Applied Sciences and Arts, Germany, 2009-2011.
- Dipl.-Ing: Mechanical Engineering, Dortmund University of Applied Sciences and Arts, Germany, 2003-2008.

Skills and Expertise

Matlab, C/C++/C#, Fortran, Python, Visual Basic, ANSYS, CFX, optiSLang, Siemens NX, DSS CATIA, MS-Office, L^AT_EX

Refereed Journal and Conference Publications

1. Marius Geller, Christoph Schemmann, Norbert Kluck *Simulation of radial journal bearings using the FSI approach and a multi-phase model with integrated cavitation*. Progress in Computational Fluid Dynamics, An International Journal 14(1):14-23, 2014
2. Christoph Schemmann, Marius Geller, Norbert Kluck *A Multi-Fidelity Sampling Method for Efficient Design and Optimization of Centrifugal Compressor Impellers*. ASME Turbo Expo 2017: Turbomachinery Technical Conference and Exposition, GT2018-75160, 11.-15.06.2018, Oslo, Norway
3. Marius Geller, Christoph Schemmann, Norbert Kluck *Optimization of the Operation Characteristic of a Highly Stressed Centrifugal Compressor Impeller Using Automated Optimization and Metamodeling Methods*. ASME Turbo Expo 2017: Turbomachinery Technical Conference and Exposition, GT2017-63262, 25.-30.06.2017, Charlotte (NC), USA
4. Marius Geller, Christoph Schemmann, Norbert Kluck *Identification of Loss Model Parameters for Highly Loaded Centrifugal Impellers*. 15th International Probabilistic Workshop, 27.-29.09.2017, Dresden, Germany

Ehrenwörtliche Erklärung

Ich erkläre hiermit ehrenwörtlich, dass ich die vorliegende Arbeit ohne unzulässige Hilfe Dritter und ohne Benutzung anderer als der angegebenen Hilfsmittel angefertigt habe. Die aus anderen Quellen direkt oder indirekt übernommenen Daten und Konzepte sind unter Angabe der Quelle gekennzeichnet.

Bei der Auswahl und Auswertung folgenden Materials haben mir die nachstehend aufgeführten Personen in der jeweils beschriebenen Weise unentgeltlich geholfen:

1. —

Weitere Personen waren an der inhaltlich-materiellen Erstellung der vorliegenden Arbeit nicht beteiligt. Insbesondere habe ich hierfür nicht die entgeltliche Hilfe von Vermittlungs- bzw. Beratungsdiensten (Promotionsberater oder anderer Personen) in Anspruch genommen. Niemand hat von mir unmittelbar oder mittelbar geldwerte Leistungen für Arbeiten erhalten, die im Zusammenhang mit dem Inhalt der vorgelegten Dissertation stehen.

Die Arbeit wurde bisher weder im In- noch im Ausland in gleicher oder ähnlicher Form einer anderen Prüfungsbehörde vorgelegt.

Ich versichere ehrenwörtlich, dass ich nach bestem Wissen die reine Wahrheit gesagt und nichts verschwiegen habe.

Ort, Datum

Unterschrift